OPTIMIZATION STUDIES ON THERMAL AND MECHANICAL MANUFACTURING PROCESSES FOR MULTIFILAMENT SUPERCONDUCTING TAPE AND WIRE

A Thesis

by

BURAK BASARAN

Submitted to the Office of Graduate Studies of
Texas A&M University
in partial fulfillment of the requirements for the degree of

MASTER OF SCIENCE

August 2003

Major Subject: Mechanical Engineering

OPTIMIZATION STUDIES ON THERMAL AND MECHANICAL MANUFACTURING PROCESSES FOR MULTIFILAMENT SUPERCONDUCTING TAPE AND WIRE

A Thesis

by

BURAK BASARAN

Submitted to Texas A&M University
in partial fulfillment of the requirements
for the degree of

MASTER OF SCIENCE

Approved as to style and content by:

Mustafa Yavuz (Co-Chair of Committee)	Peter M. McIntyre (Co-Chair of Committee)
Ibrahim Karaman (Member)	Harry A. Hogan (Member)
	Dennis L. O'Neal (Head of Department)

August 2003

Major Subject: Mechanical Engineering

ABSTRACT

Optimization Studies on Thermal and Mechanical Manufacturing Processes for
Multifilament Superconducting Tape and Wire. (August 2003)
Burak Basaran, B.S., Osmangazi University, Turkey;
M.S., Gazi University, Turkey
Co-Chairs of Advisory Committee: Dr. Mustafa Yavuz
Dr. Peter M. McIntyre

There are many parameters that significantly affect the electrical performance of ceramic-core superconducting composite wire and tapes, which remain ambiguous and require more labor on their optimization. BSCCO 2212 has not been paid the attention and investment it deserves. In this regard, all optimization efforts were made for BSCCO 2223. In our work, a practical and inexpensive manufacturing method, thermally and mechanically optimized for Pb doped BiSrCaCuO 2212 superconducting multifilament (38 filaments) wires and tapes, was successfully employed. Optimized parameters can be classified under material, mechanical (deformation) and heat treatment (thermal) subgroups. Parameters involved with materials included investigation of deformation behavior of two different sheath metals; pure silver and 0.02% magnesia dispersion reinforced silver alloy. Pb doped BiSrCaCuO 2212 ceramic superconductor powder, the other source of material related parameters, was synthesized following the “Thermal Co-decomposition or Wet Mix” method. Fabrication of mono and multifilament wires with Oxide Powder in Tube (OPIT) method followed next. Optimization of drawing deformation was practiced to achieve the best ceramic grain alignment and smoother ceramic powder core/metal sheath interface in order to avoid “sausaging” in wires. Rolling of the wire products into tapes by following different deformation regimes was the other manufacturing stage of the project. Variable and constant reduction-per-pass deformation paths were employed to reveal their effects on our composites with distinct sheath material and filament formation. The search for the best (optimum) heat treatment schedule for our Bi2212 superconductor composites, a modified version of “step solidification partial melting”, was employed successfully. A solution through tried recipes for the bubbling problem that occurred with our tapes was also addressed. Electrical performance tests of fully reacted wires were carried out in our laboratory and very promising results were attained.

This thesis is dedicated to my beloved mother, father and sister:
For their endless affection and unconditional faith in me…

ACKNOWLEDGEMENTS

This thesis is the culmination of intense effort with invaluable assistance from the individuals cited below:

First of all, I would like to thank my advisor, Dr. Mustafa Yavuz, for his guidance, trust and financial support that composed the backbone of our project.

I am very much indebted to the Physics Magnet Lab Research Group leader and my committee co-chair, Dr. Peter McIntyre, for letting me be a member of his research group and sharing technical equipment. He was also generous in covering part of our supply expenses. Without his trust and support, this work would have not been possible.

The understanding and supportive approach of my committee members, Dr. Ibrahim Karaman and Dr. Harry Hogan, is also highly appreciated.

Physics Magnet Lab research personnel, from each of whom I learned something new everyday we spent together, all deserve special thanks:

I consider myself lucky to have met Mr. William Henchel, a real companion who got me started with the hardest part of all, purchase of Ag tubes, and provided nonstop support, both technical and emotional, throughout the whole project.

My “Aga”, Dr. Akhdiyor Sattarov, is another companion I made. He guided me by his inspiring advice and critique at the most crucial time in every stage of the project. I am very much indebted for his leadership, corrections and moral support.

Mr. Timothy Elliot, the most practical man I have known, was always there for me with his broad knowledge. His precious help has been very much appreciated, as it saved me from many pit-falls, and much burden.

Dr. Alfred McInturff, Mr. Andrew Jaisle and Mr. Raymond Blackburn also made invaluable contributions. Many thanks for their skilled support and their friendship. Dr. McInturff’s invaluable guidance on the handling of cryogenics and electrical performance tests of wires deserves special appreciation.

TAMU ECAE Research Group leader, Dr. Ted Hartwig, made his lab and equipment available for our project; thus the fabrication of composite wires and tapes became possible. The very beneficial support and advice from ECAE research personnel Mr. Robert Barber were also highly appreciated.

I would like to thank Dr. Gan Liang of the Physics Department at Sam Houston State University for providing us with the power source for the electrical performance tests.

Dr. Ray Guillemette of TAMU Geology Department SEM Center deserves special thanks for his effort and the countless magnificent SEM pictures we took together. Without his contribution and support of great worth, computer image analysis would not have been possible.

Mr. William Merka of TAMU Chemistry Department Glasssshop and I spent long hours to fix the quartz tubes of the tubular furnace. I very much appreciated his sincere help, informative and entertaining conversations and patience with the tedious jobs I brought in.

My sponsor, the Fulbright Association and Fulbright Turkish Commission, made it possible for me to have this precious advancement in my life, both technical and personal, through the scholarship I was awarded. I am indebted for this invaluable chance and their trust. The personnel at the Institute of International Education, IIE Houston, also receive thanks for their support and understanding.

Ms. Violetta Cook and Ms. Nancy Barnes of TAMU Sponsored Students Service deserve the most special thanks for being my family here in College Station. Both of them saved me lots of trouble and helped me find my way through unassailable looking bureaucracy.

My former professors who encouraged and supported me to study abroad: Dr. Ali U. Erdem, Dr. Can Cogun, Dr. Hasmet Turkoglu and Dr. Nuri Yucel are paid my sincere tributes and respects.

I heartily thank my numerous friends who shared their labs, equipment, and knowledge and cheered me up. Among those, Mr. Refik Sahin and Ms. Carol Treece, deserve special thanks for their time and effort spent on the proof reading of the manuscript.

Last but not least, my beloved family: mother Atiye, father Alhas and sister Banu deserve the most special thanks for their everlasting, unconditional faith in me. Despite the endlessly seeming miles between us, I have always felt their compassionate support throughout my quest in the U.S.

TABLE OF CONTENTS

Page

ABSTRACT iii

DEDICATION v

ACKNOWLEDGEMENTS vi

TABLE OF CONTENTS ix

LIST OF FIGURES xi

LIST OF TABLES xviii

INTRODUCTION 1

- Superconductivity and Superconductors 1
- Objectives and Motivation for the Study 7

FABRICATION OF MONO AND MULTIFILAMENT WIRES AND TAPES 10

- Bi(Pb)-2212 Powder Preparation 10
- Literature Survey on Superconductor Tape and Wire Manufacturing: OPIT Method, Drawing and Rolling Processes, Silver Clad Sheath Properties 20
- Silver Clad Sheath: Silver Alloys Used In Composite BSCCO Superconductors 61
- Fabrication of Mono and Multifilament Wire 74
- Fabrication of Mono and Multifilament Tape 86

KINETICS, PHASE TRANSFORMATION AND GRAIN ALIGNMENT OF Bi(Pb)-Sr-Ca-Cu-O SYSTEM 93

- Literature Survey 93
- Heat Treatment of Bi(Pb)2212 Wires and Tapes: Step Solidification Partial Melt 133
- Bubbling Problem with Tapes: Reasons and Prevention 134

EVALUATION OF STRUCTURAL AND CHEMICAL INTEGRITY OF WIRES AND TAPES 140

- Image Analysis and Results 140
- XRD Analysis and Results 168
- Investigation of Interface and Filament Pattern for Sausaging and Cracks 179

ELECTRICAL PERFORMANCE EVALUATION OF Bi2212 MONO AND MULTIFILAMENT WIRES 190

SUMMARY, COMPARISON AND CONCLUSIONS 202
REFERENCES 207
APPENDIX 1 213
APPENDIX 2 214
APPENDIX 3 231
APPENDIX 4 234
APPENDIX 5 255
APPENDIX 6 261
APPENDIX 7 269
APPENDIX 8 272
VITA 300

LIST OF FIGURES

FIGURE Page

1 Unit cell structure of Bi-Sr-Ca-Cu-O superconductor (Bi2212) 2

2 Plate like grains as colonies and their boundaries 3

3 Brick Wall model (a) and Railroad Switch model (b) of supercurrent transport 4

4 Flow chart of parameters and procedure 9

5 Solid Works CAD assembly images of custom-made stainless steel flanges and lids 14

6 The tubular furnace used for heat treatments 15

7 Powder samples after heating and two calcining treatments, from left to right, respectively 18

8 Schematic diagram of OPIT method to make wires and tapes 20

9 Plate like BiSrCaCuO crystal and its texturing directions 22

10 Effect of roll diameter on deformation zone geometry 24

11 (a) geometry of the deformation zone (b) approximation of rolling to uniaxial pressing 25

12 Mohr circles representing the relation between confinement stresses, σ_L and σ_W, and the compaction stress, σ_H 25

13 Schematic of the direction of plastic strain in the roller gap corresponding to; (a) Small rollers and wide tape (b) Large rollers and narrow tape 26

14 Schematic representation of the three factors that the formation of non-uniformity in the core/Ag interface can be related to 27

15 Stress states for pressing and rolling processes applied for tapes 28

16 Cracking patterns during rolling and pressing processes on HTSCs 29

17 Cracks in HTSC core in Ag sheathed tape (1) transverse section after pressing (2) longitudinal section after rolling 30

18 Stress states during drawing and flat rolling processes 31

19 Schematics of compression process for slab and inhomogeneous deformation 32

20 Tape rolling 34

21 Wire drawing 35

FIGURE Page

22 Mass distribution under homogeneous and inhomogeneous deformations 37

23 Powder flow during rolling 38

24 Sausaging formation during rolling operations [5] 39

25 Cross section of an as drawn multifilament BSCCO wire and its deformed states into tape by pressing 41

26 Vickers Hardness values for BSCCO core in tape transverse cross section [5]. 43

27 Schematic illustration of changes in texturing, connectivity and J_c [12] 49

28 J_c distribution in a silver sheathed superconducting tape [15] 50

29 Longitudinal cross sections of multifilament tapes; (a) deformed via CR (constant reduction) deformation routine (b) deformed via IR (increasing reduction) deformation routine [26]. 59

30 Variation of tensile strength (σ_c) and max strain (ε_{max}) with the total amount of cold drawing [27] 65

31 Equilibrium phase diagram of silver rich magnesium alloys $Ag_{100-x}Mg_x$ [27] 70

32 SEM backscattered picture for a polished cross section on an $Ag_{99.5}Mg_{0.5}$ commercial alloy tube after annealing in air for 200 hr at 800°C [27] 71

33 Polished transverse cross section SEM picture of a monofilament Bi(Pb)2223 tape with $Ag_{81}Cu_5Ti_{14}$ after complete heat treat [27] 72

34 Hydraulic drawing bench employed for drawing operations 74

35 Ruptured part of the powder-filled-tube at very early stage of drawing operation 76

36 The big and the small swagers 77

37 BSE image of hexagonal filament with 0.0480” (~1.22 mm) diameter, BB4_h48_63x 79

38 Just after 38 hexagonal filaments packed into 8” long tube, ready for swaging and drawing operations 80

39 BSE image of Ag filament-Mg tube wire with 38 filaments, 0.0600” (1.52 mm) diameter, BB4_a60_63x 82

FIGURE Page

40 Schematic explanation of cup-and-cone-fracture, (a) initial necking, (b) small cavity formation, (c) coalescence of cavities from a crack, (d) crack propagation, (e) final shear fracture at a 45° angle relative to the tensile direction [30] 83

41 Classical cup-and-cone-fracture observed at early stage of drawing operation on Mg filament-Ag tube multifilament wire 84

42 Rolling mill used for tape rolling operations 86

43 Rolling mill calibration chart 88

44 Binary images of 38 filament tape, in sequence, to represent aspect ratio variation at each rolling deformation step 90

45 BSE images of wire and subsequent rolling deformation steps, 48, 29, 19 for 5% reduction, 0 0500” diameter, Mg tube monofilament tape, BB3_Mg_63x. 91

46 Tentative phase diagram of 2-2-(n-1)-n series: *1*=2201+23.7Å-phase, *2*=2212, *3*=2223, *CaCu* = $(Ca_{2-x}Sr_x)CuO_3$, *CaPb* = Ca_2PbO_4, *L*=Liquid [31] 94

47 Microstructures of $(Bi_{1\ 7}Pb_{0\ 4})Sr_2CaCu_{1\ 95}O_y$ samples partially melted in 21% oxygen purge, (a) at 860°C, (b) at 840°C. B= 1:1 AEC, C= 2:4 CF, D= (Bi,Pb)-2212, H= 4:5:1, L= Liquid [32]. 96

48 XRD pattern for $(Bi_{1\ 72}Pb_{0\ 34})\ Sr_{1\ 83}Ca_{0\ 97}Cu_{1\ 13}O_y$ heat treated in air at 860°C, I symbolizes (Bi,Pb)-2212 [33]. 98

49 Heat treatment schedule for melt processing by Hellstrom et al [34] 101

50 Heat treatment schedule for step solidification melt processing by Motowidlo et al [35] 103

51 Heat treatment schedule by Hu et al [36] 104

52 Tape melted in air at 890°C for (a) 0 min (b) 10 min (c) 30 min (d) 60 min. 106

53 Tape melted in 0.01 atm for 10 min at (a) 840°C (b) 842°C 107

54 Tape melted in 1 atm at 900°C for (a) 0 min (b) 10 min (c) 30 min (d) 60 min 108

55 Cooling down states of tape melted in 1 atm starting from 900°C to (a) 890°C (b) 870°C (c) 860°C (d) 840°C 109

56 Fully processed tape in 1 atm O_2 111

FIGURE Page

57 Schedule employed for partial melt heat treatment by Thangaraj et al [38] 112

58 XRD results of the starting powder and the core from the heat-treated tapes under air and oxygen purge [38] 114

59 SEM image of tape core melt processed in air with the conditions of T_m= 890°C and C_R= 10°C/hr [38] 115

60 SEM image of melt processed tapes in oxygen (a) T_m= 890°C and C_R= 10°C/h (b) T_m= 890°C and C_R= 5°C/h [38] 116

61 SEM images of tapes (a) in the flawless region (b) near the bubble defect [38] 118

62 Schematic model of Bi2212 during cooling process [39] 121

63 SEM images of tapes quenched from partially melted state at (a) 830°C (b) 865°C [39]. 122

64 SEM image of tape solidified at 865°C for 12 hours of solidification time [39] 123

65 Schematic of a typical melt-process heat treatment divided into four regions [40] 125

66 Step Solidification heat treatment original schedule by Ray et al [40] 127

67 TIG welded mono and multifilament wire specimens before heat treatment 134

68 Tapes severely deformed due to bubbling formation following step solidification melt processing 135

69 Step solidification partial melt heat treatment 137

70 XRD graphs of original (fresh) and reheated precursor powders together 138

71 BSE image of Mg filament-Mg tube wire with 38 filaments, 0.0600” (1.52 mm) diameter, BB4_m60_63x 141

72 Area change for BB1 monofilament Ag sheath tape, 25% constant reduction/pass, 0.0500” dia 153

73 Area change for BB1 monofilament Mg sheath tape, 25% constant reduction/pass, 0.0500” dia 153

74 Width and thickness change for BB1 monofilament Ag sheath tape, 25% constant reduction/pass, 0.0500” dia 154

FIGURE Page

75 Width and thickness change for BB1 monofilament Mg sheath tape, 25% constant reduction/pass, 0 0500” dia.. 154

76 Normalized aspect ratio for BB1 monofilament Ag and Mg sheath tapes, 25% constant reduction/pass, 0.0500” dia.. 155

77 Binary image comparison for aspect ratio variation of monofilament tapes (BB1) with pure silver and Mg/Ag alloy sheaths deformed by 25% constant reduction per pass 157

78 Guide picture for points where EDS and WDS analysis took place on tape sample BB2_Mg32 162

79 EDS diffraction pattern for dark (dk) gray phase... 163

80 EDS diffraction pattern for medium (med) gray phase................................ 164

81 EDS diffraction pattern for brightest phase.. 164

82 EDS diffraction pattern for lighter gray phase 165

83 EDS diffraction pattern for brighter phase 165

84 EDS diffraction pattern for 250-micron diameter area 166

85 EDS diffraction pattern for higher Pb phase 166

86 X ray maps for distribution of elements in the background 167

87 XRD pattern comparison of Bi(Pb)2212 fully reacted powder (black line) and standard 46-0431 Calcium Copper Strontium Bismuth Oxide (blue line)... 168

88 XRD pattern for Bi2212 core after step solidification heat treatment under air purge 169

89 XRD patterns of BiPbSrCaCuO and BiSrCaCuO polycrystalline precursor powders for comparison with XRD pattern for our Bi2212 powder precursor after second calcination [41] 170

90 XRD pattern for Bi2212 powder precursor after first calcination 172

91 XRD pattern for Bi2212 powder precursor after second calcination........... 173

92 XRD pattern for Bi2212 core after step solidification heat treatment under air purge... 174

93 Close view of a bubbling burst on Bi2212 tape after step solidification heat treatment under oxygen purge 175

FIGURE Page

94 XRD pattern for Bi2212 core after step solidification heat treatment under oxygen purge 176

95 XRD pattern for Bi2212 precursor powder after second calcination step under air 177

96 XRD pattern for Bi2212 precursor powder after reheating process under air 178

97 Merged longitudinal cross sectional view Ag filament-Ag tube tape with 38 filaments, 25% reduction per pass, starting wire diameter 0.0600”, AgT600_300x 182

98 Close look at core/Ag interface in longitudinal cross section of Ag filament-Mg tube tape with thickness larger than final tape thickness, starting diameter 0.0500”), AgT25_2000x 183

99 Close look at core/Ag interface in longitudinal cross section of Mg filament-Mg tube tape with thickness larger than final tape thickness, starting diameter 0.0500”), MgT25_2000x 184

100 A general look at longitudinal cross section of Ag filament-Mg tube tape with thickness (0.0135”) greater than final tape thickness (0.0060”), starting wire diameter 0.0500”, AgT25_200x 185

101 A closer look at filament discontinuity in-Ag filament-Ag tube tape with thickness 0.0060”, starting wire diameter 0.0600”, AgT600_1000x 186

102 A general look at longitudinal cross section of Mg filament-Mg tube tape with thickness (0.0135”) greater than final tape thickness (0.0060”), starting wire diameter 0.0500”, MgT25_200x 187

103 Merged BSE image of longitudinal cross section of monofilament wire with 0.0450” (1.143 mm) diameter, BB9_mono45_63x 188

104 Closer look of core/pure Ag interface monofilament wire with 0.0450” (1.143 mm) diameter, mono45up200x 189

105 Top-head of the test setup with wire samples and all cables attached ready to be immersed into cryogenic liquid 190

106 Closer view of the end of the top-head where the samples are attached with all cable connections ready 191

107 Schematic of the test setup with the top-head immersed into dewar 192

108 I-V (Current-Voltage) graph for Ag filament-Ag tube, 38 filament wire, 0.0500” diameter, in liquid He 195

FIGURE Page

109 I-V (Current-Voltage) graph for Mg filament-Ag tube, 38 filament wire, 0.0500” diameter, in liquid He 196

110 I-V (Current-Voltage) graph for Ag filament-Mg tube, 38 filament wire, 0.0500” diameter, in liquid He 197

111 I-V (Current-Voltage) graph for Ag filament-Mg tube, 38 filament wire, 0.0500” diameter, in liquid N 198

112 I-V (Current-Voltage) graph for Ag sheath, monofilament wire, 0.0500” diameter, in liquid He 199

113 I-V (Current-Voltage) graph for Mg filament-Mg tube, 38 filament wire, 0.0500” diameter, in liquid He 200

114 I-V (Current-Voltage) graph for Mg sheath, monofilament wire, 0.0500” diameter, in liquid He 201

LIST OF TABLES

TABLE Page

1 Results summary of calculations for specific amounts of nitrate crystals used to synthesize our $Bi_{1.6}(Pb_{0.6})Sr_{1.8}Ca_{1.0}Cu_{2.0}O_{8+x}$ precursor powder by Thermal Co-decomposition or Wet Mix method 13

2 Different techniques to synthesize Bi based superconductor powders [2].... 16

3 Mechanical properties of some materials for superconductor fabrication [5] 36

4 Mechanical properties of silver and BSCCO used in FEM calculations 54

5 Most common silver-magnesium alloys and their properties [27]............... 67

6 Microhardness of silver rich Mg alloys ($Ag_{100-x}Mg_x$) as cast (argon annealed or free of tension), after intense cold working and long oxidization process 72

7 Reduction ratios between successive drawing dies; the swaging dies used and the corresponding drawing steps 75

8 Wire drawing dies utilized with respect to filament structure and sheath metal type 78

9 Tape deformation schedules applied in rolling process 87

10 Phase assemblages as a function of temperature in the melt (Bi,Pb)-2212 powder under 21% oxygen (air) purge [32].. 95

11 Assembly of phases in melt-processed 2212 under air, 1% and 7.5% oxygen purge 100

12 Phase assemblages in Bi2212 melt under various atmospheres during cooling [37] 110

13 Image analysis results for tape BB1-monoAg-25% reduction-dia500-100xBSE... 143

14 Image analysis results for tape, BB1-monoMg-25% reduction-dia500-100xBSE... 143

15 Image analysis results for tape, BB2a-multiAgfilament-Agtube-25% reduction-dia500-63xBSE.. 144

16 Image analysis results for tape, BB2b-multiAgfilament-Agtube-25% reduction-dia600-63xBSE.. 144

17 Image analysis results for tape, BB6-multi-Agfilament-Mgtube-25% reduction-dia500-63xBSE.. 145

TABLE Page

18 Image analysis results for tape, BB6-multi-Mgfilament-Mgtube-25% reduction-dia500-63xBSE 145

19 Image analysis results for tape, BB8-multi-Agfilament-Mgtube-IR1 reduction-dia500-63xBSE 146

20 Image analysis results for tape, BB8-multi-Mgfilament-Mgtube-IR1 reduction-dia500 -63xBSE 146

21 Image analysis results for tape, BB3-monoMg-5% reduction-dia500-63xBSE 147

22 Image analysis results for tape, BB5-multi-Mgfilament-Mgtube-5% reduction-dia500-63xBSE 148

23 Image analysis results for tape, BB7-multi-Agfilament-Mgtube-5% reduction-dia500-63xBSE 150

24 Image analysis results for wires 151

25 XRD analysis results for Bi2212 powder (after first calcination, not fully reacted) 172

26 XRD analysis results for Bi2212 powder (after second calcination, not fully reacted) 173

27 XRD analysis results for Bi2212 powder (core) fully reacted (heat treated) under air flow 174

28 XRD analysis results for Bi2212 powder fully reacted (heat treated) under oxygen flow 176

29 XRD analysis results for Bi2212 powder (before packed in tube; not fully reacted) 177

30 XRD analysis results for Bi2212 powder (before packed in tube; reheated to prevent excessive carbon content, not fully reacted) 178

31 Results of electrical performance evaluation test for 0.0500” diameter wire samples under liquid He with respect to 1μV criteria 193

INTRODUCTION

Superconductivity and Superconductors

When current flows through normal conductor materials, resistance against the motion of electrons occurs. Application of voltage is necessary to maintain the current flow and to make up the energy lost by resistance. A superconductor has no resistance. Some materials show modest electrical resistance at room temperature but behave as superconductors when refrigerated very close to absolute zero, 0 K. Since a superconductor has no resistance, it conveys current without the need for a potential difference. The most commonly employed coolants for superconduction and their boiling temperatures are Nitrogen, 77 K; Oxygen, 90 K; Helium, 4.2 K.

The most well known ceramic based superconductors and their *transition temperatures* (T_c) [1] are YBCO (Yttrium Barium Copper Oxide) 92 K; BSCCO (Bismuth Strontium Calcium Copper Oxide) 105 K; TBCCO (Thallium Barium Calcium Copper Oxide) 115 K; HBCCO (Mercury Barium Calcium Copper Oxide) 135 K.

The fundamental criterion that names and separates High Temperature Superconductor (HTSC) and Low Temperature Superconductor (LTSC) is the closeness of the transition temperature of the previous to 100 K. HTSC exhibits considerably different magnetic properties than conventional metallic LTSC ones.

In 1986, superconductors found their way out to become HTSC. Scientists Muller and Bednorz, reported that they had achieved superconducting state at temperatures up to 38 K. This was the first time to pass over 30 K borders, which had been accepted as the theoretical T_c limit for more than 20 years. As soon as superconductors had reached the values of T_c above 77K, the concept of HTSC had been announced.

The style of this thesis follows *IEEE Transactions on Applied Superconductivity*.

A major application of HTSC is high magnetic field production, namely superconducting magnets. Ceramic superconductors are the best with respect to current carrying capacity in high magnetic fields. BSCCO (Bi-Sr-Ca-Cu-O) maintains superconductivity at 20 Tesla and 20 K.

Fig.1 shows the unit cell structure of Bi-Sr-Ca-Cu-O superconductor (Bi2212). HTSCs are variations of the crystal type known as *Perovskite*. Perovskites are minerals with chemical formula ABO_3. Anisotropic behavior of HTSC ceramics is a result of their layered structure. Anisotropy facilitates the flow of electrons in one direction and inhibits flow in another.

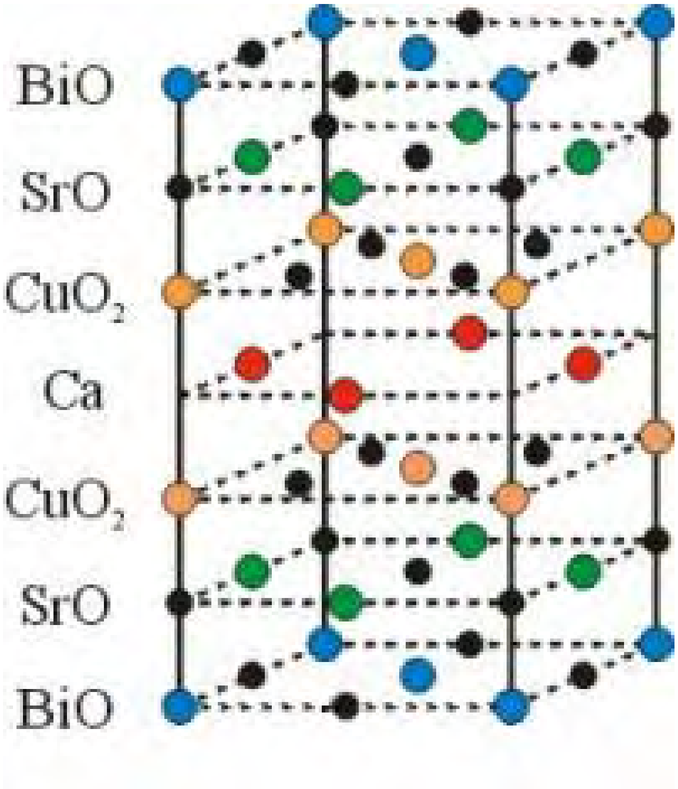

Fig.1 Unit cell structure of Bi-Sr-Ca-Cu-O superconductor (Bi2212) [2].

The CuO_2 planes are called *Conduction Planes*. These copper oxide planes are the ones through which supercurrent flow. The other planes inserted between or among the existing layers are just at the top and at the bottom of conduction planes and they are referred to as *Charge Reservoir Layers*. These planes altogether form the layered structure of superconductors (see Fig.1). When the intercalated plane contains mixed valance atoms, electrons are drawn away from the copper oxide planes. So, the holes left behind to form the pairs are needed to attain superconductivity. This mechanism is called *Charge Transfer Model*. Doping of other elements, such as Pb, provides some possible choices for placing specific atoms at various sites opened, so the electron concentrations can be arranged. T_c increases with increasing number of CuO_2 planes. *Cooper Pairs* of charge carriers move relatively freely within CuO_2 planes. When they try to move through a direction perpendicular to these planes, there comes great difficulty.

As mismatched crystal grains contact with one another, grain boundaries occur between them (Fig.2). These boundaries act as interceptors to easy flowing current, in other words they insulate layers. In superconducting state, the current is conveyed through an interwoven network of (Josephson) junctions, which are referred to as *Weak Links*.

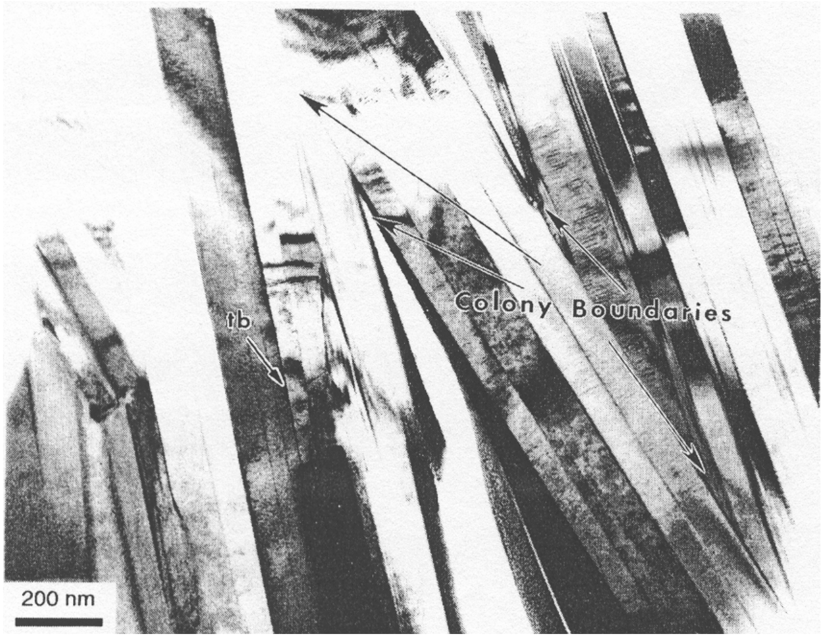

Fig.2 Plate like grains as colonies and their boundaries [2].

BSCCO conductors have polycrystalline structure, a property that requires supercurrent to cross grain boundaries. TEM studies of these superconductors reveal that they are composed of colonies of plate-like grains each 100-200 μm thick that all have about the same *c-axis* orientation.

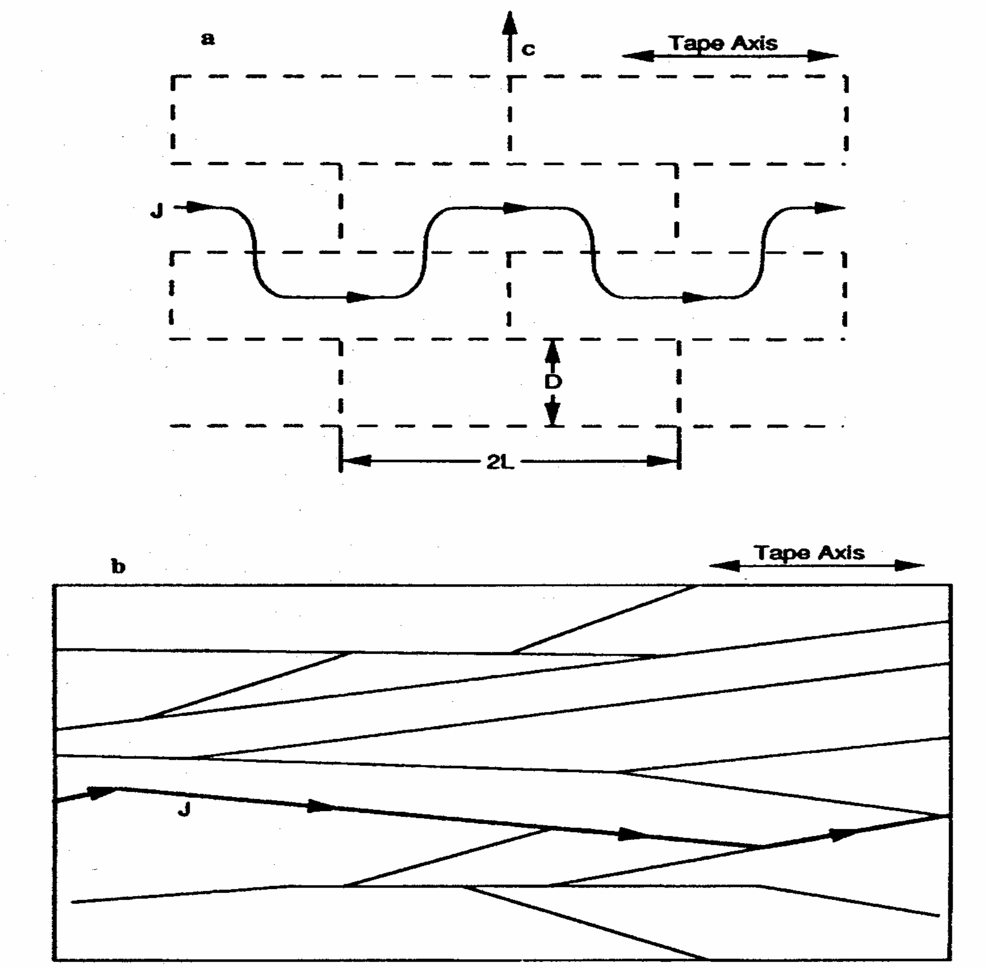

Fig.3 Brick Wall model (a) and Railroad Switch model (b) of supercurrent transport [2].

Two competing theories have been proposed to describe how the supercurrent transports across the boundaries: In the *Brick Wall model*, supercurrent flows between grains and colonies in the *c* direction, which requires the microstructure to be as highly aligned as possible to maximize the area over which current can flow in this specific direction.

The second model is known as the *Railroad Switchyard* model in which the current flows from *(001) planes* in one colony to *(001) planes* in an adjacent colony through small angle *c-axis* grain boundaries between the colonies, which permits a small amount of misalignment in the structure (see Figures 2 and 3).

As an example the most common LTSC, niobium titanium, allows lines of magnetic flux to penetrate as they show a tendency to stay put. This phenomenon is called *flux pinning*. On the other hand, the crystalline structure of copper oxide superconductors makes the flux lines fragmented. Losing the order of flux lines brings dissipation of energy and the superconductivity behavior weakens.

Ceramic superconductors exhibit anisotropic properties and the crystal structure deforms with respect to crystalline directions. Bismuth based compounds display micaceous properties and the crystal structure deforms (shears) with ease along bismuth oxide planes. This makes Bi based ceramics very versatile to shape into desired form. The main drawbacks of ceramics are their brittleness and relatively ineffective current carrying capacity.

Critical current density, (J_c), current per cross sectional area (A/cm^2), is the major electrical parameter of a superconductor's performance. There are four main problems in front of best J_c achievement: large currents in magnetic fields, fabrication of uniform long length wires, mechanical properties, joining and contact techniques.

Since ceramics have granular structure, grain boundaries impede current flow between grains. Very good alignment of grains is needed to overcome this problem. Another difficulty comes with the operating temperature of HTSC. When having high transport currents in hand, the wire heats up. Moreover, pinning of the flux lines that penetrate the material is also needed. *Lorentz Forces* move the flux lines if they are not pinned by adequate measures. Flux line movement causes losses of performance even during the superconducting state since it is a means of energy dissipation within a superconductor.

Manufacturing HTSC is not easy to accomplish. To overcome the brittleness of the ceramics, a ductile material, usually silver and its alloys is employed as the surrounding sheath. For superconducting ceramics, the raw ingredients are oxide powders. These powders are treated at high temperatures to get the desired composition. As an example, $(Bi_xPb_{2-x})Sr_2Ca_2CuO_y$ is known as 2212 by its subscripts. Here is a partial substitution of Pb for Bi. The powder is packed into a metal tube and the process of swaging-drawing-rolling takes place. The diameter of the wire may be well below 1 mm. To restore the ceramic core to superconducting state prolonged heat treatment is required. At the end, the wire may be annealed in oxygen very slowly in order to grow oxygen atoms to recover their proper positions in the lattice of crystal.

Bending radius and insulation are the other problems to overcome for magnet applications [1, 2].

The following major sections will provide information about parameters involved in powder preparation, wire/tape fabrication and heat treatment schedules of Bi2212 superconductors under the projection of the theory briefly mentioned above.

Objectives and Motivation for the Study

Superconductors mean to convey current via the most efficient way. In order to achieve that, various manufacturing parameters have been subjected to optimization by researchers. The ultimate goal of all these efforts is to increase the critical current density.

In this study, Pb doped Bi2212 ceramic core single and multifilament (38 hexagonal filaments) superconductor cable and tape manufacturing parameters are targeted for optimization.

The parameters to be modified and results of which to be observed are three folds:

Material Parameters

This group includes two different sheath materials and the powder used. The first sheath metal is 99.99% scientific grade pure silver (Ag) and the second one is precipitation hardened 0.20% Mg silver alloy. The ceramic powder employed is self-made Bi(Pb) 2212 superconducting powder with a certain particle size distribution. Packing density (OPIT), evaluation of core density for the tape having mixture of fine and coarse powder particles by micro hardness measurement.

Mechanical Manufacturing Parameters

Drawing and rolling process parameters (mechanical deformation) are under this title. Drawing die angle, drawing reduction rate, roll diameter, roll shape (flat rolling), rolling reduction per pass (h/L ratio), roll speed, working friction (use of lubricant), and varying/constant % reduction per pass are the parameters to be investigated for their effects.

Heat Treatment Parameters

The best (optimum) heat treatment schedule for Bi 2212 in accordance with mechanical deformation: the method employed is called “Step Solidification Partial Melting”. Kinematics of formation reactions of the superconducting and non-superconducting phases will be considered in detail.

Fig.4 explains the objectives and the procedure (changing parameters as well) of the study in detail, respectively.

2212 Powder preparation: same stoichiometry & synthesis method (Thermal co-decomposition) for the powder to be used
Technique for powder packing into tube: compacting with a ramrod

Powder particle size evaluation: ***affects compaction behavior during mechanical deformation (eventually sausaging) and kinetics (rate of chemical reactions under heat treat)***

Drawing process: constant die angle, constant hydraulic piston pulling speed, proper cross sectional reduction ratio: ***affects powder compaction, eventually sausaging***

Sheath material #1: pure Ag, ductile
Sheath material #2: Mg - Ag alloy, relatively brittle and durable; [pure Ag filament and outer tube], [Mg alloy filament and outer tube], [pure Ag filament - Mg alloy outer tube], [Mg alloy filament – pure Ag outer tube]: ***affects mechanical deformation characteristics (eventually sausaging) and possible poisoning of core by Mg alloy filament***

Wire manufacture (OPIT): single (∅0.045 “) and multifilament (38 hex filaments, total ∅0.076 “) cables;
heat treatment (optimum partial melting for 2212) under air or oxygen (final wire product): ***affects phase formation, bubbling, grain alignment, eventually sausaging***; no heat treatment (for further deformation to produce tape)

Rolling process: fixed roller diameter (stress distribution in core, grain alignment, sausaging), constant and varying reduction rate per pass (stress distribution in core, grain alignment), constant rolling speed, lubricant use (constant friction condition),: ***affects powder compaction, eventually sausaging***

Tape manufacture: rolling of single and multi filament wires to have single and multifilament (38 filaments) tapes, heat treatment (optimum partial melting for 2212) under air or oxygen (intermediate and final): ***affects phase formation, bubbling, grain alignment, eventually sausaging***

Electrical performance tests for all wires and tapes (4 probe technique, 1μV criteria, I_c measurement, J_c calculation)
Characterization (SEM, EDS, XRD): to observe proper grain alignment, smooth Ag /core interface formation (longitudinal cross sectional area observation for sausaging), phase formation, final product (tape & wire) transverse cross sectional area calculation by image processing: compaction calculations, Ag / core final ratio (sheath wall thickness variation)

Fig.4 Flow chart of parameters and procedure.

FABRICATION OF MONO AND MULTIFILAMENT WIRES AND TAPES

Bi(Pb)-2212 Powder Preparation

There are many different techniques to synthesize Bi based superconductor powders. Table 1 shows the major ones and provides brief explanation for each of them. In this study, $Bi(Pb)_2Sr_2CaCu_2O_x$ powders were produced by means of *Thermal Co-decomposition* or *Wet Mix* method after Yavuz [3].

The other methods and chemicals employed by various researchers will be precisely cited under the next major section Heat Treatment: Kinetics, Phase Transformation and Grain Alignment in Bi(Pb)SrCaCuO System.

Thermal Co-decomposition Method was preferred since it is one of the simplest and most inexpensive techniques. Precisely, it begins with mixing nitrates of Bi, Pb, Sr, Ca, and Cu elements in appropriate amounts with respect to the desired stoichiometry and then continues with reacting the bulk at elevated temperature where no melting occurs. Grinding the sample and re-firing are the other operations held until the reaction is completed. Large grain size of reactants can cause slow reactions and can yield larger grain size in the final product. Introduction of impurities during grinding operations in between firing is a possibility to be avoided.

In order to achieve our $\mathbf{Bi_{1.6}(Pb_{0.6})Sr_{1.8}Ca_{1.0}Cu_{2.0}O_{8+x}}$ precursor powder, nitrate crystals in the specific amounts described below are dissolved by mechanical stirring in a solution consisting of 300 ml HNO_3 (nitric acid) and 150 ml distilled water:

1) Calcium nitrate: $Ca(NO_3)_2\ 4H_2O$

Ca : 1*40.080 = 40.080
N : 2*14.007 = 28.014
O : 10*15.999 = 159.990
H : 8*1.008 = 8.064
Σ atomic weight = 236.148

Stoichiometric ratio of Ca is given as 1 (one) in the powder formula. Therefore, we need 1 (one) part of calcium nitrate to have the required element amount.

1*236.148 = 236.150 gr is found as the weight of calcium nitrate to be used.

2) Copper nitrate: $Cu(NO_3)_2\ 2\frac{1}{2}H_2O$

Cu : 1*63.546 = 63.546
N : 2*14.007 = 28.014
O : 8.5*15.999 = 135.992
H : 5*1.008 = 5.040
Σ atomic weight = 232.592

Stoichiometric ratio of Cu is given as 2 (two) in the powder formula. Therefore, we need 2 parts of copper nitrate to have the required element amount.

2*232.592 = 465.184 gr is found as the weight of copper nitrate to be mixed.

3) Lead nitrate: $Pb(NO_3)_2$

Pb : 1*207.200 = 207.200
N : 2*14.007 = 28.014
O : 6*15.999 = 95.994
Σ atomic weight = 331.208

Stoichiometric ratio of Cu is given as 0.6 in the powder formula. Therefore, we need 0.6 part of lead nitrate to have the required element amount.

0.6*331.208 = 198.725 gr is found as the weight of lead nitrate to be taken.

4) Strontium nitrate: $Sr(NO_3)_2$

Sr : 1*87.620 = 87.620
N : 2*14.007 = 28.014
O : 6*15.999 = 95.994
Σ atomic weight = 211.628

Stoichiometric ratio of Sr is given as 1.8 in the powder formula. Therefore, we need 1.8 part of strontium nitrate to have the required element amount.

1.8*211.628 = 380.930 gr is found as the weight of strontium nitrate to be mixed.

5) Bismuth nitrate: $Bi(NO_3)_3\ 5H_2O$

Bi : 1*208.980 = 208.980
N : 3*14.007 = 42.021
O : 14*15.999 = 223.986
H : 10*1.008 = 10.080
Σ atomic weight = 485.067

Stoichiometric ratio of Bi is given as 1.6 in the powder formula. Therefore, we need 1.6 part of bismuth nitrate to have the required element amount.

1.6*485.067 = 776.107 gr is found as the weight of bismuth nitrate to be mixed.

A summary of all the results can be seen in Table 1, below.

Table 1. Results summary of calculations for specific amounts of nitrate crystals used to synthesize our **$Bi_{1.6}(Pb_{0.6})Sr_{1.8}Ca_{1.0}Cu_{2.0}O_{8+x}$** precursor powder by Thermal Co-decomposition method.

Name of Nitrate Employed	***Total Amount of Composing Elements (Atomic Weight)***								
	Ca	***Cu***	***Pb***	***Sr***	***Bi***	***N***	***O***	***H***	***Total atomic weight***
Calcium Nitrate	40.080		-	-	-	28.014	159.990	8.064	236.148
Copper Nitrate	-	63.546	-	-	-	28.014	135.992	5.040	232.592
Lead Nitrate	-	-	207.200	-	-	28.014	95.994	-	331.208
Strontium Nitrate	-	-	-	87.620	-	28.014	95.994	-	211.628
Bismuth Nitrate	-	-	-	-	208.980	42.021	223.986	10.080	485.067

After dissolving was complete, the solution of nitrates was heated to evaporate the water at 75-80°C for approximately 10 hours, without boiling. The remaining was a green-bluish-white muddy bulk. Upon further heating, the melt became solid and was then removed from the steel container.

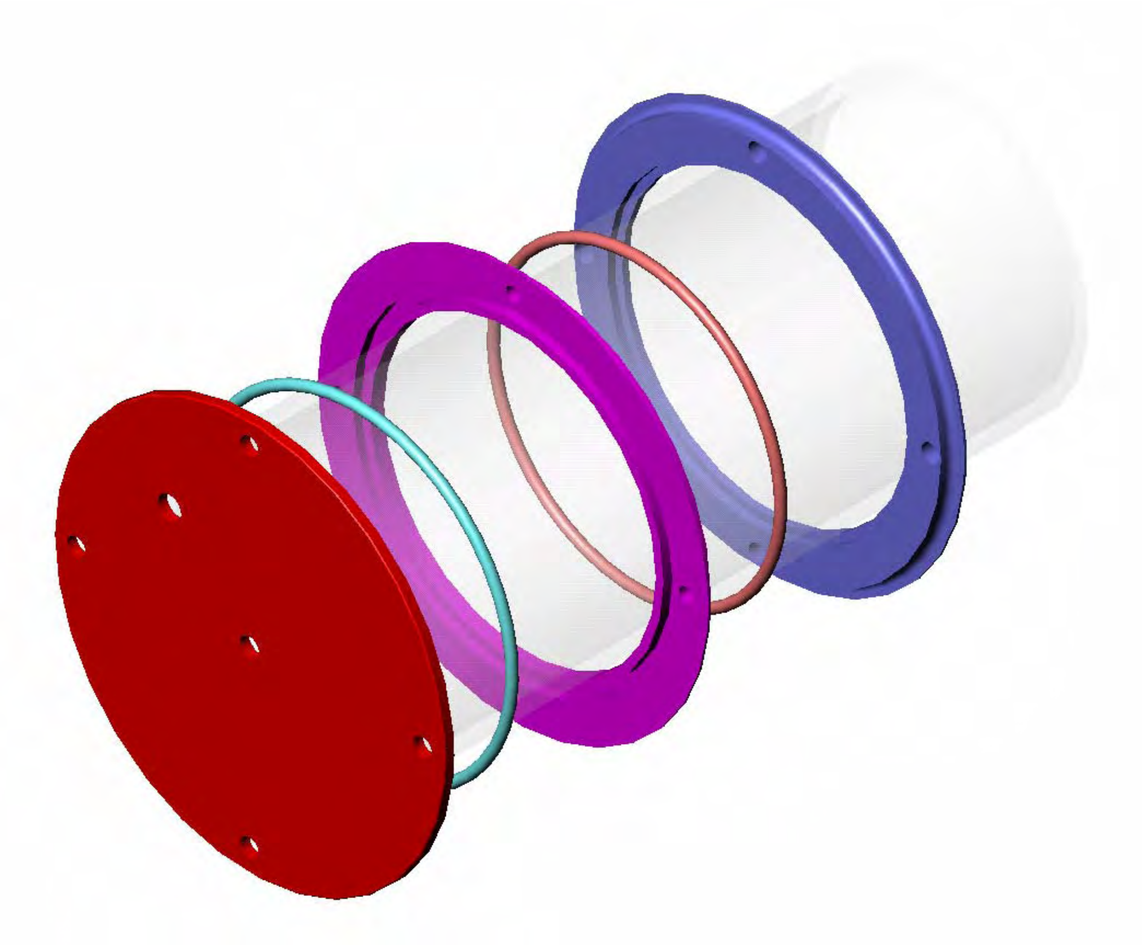

Fig.5 Solid Works CAD assembly image of custom-made stainless steel flanges and lids.

The furnace utilized for all heat treatment processes was a *Chromalox 2104 temperature controller* driven *Lindberg 59544 tubular furnace* with quartz dimensions 4.25” by 43.5” (~ 617.1 cubic inch). The quartz was sealed at two ends by o-rings nested in stainless steel flanges and lids custom-made in the machining facilities of TAMU Mechanical Engineering and Physics departments. The lids were designed to accommodate input and output tubing for gas purge and thermocouples. With proper sealing, a thermally stable control volume was provided.

Fig.6 The tubular furnace used for heat treatments.

Calibration and actual temperature gradient check of the furnace were done using a K type custom length thermocouple that was fixed into position in the tube through the lid. The difference between the readings of the furnace's own feedback thermocouple and the K type thermocouple was examined for the required temperature ranges as the lids were sealed. The hot zone control calibration curve is presented in Appendix 1.

In order to dispose of the residual water, the bulk was first heated to 300^{o}C for 60 min in air purge. Eventually, the solid achieved a dark color and was then mechanically grinded for 15 min in a mortar with pestle after the cooling to room temperature.

Table 2. Different techniques to synthesize Bi based superconductor powders [2].

Method	***Description***	***Advantages***	***Disadvantages***
Solid state reaction	Mix oxides, peroxides, carbonates, or nitrates of Bi, (Pb), Sr, Ca, and Cu. React at elevated temperature where no melting occurs. Grind sample and re-fire. Repeat until reaction is complete.	Simple, inexpensive technique.	Large grain size of reactants can cause slow reactions. Can have large grain size product. Can introduce impurities during grinding.
Co-precipitation	Dissolve Bi, (Pb), Sr, Ca and Cu compounds in acid. Add base to precipitate cations. Fire precipitate to yield the desired phase.	Intimate mixing of cations.	Not all cations may precipitate out at the same pH, causing segregation. Initial composition and precipitate composition may be different.
Aerosol Spray Pyrolysis	Make solution of cations. Produce fine mist of solution; pass it through hot furnace to form a powder of mixed oxides. Fire mixed powder to yield desired phase.	Intimate mixing of cations. Product has very fine grain size (1-2μm). Product can have low C content (using nitrates).	Can lose species, particularly Pb during pyrolysis. Powder formed in pyrolysis is not fully reacted to the desired phase.
Freeze drying	Spray aqueous nitrate solution of Bi, (Pb), Sr, Ca and Cu into liquid nitrogen. Collect frozen droplets; freeze dry them to remove water. Fire dried powder to yield desired phase.	Intimate mixing of cations. Powder can have low C content.	Cations may demix during freeze drying if the temperature is not carefully controlled. Nitrates present after freeze drying may melt during firing leading to large grains of nonsuperconducting phases. Product may contain C.

Table 2. (continued)

Method	***Description***	***Advantages***	***Disadvantages***
Bum technique	Form nitrate solution of cations. Add organic species (sugar). Heat solution to remove water, heat powder at elevated temperature. Sugar (fuel) and nitrate ion (oxidant) react (Le. bum) yielding a high temperature that forms mixed oxides. Fire powder to yield desired phase.	Intimate mixing of cations. Powder can have fine grain size.	Can lose species, particularly Pb, during bum process. Powder formed in bum process is not fully reacted to the desired phase. Product may contain C.
Liquid mix method	Form nitrate solution of cations; add glycol or citric acid. Heat to remove water and form polymerized gel, heat to elevated temperature to yield desired phase.	Intimate mixing of cations. Powder can have fine grain size.	Product may contain C.
Micro emulsion	Form suspension of micro droplets of aqueous nitrate solution of Bi, (Pb), Sr, Ca and Cu in oil. Add base to form precipitates. Separate precipitate from oil by washing in solvent. Fire precipitate to yield desired phase.	Intimate mixing of cations. Powder can have fine grain size.	Product may contain C.
Sol Gel	Form alkoxide solution of cations. Add water or alcohol to cross link molecules; form gel through polymerization/condensation reactions. Heat to elevated temperature to bum off the organics yielding desired phase.	Intimate mixing of cations. Powder can have fine grain size.	Method is better suited to making films than bulk powders.

Fig.7 Powder samples after heating and two calcining treatments, from left to right, respectively.

The next heat treatment step, *1^{st} calcination*, was held at 600°C for 10 hours (soaking) under air purge. The tube furnace was set at heat up ramp of 2°C/min. The cooling stage was furnace cool down. This was followed by 30 min of intermediate grinding. The *2^{nd}* and the last *calcination step* was at 700°C for 10 hours again under air purge. The heating ramp and cool down were identical with those of the previous one. 30 min intermediate grinding followed.

Fig.7 shows the same powder after each heat treatment step. After evaporation of residual water it had a dark olive green color. Following the 1^{st} calcinations and grinding color changed into dark brown. The last calcination resulted in black colored powder.

During all these experiments, nitric acid evaporation was the main concern. It contaminated and rusted the lid fasteners, attacked the o-rings and the polymer exhaust line. That is why after the fist powder manufacture trial run it was decided to purge air in the tube for faster discharge of nitric acid vapor. Furthermore, a sodium hydroxide trap was introduced for filtering purposes to the exhaust line. The vapor that came out during the calcination processes eventually caused a thermal shock in the quartz tube due to its condensation on the relatively cooler exhaust side sealing lid. The liquid was observed to accumulate at the bottom of the quartz tube and cracked it.

Literature Survey on Superconductor Tape and Wire Manufacturing: OPIT Method, Drawing and Rolling Processes, Silver Clad Sheath Properties

Oxide Powder In Tube (OPIT) method is the most common manufacturing process employed in superconductor wire and tape fabrication. It starts with packing of the precursor powders into the silver tube, which will serve as the sheath material for the superconductor core. The tube is then sealed and continuously deformed by drawing process to get the desired monofilament wire. If these monofilaments are restacked into another tube and then drawn again, multifilament wires are made.

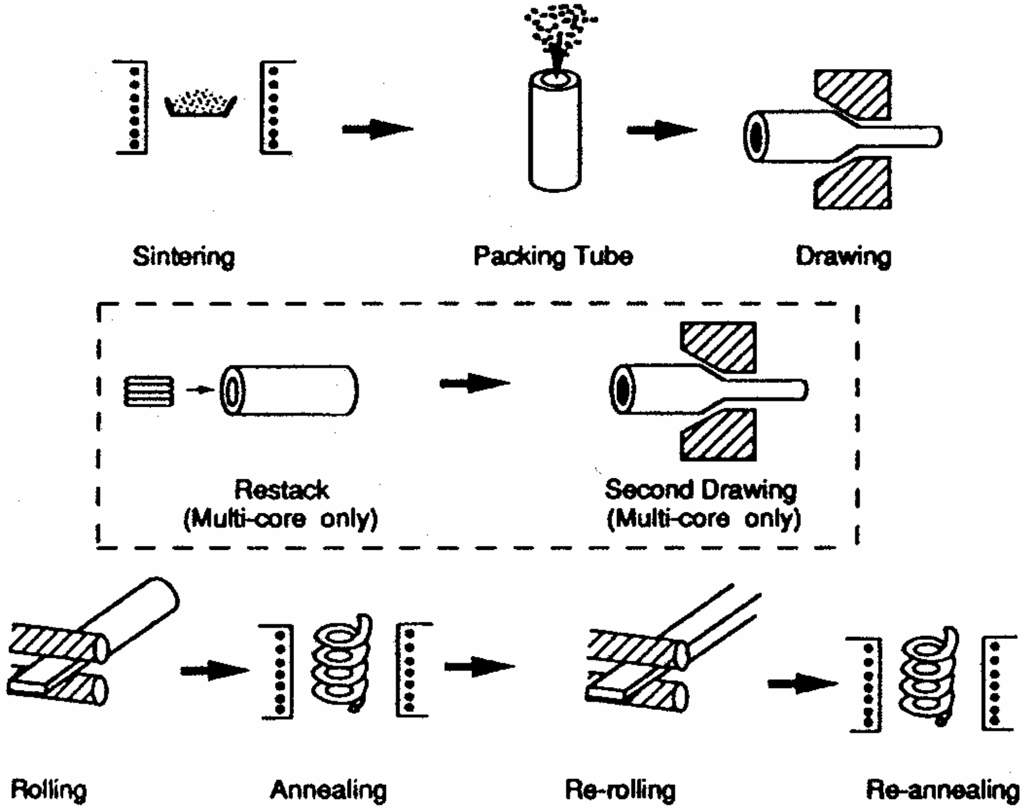

Fig.8 Schematic diagram of OPIT method to make wires and tapes. Last two steps are optional [2].

Rolling is employed to achieve either mono or multifilament tapes out of these wires. Fig.8 shows a schematic diagram of the OPIT method.

Deformation steps of drawing and rolling are followed by partial melt heat treatment for BSCCO superconductors. For wire making, intermediate annealing steps can be utilized in case hardship is encountered during drawing operations. The rolling process can also comprise intermediate annealing steps, especially to obtain better alignment of grains. OPIT is considered as one of the most promising methods to fabricate superconductor wires and tapes. It provides ease to overcome the granularity and limited ductility of the ceramic core. BSCCO ceramic cores offer good grain alignment upon drawing and rolling. Between the two Bi based ceramics, Bi2223 and Bi2212, the latter is the easier one to synthesize. Its critical current density values in high magnetic fields at low temperatures (less than 20 K) are higher than those of its rival. By use of reduced residual carbon in precursor powders, and employing high oxygen partial pressure researchers succeeded in achieving improved characteristics for the superconducting composites. Size and size distribution of the precursor powder, dimensions of the silver tube, initial packing density of the powder all can be cited as prominent factors for fabrication [4].

The mechanical deformation process comprised of swaging, drawing and rolling operations plays a key role in the OPIT method. Outcome of the mechanical deformation is expected to be as follows: Homogenous outer geometry that is also fit for design requirements, homogeneous core free of cracks as possible with sufficiently high density and texture, i.e., well aligned BSCCO grains.

Homogeneity is a very important criterion for the quality of the tape since the wavy interface between the oxide core and the Ag sheath, referred to as “sausaging”, occurs due to the mechanical deformation and the narrow sections of the sausage decreases the actual cross sectional area, thus reducing I_c. Microcracks can be cited as another very serious defect, limiting J_c or even blocking the supercurrent. Ag sheath promotes the alignment of 2212 crystals along the interface as a malleable metal.

Sausaging has also been observed to be detrimental for bending and tension capacities of tapes.

It has been demonstrated that higher core density results in higher J_c. In order to achieve good J_c values, the oxide core should be highly textured with the *ab-plane* parallel to the length direction, i.e., the direction of the current flow (see Fig.9).

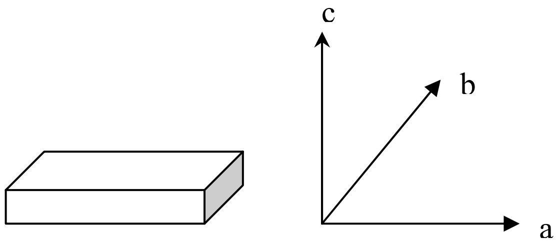

Fig.9 Plate like BiSrCaCuO crystal and its texturing directions. Dimension in *c* direction is much smaller than those in *a* and *b* directions, adapted from [5].

Mechanical properties of BiSrCaCuO materials are anisotropic. It was found by researchers that shearing in *ab-plane* was easier compared to other planes and compression that resulted in fracture through *ab-plane* required more strength [5].

The *geometric variables,* which are related with the deformation process include *tube dimensions, wire drawing die angle, reduction schedules* and *roll diameter* [6]. *Strain rate, lubrication conditions, initial packing density* of the powder in tube can be mentioned as the other parameters of importance. Korzekwa et al. [6] investigated these parameters involving the deformation processes for both wire and tape superconductors fabricated by OPIT method.

Geometric uniformity and cracks in the ceramic core are likely to have a significant effect on the texturing and kinetics of reactions for heat treatment. HTSCs are known to develop favorable texture when subjected to deformation. Compaction characteristics of the core depend on microstructural powder properties such as *particle shape*, *particle size, particle size distribution*, and *initial packing density*.

Rearrangement, deformation and *crack initiation* are the three steps of powder compaction affected by the afore-mentioned characteristics.

Regarding the rolling parameters, Korzekwa et al. [6] revealed that large rollers yielded a reduced thickness along the centerline of the tape compared to the small roller case. They also observed that the tape core split into two lobes, and they concluded that the powder density was low and the roller diameter was too large with respect to wire diameter. Smaller rolls also contribute positively to achieve a uniform core. For their tape samples, uniformity of core along the length is better for overall tape thickness bigger than 0.20 mm. Tapes with dimension thinner than 0.20 mm display poor core conditions.

Roll diameter and the *reduction schedule* are the key factors to decide about the deformation path. If uniaxial compression of an isotropic and incompressible material is taken into account, the strain rate along the length of the tape is the same as the strain rate in the width direction, which is the half of the strain rate in the thickness direction. In other words, under use of *large rolls*, for a given reduction in thickness, the tape will be increasing its length and width by the same percentage. For *smaller rolls*, the width strain is small compared to the length strain. Then, the deformation path can be concluded as plane-strain.

The shape of the *deformation zone* in the roll gap is related to the width of the tape, the roll diameter and the amount of thickness reduction. As the specimen is compressed in the roll gap, frictional constraints along transverse and length directions make an impact on the amount of strain experienced by the sample. The amount of length constraint increases with increasing roll contact length. When smaller rolls are in use, the constraint along the rolling direction is less than that transverse to the tape.

Most of the deformation happens in the length direction. For larger rolls, the frictional constraint is more or less the same in both directions. The strain component in each direction for a certain pass is approximately equal, as well. *Reduction per pass* is another factor that significantly influences the deformation path. Rolling schedule with large reduction naturally results in more width strain and a wider tape. Increasing the roll diameter by a certain factor has a more substantial effect than increasing the reduction per pass by the same factor.

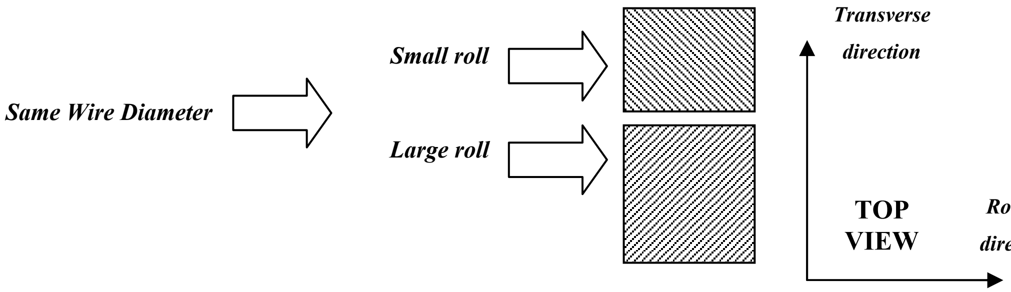

Fig.10 Effect of roll diameter on deformation zone geometry. Adapted from [6].

Willen et al. [7] have also presented a good approach to the deformation zone concept for rolling operation. The compressive forces exerted through the roller provoke the deformation of the composite tapes during rolling process. The zone of plastic deformation (Fig.11a) in the roller gap is denoted with the relation

$$L \approx [R(H_1 - H_2)]^{1/2} \quad \text{(E.1)}$$

Here, L is the length of the zone, R is the roller radius, H_1 and H_2 are the thickness of the tape before and after the deformation, respectively.

With the roller diameter much greater than both the initial and final thicknesses of the tape (thin tape fabricated by small reduction per pass), it is possible to assume uniaxial pressing of the deformation zone, for the sake of simplicity (Fig.11b).

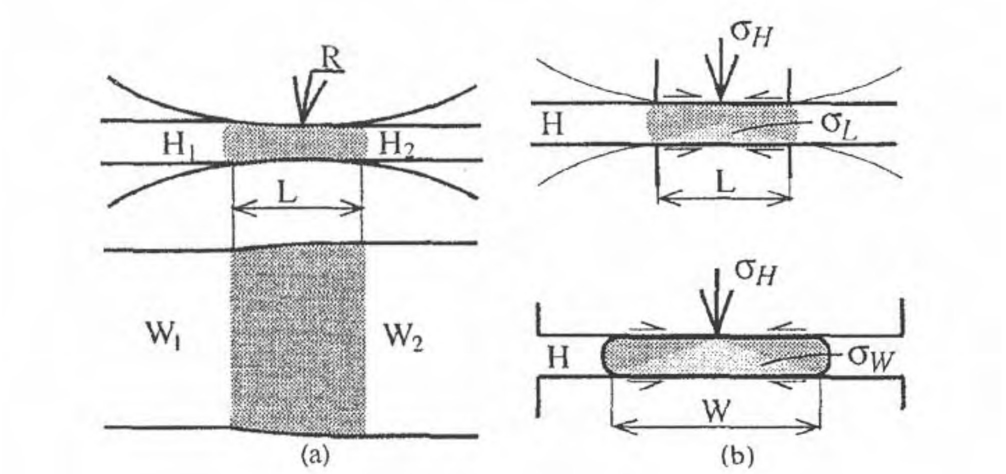

Fig.11 (a) geometry of the deformation zone (b) approximation of rolling to uniaxial pressing [7].

The principal stresses that occur in the tape rolling process are σ_H, σ_L, σ_W as parallel to the height, length and width of the deformation zone, respectively.

The stress σ_H is the pressing (rolling) load distributed over the deformation zone surface. The other two stresses, σ_L and σ_W, are because of the restrictive forces, which develop from the edges of the deformation zone due to surface friction between the tape and the roller shaping it.

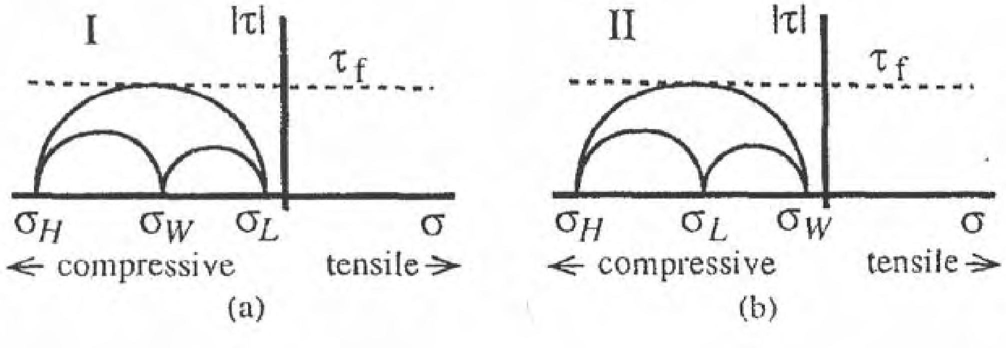

Fig.12 Mohr circles representing the relation between confinement stresses, σ_L and σ_W, and the compaction stress, σ_H. (a) When $|\sigma_H| > |\sigma_W| > |\sigma_L|$ (b) When $|\sigma_H| > |\sigma_L| > |\sigma_W|$ [7].

These restrictive forces are compressive and distributed over the tape cross section with their normals in the length and width directions, respectively. Thus, σ_L and σ_W *are* proportional to the distance from the edge of the deformation zone and their amplitudes change with respect to deformation zone geometry.

The *condition of plastic flow* is that the difference between any of the principal stresses exceeds the shear strength of the metal sheath. The Mohr circles seen in Fig.12 can be used to determine the direction of plastic strain. The shear occurs in planes approximately 45^o between the two principal planes of largest and smallest stresses. Thus, the direction of the plastic strain differentiates in the deformation zone from lengthways to sideways. Fig.13 shows an example of this variation: (a) with small roller radius and wide tape, (b) with large roller radius and narrow tape. In both cases, a zone (stripe like) in sideways and lengthways will sweep the tape along as it passes the roller gap. Final shape of the tape and alignment of the plate shaped grains (i.e., core texture) depend on this variation.

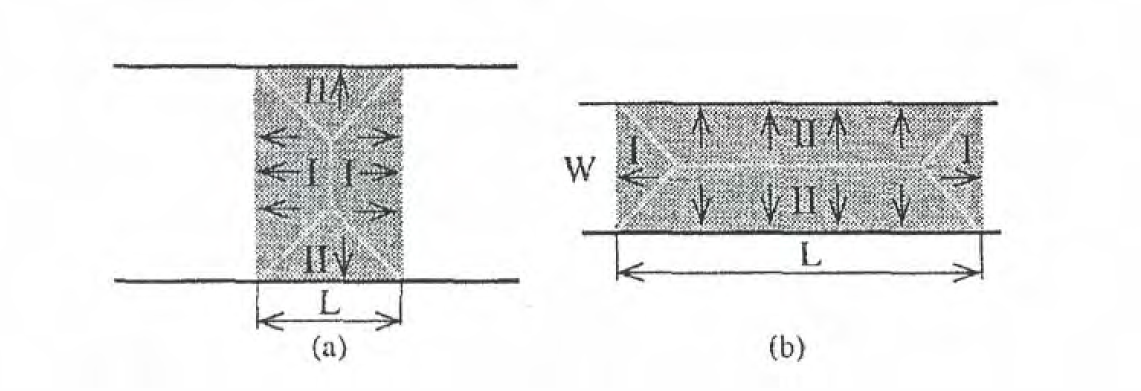

Fig.13 Schematic of the direction of plastic strain in the roller gap corresponding to; (a) Small rollers and wide tape (b) Large rollers and narrow tape. I represents the strain direction under the stress condition $|\sigma_H| > |\sigma_W| > |\sigma_L|$ and II represents the strain direction under the stress condition $|\sigma_H| > |\sigma_L| > |\sigma_W|$ [7].

The restrictive forces increase the compressive stresses required to stimulate the plastic flow (Fig.12). The hydrostatic pressure, $P_h = (\sigma_H + \sigma_L + \sigma_W)/3$, in the tape then depends on the surface friction coefficient (i.e., lubricant use) and geometry of the deformation zone.

At high values of hydrostatic stress, the shear strength of the Bi based ceramic powder exceeds the yield strength of the silver and then the flow of the silver applies tensile stresses on the core. That is, the sheath and the core experience different stress states because of their distinct mechanical properties.

The formation of non-uniformity in the core/Ag interface can be related to three factors:

Plastic flow of silver away from the hard powder core to a zone with softer powder,

Fracture of the core in the planes of maximum tensile stress, approximately 90° to the tape plane,

Shear fracture of the core at approximately 45° to the tape plane.

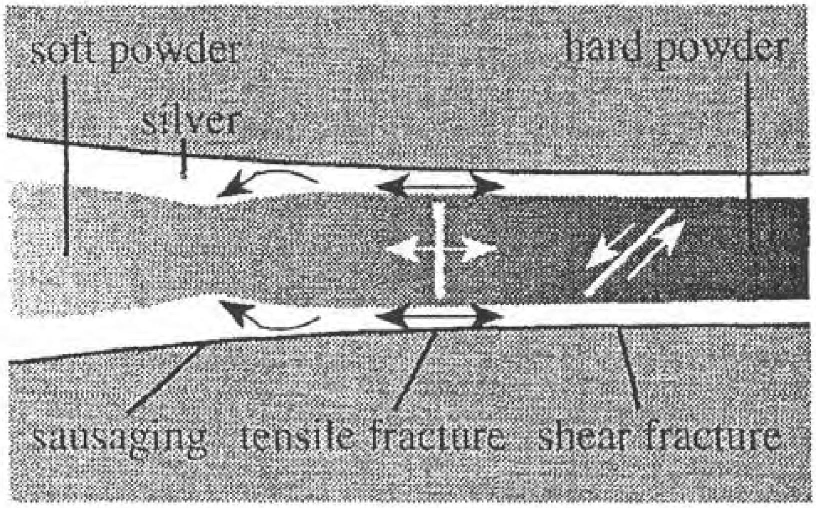

Fig.14 Schematic representation of the three factors that the formation of non-uniformity in the core/Ag interface can be related to [7].

The hardness of the core has also been claimed to depend on the alignment of the grains, where alignment in one direction yields to interlocking of the particles as a brittle behavior of the powder, thus becomes possible to see properties such as high density and good texture [7].

Tape samples experience extension along rolling direction and variable width strain in the range of zero to one half of the thickness strain. When the width strain is zero, "plane strain" stress condition is valid. This means, the stress component along rolling direction is zero. Along the width of the tape, there exists a compressive stress component of some value. This compressive stress component is caused by frictional constraint and is less than the compressive stress applied by the rolls in the thickness direction.

The max shear stress is expected to be along a plane normal of which has a component along the rolling direction, but no component along the width.

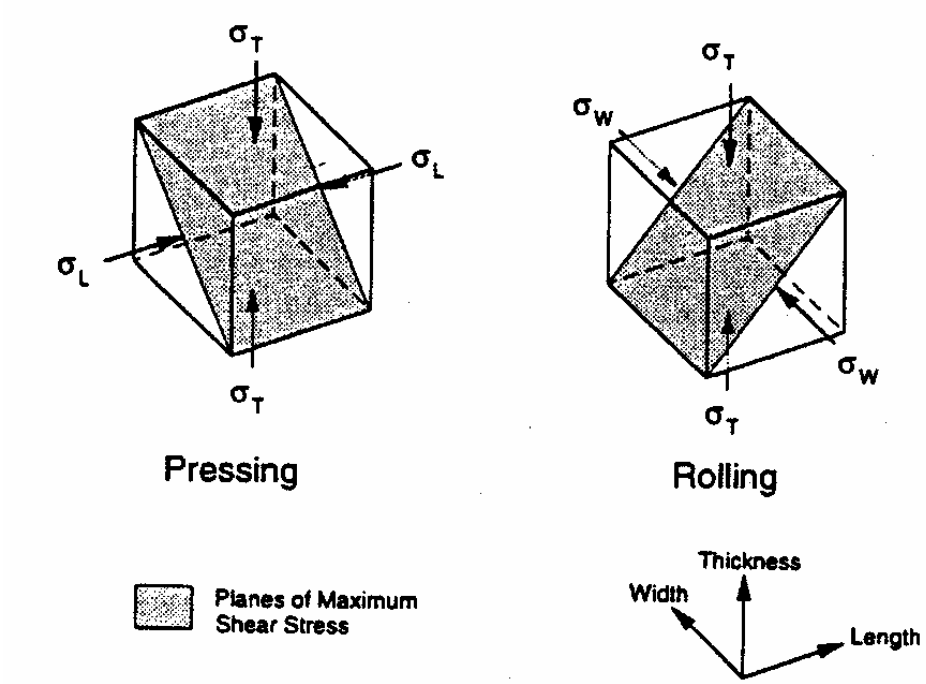

Fig.15 Stress states for pressing and rolling processes applied for tapes [6].

Presence of *cracks* in the oxide core can be detrimental to superconductor's performance. It is necessary to keep the crack initiation at minimum by means of optimum deformation and heat treatment. Under the assumption of rolling and pressing operations as simple uniform stress states, in the absence of tensile stresses, cracks are expected to form along planes of maximum shear [5].

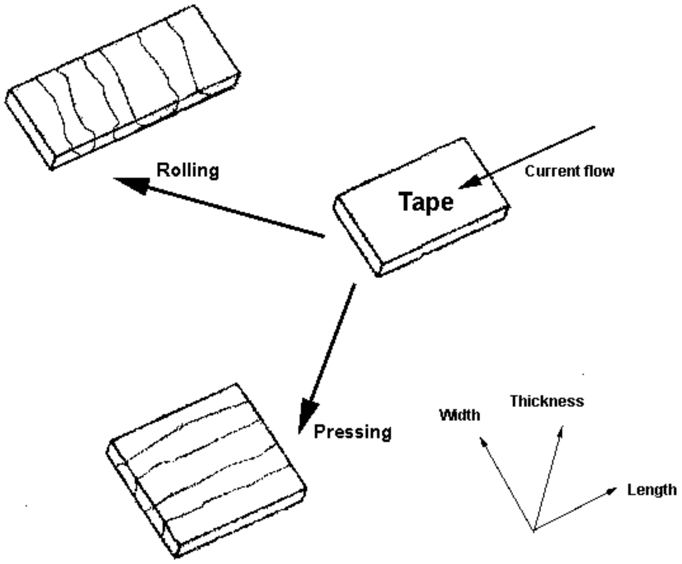

Fig.16 Cracking patterns during rolling and pressing processes on HTSCs [6].

The stress state for rolling shown in Fig.15 promotes cracks aligned transverse to the supercurrent flow direction (Fig. 16). Since the structure of HTSC is very anisotropic, the angle between the plane and the plane of max shear stress is not known precisely normal to the thickness of the tape. In pressing, the stress state is the same as in rolling but rotated 90^o with respect to the tape normal. Compressive stress is aligned along the length direction of the tape.

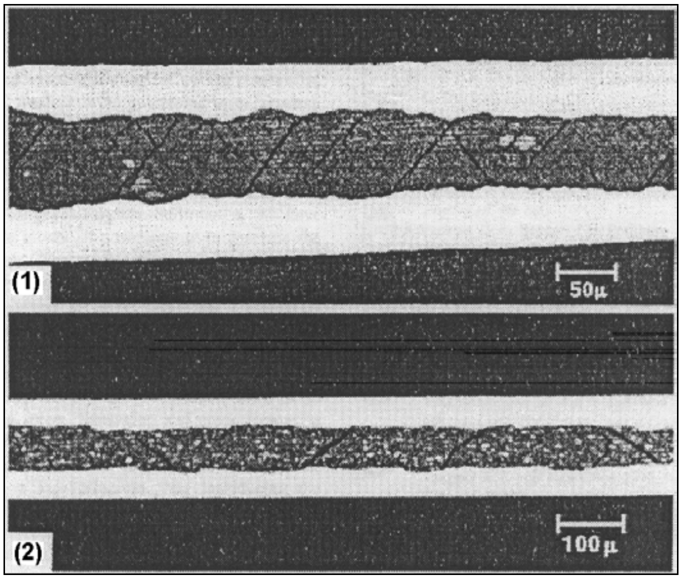

Fig.17 Cracks in HTSC core in Ag sheathed tape (1) transverse section after pressing (2) longitudinal section after rolling [6].

Since the length of the tape is much bigger than its width, the frictional constraint along the length is bigger as well. Therefore, the width strain is much greater than the length strain. This stress-strain conditions help cracks initiate, planes of which are aligned along the supercurrent flow direction.

As a conclusion, cracks aligned in transverse direction to the supercurrent flow direction by rolling have more deleterious effects on the performance of the superconductor compared to the ones along the supercurrent flow direction by pressing (see Figures 16-18) [5].

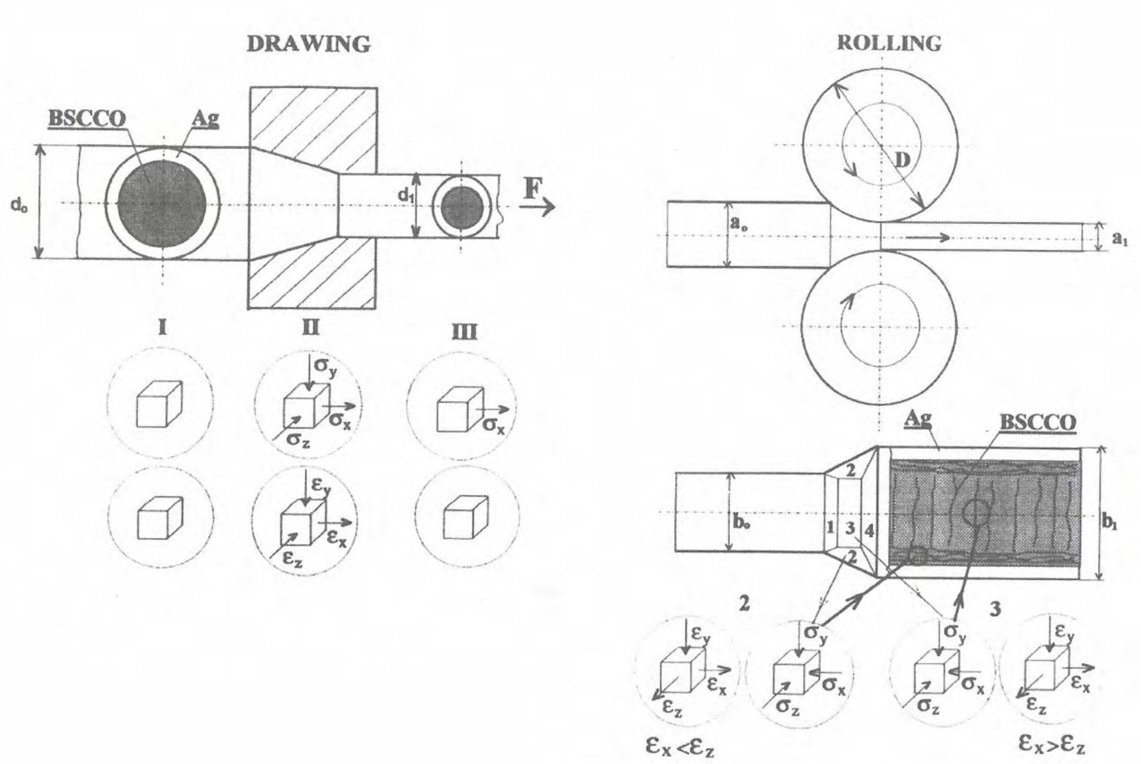

Fig.18 Stress states during drawing and flat rolling processes. Transversal and longitudinal crack formation is also displayed in rolling schematic [8].

It is known that superconductor wires and tapes, once employed for applications, are subject to mechanical strains produced by manipulation, winding or Lorentz forces due to induced self field. Malachevsky et al. [9] made an investigation to reveal how the brittle ceramic filaments crack under these loads in spite of being embedded in ductile metal matrix, i.e., pure silver or alloys. Upon bending, the gradient of stresses is such that max tensile and compressive stresses occur at the outer faces of the tapes. Therefore, the portion of the metal/ceramics interface, which is located closer to the composite's surface, takes larger strains. The cracks originate at the ceramics side of the interface. J_c is known to degrade when the transverse cracking of the ceramic takes place. These cracks reduce the effective cross section of the current flow. For multifilamentary tapes, cracks happen in each filament separately and are kept aloof from the others by the clad sheath of this certain filament. Malachevsky et al. also observed that a major portion of the supercurrent flows close to the core/Ag interface. The surface of the tapes is the area that is affected most under bending loads, thus the core/Ag interface. Cracks initiate at the core side of the interface and decrease overall I_c. Due to the difference in material properties of ceramic and metal parts of the composite, thermal cycling can also be cited among the stress builders against BSCCO superconductors. After conducting bending tests, the authors revealed that cracks (intergranular) had developed preferentially at the grains boundaries. The majority of these cracks were located at the tension stress-built-up-part (upper side) of the tape. The compressive stress-built-up-part looked intact.

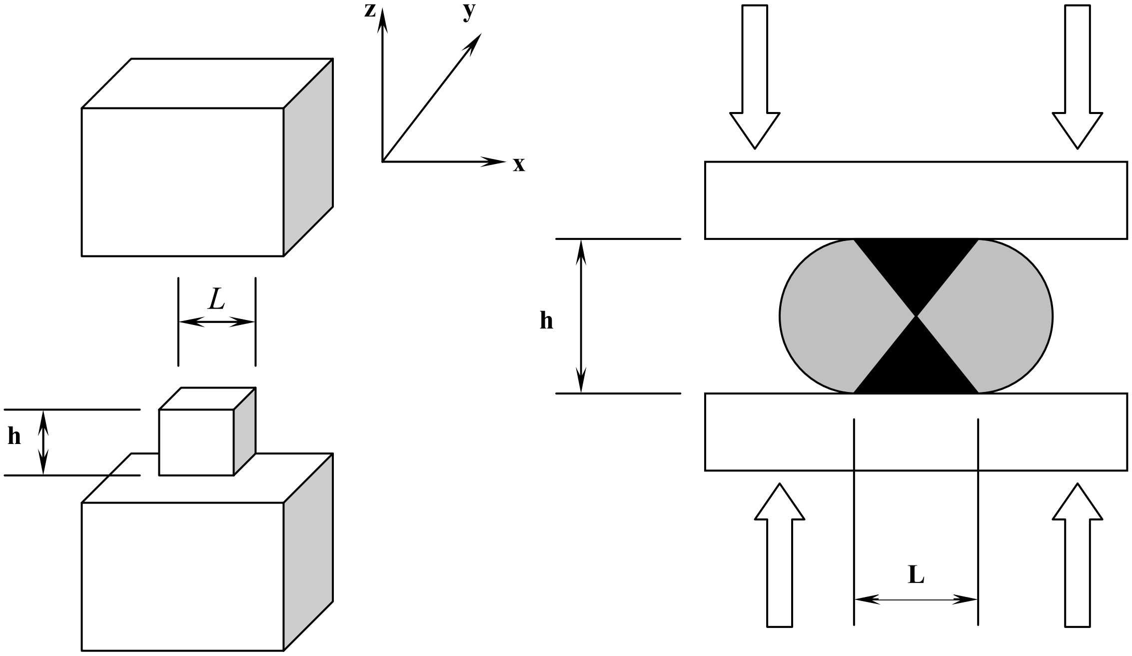

Fig.19 Schematics of compression process for slab and inhomogeneous deformation. Adapted from [5].

Transgranular cracks vary in direction from grain to grain while they are located with respect to *ab-plane* orientation of each domain. As the crack arrives at a new grain, it follows the simplest way to propagate. *Intergranular fracture* happens at the

boundary, which is the natural flaw already with more brittle and softer material. The micaceous way in which the grains grow favors this type of crack propagation under tension. When put under pure compression, despite their well alignment along *ab-plane*, ceramic grains at the interface were also observed to suffer from transgranular crack formation. As a conclusion, while tension stress favored the formation of intergranular cracks, compressive stresses favored the formation of transgranular cracks.
Larger particles in the powder core appear to influence the uniformity of the core as the core thickness decreases to approximately the same order of magnitude as the largest particles in the powder, i.e., finer powder results in a more uniform core.

Slab analysis (Fig.19) is a very inspiring approach to deal with the inhomogeneous deformation for tapes. The *ratio between the specimen height and the contact length* (*h/L*), designated as "Freedom Parameter" (Δ_f), aids to understand the correlation between deformation and applied pressure [5]. If the ratio is large, the pressure needed to acquire the required deformation is low. If the ratio is small, then the pressure to initiate material flow is higher. Schematics in Fig.19 above show the compression process for slab and inhomogeneous deformation in sequence. Darker regions experience less deformation than the remainder of the slab.

The width increase of a narrow thick tape will be larger than that of a wide thin tape under the same applied pressure. Naturally, the contact lengths in *x* and *y* directions affect the deformation amount in these directions; if the contact length is shorter in one direction the deformation in this direction will be larger due to less friction involved. Schematic representation of *rolling process* can be seen in Fig.20.

Due to the friction between the rollers and the specimen, a friction hill builds up. Lubrication is thought to decrease the stress in the sample. If the sample's height is much smaller than the roller's diameter, a rough estimation of the average pressure occurs can be achieved by

$$P_{av} = 2k\left(1 + \frac{L}{4h}\right) \qquad \text{(E.2)}$$

where, *2k* is the flow yield strength of the material,

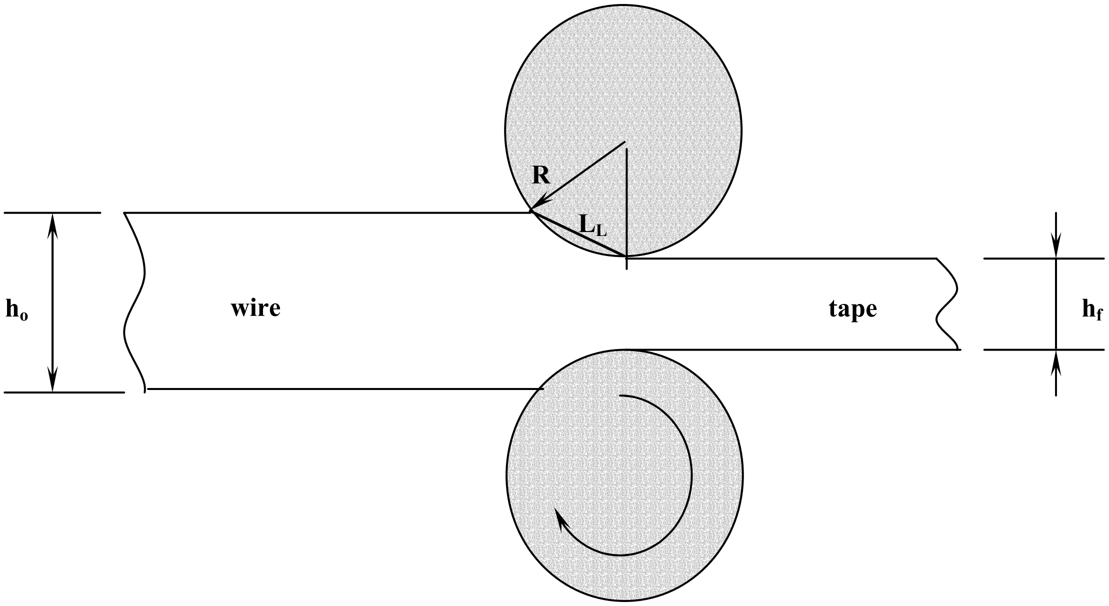

Fig.20 Tape rolling. Adapted from [5].

$$L \approx L_L = \sqrt{R(h_o - h_f)} = \sqrt{R\delta h} \qquad \text{(E.3)}$$

is the contact length (in the sample length direction) and

$$h = {(h_o + h_f)}/{2} \qquad \text{(E.4)}$$

is the average specimen thickness. δh is the height reduction of the sample.

Two freedom parameters, one in the sample length direction

$$\Delta_{f,L} = h / L_L = h / \sqrt{R\delta h} \qquad \text{(E.5)}$$

and the other in the sample width direction

$$\Delta_{f,w} = h / L_w \qquad \text{(E.6)}$$

help determine the effect of large and small rollers with respect to specimen thickness.

The ratio of freedom parameters, $\frac{\Delta_{f,L}}{\Delta_{f,w}}$, is a criterion to estimate the direction which favors greater deformation (Fig.20). For instance, large rollers with large reduction per pass and small tape width will result in substantial deformation in rolling.

For drawing process (Fig.21), the freedom parameter $\Delta_f = \frac{h}{L}$ can be determined by

$$h = {(h_o + h_f)}/{2} \tag{E.7}$$

and

$$L = \frac{(h_o - h_f)}{2\sin\alpha} = \frac{\delta h}{2\sin\alpha} \tag{E.8}$$

where, h_o is the original diameter of the wire, h_f is the diameter after drawing, δh is the reduction and α is the half angle of the drawing die.

The stress in the sample is expected to be larger if the die angle is small or the reduction is large.

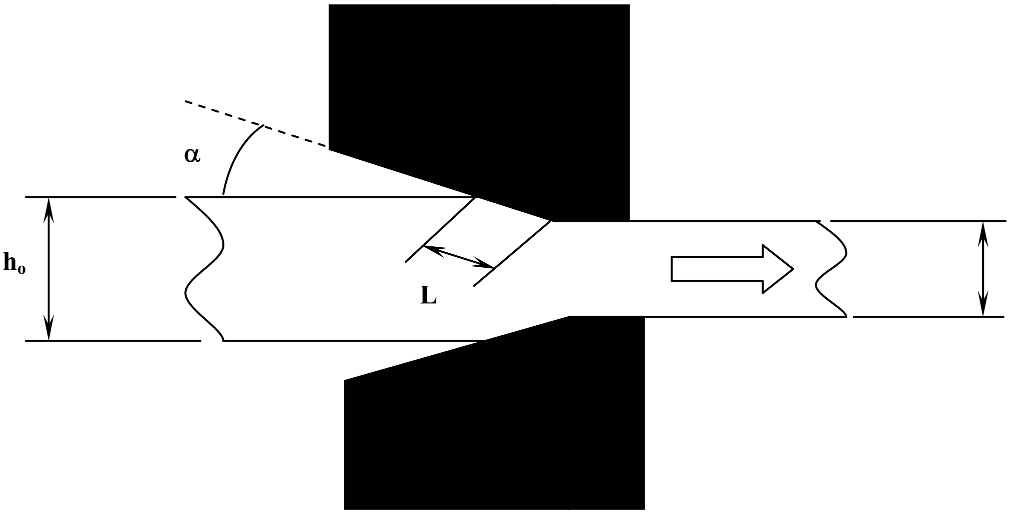

Fig.21 Wire drawing. Adapted from [5].

When dealing with composites, such as BiSrCaCuO-Ag wires and tapes, mechanical properties of each constituent are different. This brings up different behavior of mass flow for all elements and yields in mass redistribution.

The table below gives some mechanical properties of relevant materials for superconductor fabrication.

Table 3. Mechanical properties of some materials for superconductor fabrication [5].

MATERIAL	***YOUNG'S MODULUS [GPa]***	***YIELD STRENGTH [MPa]***	***ULTIMATE TENSILE STRENGTH [MPa]***	***DENSITY [g /cm^3]***
Bi 2212	118 (in *a* and *b directions*) 44 (in *c direction*)	-	180 ($\sigma_{a,b}$)	6.5
Ag (99.9%)	75.9-80	65	170 (annealed) 350 (cold worked)	-
Ag-1.2%Mg	48 (annealed) 383 (oxidized)	74 (annealed) 85.8 (oxidized)	-	-
Bi 2212 Ag wire, dia 1.3 mm	51	20	-	-
Bi 2212 Ag-1.2%Mg wire, dia 1.3 mm	83	>100	-	-

Naturally, the deformation of a weaker element will be more than that of a stronger one under the same loading conditions. Weaker element can be considered as the one with lower yield strength. Therefore, symmetry of the element mass redistribution changes during deformation and this must be the reason behind the structural inhomogeneity like sausaging. The weaker component might be deformed with ease but it could still convey the high pressure it experiences to the stronger element.

If the freedom parameter is small, i.e., the height of the sample is much smaller than its own width; high stress can be built up in the center zone of the weaker component.

High pressure is more likely to be transported through this center zone to the stronger component. At the ends of the composite, the weak component is constrained less and it handles more pressure and therefore conveys less. Nevertheless, shearing force can still be at a considerable level such that edges of the strong component are deformed. In the rolling process of BiSrCaCuO-Ag composite wires and tapes, if the density of the core is not very high, then it is possible to assume that the core is the weaker component (Fig.22). Especially at the beginning of OPIT process, loosely packed powder into the tube by tapping and/or ramming (by a rod) yield more when under pressure with respect the silver sheath around itself. As the deformation progresses, the core gets denser and at some point its behavior can be considered the same as that of a solid and hence the stronger component.

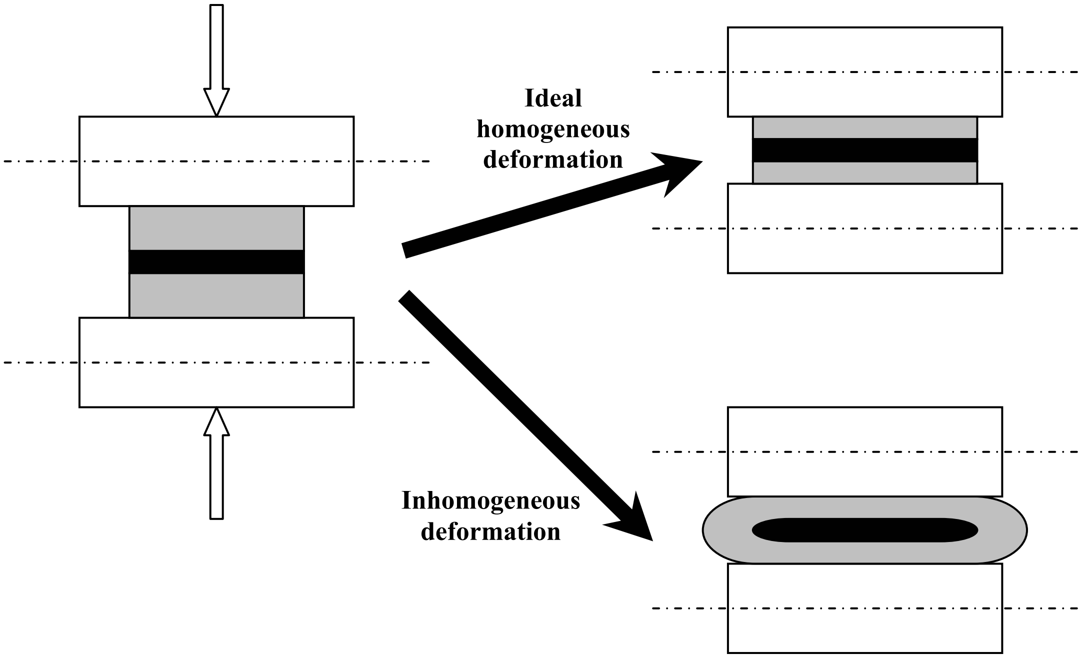

Fig.22 Mass distribution under homogeneous and inhomogeneous deformations. Adapted from [5]. Darker zone represents stronger component.

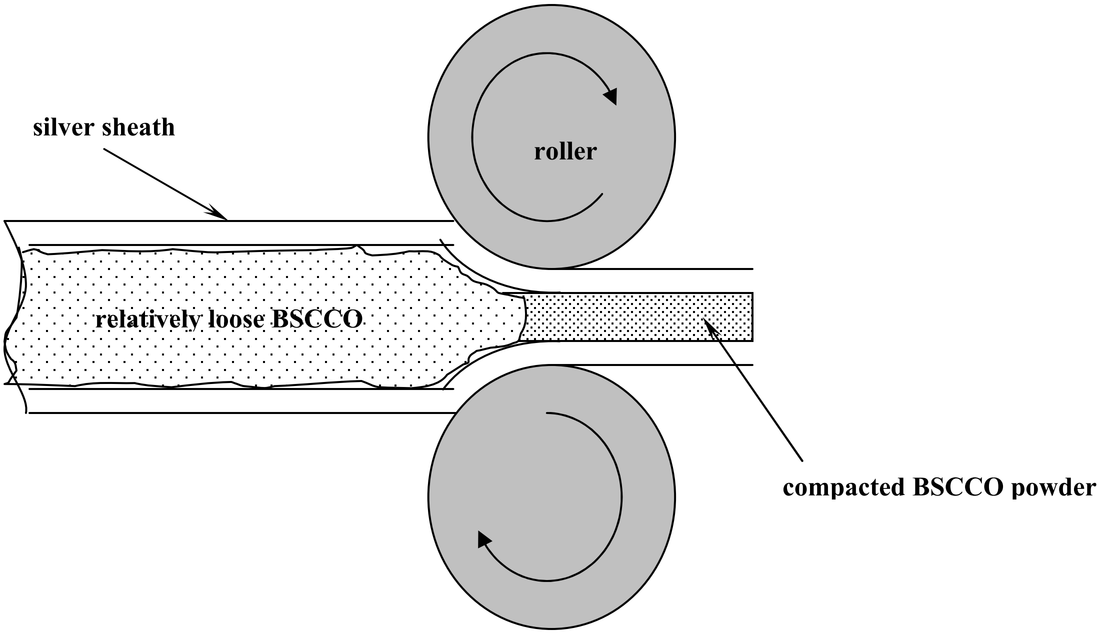

Fig.23 Powder flow during rolling. Adapted from [5].

As stated before, the wavy interface between the oxide core and the Ag sheath, referred to as “sausaging”, occurs due to the mechanical deformation, and the narrow sections of the sausage decreases the actual cross sectional area, thus reducing I_c. The sausaging formation mechanism can be precisely explained as follows [8]:

At the beginning of the rolling process, the powder flow is dominated by the Ag sheath reduction and the core densifies gradually. The powder flow stops upon reaching its critical value due to the friction between the particles in spite of the fact that the density of the powder in the zone just before the powder flow is much less. The freedom of silver in the length direction restraints the max pressure that it can transfer on the powder. Thus, silver flows over the densified powder along the tape length. When less dense portions of powder are reached, silver sheath drives the powder flow once more; hence formed the periodical undulated pattern at the core/sheath interface (Fig.23 and 24). If the freedom of the powder is larger, i.e. the diameter of the rollers is smaller, the sausaging (at least the repetition of bulges) and the density of the core is expected to reduce. Drawing process is usually not expected to cause severe sausaging.

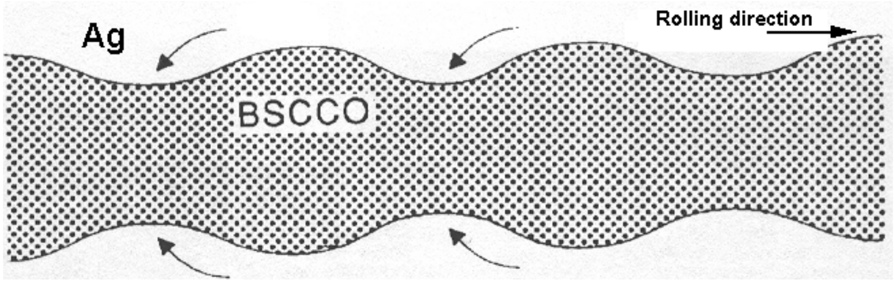

Fig.24 Sausaging formation during rolling operations [5].

Small reduction ratio per pass (around 10%) is another remedy to diminish sausaging possibility. It gives more freedom to silver in length direction. Without doubt, the core density achieved in this way will be lower compared to use of bigger rollers and/or larger reduction ratio per pass.

Post pressing after rolling can be beneficial to suppress sausaging and crack formation, and help grain alignment to promote texture of the core and lead less J_c degradation.

The *powder flow model* [10] implies that the velocity of the powder grains changes according to the depth of tape. The speed of powder adjacent to the core/Ag sheath interface is as low as zero. In the center region there exists higher flow speed. The powder grains look like flat plates (see Fig.9), and the speed profile tends to align the grains in the length direction of the tape with the c-axis perpendicular to the tape surface. The crystals usually maintain the unity of their structure during deformation, suggesting that the stress build up does not exceed the strength limit of the ceramic powder. It is also revealed that the mechanical process aligns the powder inside, and some defects may be introduced to grains. These are the mechanical characteristic of the composite before annealing. After annealing, the grains become larger thus the connections between them get stronger.

The powder flow model is not valid for the annealed powder since the particles don’t flow individually but behave as an integrated bulk material.

As mentioned earlier, the OPIT method utilizes Ag, a ductile metal as clad metal and BSCCO powder with brittle, fine particles inside the tube. Plastic deformation of the powder particles can be neglected during any deformation process such as drawing. Initial packing density of powder is usually very low before the deformation process unless it is pre-pressed and formed as a bar. Under sufficient force applied, the powder flows and packing density of the powder changes accordingly. Fundamental assumptions for the powder flow model are 3 folds [10]:

It is the force exerted on the metal sheath by the dies in drawing process and rollers in rolling process that drives powder flow.

Flow of powder halts as the friction force between powder grains and the driving force exerted on the powder equal each other. In other words, flow stop when the powder density reaches a critical limit and further deformation may lead cracks in the core.

The material at the interface between the working tools and the Ag sheath as well as between the Ag sheath and the core, have no relative movement.

Upon those assumptions, it can be inferred that critical packing density of the powder depends on geometry and size of the particles and mechanical properties of the sheath material. Freedom parameter is the second affecting factor. It has been revealed by researchers that higher initial packing density of the powder does not necessarily result in a larger value of final core density.

Small freedom parameter is expected to build up large stress in the sample and yield high core density with the risk of cracks. Large rollers help to have denser a core. Drawing generally results in rather low density since the max stress applied is limited by the strength of the Ag sheath (for annealed pure Ag, yield strength is about 50 MPa and ultimate tensile strength is about 150 MPa). Use of stronger Ag alloys may help increase applied stress, hence the final core density.

The latest deformation procedure is the one that decides the final density of the core if the composite experiences several sequential deformation procedures. For tapes, naturally, rolling follows drawing operations and is the last deformation process unless pressing is considered for better texturing. The shape and arrangement of the filaments give clues about mass flow and mass distribution in the tape. The cross sectional area of the individual filaments reflects the powder density; therefore the stress distribution in the tape.

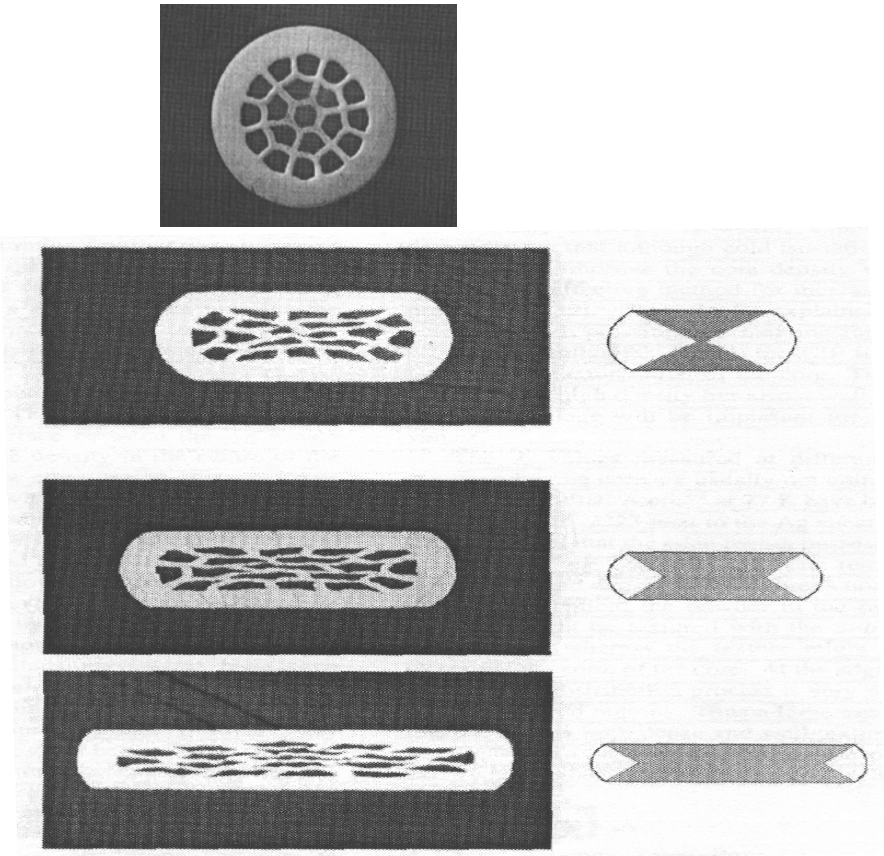

Fig.25 Cross section of an as drawn multifilament BSCCO wire and its deformed states into tape by pressing. Illustrations on the right hand side denote stress distribution in the core, darker regions meaning higher stress [5].

Before the rolling process, the powder density is limited to the level reached by drawing, i.e., relatively lower compared to after rolling values. With the start of rolling, a radial component of powder flow towards the center until the powder reaches its critical density. Subsequently, the powder mainly flows in the length direction of the tape.

Pressing of multifilament wires, if accepted as a simplified appropriate approach to rolling deformation, is given in Fig.25 above. The cross sectional area of filaments close to the center of the tape is smaller than that of the ones by the edge. This observation can be inferred as the powder density as well as the stress concentration at the center is higher. The high powder density or the high stress regions are dark colored, cone shaped regions in Fig.25. They follow the max shear lines from the interface of the deformation tools and the sample (see Fig.15).

In Fig.25 above, the filaments of the tapes shown exhibit a very similar deformation pattern. In each picture, the cores in the middle having other cores around which stay above or below are thinner and wider. The cross sections of the filaments close to the edges are rather large and their shapes are not as wide, indicating the powder density thus the stress experienced by these filaments is low.

Since the force that drives the powder flow is transmitted through the silver sheath, and the max stress occurring in the core/Ag interface depends on the freedom parameter, it can be considered that silver has less freedom to deform at the beginning of deformation process and more stress is built up in the core. If silver had more freedom to flow the stress built would be less and instead or pressing the cores down the metal would flow around.

If drawing operation is considered, initially because the powder is not dense it has the freedom to move in radial direction towards the center of the wire. As the core density reaches the critical value, there exists no room for radial movement and flow takes place along the length direction only.

Since the influence of the friction constraint is smaller at the edges, the deformation of this region is considered mainly governed by yield strength of silver. At this local position, the silver has freedom to flow sidewise and applies tensile force to the filaments in the center. Therefore, the width/thickness (aspect ratio) of the cross section of the filaments at the sample are bigger.

When the thickness of the sample decreases, the freedom parameter $\Delta_f = \frac{h}{L}$ also decreases, thus, the high stress and the high-density region expand. When the density reaches a critical value that does not allow Ag drive the powder further, silver starts to flow in the width direction of the tape applying a shear force on the sheath/core interface. This causes an increase in the filament aspect ratio. The abundance of silver is more at the edges of the tape than the center.

It is possible to determine the core density approximately by comparing the relative change in cross sectional area before and after drawing operations. Assuming the weights of the silver sheath and the powder inside do not change, the following formulation can be utilized for core density predictions where L is the length of wire, A is the cross sectional area, ρ is the density. Subscript s stands for silver and b for BSCCO. Superscript prime denotes the parameters after drawing.

$$LA_s\rho_s = L'A_s'\rho_s' \tag{E.9}$$

$$LA_b\rho_b = L'A_b'\rho_b' \tag{E.10}$$

Assuming $\rho_s = \rho_s'$, i.e., density of silver remains constant during deformation, the preceding equations result in

$$\rho_b' = [\frac{A_b A_s'}{A_b' A_s}]\rho_b \tag{E.11}$$

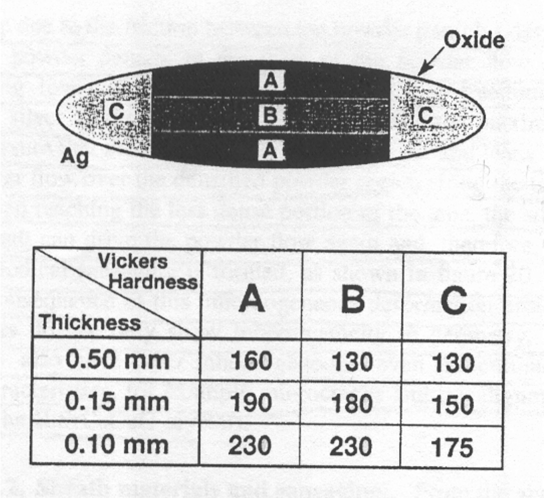

Vickers Hardness / Thickness	A	B	C
0.50 mm	160	130	130
0.15 mm	190	180	150
0.10 mm	230	230	175

Fig.26. Vickers Hardness values for BSCCO core in tape transverse cross section [5].

Reduction in drawing die angle or increase in reduction ratio helps increase the core density. The max density that can be reached is determined by the strength of the sheath. To mention again, the final (critical) density of the core does not directly depend on the initial packing density.

The core density distribution has been studied by means of micro hardness measurements on the tape cross section. Fig.26 shows the density levels in the various zones of the core and the surrounding sheath. It can be easily inferred that the density level is higher at the interface of the core and Ag compared to the inside of the core.

Areas labeled as *A* are restricted by the friction between anvils and the sample in the sidewise expansion direction. Areas *B* are the low stress regions and areas *A* and *B* are under higher stress. *B* is allowed to flow sidewise. As the tape gets thinner the freedom parameter gets lower and density gets higher.

Yuan et al. [11] declared that wire drawing can be easily made into a continuous operation, therefore, it becomes commercially desirable and economical over wire extrusion. However, hydrostatic extrusion is known to provide better products as it ensures better compaction of ceramic powder through higher compressive stress built up. On the other hand, extrusion is limited in rod length that can be loaded into the chamber. It has been reported that critical current density, J_c, is dependent to wire diameter and it increases with decreasing composite dimensions. Drawing die sequence, i.e., the amount of reduction per pass has also been reported to have a considerable effect on the dimensional uniformity of the superconductor composites. Composites fabricated by tubes with thin walls are anticipated to yield lower silver to core volumetric ratio than those manufactured by using tubes with thick walls [11]. Higher relative density of powder in the starting billet is also expected to provide wires and tapes with less porosity. Researchers stated that uniaxial and hydrostatic compaction behaviors of Bi2212 powders were closely dependant on the particle size and distribution.

Yuan et al. used two different powder particle sizes to see its effect. The particle size of the Bi2212 powder prepared by spray pyrolysis method was 2.8 μm and that of the other one prepared by melt casting process was 14.7 μm. Theoretical densities of the powders were given as 6.45 g/cm^3 and 6.41 g/cm^3, respectively. 99.9% pure silver tubes with 6.35 mm OD, having 1 mm and 0.25 mm wall thicknesses were utilized. Initial powder densities were also two folds; 30% and 40%. They made use of a ramrod. The lubricant employed for their drawing operations was zinc stearate. The cross sectional areas deformation routine consisted of a constant reduction of 20.7% per pass. Final diameter of the wire products was measured as 1.62 mm (~0.0638”).

According to their findings, fine particle size powder with 40% initial packing density displayed higher elongation than the others. The combination of less porosity in the core and poor consolidation of fine size particles makes the powder behave more like a solid material. Thin sheath seemed less effective in constraining and consolidating the powder in the core than the thick one. Percentage elongations were found to be lower for the thin sheaths. Final wires became at least ~7 times longer using a thin walled billet compared with ~12 fold increase in length for a thick walled billet.

The authors also asserted that drawing force reached its max at an intermediate wire dimension.

Regarding their report, for the thick walled billets, sheath thickness remained unchanged after the first two drawing passes. As the diameter of the wires got smaller, the silver sheath became thinner at a faster pace than the increase in total reduction of area. Higher starting packing densities invariably resulted in wires with thinner sheath.

Yuan et al. also declared that persistent reductions in the cross sectional area during the drawing process assisted the consolidation of Bi2212 powder. As a result, the relative volume occupied by the powders continued to decrease with the wires becoming smaller. The core became stronger and therefore more resistant to further deformation as the relative density of powder increased. This is why sheath material was prone to more reduction in wires with high-density core than in wires with low-density core.

Unreacted cores, in other words, ‘green compacts’ comprising of fine particles yield much higher strength than coarse particles. During deformation, fine particles are expected to resist more and consequently decrease the corresponding sheath thickness leading to higher Ag/core area ratio. Small Ag/core area ratio is desirable since it reduces the cost of cladding material. Use of thin walled tubes lead the authors to get wires with considerably smaller area ratios. Nonetheless, Yuan et al. [11] stated that fabrication of long wires containing fine powder was harder. Also, the pace at which the core density increased was found to be initially very rapid. Then, with the increasing amount of mechanical deformation, the pace became sluggish.

Specifically, powders with larger mean size and wide particle size distribution were found to reduce the void space in the core and this was helpful for better electrical performance. Finally, the authors claimed that higher initial core packing density yielded denser final cores. However, the degree of this progress became much less noticeable as the practical density converged on the theoretical density of the Bi2212. They also found denser initial packing beneficial in acquiring wires with longer length, thinner sheath and less void in the core.

Yuan et al. [4] came up with a formula for tape spread estimation during rolling deformation. Their *tape spread estimation* formula was given as:

$$\frac{W_{final}}{W_o} = A(\frac{H_o}{H_{final}})^P \tag{E.12}$$

$$P = 10^{(-1.269)(\frac{W_o}{H_o})(\frac{H_o}{D})^{0.556}} \tag{E.13}$$

where W_{final} is the final width, W_o is the initial width, H_{final} is the final thickness, H_o is the initial thickness of the tape, respectively. A is the correction factor and D is the roller diameter. Regarding this formula, as the reduction increases the spread is expected to increase and the aspect ratio (width/thickness) to decrease.

The tendency for lateral spread (in the transverse direction of the tape) is opposed by transverse friction forces. These forces are higher toward the center of the tape and they cause the elements in the central region to spread considerably less than those near the edge. Thus, as the cold working proceeds thinning of the oxide core becomes more noticeable toward the edges than it is at the center of the tape.

Larger roll diameter observed to yield wider tapes. Greater reduction also resulted in wider tapes. Coarse powder particle yields in less spread. High packing density is achieved since small particles filled interstitial voids among larger particles. Smaller particles suggest increase in surface area, and relatively lower particle mass. Coarser particles lead to higher core/Ag ratio (fill factor).

Using powder with small particles, core/Ag area ratio initially increases because of continuous and very minute densification of powder, which reduces the relative size of oxide core. For densely packed material, differential shear between planes of particles requires either volume dilatation or fracture of aggregates. The shear resistance of granular materials depends on the packing density, shape and surface characteristics of the particles. As the tape with fine powder particles gets thinner, the resulting decrement in the core density suggests higher reduction in sheath dimension and therefore lowers core/silver area ratio. As particle size increases, particle strength decreases because of additional flaws that larger particles employ. Fracture is thought to improve repacking of the powder.

Small roll diameter and small reduction per pass yield smaller geometric variations in the tape dimensions.

According to Yuan et al., the geometric relationship between contact area of the rolls and the work-piece dimensions is represented by Δ, *the ratio of mean thickness to contact length between tool and work-piece,* a.k.a freedom parameter as mentioned earlier by [5] and [10]:

$$\Delta = \frac{h}{L} = \frac{(2-r)}{2}\sqrt{\frac{h_o}{rR}} \tag{E.14}$$

where, r is ratio of decrease in thickness, h_o is starting tape thickness, and R is roller radius. Deformation zones with high Δ may denote "hydrostatic tension state" near the centerline of the tapes, which can lead to density decrease or internal cracks. With inhomogeneous flow, surface to center gradients of crystallographic texture (structure) appears. As Δ decreases, the height of the tape decreases as well. Using small roller can improve the oxide compaction level toward the interface, because there exists relatively high hydrostatic tension. Small compaction density increase can transform into a stronger Bi2212 body along the interface region. This helps regulate the thinning of the silver sheath in a more uniform fashion.

Small roller size and small thickness reduction help maintain a high Δ value that yields enhanced alignment of grains and thus, smooth core/Ag interface.

Small powder particle size yields uniform dimensions. Final packing density of the powder with larger size particles is higher than fine powder but fine particles act to retain a smooth thinning of Ag sheath.

Sakai et al. [12], investigated the influence of double sintering with intermediate rolling process, roller diameter, reduction and number of passes per pass on current density of superconducting tapes. They also defined the freedom parameter, but this time it was called as 'roll gap geometry', Δ, and defined as *ratio of projected length of contact arc to the average of tape thickness* before and after rolling. Rolling pressure was decided to increase with increasing roll gap ratio and rise in rolling pressure improved grains connection of the oxide core. Small reduction in one pass was preferred accompanied with large diameter roll to improve texturing. Share deformation induced in the oxide core during rolling was also observed affective on texture of core. The slip plane of the crystals is the *c-plane.* Rotation of crystals to align their slip plane parallel to the shear plane occurs upon deformation. Superfluous shear deformation parallel to the rolling plane appears when roll gap ratio is small. Connectivity of grains in the core is known to be sensitive to the applied pressure during rolling. The mean rolling pressure is a function of roll gap geometry with the condition of constant friction coefficient. The tapes fabricated with large Δ are pressed well during rolling and grains in them are expected to acquire better connection through high pressure. The authors claim that increasing reduction per pass increases grain connection.

With increasing pass number at every rolling reduction step (Fig.27), connectivity was observed to deteriorate. Decline in roller diameter was also observed to weaken the grain connectivity. The authors concluded that for deformations below 30% reduction per pass, J_c increases with increasing reduction rate. Increasing roller diameter also enhances J_c. A rise in pass-number-per-rolling-reduction deteriorates J_c [12].

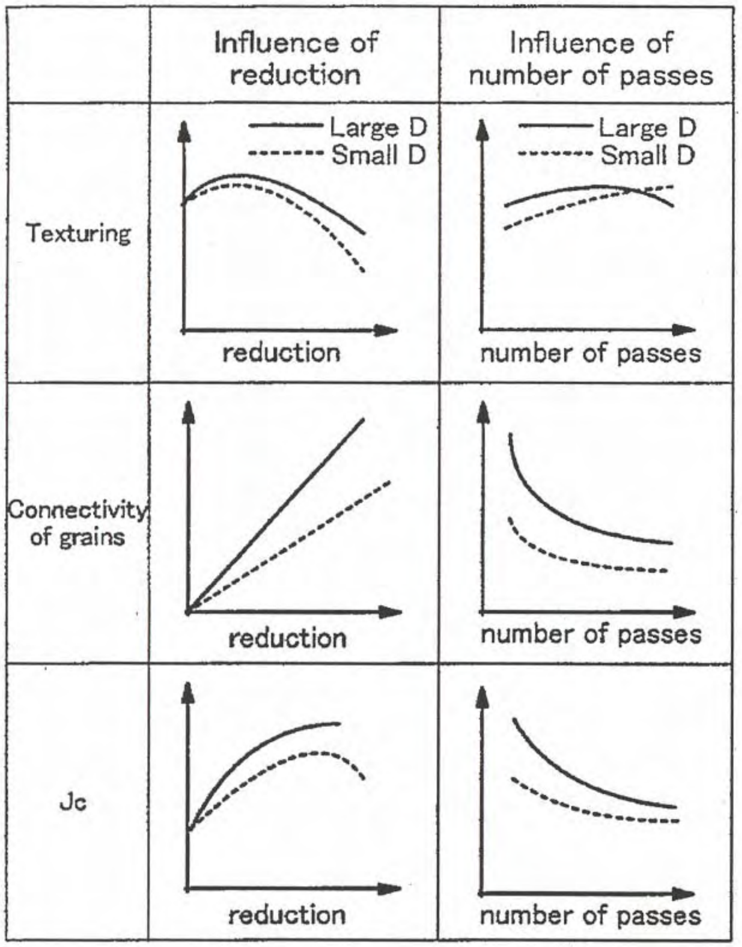

Fig.27 Schematic illustration of changes in texturing, connectivity and J_c [12].

Bigoni et al. [13] reported that the capability of endurance to bending strain is a major factor to be considered for HTSC applications in terms of windings to be integrated with electric power devices. Ag alloy sheaths have been observed to improve the strain tolerance. In addition, reducing the thickness of the filaments through lowering the fill factor and/or increasing the count of the filament could also be beneficial in achieving better strain tolerance results.

According to Oota et al. [14], an optimum value of rolling pressure, which is 0.27 GPa, was determined by a competition between strengthening grain connectivity and the occurrence of sausaging effect. Inspection on variation of current capacity along the width direction in the core revealed that local J_c at the interface is 4-5 times greater than the value at the core center since the grains are better aligned at the edge of the core with being smaller compared to those at the core center. Their rolling process started from wires with 2 mm diameter, ended up with 0.2 mm thick tapes. For low rolling pressure, they reported that the co-deformation between Ag sheath and ceramic core took place leaving poorly oriented grains with a porous general look. This structure results in weak links to occur between the grains, thus current paths will be almost restricted within the grains themselves. An increase in rolling pressure enhances core density and helps grain texturing. With respect to their results high pressure beyond 0.3 GPa causes detrimental sausaging.

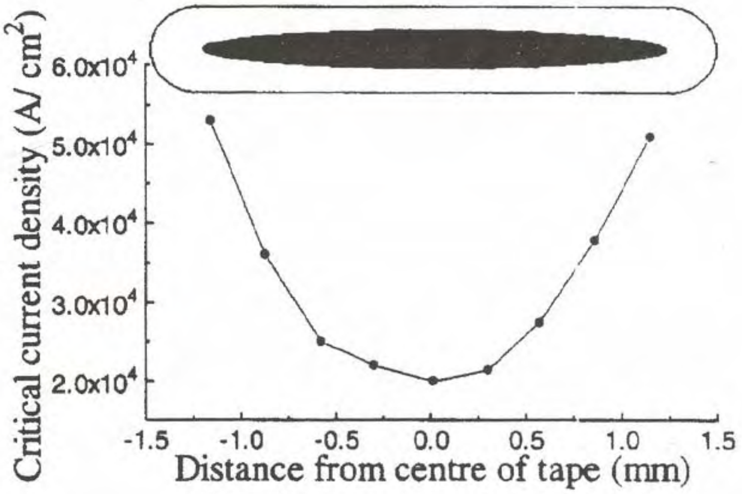

Fig.28 J_c distribution in a silver sheathed superconducting tape [15].

Critical current density in monofilament superconductors has been observed to vary across the width of the tape. After magneto optic scans of flux penetration, Chesneau et al. [15], found that the magnetization currents flew preferentially near the core/Ag interface, while the current flow in the center appeared poor with a lower density. The factors probably participated to this variation were suggested as better grain alignment near the sheath, better connection between grains at the interface, faults in phase transformation in the central regions of core, more impurities in the center. It was not clear whether there is an effect due to stress built up by cooling after heat treatment. By FEM calculations and experiments the authors concluded that the thermal stresses induced during heat treatment processes were not responsible for the critical current density distribution fashion showed in Fig.28. However, they claimed that local increases in stress caused by morphology of the core were found insufficient to cause significant variation of J_c.

Grasso et al. [16] also conducted an investigation on path preference of supercurrent and measured the current distribution in the filament in lateral direction by a simple and novel strip cutting technique. They proposed two explanations for the shape of the J_c distribution. The first one anticipated the J_c dependent on the density of the secondary phases, which strongly reduced going from the center to the sides of the filament. The next and the last explanation suggested J_c be enhanced by the local compression factor which was higher at the sides of the filament than in the center.

Huang et al. [17], described *filling factor* as the ratio of the superconductor to the total cross section. 20% filling factor was reported to give the best J_c values with tapes so far. Very high filling factor yields to poor workability and large sausaging in filaments along their longitudinal direction. Authors also observed that a non-uniform shape of filaments in a cross section view generally corresponded to strong sausaging in the longitudinal direction of the tapes. Tapes with filling factor of 35% found to have poor workability since higher filling factor leads to higher deformation force and lower ductility in the composite [17]. According to Huang et al., tape and filament thicknesses of 205 and 20 μm were found to be the optimum size for best J_c and J_e values, respectively. Looking at the SEM pictures, they observed detrimental sausaging to start when thickness of the tape was smaller then 205 μm. This could be associated with higher misalignment angle of the grains yielding deterioration in J_c. However, if the filaments were too thick it would have negative effects on phase formation such as secondary phase formation in large amounts disturbing the grain alignment at the same time. They concluded that a smaller filament with less sausaging is the key for better conductive performance.

Carter et al. [18] claimed that engineering current density, J_e, is expected to be 10 kA/cm^2 for making commercial applications practical. Increasing the volume fraction of the oxide core, i.e. fill factor, is necessary to increase the current density. Factors that influence fill factor include dimensions of the silver tubes used, packing density of the precursor powder filled in the tubes, dimensions of the tube that filaments are bundled in and the number of bundling steps till reaching the aimed composite structure. Deformation schedule and heat treatment are also important since they decide the degree of densification, thus the fill factor. Authors reported that max J_e was achieved for the greatest fill factor in spite of the decrease of J_c in filaments. Increase in fill factor observed to adversely affect the uniformity of the core/Ag interface. For a vigorous fabrication process, fill factor of the composite is limited. Precursor powder packed into the tube demonstrates no strength against tensile during drawing. For that reason, Ag sheath has to take all the load of the drawing process and if it is filled too much, early consolidated powder will act like a solid and cause the metal flow more than expected.

Researchers revealed that decreasing the fill factor improved the strain tolerance of monofilament tapes. Reduced thickness yielded an increase in critical fracture stress of monofilaments. As for multifilament tapes, increasing the count of filaments also increases the overall strain tolerance but the fill factor may vary. However, at a constant fill factor, decreasing filament thickness by increasing the count of filaments was proved to enhance strain tolerance. All these results suggested that the composite consisting of core and Ag sheath behaved as a brittle filament/ductile matrix composite. There exists a considerable range of actual filament critical strains within the conductor and it is believed to rise from varying in-filament-densities and microstructural differences due to non-uniform deformation in rolling of a round wire into a shape with aspect ratio, i.e., a tape. Nevertheless, J_c did not display sharp drops under high strain conditions as anticipated because cracks which incorporated large regions of slip long c-axis grain boundaries as yet maintained sufficient grain to grain contact that could provide a path for current flow.

It has been observed that silver sheathed tapes fabricated using OPIT method display sausaging problems due to deformation by rolling at the core/Ag interface that could be detrimental to conductor properties. Creep has also been cited as trouble aroused due to heat treatment. Moreover, for some applications, high field magnets require a sufficient mechanical strength to withstand deformation under the influence of large electromagnetic force that can cause cracks in the core. Yoo et al. [19] made 1 mm OD monofilament wires and then, flat rolled them into tapes with 0.13 mm thickness and 2.5 mm width. Solid solution or dispersion hardening has been used to reinforce silver sheaths as Mg, Cu, Au and Mn alloys. Mg is solid soluble to silver to some extent and tends to form oxides very quickly as exposed to O_2. Since Ag has a considerable permeability for oxygen; it is very likely for Mg precipitates to form MgO that can act as dispersion hardening agents. Pure Ag is soft, HV=33, in comparison to ceramic core, HV=120 [19]. This difference is the reason for sausaging formation at the interface. Authors observed that Mg in the $Ag_{0.999}Mg_{0.001}$ alloy was internally oxidized during heat treatment under air and dispersed as MgO particles. Compared to Mg alloy, pure silver sheathed tapes were found to display more sausaging. Matching the hardness of sheath material and the ceramic core was considered helpful in reducing the sausaging effect or rolling process even the sheath materials could be annealed before deformation.

Olusoji et al. [20] presented the variation of the transverse stress, σ_{yy}, across the width of their 37-filament superconductor tape by FEM. Assumptions employed for finite element computations were as follows:

At sintering-annealing temperature (~840^{o}C) the superconducting tape is stress free.

Silver is ductile and behaves elastically. BSCCO core is brittle and behaves plastically.

The structure is symmetrical about the *x* and *y*-axes thus, one quarter of the tape cross section is enough to model.

The magnitude of the yield stress of silver is assumed to be the same in tension and compression.

The structure is infinitely long so that plane strain conditions apply.

The mechanical properties of silver and BSCCO are isotropic.

BSCCO core center is assumed to be 65% dense and the outer regions of the core are assumed to be 85% dense.

Some mechanical properties of silver and BSCCO used in their FEA were given in Table 4.

Table 4. Mechanical properties of silver and BSCCO used in FEM calculations. K_p is the slope of the stress-strain curve after yielding, σ_{yp} is the yielding stress, α is the thermal coefficient, ν is the Poisson's ratio [19].

Property	***BSCCO***	***Silver***
α [K^{-1}]	$13.6x10^{-6}$	$21.9x10^{-6}$
E [GPa] 100% dense	127	71
E [GPa] 85% dense	83.80	-
E [GPa] 65% dense	54.10	-
σ_{yp} at 300K [Mpa]	-	12.60
K_p at 300K [Gpa]	-	0.57
ν	0.14	0.37
σ_{yp} at 77K [Mpa]	-	13.20
K_p at 77K [Gpa]	-	0.70

Wand et al. [21] claimed that in order to achieve high superconductor filling factor, thus enhance J_c and reduce the cost by reducing the proportion of Ag used, a harder outer sheath must be employed to clad the filaments with softer sheath material. They utilized a hard metal outer sheath for their OPIT fabrication process and then etched it away following the drawing and rolling operations. They reported that their tapes reached a filling factor of 45%.

There exists no doubt that sausaging and core density depend on deformation process. Some important parameters are powder packing method (initial powder density), drawing die geometry, and reduction ratio all of which cited before. Hardness was also mentioned as an indicator for densification of powder during deformation processes. Ha et al. [22] used 20 mm OD pure silver tubing for OPIT method to achieve monofilament wires with 2.69 mm diameter. The die geometry they employed changed with approach angle (half angle of entrance), reduction ratios and bearing lengths. Then, they made hexagonal filaments out of these wires and bundled 37 of these filaments into a silver alloy outer tube with 20 mm diameter. This assembly was then drawn down to 1.4 mm. Flat rolling was employed to deform the multifilament wire into a tape with 0.25 mm final thickness through 30% reduction ratio. They could not find much of a difference between cold-isostatic-pressure-compacted powder core inserted wires and loosely packed powder core wires by tapping after the drawing operations in terms of final powder density and filling factor. However, hardness was observed to increase with the filament position shifting to the outer layer from the center of the wire. Outer layers of the wire close to the contacted die surface became denser due to the stress distribution by drawing operation. This distribution was attributed to the friction between the die and the wire. The filling factor increased starting from the bigger wire diameter to the final size because of the increasing difference of deformation resistance between the oxide core and silver sheath. Regarding the results, the authors concluded that drawing dies with different geometry were not considerably influential on hardness and fill factor. As for the sausaging, both after drawing and rolling processes, they came across interface irregularities. Sausaging is known to occur as a result of non-uniform shape change of the oxide core and Ag sheath due to different deformation resistance. The oxide powder packed into the tube gets compacted and solidifies as the deformation processes proceed. Smaller approach angle was claimed to reduce sausaging in multifilament wires.

Malberg et al. [23] investigated effects of the reduction-per-pass and semi-die (approach) angle, which are the two dominant parameters on drawing stress and powder compaction of the single filament wire. Optimum die angle and greatest acceptable reduction per pass were determined. A linear relationship between microhardness and powder density was also claimed. Increase in the powder compaction near the interface was noticed. However, increase in density near the center axis of the tube found smaller in comparison. They reported that due to compaction of the powder and strain hardening of the silver, the drawing stress increased with each drawing step. The relative drawing stress, which is determined as the ratio between the drawing stress and the flow stress of silver, was taken as an indicator of safety for the drawing process. Annealing was found useful in reducing the drawing stress when employed in between drawing steps. Authors also observed the optimum semi die angle about 7-10^{o} to minimize the drawing stress. For smaller angles the core/sheath interface becomes too large and ends up with greater friction work required. For larger angles, the redundant work in the deformation zone increases. They also declared the limit of reduction per pass as 30%.

Tape deformation must be carefully controlled for powder density improvement and obtaining an interface free of sausaging as much as possible. Grasso et al. [24] avowed that a reduction per pass of 10% for wire drawing process seemed ideal. The final wire diameter after drawing determines the tape width and it is considerably important for current transport properties, as well. As a trade off between high J_c and sufficient mechanical strength, authors chose to fabricate tapes from wires with 1-2 mm diameter. Setting the thickness reduction to 10% for rolling operations reduced sausaging of the monofilament tapes. Optimum core thickness for monofilament tapes was targeted as 40 μm for best J_c. With both lower and higher tape thicknesses, degradation of J_c found to be severe. Drop of J_c in case of lower thickness was attributed to sausaging formation while main cause of low J_c values in high thickness tapes was due to poor texture of the grains. They revealed that the pressure exerted on the tapes during rolling is highly correlated to the J_c. 0.6 GPa was found as the optimum value for rolling pressure yielding for the best tape performance. Values above 0.6 GPa worsened J_c due to crack formation in the transverse direction of the core.

Kajuch et al. [25] used Bi2212 precursors with particle size of 2-5 μm prepared by spray pyrolysis method. They employed 99.9% pure silver tubes with 6.35 mm OD and 1 mm wall thickness to fabricate wires by OPIT method. Prior to drawing, each sample was weighed and measured to determine the initial powder packing density. The diameter for their final wire product was 1.63 mm (0.0642”). The drawing dies had a semi die angle of 8^o. The corresponding reduction of area per pass was 16, 20.7 and 25.2%, respectively, for the three different deformation schedules they carried out. Packing densities of the wire samples with 10 cm length were cut and amount of Bi2212 powder in these samples was calculated by subtracting the mass of silver from the total weight. Dimension of the silver tube were already determined. Theoretical density of Bi2212 powder was taken as 6.45 g/cm^3.

After their experiments to see variation of powder packing density vs. area reduction in drawing process, Kajuch et al. revealed that there occurred an increase in powder densification at the initial stages of deformation. However, the overall relative density decreased eventually. Rapid densification of the powder is not desired because of microcrack formation led by continued deformation of brittle ceramic powders. Lower reduction per pass allows temporary holdup of powder densification to the latter stages of deformation, therefore decrease the extent of powder cracking. Variation of wall thickness of the silver tubes during drawing process was measured optically on the transverse cross section of the composites. With increasing total area reduction, the wall thickness of the sheath decreased. Nevertheless, up to 50% of total reduction area, the authors did not notice any significant reduction in wall thickness. Beyond this point, the reduction in wall thickness was measured as 65%. The authors concluded that, there was no noteworthy difference in wall thickness reduction with increasing area reduction per pass indicating a relation between silver material (intrinsic) properties and powder packing density. They considered this rather the effect of drawing process parameters. As a natural conclusion of the relative augmentation in powder packing density and reduction in wall thickness of the sheath, proportion of oxide core to Ag increases along a continuous trend in accord with furthering drawing deformation. However, the authors stated that there was no clear correlation between core/Ag ratio and % reduction per pass. Kajuch et al. used drawing dies with 8^o semi die angle and zinc stearate for lubricant. Drawing stress was reported to increase with increasing total area reduction and high reduction rate per pass. Lubricant use is known to serve creation of film between work piece and die surfaces and decrease the coefficient of friction. Lubricant also helps heat dissipation where almost 90% of kinetic input energy is converted to thermal energy. During drawing process, due to the powder compaction, the wire does not elongate according to the ideal constant volume law for the initial part of the deformation until the powder gets solidified.

Zeng et al. [26] looked for optimal reduction in rolling. They reported that greater geometric uniformity was achieved in the oxide core of the superconducting tapes when smaller diameter rollers were used. Smaller reduction per pass is known to provide low density and less homogeneity in the core. On the contrary, high reduction per pass was found to yield more densification of the core center compared to the sections closer to the edges of the tape. Authors used a powder with an average particle size of 2-4 μm. The silver tubes used for OPIT method had 10 mm OD and 8.5 mm ID. The packing density of the powder as filled in tube was 2.5 g/cm^3. Drawing operations was carried out at 5% reduction per pass. Final outer diameter of the monofilament wires was 2 mm.

They used two different deformation routes for flat rolling process, which were also employed in our project. The first one was defined as constant rolling per pass (CR) and the second as increasing rolling per pass (IR). Comparing these two procedures, CR reduction was of the order of 5% per pass and IR reduction increased gradually from 3 to 30% per pass. Authors fabricated 81 filament multifilament wires and deformed them into tapes starting from 2 mm (0.0787”) diameter wire and ending up with 0.16mm (0.0063”) thick tape. By employing the IR deformation route, the shear stress on the oxide core was gradually increased to allow free flow of powder. Therefore, better-textured filaments were aimed after final mechanical deformation. Upon inspection of 81 filament tapes fabricated by CR deformation route, it was revealed that central filaments and edge filaments surrounding them experienced distinct deformations. Rolling process was observed to make the tape elongate along the rolling direction (*ab-plane*). With respect to the rolling deformation theory, authors suggested different stress states at different positions along the *c-axis*. At the core center, compressive stresses were considered to exist while the tape edges were subjected to shear stresses. Zeng et al. also reported that, multifilament tapes deformed under CR deformation route led to higher deformation force in the central filaments than the ones close to the tape edges. However, the filamentary cross sections of IR deformed tapes looked more uniform. The cores of filaments near the tape edges appeared more porous in CR deformed composites whereas those in IR deformed tapes seemed denser. That is, IR procedure yielded a more uniform deformation (effective compaction) at the edge filaments compared to CR procedure. Since there is a difference in cross sectional morphology between mono and multifilament tapes, this reflects on the distribution of transport current.

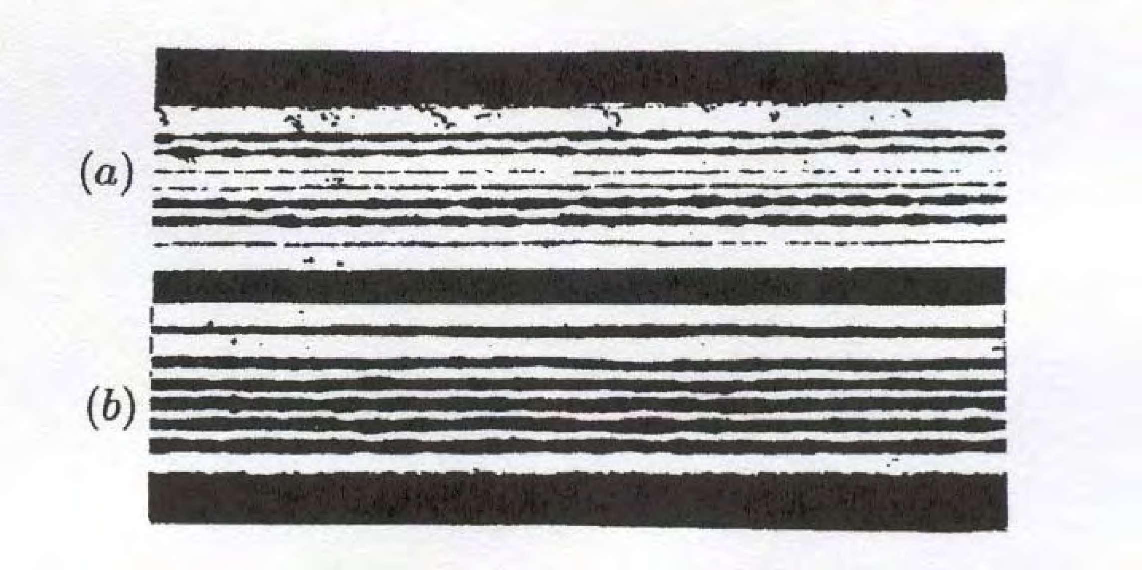

Fig.29 Longitudinal cross sections of multifilament tapes; (a) deformed via CR (constant reduction) deformation routine (b) deformed via IR (increasing reduction) deformation routine [26].

Along the cross section of monofilament tapes, the density of the ceramic in the center is lower than that of the ceramic at the core/Ag interface. On the contrary, multifilament tapes accommodate denser core in the center filaments then in the surrounding ones. Filaments at the center (less *ab-plane* shear layer) may be under the influence of a strain state that micro cracks can develop in the filaments located near the rolling surface and at the edges (more *ab-plane* shear layer) of the composite although insufficient force has been applied to get the aimed texture and densification level. Low density filaments are deemed to reduce current carrying capacity and affect sintering kinetics during heat treatment. These two factors are important since they directly act on J_c. Through their observation on longitudinal cross section images of multifilament tapes, Zeng et al. declared a better interface homogeneity via IR reduction in comparison to CR reduction routine (see Fig.29**).** Zeng et al. also put an opposite idea about stopping of powder flow upon friction, compared to what Han [10] claimed. According to them, during practical cold working, powder does not stop flowing in reality. However, it increases in density such that the resistance to the powder flow force is sufficient to overcome the yield strength of the sheath metal. Thus, the sheath metal deforms more than the solidified powder and causes sausaging at the interface. In order to prevail over sausaging and any powder flow resistance, the shear strain on the powder must be successfully transmitted through the sheath metal and any area reduction must be such that the powder is allowed to flow freely. Investigation of Zeng et al. [26] showed that sausaging strongly depends on the shear strength of the sheath material (elasticity modulus, Poisson’s ratio and wall thickness of the tube) and the ability of the Bi based powder to flow freely (order and distribution of particle size with core dimensions). The sausaging effect has also been claimed reduced by cut in annealing temperature and time, which brings up the concept of increased sheath strength by work hardening. IR deformation path let the authors increase the applied shear stress gradually on the core and allowed the powder flow freely. Introducing no intermediate annealing in between rolling steps improved strength of the silver sheath due to work hardening. Therefore, IR deformed multifilament tapes seemed to fulfill the requirements of high density, homogeneous deformation and good grain alignment (texture) much better than CR deformed ones.

Silver Clad Sheath: Silver Alloys Used in Composite BSCCO Superconductors

In his broad research Navarro [27] investigated development of electrical and mechanical properties, of silver alloys used in composite BSCCO tapes.

Ag clad BSCCO composite tapes and wires are known to be mechanically weak and vulnerable to tensile and compression stresses (such as in bending and coil winding) that rise during applications. Electromagnetic forces in operation and cooling thermal stresses are the other factors that might require the silver clad composites to have more support.

The *yielding strength* ($\sigma_{0.2}$), which is the stress for 0.2% strain is a crucial characteristic for superconductors after sintering in air or other oxidizing atmospheres at elevated temperatures. It is the elastic deformation limit, which draws the border before the irreversible strain limit without deterioration of the electrical performance.

Nonetheless, the OPIT method makes use of very different components in terms of mechanical properties, i.e., ceramic powder and metal sheath surrounding it and these properties are the main parameters to determine the flow of the powder and the metal.

In addition to this, the final $\sigma_{0.2}$ values are also effective on overall stress tolerance of the composite.

The variation of the deformation rate between the brittle ceramic powder core and the surrounding soft metal sheath makes it very hard to get a homogeneous plastic deformation. Vickers Micro Hardness measurement is the easiest way to check the local elastic-plastic deformations and the micro-crack formation, especially in the core.

Drawing procedure brings up the metal sheath yielding under the dominant tensile stress and precursor powder may reach 60-70% of its maximum theoretical density, which is roughly 6.4–6.6 g cm^{-3} for Bi2212.

On the other hand, swaging and flat rolling are the deformation procedures dominated by compression and the density of the core may go up to 80–90 % of the theoretical, i.e., the hardness gradient between the solidified powder and the metal sheath drastically increases.

Researchers have stated that by using harder cladding sheaths it could be possible to reduce the roughness of the core/sheath interface (sausaging) and increase powder filling factor [27].

Workability is an important factor in selection of sheath metals for superconducting composites. It is desirable to have a metal that is malleable enough to satisfy OPIT method. Permeability of the clad, which is involved with the oxygen balance for superconductor phase growth reactions of powder (inside the metal tube) during heat treatment steps, is another important point. The metal employed is expected to provide large areas of contact between core and sheath, i.e., large interfaces which are supposed to enhance the chemical reactivity and promote proper texturing of the core. The reaction heat treatment of the powder after its packing into the metal tube and going under drawing and/or rolling deformations gives the core a higher hardness and this is expected to reduce the roughness of the interface between the sheath and the core, in other words sausaging. Researchers have claimed that this happens through the improved densification of the powder core and therefore the overall uniformity of the composite yielding higher critical current density (J_c) values [27]. It is also put forward that the elastic limit and the ultimate strength of the composite are prolonged sintering times under oxidizing atmosphere only noble metal alloying elements avoid having oxide precipitates. All these reasons restrict the spectrum of the available clad sheath to pure silver and a few silver rich alloys.

Most commonly used silver alloys include Mg, Cu, Mn, Au and Pd. However, highest of the J_c values reported so far have been obtained with pure silver. The disappointing probability of chemical reaction between the silver alloys and the ceramic core, texturing irregularities and oxygen diffusivity hardships are all attempted to avoid by making multifilament composites consisting of pure silver around the core as filaments and the alloy as the clad tube around them all.

In order to identify the mechanical behavior of mono core tapes and multi core tapes with untwisted filaments, it can be assumed that there is equal strain in both the ceramic core and the metal sheath surrounding it considering tensile stress along the whole composite.

The *elastic modulus of the tape* can be given as:

$$E_{tape} = (1-f)E_{sheath} + fE_{core}(p) \tag{E.15}$$

In the equation above;

f : filling factor for the superconductor

E_{sheath} : Young modulus of the metal clad sheath

$E_{core}(p)$: Young modulus of the BSCCO core with porosity, p

Experimental results for the mono core Ag clad tapes are reported in the range of $p = 0.06 - 0.2$

For mechanical design, researchers for sure approached the behavior of the tapes as composites consisting of ductile sheath metal and brittle ceramic core inside. Along this approach, the *rule of mixtures* can be given with the following expression:

$$\sigma_{tape}(\varepsilon, p) = (1-f)\sigma_{sheath}(\varepsilon) + f\sigma_{core}(\varepsilon, p) \tag{E.16}$$

A linear variation with the external strain ε yield the assumption for *core stress* as:

$$\sigma_{core}(\varepsilon, p) = (\varepsilon_{r,core} + \varepsilon)E_{core}(p) \tag{E.17}$$

where, $\varepsilon_{r,core}$ is the *average of the residual strains* in the core(s). Another assumption for the metal sheath as having linear *strain hardening coefficient* gives:

$$\omega = (\partial\sigma_{sheath} / \partial\varepsilon)/(\varepsilon E_{sheath}) \tag{E.18}$$

and the *stress in the yielded sheath* is:

$$\sigma_{sheath}(\varepsilon) = (1-\omega)\sigma_{0.2,sheath} + \omega E_{sheath}(\varepsilon_{r,sheath} + \varepsilon) \tag{E.19}$$

In the equation above $\varepsilon_{r,sheath}$ is the *residual strain of the metal sheath*. The *linear strain-hardening coefficient* at room temperature was estimated by the researchers for mono core tapes as $\omega = 0.008$ and for multifilament tapes as $\omega = 0.02$.

Mechanical behavior of compressed ceramic rods (Bi2212) with a density of 87-92% of the theoretical value textured having the c-axis of the grains aligned in the pressing direction was examined by various researchers as a model for ceramic cores. Results derived from these experiments are as follows [27]:

Young modulus along the c-axis : $E_c = 44GPa$

Young modulus parallel to the ab-plane : $E_{a-b} = 118GPa$

Single crystal value of Young modulus in ab-plane : $E_{a-b} = 105GPa$

Shearing strength in ab-plane : $\tau_{a-b} = 25MPa$

Compression stress when ab-planes get cracked : $\sigma_{fracture} \approx 180MPa$

Ultimate tensile strength in ab-plane : $\sigma_{c,a-b} \approx 42MPa$

Isotropic thermal expansion coefficient : $\alpha_{a-b} = 10x10^{-6} K^{-1}$

Characteristic properties of pure silver (99.99%) do not change by annealing process under air or oxygen. This provides a reference in the selection of sheath metal. Properties of Ag at room temperature (unless other wise stated) are summarized below [27]:

Density : $d = 10.49g / cm^3$

Young modulus : $E = 44GPa$

Modulus of shear : $G = 32GPa$

Yielding strength : $\sigma_{0.2} = 55 - 64MPa$

Ultimate tensile strength : $\sigma_c \approx 130 - 170MPa$

Vickers Hardness : $HV \approx 20 - 33kg / mm^2$

Thermal expansion coefficient (77-1113^{o}K) : $\alpha = 21.6x10^{-6} K^{-1}$

Young modulus at 77^{o}K : $E = 77GPa$

Yielding strength at 77^{o}K : $\sigma_{0.2} \approx 13MPa$

After intense plastic deformation (work hardening) considerably high values of $\sigma_c \approx 350MPa$ and $HV \approx 103kg / mm^2$ were reported. It is also claimed that this reduced the malleability of silver by a factor of ten.

Fig.30 below represents the variation of max strain and ultimate tensile stress (both in normalized units) vs. total area reduction on a commercial fine silver wire.

The full curves and the dashed curves denote commercial fine silver and sterling silver (12.1%Cu) wires with 2-3 mm diameter, respectively. These wires are deformed after annealing. Normalization factors for commercial fine silver are $\varepsilon_{\max} = 0.5$ and $\sigma_c = 170MPa$ and for sterling silver $\varepsilon_{\max} = 0.3$ and $\sigma_c = 275MPa$.

Ability of the pure and sterling silver to undergo substantial plastic deformation without fracture (workability) is represented by $\varepsilon_{\max}$ and it is obviously seen that workability of both of the metals decreases in a stable manner along with the increasing deformation percentage.

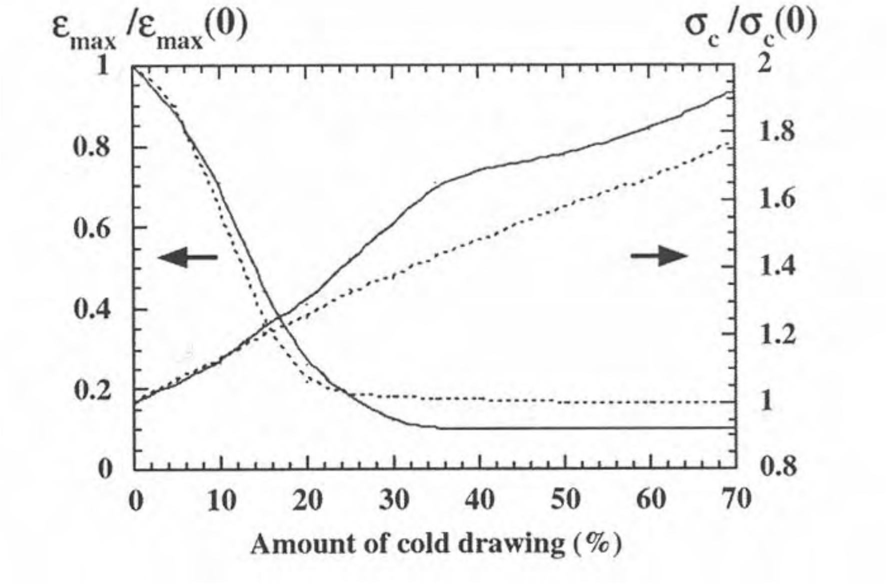

Fig.30 Variation of tensile strength (σ_c) and max strain (ε_{max}) with the total amount of cold drawing [27].

Annealing pure silver at temperatures over 300°C allows the metal to recrystallize thru stress relief and recover initial mechanical properties. Melting temperature for pure silver, $T_m = 961.93^o C$, is higher than the required value for Bi2212 to melt which is around 900°C.

At around 800^o C, alloying elements Mg, Cu and Mn has good solubility in silver. Use of oxygen free atmospheres in manufacturing process of these alloys let them demonstrate better results in terms of HV and $\sigma_{0.2}$ compared to those of pure silver. Solid solution is the most common way to alloy silver with the elements cited. Replacement of atoms one by one makes it more convenient to use compositions in atomic percent (atomic fraction).

Alloyed elements in silver, the solubility of which decrease with temperature, such as Mn and Cu, processes like ageing, annealing or slow modification may result in metallic aggregates. Nucleation of oxide precipitates during annealing in oxidized atmospheres is also inevitable and they are likely to form in very different sizes.

During tape manufacturing processes, hardening by metallic and oxide segregations, solid solution effects and cold working is possible to come up. Meanwhile, softening by annealing (dislocations relieved), grain growth and diffusion of alloying elements towards precipitates and BSCCO core also take place. Therefore, the overall strengthening mechanism turns out to be the balance of these two.

In fully oxidized alloyed sheaths final values for HV and $\sigma_{0.2}$ increase compared to pure silver, i.e., workability diminishes.

On ductile materials, it is assumed that $\sigma_{0.2}$ can be more or less estimated as 1/3 of the HV values, provided the deformation zone is well defined. Table 4 below illustrates the most common Ag-Mg alloys available and their properties for use in superconductor composites making.

OPIT (Oxide Powder In Tube) method gives results in composites manufacturing that heavily depend on the mechanical properties of the precursor powder all the way through the tape deformation before reaction baking. Putting the ceramic powder into the desired core shape is a process driven through the deformation of the metal sheath surrounding it. This process characterizes the final level of irregularity in the interface between the core and the sheath, in other words, *sausaging*.

Table 5. Most common silver-magnesium alloys and their properties [27].

Most common Ag-Mg alloys and properties		
Name	***Vickers Hardness (kg/mm^2)***	***Yielding strength (MPa)***
$Ag_{99.9}Mg_{0.1}$	79	-
$Ag_{98.8}Mg_{1.2}$	142	383
$Ag_{98.3}Mg_{1.1}Ti_{0.6}$	198	-
$Ag_{98.4}Mg_{1.1}Ni_{0.5}$	215	-
$Ag_{95}Mg_{2.5}Au_{2.5}$	173	-
$Ag_{95}Mg_{5}$	260	-

Powder density is generally not homogenous and Vickers Micro hardness measurements with a linear variation assumption can be used to determine it locally. Thickness of the sheath and the powder particle size can be both effective on density variations of the core.

Researchers have found out that starting with powder densities below 60% yields considerable solidification of the powder along with drawing [27]. Following the whole deformation process, the balance between friction shear and compressive stress in the interface of sheaths and compacted powder comes up due to reaching the critical value of powder density. Regarding lower compaction levels, amount of shearing stress transferred from the sheath to the powder is smaller but enough for making powder flow. On the other hand, the compressive stress built up is larger in scale and helps the powder solidify.

For the very dense powder at the beginning, stresses due to friction are larger. Deeper inside the core on the nested portions of the powder, either volume dilation or fracture takes place to allow relative displacements of grains. Use of alloys may promote drawing forces, thus yields denser cores accordingly.

As for the other deformation processes for the monofilament composites such as swaging, the major stresses are of compressive type. These stresses have been reported to yield 80% dense core and a HV value of around 170 kg/mm^2.

In another study it has been observed that when mono core Bi based wires with 60-70% initial density were deformed by cold rolling, the density of the cores reached up to 80% with HV values of 115-160 kg/mm^2. Nevertheless, the same deformation procedure starting with denser cores than the previous ones mentioned was reported to give the same HV values eventually.

Furthermore, some researchers stated that harder silver sheaths help obtain higher HV values thus, higher core density and less sausaging. These advantages come with the cost of greater inhomogeneities in the BSCCO cores.

The final shape and structure of filaments within the clad sheath depend on the location of the filaments in the composite under rolling process. Higher HV values and better texture were claimed for the filaments close to the edges of the composite. The difference mentioned rise up from the non-uniform distribution of shearing stresses across the tape while it is deformed. According to the findings of researchers, texturing begins at regions where the shear stresses reach the yield, i.e., regions close to the core-sheath interface. Annealing at 500^{o}C can reduce the increase in hardness values due to the plastic deformation of the powder particles.

Following the first sintering, usually microhardness of the core diminishes, because hard components in the precursor vanish and superconductor phases start to grow. Meanwhile, the density of the OPIT tape core may reach up to 90%. Mechanical deformation between in tandem sintering steps is ruled by compressive stresses. This helps maintain good c-axis oriented texturing along with strong intergranular contacts.

Upon sintering pure silver clad sheaths become very soft, at the same time as the alloy ones exhibit closer HV values to the core they surround.

During sintering of BSCCO precursors under oxidizing atmospheres Mg, Cu, Mn alloyed sheaths are not in a stable chemical state. Oxide precipitates formed in the metallic (Ag rich) matrix make them gain weight. This indicates the diffusion of oxygen through the sheaths very clearly. It is known that internal oxidation of silver alloys winds up an overall mechanical strengthening of the sheath by blocking the glide planes by tiny oxide precipitates. After this stage, the initial condition for the metal cannot be restored and the irreversible reaction given below takes place:

$$X+\frac{n}{2}O_2\rightarrow XO_n \tag{E.20}$$

where, X is one of the alloying elements. Solubility and distribution of the alloyed elements in a homogeneous solid solution or in heterogeneous precipitates modify the internal oxidation of the composite. Because the tapes usually consist of very thin (<100μm) metallic sheaths, oxygen concentration inside the composite reaches values sufficient to finalize the oxidation of alloying element(s) inside before the growth of the superconducting phases.

Researchers have observed small MgO particles of about 1μm and oxide precipitates 8-9μm long and 1-2μm thick on Ag-Mg alloy sheaths of Bi212 composites annealed in air [27]. Silver alloys play an important role in the formation of all superconducting phases during the reaction heat treatments regarding their oxygen permeability, diffusion of the alloying elements towards the ceramic core and the stability of their oxides. Fast nucleation of oxide precipitates inside the alloys accompanied with low diffusivity in silver produces very small overall chemical interaction of the core and the sheath. Reduction of the core and sheath interface area and smaller concentrations yield smaller amount of alloying elements transferred into the core and therefore a decreasing chemical reactivity.

Oxides having higher stability nucleate easily at alloy grain boundaries by use of the dissolved and diffused oxygen. In accordance with this, small size precipitates in large numbers occur. The oxygen needed for the superconductor phase growth mainly comes from diffusion through grain boundaries by the annealing atmosphere.

The differences in the oxygen diffusivity between the initial and work hardened alloy sheaths vary the partial pressure of oxygen inside of the filament(s) and affects the formation of superconductor phases directly. Another complex parameter affecting phase formation in a time dependant manner is the nucleation and coarsening of oxide precipitates at alloy grain boundaries. Migration of small amounts of alloying elements into the core where they contact with each other may also be disturbing for the phase growth.

In the light of experience, thick layers have been found necessary to enhance the mechanical properties of the composite at the expense of small crack formation at the interface between filament sheaths. These cracks may be detrimental as the deformation procedure advances. Filaments made of pure Ag tubes in contact with BSCCO powders and different silver alloys surrounding them have been used as an alternative to develop structural integrity and decrease the chances of core-sheath chemical interaction. This formation is expected to minimize the direct mechanical interactions of adjacent metal sheaths (filaments) and reduce transmit of shear stresses allowing ease in OPIT fabrication.

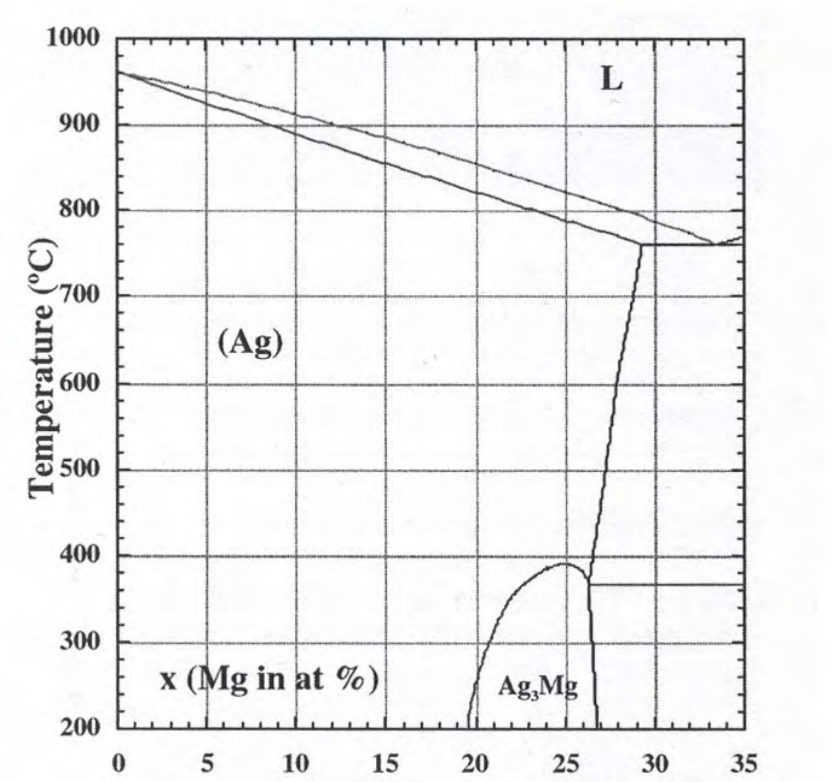

Fig.31 Equilibrium phase diagram of silver rich magnesium alloys $Ag_{100-x}Mg_x$ [27].

As seen in the phase diagram (Fig.31) above, silver rich silver rich magnesium alloys $Ag_{100-x}Mg_x$ are homogeneous solid solutions up to $x_s = 29.3$. In the range of interest for composite tapes, the solubility of Mg does not fall below the solidification line.

Melting temperature, T_m, is reduced by Mg addition. This limits the use of Mg alloys with Bi2212 powders to concentrations of x<7-8. Mg atoms randomly substitute Ag atoms and expand the FCC lattice parameter of pure silver that is $a = 0.4086nm$ to 0.4102nm for $Ag_{96}Mg_4$ alloy.

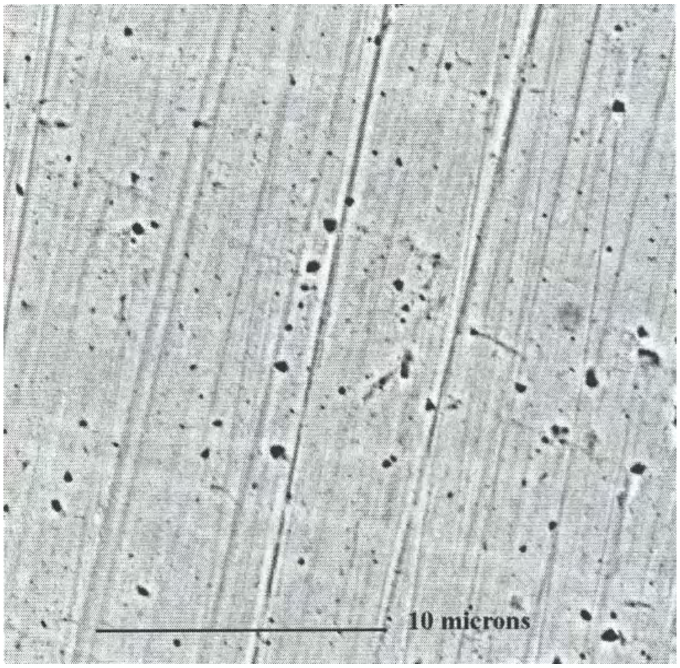

Fig.32 SEM backscattered picture for a polished cross section on an $Ag_{99.5}Mg_{0.5}$ commercial alloy tube after annealing in air for 200 hr at 800°C [27].

At room temperature, mechanical properties of as cast Ag-Mg alloys that are similar to ones of pure silver is listed below for $Ag_{98.8}Mg_{1.2}$ as an example:

Yielding strength $: \sigma_{0.2} = 78MPa$

Young modulus $: E = 74GPa$

Table 6 below further demonstrates some Mg alloys with HV values increasing linearly along the Mg content.

The variation in the HV values rise from local distortions by the substituted Mg atoms. At the beginning of oxidation under air at 350°C, researchers state that sheaths became harder by the MgO precipitates formed. After one or two hrs of treatment at 820°C, HV values were found to diminish and finally reached the values in Table 5.

Table 6. Microhardness of silver rich Mg alloys ($Ag_{100-x}Mg_x$) as cast (argon annealed or free of tension), after intense cold working and long oxidization process [27].

Mg (atomic%)	**HV as cast (kg mm^{-2})**	**HV cold worked (kg mm^{-2})**	**HV oxidized (kg mm^{-2})**
0.0	20-33	103	20-30
0.1	33	55	79
0.5	26-32	111	108-117
1.2	36	120	142
2.0	35	200-220	130-150
5.0	-	125	260

According to the SEM and XRD evaluations is also stated that alloy grains were refined and turned into pure silver in a practical manner.

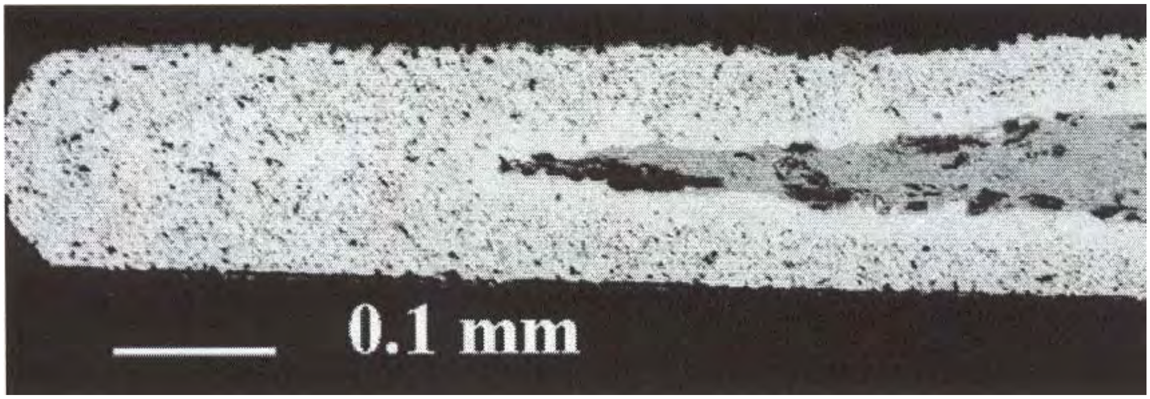

Fig.33 Polished transverse cross section SEM picture of a monofilament Bi(Pb)2223 tape with $Ag_{81}Cu_5Ti_{14}$ after complete heat treat. Large and small oxide precipitates seen are of Cu and Ti, respectively [27].

The HV values of alloys that are fully oxidized always turn out to be bigger compared those of silver and smaller compared to those of compacted BSCCO powder under the same conditions. If the content of Mg is above 3% sheath is almost as hard as the core. Young modulus of the sheath changes in a linear trend with the amount of the MgO dispersed in silver. Young's modulus for magnesium oxides is $E_{MgO} = 311 GPa$.

For $Ag_{98.8}Mg_{1.2}$ the yield stress is $\sigma_{0.2} = 383MPa$ and Young modulus is $E_{alloy} = 86GPa$.

As a summary, there are two mechanisms reducing the ductility of the sheath; the first and the faster one is the nucleation of MgO precipitates and the second, slower one is the coarsening of precipitates at alloy grain boundaries.

The precipitates found to be slightly larger at the surfaces in contact with the oxidizing atmosphere compared to the other portions of the sheath. The total amount of Mg in exposed places was also found to be larger. Researchers discovered that Cu was taken up from the BSCCO cores to produce mixtures of Cu and Mg oxides due to the high diffusivity of Cu into the fully oxidized alloy sheath.

Since the precipitates limit the growth of host alloyed grains, the size of precipitates is influential on the average distance between them, thus, the final hardness. Typical grain sizes of the host metallic alloy are 2-10 mμ; on the other hand, for pure silver it is 50-100 mμ. Through the refinement of the host matrix, grains of the segregated particles increase and the number of the intergranular boundaries, opening effective diffusion paths, which enrich the overall diffusivity of oxidized sheaths.

At the core-sheath interface, disoriented BSCCO grains may be at all positions but perpendicular to the filaments. This orientation of grains is detrimental in terms of current transportation. The interaction between the alloyed sheaths and the superconducting filaments that produce these intergrowths of BSCCO grains remains a secret. On the other hand, oxidization of sheath increases the oxygen diffusivity and parallels to this the partial pressure of oxygen in the core. Therefore, the optimum sintering temperatures for superconducting phases are shifted up and the development of intergrowths is promoted. Researchers have also considered an uneven distribution of MgO-precipitates across the sheath thickness. This finding indicates that diffusion of Mg towards the filaments during sintering together with the opposite diffusion of Cu form the cores to the sheaths, produces a small degradation of superconducting properties of the tape. However, the diffusivity of Mg on pure silver and silver alloys has not yet been quantified [27].

Fabrication of Mono and Multifilament Wire

In our project, OPIT method was utilized to manufacture both mono and multifilament wires. The type of clad sheath was one of the parameters involved with the fabrication of two monofilament and four multifilament wires attempted for fabrication. The metal tubes used were 99.9% pure silver or 0.2% Mg-Ag alloy with dimensions of $OD = 10mm$ (0.394") and $ID = 8mm$. In the manuscript, pure silver sheath will be denoted as "Ag" and silver-magnesium alloy sheath as "Mg", respectively.

Fig.34 Hydraulic drawing bench employed for drawing operations. Courtesy of TAMU ECAE research group.

Before the Bi2212 precursor powder was packed into them, acetone and isopropanol were employed to assure cleanliness of the tubes, in and out. Pressing the end of the tubes in a vise and then hammer clamping the flattened corners turned out to be the best method for sealing after unsuccessful trials of dead-annealed Ag plugs tapered at one end to ensure a smooth reduction transition area of reduction between powder and plug itself (see Fig.35). All of these plugged tubes ruptured soon after the first few steps of drawing operation at locations very close to the plug’s beginning regardless of the sheath material. The tubes were all 15” long. As explained in the schematics in Fig.7, prepared Bi2212 precursor powders were first filled into the tubes loosely by tapping the tube against a hard surface and finally compacted by a ramrod. After filling up to the desired level, the open end of the tube was clamped identical to the preceding one.

Table 7. Reduction ratios between successive drawing dies; the swaging dies used and the corresponding drawing steps.

Drawing Step	***Reduction ratio between drawing steps (%)***			***Drawing Die Diameter [10^{-4}inch]***	***Swaging Die Diameter [10^{-4}inch]***
01	*(01-02)*	20.74	***Big swager***	3555	3660 and 3430
02	*(02-03)*	20.73		3165	3230 and 3040
03	*(03-04)*	6.15		2818	2670
04	*(04-05)*	12.07		2730	2670
05	*(05-06)*	8.41		2560	2340
06	*(06-07)*	11.10		2450	2340
07	*(07-08)*	6.47		2310	2190
08	*(08-09)*	13.31		2234	2050
09	*(09-10)*	8.56		2080	1920
10	*(10-11)*	16.27		1989	1800
11	*(11-12)*	5.31		1820	1680
12	*(12-13)*	16.33		1771	1680
13	*(13-14)*	5.24		1620	1570
14	*(14-15)*	16.62		1577 (1530)	1470
15	*(15-16)*	17.24		1440 (1404)	1380
16	*(16-17)*	8.95		1310	1290
17	*(17-18)*	13.88	***Small swager***	1250	1210
18	*(18-19)*	13.32		1160	1140
19	*(19-20)*	7.27		1080	1000
20	*(20-21)*	5.69		1040	1000
21	*(21-22)*	9.66		1010	0940
22	*(22-23)*	10.74		0960	0940
23	*(23-24)*	10.10		0907	0780
24	*(24-25)*	11.73		0860	0780
25	*(25-26)*	11.53		0808	0780
26	*(26-27)*	10.25		0760	0730
27	*(27-28)*	10.80		0720	0630
28	*(28-29)*	11.42		0680	0630
29	*(29-30)*	12.11		0640	0550
30	*(30-31)*	9.75		0600	0550
31	*(31-32)*	10.25		0570	0510
32	*(32-33)*	14.27		0540	0510
33	*(33-34)*	7.84		0500	0470
34	-	-		0480	0430
35	-	-		0480 HEX	0430

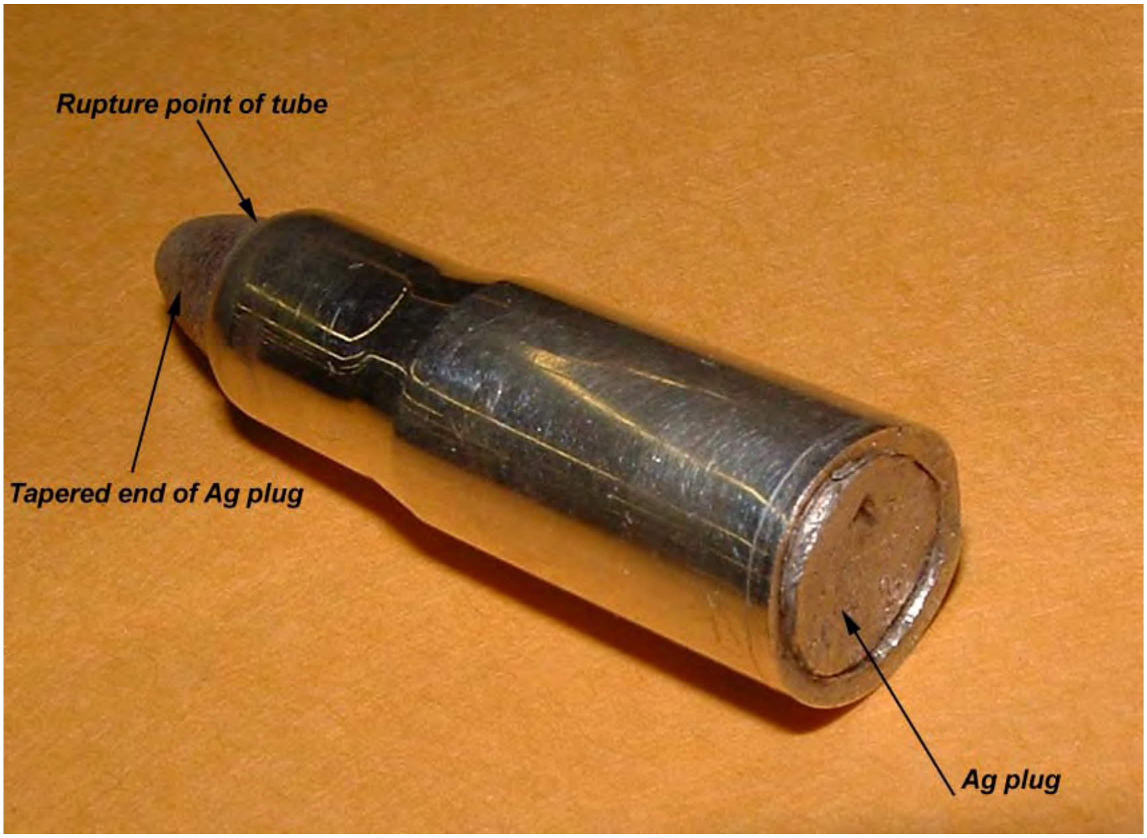

Fig.35 Ruptured part of the powder-filled-tube at very early stage of drawing operation. It shows *dead annealed pure-silver-plug with tapered end* as inserted in the tube for sealing. This tube failed during drawing operations just at the (ending) border of the taper, indicated by arrow. The length of the whole part is ~2.5 cm and the largest diameter is 10 mm in this picture.

The initial packing density of the billets was calculated by weighing the sealed tube as full of powder. Assuming the clamped-end tubes completely filled and knowing the occupied volume along with the theoretical density of the occupant powder (6.45 g/cm^3), the average value for initial packing density was found as ~32% of the theoretical density.

Having its ends sealed, the tube full of powder then was swaged at both ends by the big swager (see Fig.36). Before each drawing step either of the swagers loaded with the appropriate swaging die utilized to form and make the end of the tube fit through the drawing die. The swaging dies and the drawing steps they correspond to are presented in

Table 7. Properties of the drawing dies, the effects of which were discussed in the literature survey section, were held fixed as parameters. All the drawing dies were polished before drawing operations held and washed with alcohol in ultrasonic cleaner to assure any remaining material and lubricant was avoided.

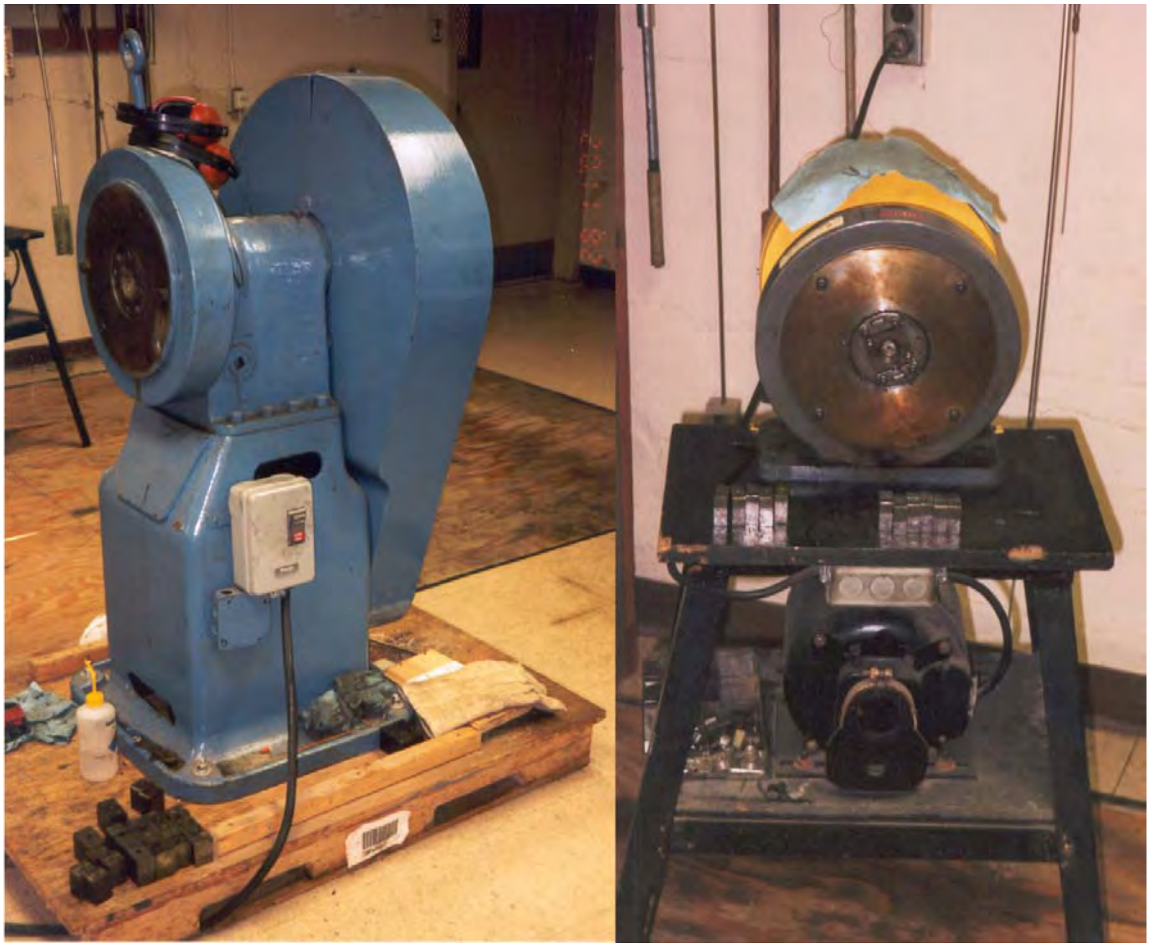

Fig.36 The big and the small swagers from left to right, respectively. Swaging dies for each swager are also shown as grouped. Both courtesy of TAMU ECAE research group.

The whole collection of the drawing dies used comprised of tungsten carbides with polished bells and blended back and front having a standard $\alpha = 10^o$ angle. The original reduction schedule adopted was according to *B&S copper wire reduction scale* with a fixed reduction per pass rate of 20.71% between each successive step [28, 29].

However, the drawing schedule was modified by inserting new drawing dies in between steps with respect to the requirement of the wire structure and sheath metal type as hardship experienced along the drawing operations. The dies utilized for drawing operations of different wire types are demonstrated in Table 8.

Table 8. Wire drawing dies utilized with respect to filament structure and sheath metal type. Check marks in parenthesis denote use of alternative dies.

Wire Drawing Dies Utilized With Respect To Filament Structure and Sheath Metal Type						
Drawing Die Diameter [10^{-4}inch]	***Ag Sheath Monofilament***	***Mg Sheath Monofilament***	***Ag filament Ag tube Multifilament***	***Ag filament Mg tube Multifilament***	***Mg filament Mg tube Multifilament***	***Mg filament Ag tube Multifilament***
3555	✓	✓	✓	✓	✓	✓
3165	✓	✓	✓	✓	✓	✓
2818	✓	✓	✓	✓	✓	✓
2730			✓	✓	✓	✓
2560				✓	✓	✓
2450	✓	✓	✓	✓	✓	✓
2310				✓	✓	✓
2234	✓	✓	✓	✓	✓	✓
2080				✓	✓	✓
1989	✓	✓	✓	✓	✓	✓
1820		✓	✓	✓	✓	✓
1771	✓	✓	✓	✓	✓	✓
1620				✓	✓	✓
1577(1530)	✓ (✓)	✓ (✓)	✓ (✓)	✓(✓)	✓(✓)	✓(✓)
1440(1404)	✓ (✓)	✓ (✓)	✓ (✓)	✓(✓)	✓(✓)	✓(✓)
1310				✓	✓	✓
1250	✓	✓	✓	✓	✓	✓
1160			✓	✓	✓	✓
1080	✓	✓	✓	✓	✓	✓
1040				✓	✓	✓
1010				✓	✓	✓
0960	✓	✓	✓	✓	✓	✓
0907				✓	✓	✓
0860	✓	✓	✓	✓	✓	✓
0808				✓	✓	✓
0760	✓	✓	✓	✓	✓	✓
0720				✓	✓	✓
0680	✓	✓	✓	✓	✓	✓
0640				✓	✓	✓
0600	✓	✓	✓	✓	✓	✓
0570				✓	✓	✓
0540	✓	✓	✓	✓	✓	✓
0500	✓	✓	✓	✓	✓	✓
0480	✓	✓				
0480 HEX	✓	✓	not applicable	not applicable	not applicable	not applicable

Ag sheath monofilament and Mg sheath monofilament wires were the easiest ones to shape. They deformed smoothly throughout all the steps along the original reduction rate, but Mg wire showed more resistance at the last three steps of the drawing operations due to its work hardening characteristic and even ruptured.

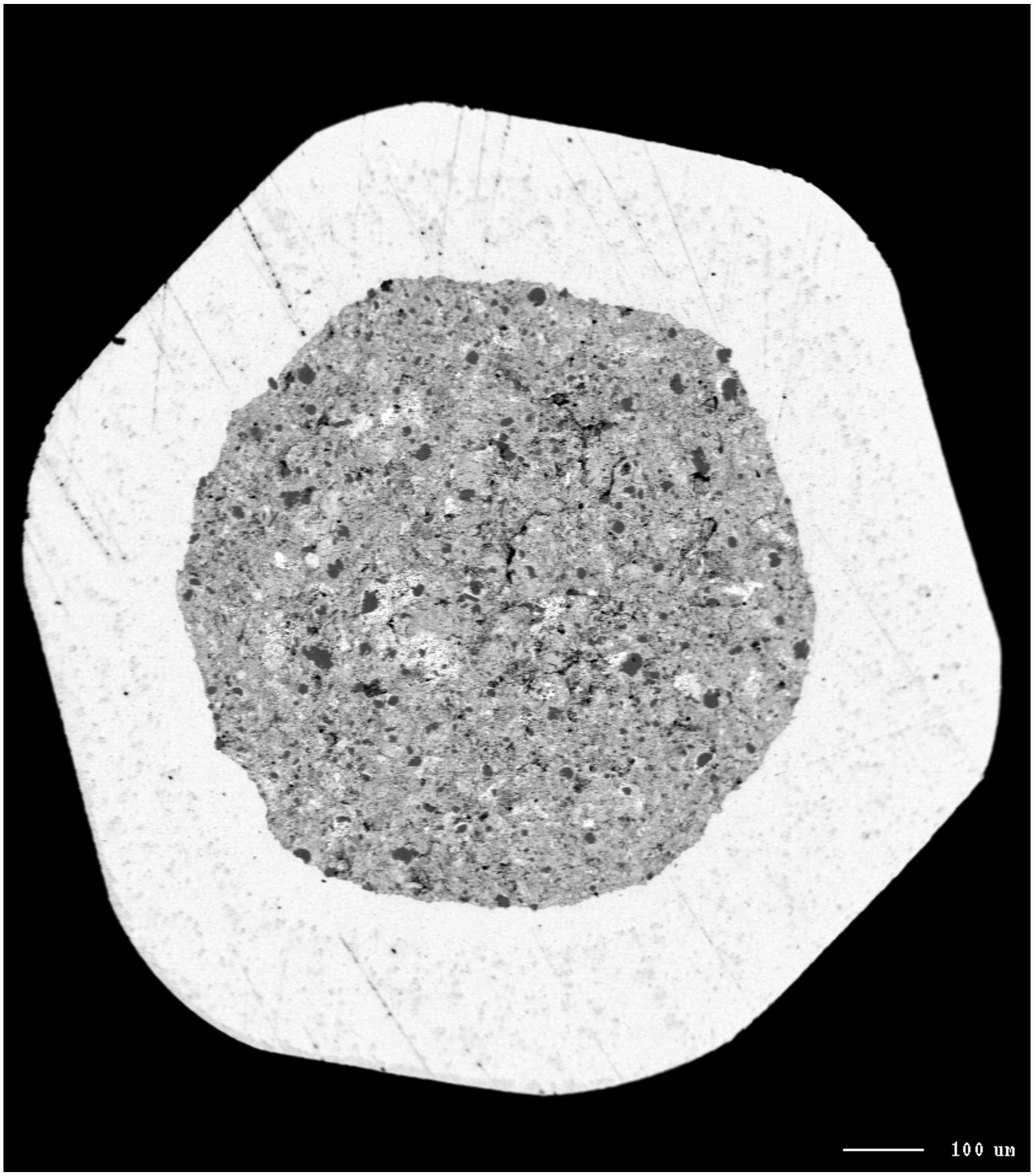

Fig.37 BSE image of *hexagonal filament* with 0.0480" (~1.22 mm) diameter, BB4_h48_63x. Dark gray circular area is Bi2212 compacted powder.

Drawing the monofilament wires one step further through 0.0480” diameter hexagonal die yielded in hexagonal filaments (Fig.37) to be stacked in Ag or Mg tubes for achieving multifilament wires.

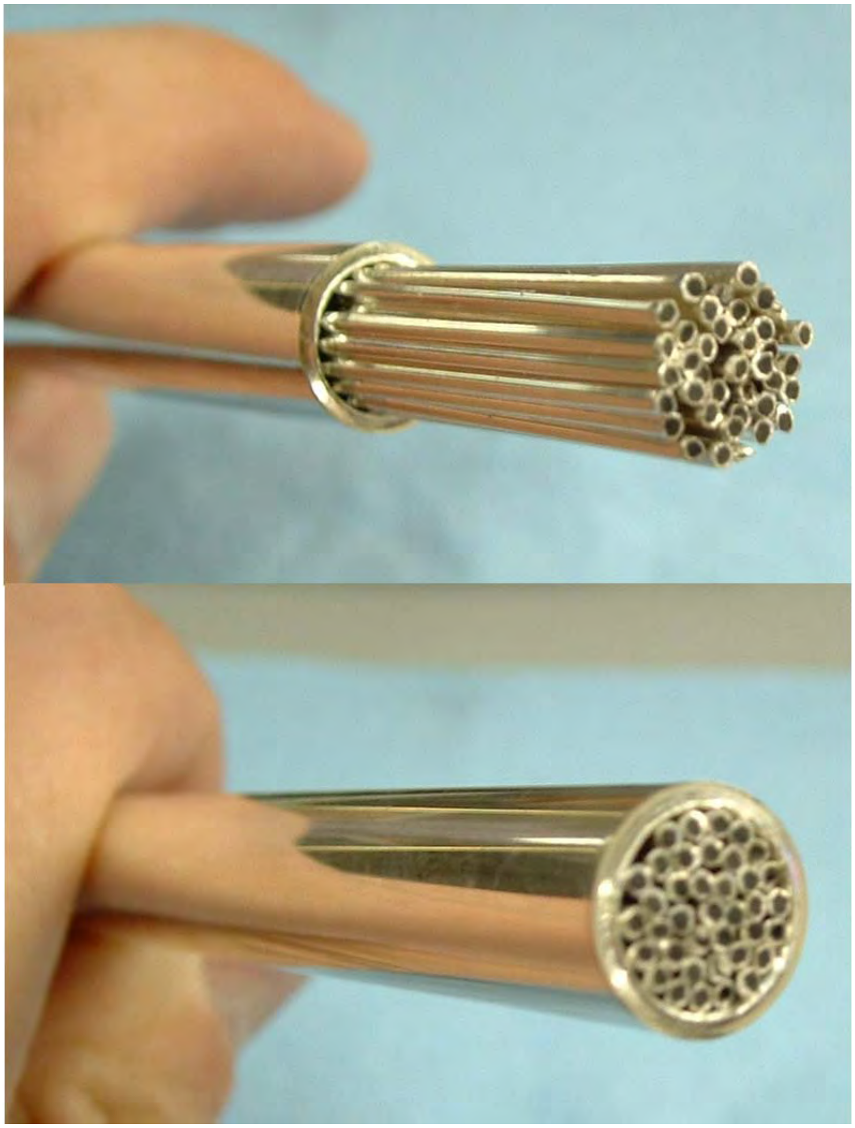

Fig.38 Just after 38 hexagonal filaments packed into 8” long tube, ready for swaging and drawing operations. Filaments are specifically longer than the tube they are bundled in.

Use of a 10:1 mixture of *Slick50* and *MobilOne* motor additives respectively, provided perfect lubrication for all drawing operations carried out [28].

Following the cleaning of each hexagonal wire, they were cut at appropriate length with respect to the outer tube that they would be inserted in. Fig.38 shows “38 filaments” as packed into the tube. The filaments were held specifically longer than the tube to allow the tube to elongate and cover them all after the first few steps of drawing operation and, since the tube tended to deform more than the pack of filaments inside, this arrangement was employed upon experience.

Eventually, the filaments and the surrounding tube demonstrated similar and compatible amount of elongation with each other.

All swaging and drawing operations of multifilament wires were carried out in the same fashion with that of the monofilament wires. Among all the multifilament wires fabricated, *Ag filament-Ag tube* was the best in terms of malleability. It yielded softly without any problem, providing a shiny and scratch free outer surface. No rupture was observed through out the drawing operations with the indicated reduction schedule in Table 7. Besides, the overall shape of the wire was straight.

Hardship and occasional rupturing were experienced with the *Mg filament-Mg tube* wires after the first five steps. Nevertheless, the process was completed with a satisfactory result. The final wire with 0.0500” diameter as for all the mono and multifilament wires manufactured, had a curvy shape eventually.

Both of the variant material wires, *Ag tube-Mg filament* and *Mg tube-Ag filament*, failed quickly under the usual drawing conditions.

Ag filament-Mg tube lasted till drawing die 1820, Mg filament-Ag tube till die 2310 at the first attempts. The deformed portions of the wires both looked good without dents or scratches. The failure was then attributed to the different deformation characteristics of Mg alloy and pure Ag displayed under the same load and conditions.

Contrary to the wires that filaments and outer tubes of which were of the same metal, variant material filament and tube composites needed more drawing steps introduced to the regular schedule. The steps were reduced to an average of 10% per pass where constant failure was observed, but because the ratio of [*tube wall thickness/wire diameter*] diminished rapidly, this alone seemed not enough as remedy.

Then, annealing was considered for the first time in the drawing operations. Upon failing at step 1550, *Ag filament-Mg tube* multifilament wire was annealed at 500^{o}C for 1.5 hours under air. Remaining drawing steps were performed successfully for the composite this time to achieve 0.0500" diameter product.

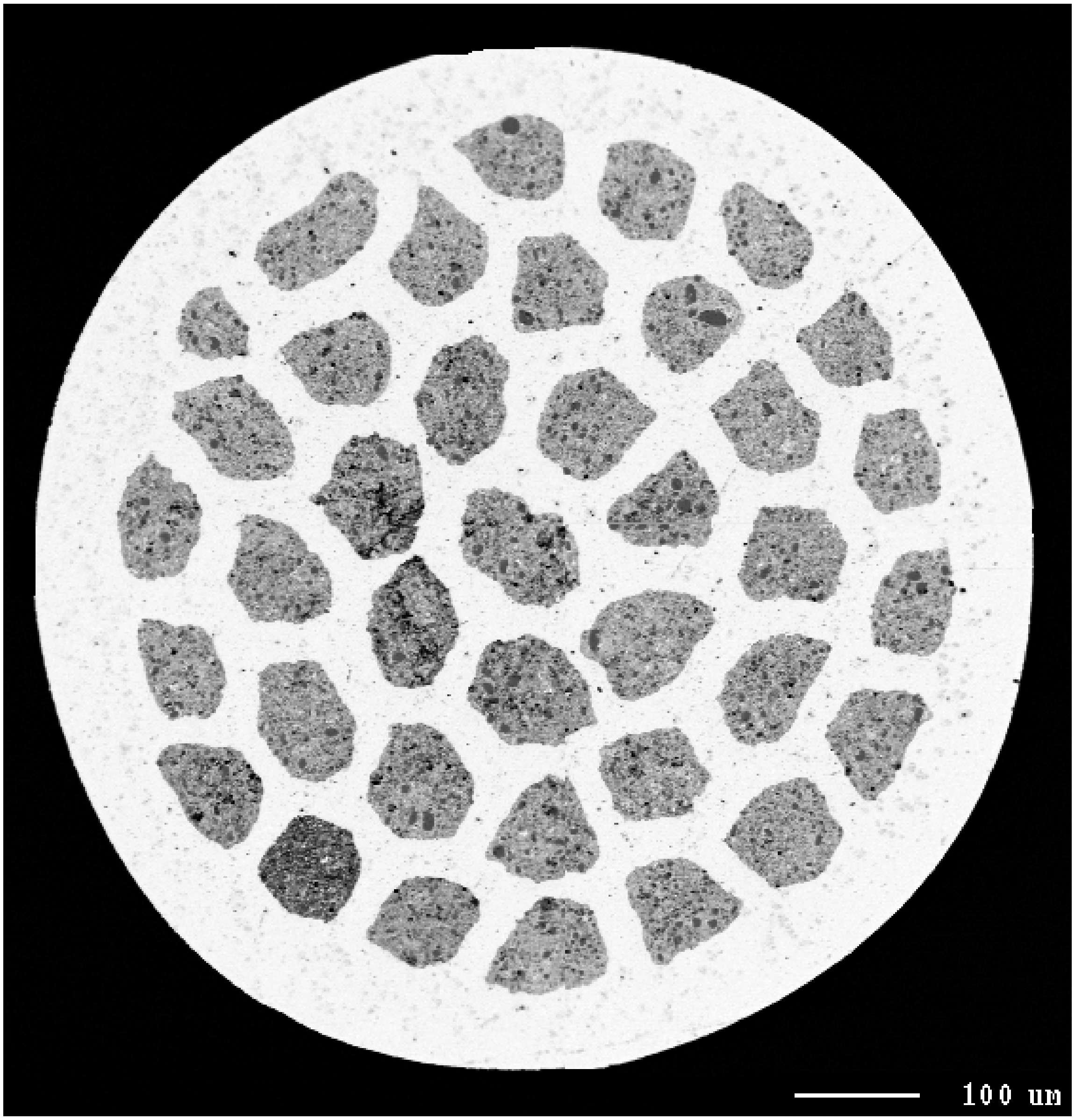

Fig.39 BSE image of *Ag filament-Mg tube* wire with 38 filaments, 0.0600" (1.52 mm) diameter, BB4_a60_63x.

Unfortunately, the same annealing schedule did not work with the *Mg filament-Ag tube* wire. Although annealed before drawing, rupturing at steps 1440, 1160, 0960 and 0760 consecutively this composite was not possible to reduce to the targeted dimension. The reason for the failure of this variant was the substantial difference in deformation between the pure silver tube and comparatively very rigid Mg alloy sheathed pack of filaments. The soft pure silver tube must have taken the major portion of the tensile load despite the filaments, which remained almost the same in length.

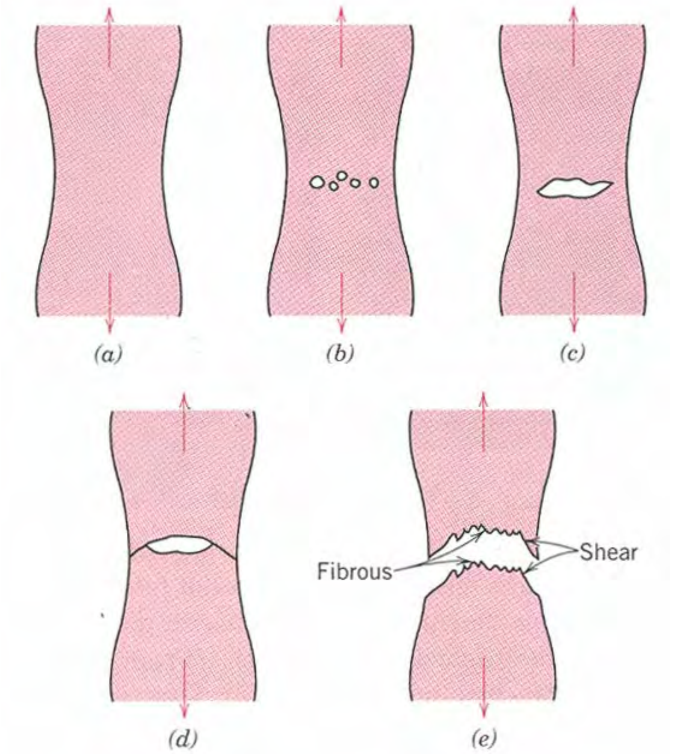

Fig.40 Schematic explanation of cup-and-cone-fracture, (a) initial necking, (b) small cavity formation, (c) coalescence of cavities from a crack, (d) crack propagation, (e) final shear fracture at a 45^o angle relative to the tensile direction [30].

As an alternative fabrication schedule for Mg filament-Ag tube multifilament wires, the assembly, just like shown in Fig.38, was annealed for 2 hours at 500^{o}C prior to drawing. Subsequent drawing operations raised excessive elongation of the pure silver tube compared to previous experiences with the same variant.

The failure came at a very early step, 2818. Preceded with a sense and noise of work hardening, rupturing continued at every first or second step followed, although 1.5 hour annealing at 500°C was practiced before each drawing step. Eventually, packing of annealed Mg filaments into not annealed Ag tube was tried. However, going a few more steps down compared to the other, this attempt also turned out to be in vain.

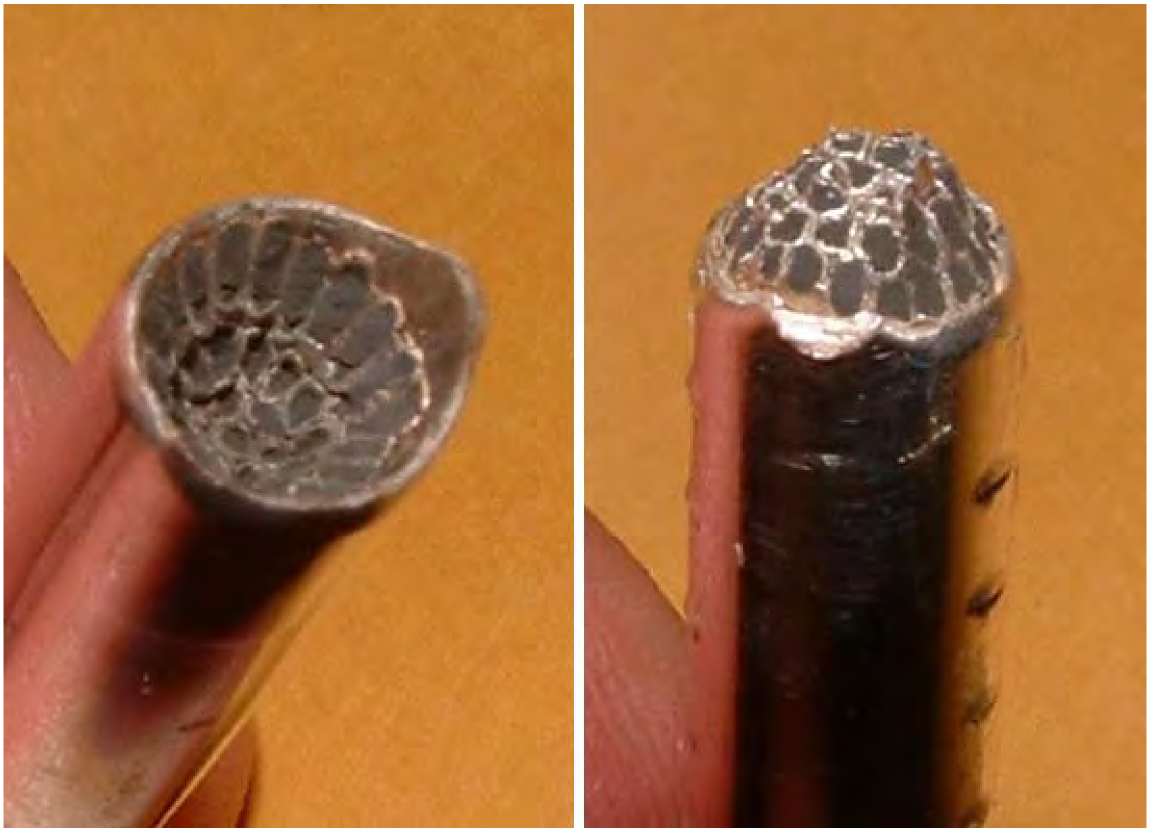

Fig.41 Classical cup-and-cone-fracture observed at early stage of drawing operation on Mg filament-Ag tube multifilament wire.

Therefore, the only reasonable solution appeared to be following a schedule with cooperative use of annealing and 5% reduction per pass for this variant of multifilament wires. Due to financial restrictions, new drawing dies could not be introduced to the collection we had in hand. All of the multifilament wires demonstrated a final deformed state very similar to well-known *cup-and-cone-fracture* of ductile materials as they failed (Fig.41). Taking a good look at the fractured surfaces of the multifilament wires brought up the idea that the outer tube failed first as it reached an insufficient wall thickness to contribute the strength of the composite and then, the filaments ruptured in accordance with the cup-and-cone-fracture theory (see Fig.40).

As a result, fabrication of 0.0500" diameter Ag sheath and Mg sheath monofilament wires with Ag filament-Ag tube, Ag filament-Mg tube and Mg filament-Mg tube variant multifilament wires was satisfactorily achieved. Transverse cross sectional BSE (back scattered electron) images of all wires can be seen in Appendix 3. Sausaging interpretation of wires at different stages of drawing represented with axial cross section BSE images are given under subtitle Investigation of Interface and Filament Pattern for Sausaging.

Fabrication of Mono and Multifilament Tape

After fabrication of mono and multifilament Bi2212 superconductor wires, the next goal was making tapes out of these available wires by means of optimized rolling operations. The rolling mill employed with a roller diameter of 4.230" (~107 mm) was first calibrated to perform constant and variable reduction schedules of rolling deformation (Table 9, and Fig.42). For this purpose, a monofilament wire was used as a calibrator model and after each step of reduction by one increment on the scale of the mill; thickness of the tape was measured, thus was acquired the calibration chart in Fig.43. The tape was put through the same deformation level three consecutive times at every step. The lubricant utilized was WD40 and helped maintain smooth surface on tapes.

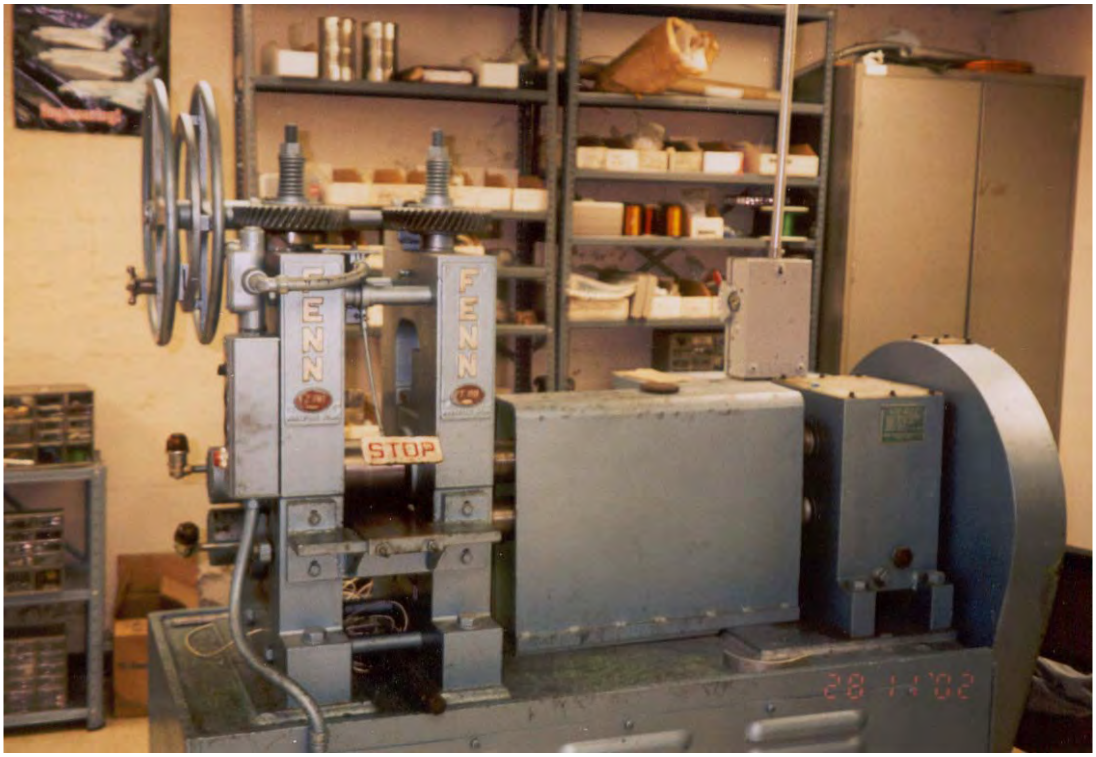

Fig.42 Rolling mill used for tape rolling operations. Courtesy of TAMU ECAE research group.

Table 9. Tape deformation schedules applied in rolling process. *0.05dia* and *0.06dia* indicate the diameter of the wire before rolling process as 0.0500” and 0.0600”, respectively. IR1 and IR2 correspond to *increasing rolling rate per pass* schedules #1 and #2, respectively. Bold face reductions denote the tapes that SEM samples were prepared out of.

Tape Deformation Schedules Applied in Rolling Process									
Monofilament				***Multifilament***					
Ag sheath		***Mg sheath***		***Ag filament-Ag tube***		***Ag filament-Mg tube***		***Mg filament-Mg tube***	
Constant reduction/pass	***Variable reduction/pass***	***Constant reduction/pass***	***Variable reduction/pass***	***Constant reduction/pass***	***Variable reduction/pass***	***Constant reduction/pass***	***Variable reduction/pass***	***Constant reduction/pass***	***Variable reduction/pass***
5%(0.05dia)	IR1(0.05dia)	**5%(0.05dia)**	IR1(0.05dia)	5%(0.05dia) 5%(0.06dia)	IR1(0.05dia) IR1(0.06dia)	**5%(0.05dia)**	**IR1(0.05dia)**	**5%(0.05dia)**	**IR1(0.05dia)**
10%(0.05dia)	IR2(0.05dia)	10%(0.05dia)	IR2(0.05dia)	-	-	-	-	-	-
15%(0.05dia)	-	15%(0.05dia)	-	-	-	-	-	-	-
20%(0.05dia)	-	20%(0.05dia)	-	-	-	-	-	-	-
25%(0.05dia)	-	**25%(0.05dia)**	-	**25%(0.05dia)** **25%(0.06dia)**	-	**25%(0.05dia)**	-	**25%(0.05dia)**	-
30%(0.05dia)	-	30%(0.05dia)	-	-	-	-	-	-	-

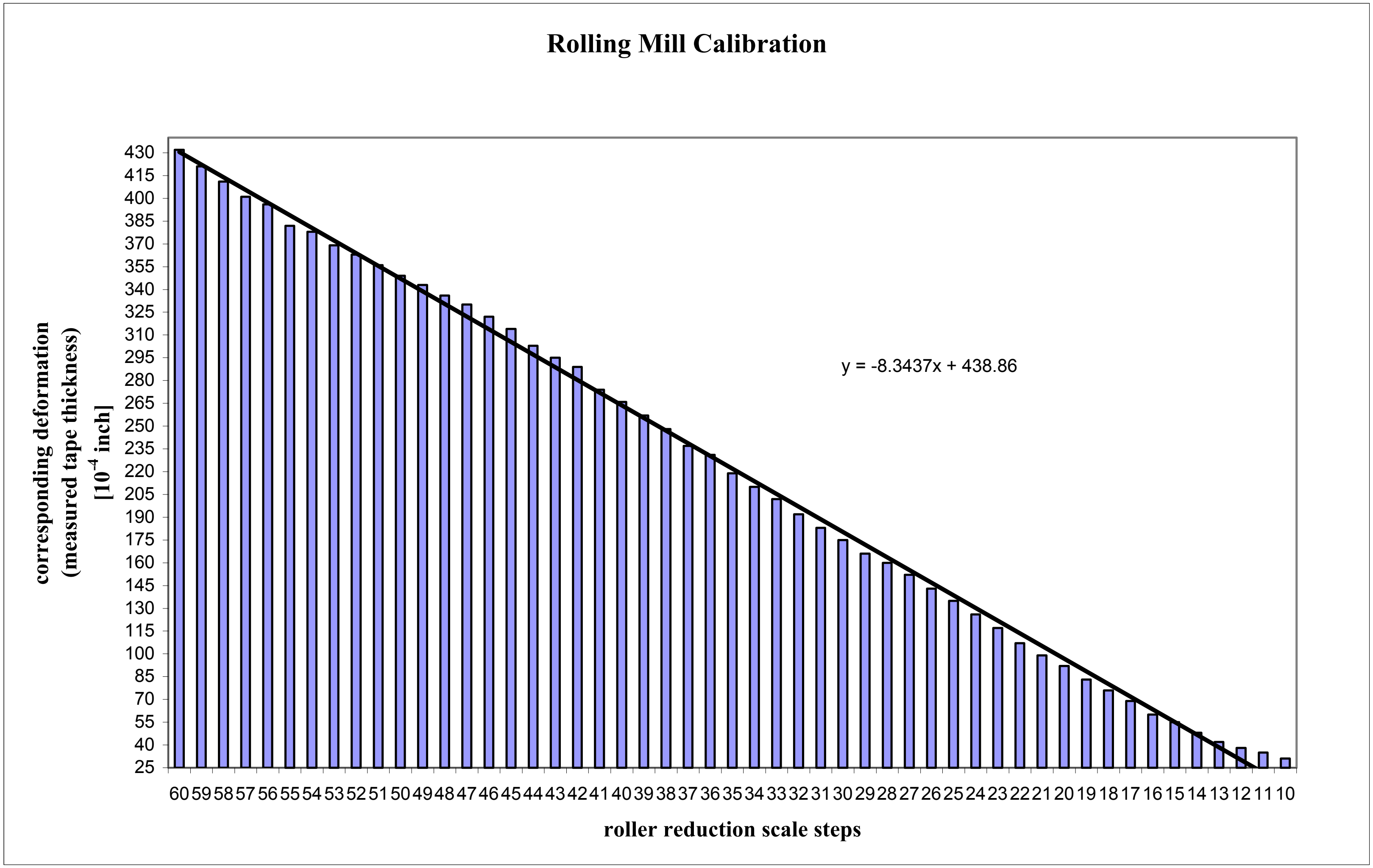

Fig.43 Rolling mill calibration chart. Tape deformation schedules were all arranged with respect to corresponding *roller reduction-scale-steps* in this chart.

Knowing the initial size of the wire to be deformed and the aimed thickness of the tape, constant and variable reduction per pass rolling schedules were designed to reveal the effect of deformation regime on mono and multifilament tapes with different sheath metals. These regimes comprised of 5, 10, 15, 20, 25, and 30% constant-reduction-per-pass and IR1 and IR2 variable-reduction-per-pass schedules. *IR1 schedule* included successive steps of 5, 10, 15, 20, 25, 30, 35, 40, 30% reductions per pass while *IR2* consisted of consecutive steps of 10, 20, 30, 40, 50, 8% reductions per pass. For every pass in each deformation regime the thickness sought was calculated and the corresponding roller reduction scale step was determined. Table 9 demonstrates the tape deformation schedules applied to various composites. Appendix 8 contains pictures and thickness measurements of the tape samples taken at every step for all schedules applied. Image analysis was performed to expose the outcomes of the deformation regimes, i.e., of tape sheath and core areas were calculated on BSE pictures transformed into binary images by means of software. The results are presented in detail under the major section; Evaluation of Structural and Chemical Integrity of Wires and Tapes.

During deformation, the main problem experienced with tapes was "curving". It was very hard to have both mono and multifilament composites deform as straight tapes.

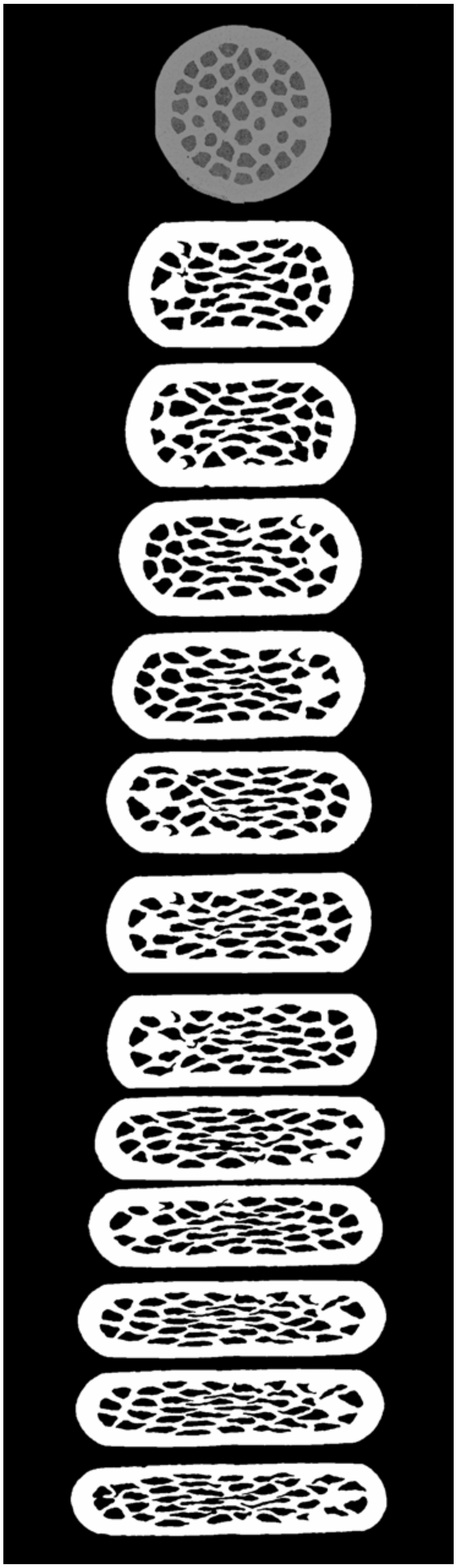

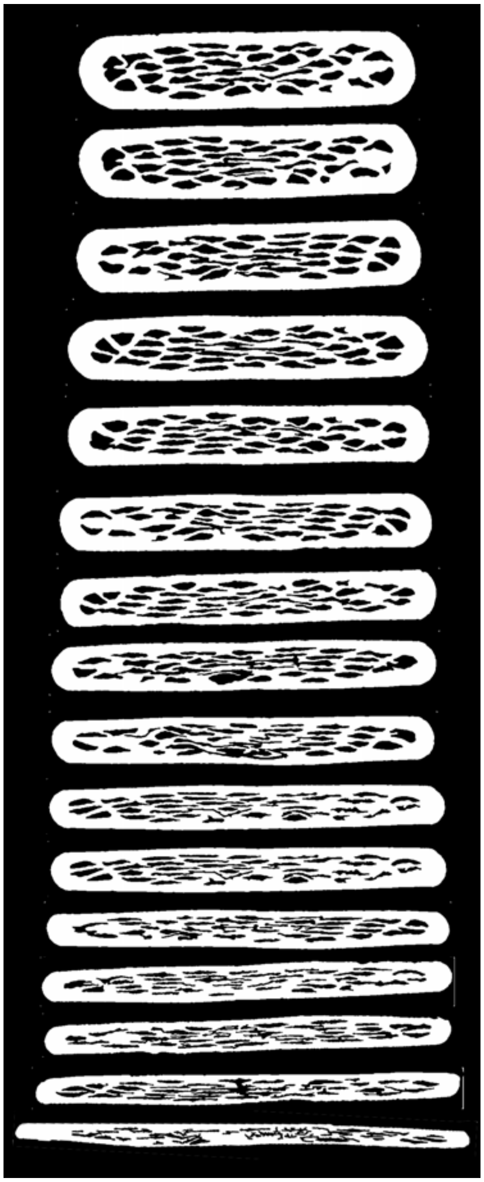

Fig.44 Binary images of 38 filament tape, in sequence, to represent *aspect ratio variation* at each rolling deformation step. BB5_multi_Mg filament_Mg tube_5% reduction_dia500_63xBSE.

Fig.44 shows all rolling deformation steps and corresponding variations in aspect ratio for a multifilament tape sample, BB5_multi_Mg filament_Mg tube_5% reduction_dia500_63xBSE. The numerical values of deformation can be seen in Tables 13-23 under section titled Image Analysis and Results.

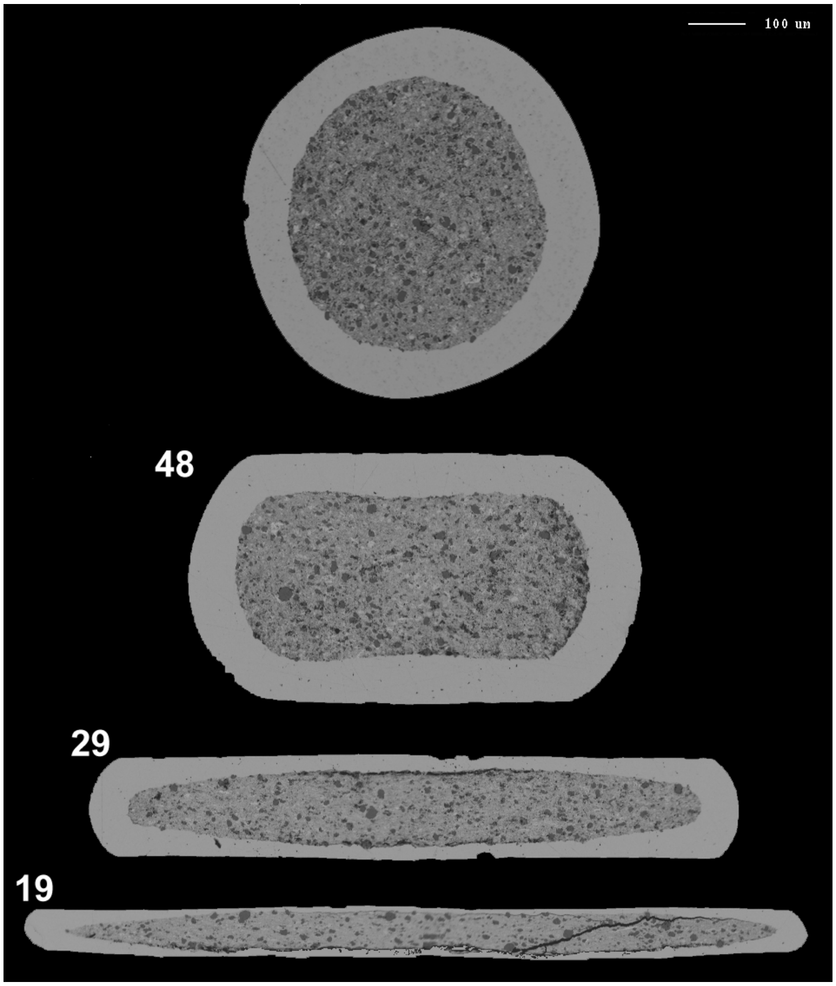

Fig.45 BSE images of wire and subsequent rolling deformation steps, 48, 29, 19 for 5% reduction, 0.0500” diameter, Mg tube monofilament tape, BB3_Mg_63x.

BSE images of later rolling steps (thinnest ones) somewhat appeared kinky for all tapes compared to those of earlier/thicker steps (Fig.44 and 45). This was due to lack of earlier SEM image sample preparation technique. The tape pieces seen in Appendix 8 were inserted into holes drilled on pre-molded epoxy sample holders, one by one. They were first cut by Dremel tool in expectation of a better cross section to avoid squeezing effect of scissors. However, most of the thinner samples appeared so damaged that all the rolling process had to be repeated to prepare new sets of samples. This time, the tapes were cut by scissors after every reduction step and worn out more by means of abrasive agents to achieve the desired view and polishing level.

Sausaging interpretation of tapes at different stages of rolling process represented with axial cross section BSE images are given under subtitle Investigation of Interface and Filament Pattern for Sausaging.

KINETICS, PHASE TRANSFORMATION AND GRAIN ALIGNMENT OF Bi(Pb)-Sr-Ca-Cu-O SYSTEM

Literature Survey

The Bi(Pb)SrCaCuO system offers a very rich crystal chemistry including the three superconducting phases: 2201, 2212 and 2223 (these numbers indicate the Bi:Sr:Ca:Cu cation ratios of the superconductor phases mentioned).

Researchers revealed that 2223 is the hardest of all to prepare. On the other hand, lead substitution made synthesis of this phase somewhat easier.

In their work, which draws a general picture of kinetics and phase transformation of Pb doped BSCCO systems, Strobel and Fournier [31] assumed a constant oxygen pressure (air) and a constant Pb/(Bi+Pb) ratio of 0.20. They prepared samples with composition $(Bi_{0.8}Pb_{0.2})_2Sr_2Ca_{n-1}Cu_nO_x$. Here *n* changed as follows; n=0, 1, 2…7, 10, 15.

For n=1, the formula becomes $(Bi_{0.8}Pb_{0.2})_2Sr_2Cu_1O_x$. In the absence of Ca, they found two dominant phases for this step. The first was 2201. The next one was another BiSrCuO phase named *23.7Å-phase* due to its *c-axis* being equal to 23.7Å.

The expected 2201 phase was found to form below 830°C and 23.7Å phase found to form below partial melting temperature. Sr_2PbO_4 was also detected at 868°C, above partial melting.

For n=2, the formula becomes $(Bi_{0.8}Pb_{0.2})_2Sr_2Ca_1Cu_2O_x$. The 2212 phase was observed to be stable up to ~875°C. In a certain range, 2201, 2212 and liquid phases coexisted. The presence of Ca_2PbO_4 remained at all temperatures indicating the incomplete Bi/Pb substitution in 2212 in the experimental conditions used. Ca_2CuO_3 appeared to be a major phase at 868-889°C, which is a temperature range of extensive melting.

For n=3 and 4, the formula becomes $(Bi_{0.8}Pb_{0.2})_2Sr_2Ca_2Cu_3O_x$ and $(Bi_{0.8}Pb_{0.2})_2Sr_2Ca_3Cu_4O_x$, respectively. This region corresponds to the lowest melting temperatures. The successive reactions with increasing temperature are:

$$2212 \rightarrow 2223 \rightarrow 2212 \rightarrow 2201 \rightarrow (2201 + 23.7\text{Å-phase})$$

Ca_2PbO_4 was detected below 860°C, and Ca_2CuO_3 appeared in the partial melting temperature zone. The 2223 phase did not disappear at the solidus line; however, a coexistence range of 2223, 2212 and liquid phases turned out to be present.

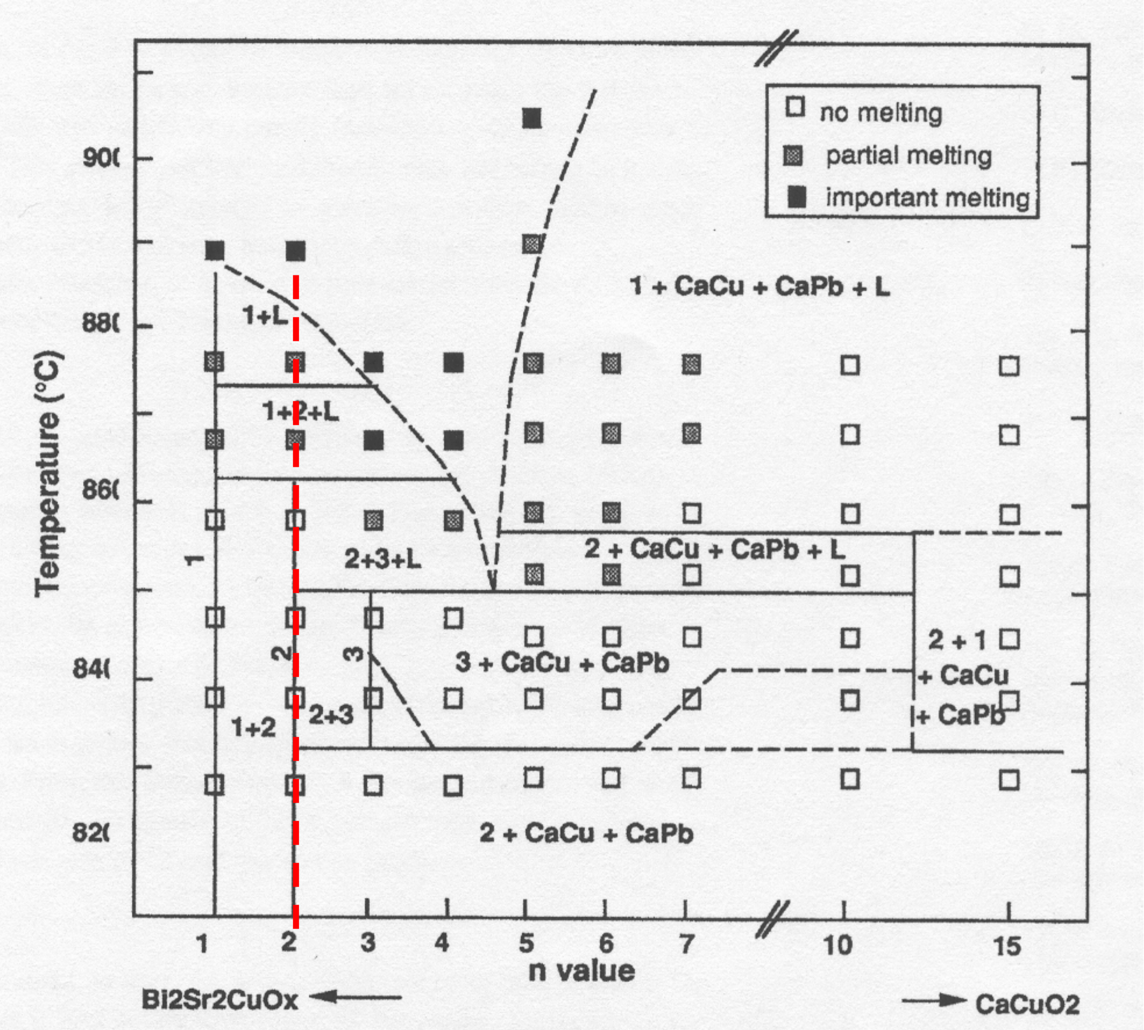

Fig.46 Tentative phase diagram of 2-2-(n-1)-n series: *1*=2201+23.7Å-phase, *2*=2212, *3*=2223, *CaCu* = $(Ca_{2-x}Sr_x)CuO_3$, *CaPb* = Ca_2PbO_4, *L*=Liquid [31].

The transformation reaction 2212→2223 was observed to be slow, and the oblique dotted line between n=3 and n=4 close to 840°C shown in Fig.46 defines a zone with observed composition 2212>2223. This can be associated with slow kinetics.

Strobel and Fournier figured out that traces of 2212 was found only with 2223 at the end of a quenching experiment under the same conditions and 150 hours of annealing time.

They also used EDX (energy dispersive x ray) and noticed that crystallized 2223 grains had the composition of $(Bi_{1.64}Pb_{0.28})Sr_2Ca_2Cu_3O_x$. This indicates a lower Pb content than the initial mixture. Furthermore, their analysis showed that lead and bismuth tend to accumulate in liquid phase. Meanwhile crystallized phases included mostly 2223 and $(Ca_{2-x}Sr_x)CuO_3$.

For n≥5, the reaction 2212→2223→2212→2201 was observed. The liquid phase and 2223 could not be found to coexist in this region [31].

Pb is widely used to ease the synthesis of 2223, but not very much is used in 2212. Researchers showed that replacing part of Bi with Pb increased the electrical three dimensionality of the phase. Zhang et al. [32] investigated the phase assemblage in (Bi,Pb)-2212 powder and in the melt as a function of Pb content, temperature and oxygen partial pressure.

The OPIT tapes they manufactured used Pb doped 2212 powders annealed under Nitrogen purge with the composition $(Bi_{2.1-x}Pb_x)Sr_2CaCu_{1.95}O_y$. The packing density of the powder was 30%, and the dimensions of the Ag tube were 6.35mm and 4.35 mm OD and ID, respectively. The final dimensions of the tapes were 150μm x 3mm with the core dimensions 60μm x 2mm. The ends of the 5 cm long samples were hammered for sealing. *Melt processing* took place under 1, 21 (air) and 100% of oxygen content atmosphere. Their heat treatment for melt processing in air was as follows: Heat up at the rate of 300°C/h to T_{max}=880°C, soak for 10 min, then cool at 10°C/h to 820°C, hold for 48 h, then cool at 700°C/h to room temperature.

Table 10. Phase assemblages as a function of temperature in the melt (Bi,Pb)-2212 powder under 21% oxygen (air) purge [32].

Phases present in the melt under air purge					
T°C	***2212***	***Liquid***	***1:1 AEC***	***2:4 CF***	***2:1 AEC***
890	-	X, O	X, O	X, O	X, O
880,870,860	-	X, O	X, O	X, O	-
850,840	X, O	O	O	O	-

In the table above phase assemblages as a function of temperature in the melt in 21% oxygen (air) are given. *X phase* is present during heating and *O phase* is present during cooling. *1:1 AEC* is (Alkaline Earth Cuprate) $(Sr,Ca)CuO_x$, *2:4 CF* is (Copper Free) $(Bi,Pb)_2(Sr,Ca)_4O_x$ and *2:1 AEC* is $(Sr,Ca)_2CuO_x$.

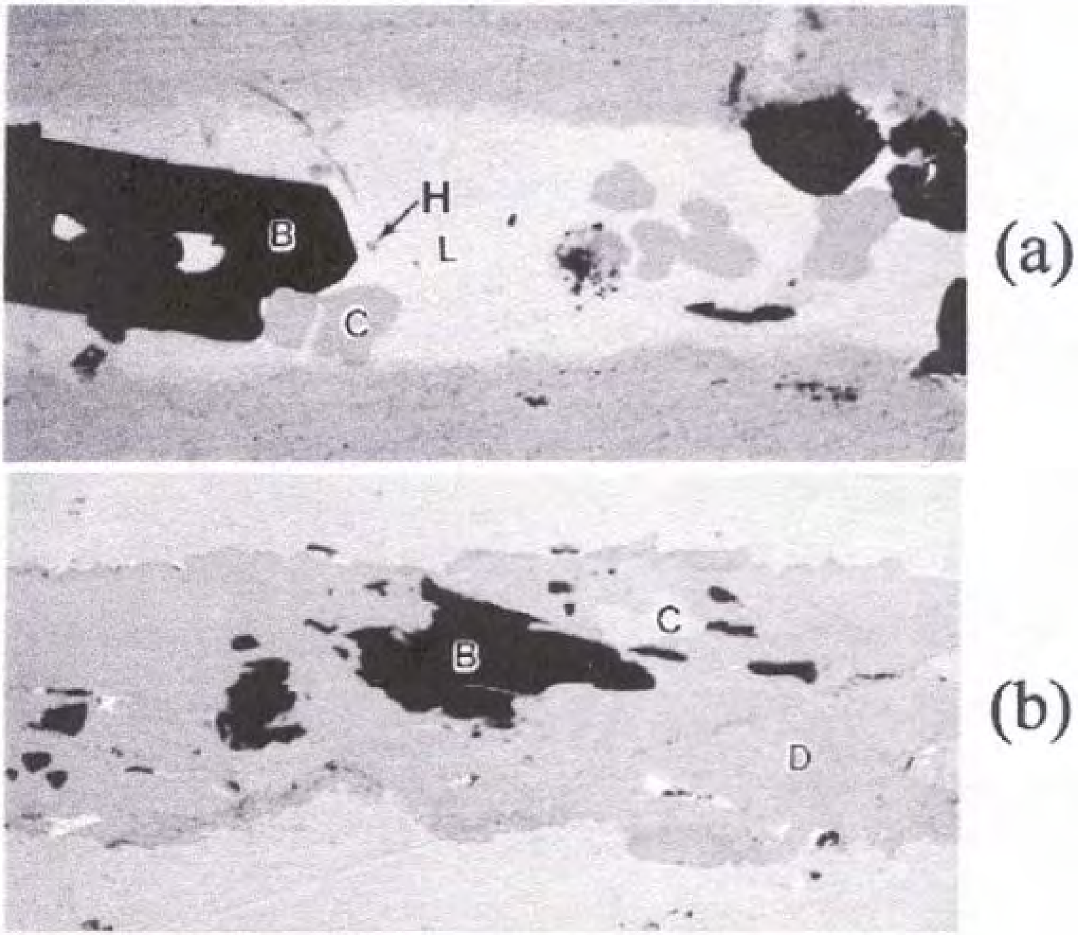

Fig.47 Microstructures of $(Bi_{1.7}Pb_{0.4})Sr_2CaCu_{1.95}O_y$ samples partially melted in 21% oxygen purge, (a) at 860°C, (b) at 840°C. B= 1:1 AEC, C= 2:4 CF, D= (Bi,Pb)-2212, H= 4:5:1, L= Liquid [32].

At the end of their experiments, Zhang et al. observed that 1:1 AEC grains did not fully react to form (Bi,Pb)-2212 during cooling; they dominated and controlled the microstructure of the fully processed core. Adding Pb found to increase the amount of remnant 2:4 CF phase. The transport J_c was observed to be decreasing by increased Pb content and decreased oxygen partial pressure. Enhancing the Pb content also found to be effective on the proportion of 2212 formed with respect to the nonsuperconducting phases. In addition, with increasing Pb content the structure of (Bi,Pb)-2212 phase was found to change from pseudotetragonal to orthorhombic.

In 21% oxygen atmosphere, 1:1 AEC grains were observed to grow to a larger size in the melt. This was valid for both Pb doped and Pb free powders. The large size of the grains is the reason to have these phases stay as the remnant grains in fully reacted tape.

The microstructure of their tapes was heterogeneous with remnant 1:1 AEC and badly aligned 2212 grains. Due to this fact, J_c measurements came out with poor results with increasing Pb content.

During melt processing, (Bi,Pb)-2212 was observed to decompose forming 2201 upon heating, and it became a mix of liquid and crystalline phases. On cooling, some Pb seemed to come out of the liquid and went into (Bi,Pb)-2212. Moreover, the amount of Pb in (Bi,Pb)-2212 that formed during melt processing was lower than that of the overall Pb. Therefore, the missing Pb amount was considered to be present in the liquid. As a result, Pb content of (Bi,Pb)-2212 phase showed an enhancement with increasing overall Pb content and decreasing partial pressure of oxygen. This also suggested that Pb solubility is less in crystalline (Bi,Pb)-2212 than in the liquid phase.

Zhang, Hellstrom and Polak considered two main difficulties with melt processing of (Bi,Pb)-2212 conductors in terms of forming homogeneous and highly aligned microstructures:

The first hardship is the huge size of nonsuperconducting phases. This requires the employment of *step solidification* (this is the reaction heat treatment method used in this thesis work, actually) to get them to react during the cooling period. As the second difficulty, they stated that decreasing Pb solubility in 2212 with increasing temperature and partial pressure of oxygen could be a substantial problem. They expected a part of

Pb present in the melt not to react during cooling down and end up with a multiphase heterogeneous microstructure with poor alignment.

In conclusion, Pb doping is helpful to form phase pure (Bi,Pb)-2212 at low temperatures and low oxygen partial pressures; high oxygen partial pressure makes pure (Bi,Pb)-2212 decompose into 2201, 2212 and 4:5:1 (or in open form $Pb_4(SrCa)5CuO_x$) with lower Pb content; temperature at which 4:5:1 phase precipitates from (Bi,Pb)-2212 is called *decomposition temperature* and is a function of Pb content and oxygen partial pressure and it increases with both decreasing pressure and Pb content. In melt processing, 2212 phase that experiences melting contains small amount of Pb.

Overall, Zhang et al. declared that it is detrimental for J_c to substitute Pb for Bi in 2212 due to eventual inhomogeneous microstructure formation [32].

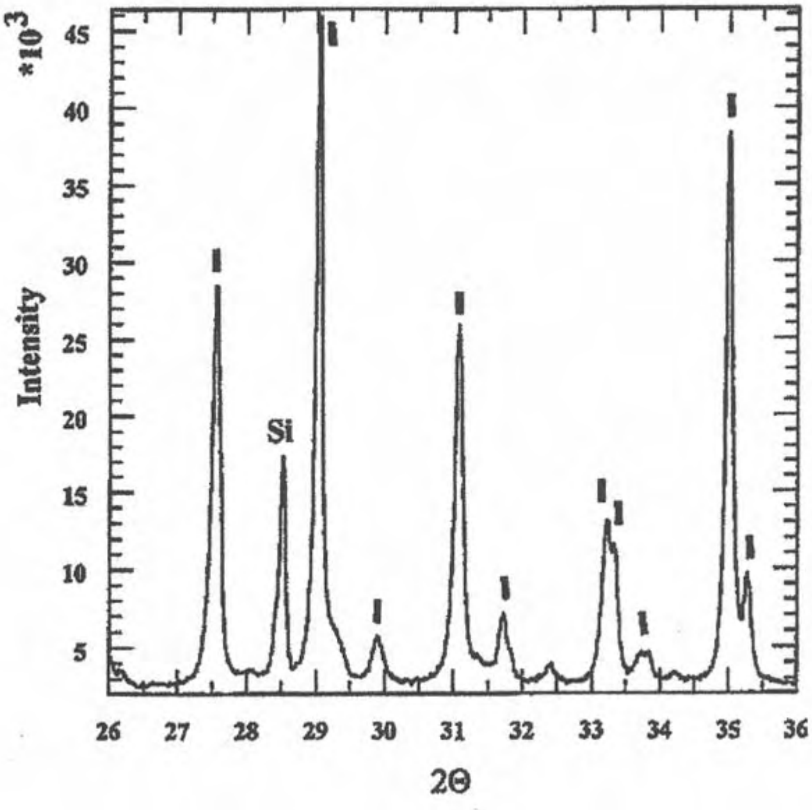

Fig.48 XRD pattern for $(Bi_{1.72}Pb_{0.34})\,Sr_{1.83}Ca_{0.97}Cu_{1.13}O_y$ heat treated in air at 860°C, I symbolizes (Bi,Pb)-2212 [33].

Jeremie et al. [33] used oxides (Bi_2O_3, PbO, $SrCO_3$, $CaCO_3$, CuO) and heat treated them in air to reach the nominal composition of ($Bi_{2-x}Pb_x$) Sr_2CaCu_2Oy. For x= 0.4, the treatment temperature was 840°C and 860°C. According to XRD results, at 860°C the patterns demonstrated characteristic (Bi,Pb)-2212 with (020) and (200) peaks clearly separated. This was considered as a sign of Pb addition to induce the formation of the orthorhombic phase. At 840°C, the XRD patterns did not show the same trend for (020) and (200) peaks, but displayed the characteristic peaks for Ca_2PbO_4. The researchers found it more beneficial to have the heat treatment at 860°C rather than at 840°C in order to get higher content of dissolved Pb. This dissolving is known by the structural transformation from tetragonal to orthorhombic [33].

Hellstrom et al. [34] investigated the formation of major phases 1:1 AEC $(Sr,Ca)CuO_2$, 2:1 AEC $(Sr,Ca)_2CuO_3$ and copper free phase 2:3 CF $Bi_2(Sr,Ca)_3O_x$ during melt processing of 2212 powder under air (21%), 1% and 7.5% oxygen purged (rest of the gas was nitrogen) atmospheres. They presented a detailed presentation of phase transformations in a tabulated manner.

They used melt processing in anticipation of better J_c in Ag sheathed Bi2212 superconductors. It is known that in air, 2212 melts incongruently forming liquid, AEC and CF phases. The size of the grains and the chemical reactivity of phases in the melt when 2212 starts to form during cooling found to be crucial for achievement of homogeneous and highly aligned microstructure in the core. Grain size of the crystalline phases is targeted to be small (few μm) in order not to agitate the alignment much and react as quickly as possible.

Under air purge, increasing temperature was observed to change the melt phases into 1:1 AEC, CF, 2:1 AEC and CaO. Upon cooling, while the 2212 phase starts to form, 1:1 AEC and CF were found to be the major phases to coexist with the liquid. The size of CF phase was also observed to be a function of the maximum melt processing temperature. If it were low enough that CF was still seen in the melt, grain size occurred would be small, eventually. However, if the melting temperature were higher and therefore, little or no CF would be present in the melt, all the CF phase later on would be formed during cooling and would become very large.

Table 11. Assembly of phases in melt-processed 2212 under air, 1% and 7.5% oxygen purge. *X* denotes heating and *O* denotes cooling. CF is copper free [34].

T°C	***2212***	***Liquid***	***1:1***	***2:1***	***CF***	***CaO***
820	(7.5%)O	(7.5%)O	(7.5%)O	(7.5%)O	-	-
830	(7.5%)OX (1%)O	(7.5%)O (1%)O	(7.5%)X (1%)O	(7.5%)OX (1%)O	(7.5%)O (1%)O	(1%)O
840	(7.5%)OX (1%)X	(7.5%)O (1%)O	(7.5%)X (1%)OX	(7.5%)OX (1%)OX	(1%)O	-
850	(7.5%)OX	(7.5%)O (1%)OX	(7.5%)X (1%)OX	(7.5%)OX (1%)OX	(1%)OX	(1%)O
860	(7.5%)X	(7.5%)O **(air)X** (1%)OX	(7.5%)X	(7.5%)OX (1%)X	(7.5%)O (1%)X	(1%)OX
870	-	(7.5%)OX **(air)X** (1%)OX	(7.5%)X **(air)X**	(7.5%)OX (1%)X	(7.5%)OX **(air)X** (1%)X	(1%)OX
880	-	(7.5%)OX **(air)X** (1%)OX	(7.5%)X **(air)X**	(7.5%)OX	(7.5%)X **(air)X**	(7.5%)O (1%)OX
890	-	(7.5%)X **(air)X** (1%)X	**(air)X**	(7.5%)X **(air)X**	**(air)X**	(1%)X
900	-	(7.5%)X **(air)X**	**(air)X**	(7.5%)X **(air)X**	**(air)X**	(7.5%)X **(air)X**
910	-	**(air)X**	**(air)X**	**(air)X**	-	**(air)X**
920	-	**(air)X**	-	-	-	**(air)X**

Since the small CF grains almost completely react during annealing, their role in the core's microstructure forming was not recognized in general.

The most common nonsuperconducting phase in 2212 cores fully heat treated in air was revealed to be (Sr,Ca)CuO_2 or 1:1 AEC. It quickly grows to huge sizes and reacts very slowly in the sheath during final heat treatment. That is why this phase is considered detrimental to homogeneous and well-aligned grain structure. It was seen to be possible to change the size of CF phase by means of maximum melt temperature. Nevertheless, this option was not successful for the 1:1 AEC phase. This made the researchers look for other ways to improve the 1:1 AEC phase's size, such as *step solidification*. This method aims to minimize the length of melt state duration. The heat treatment schedule they employed can be seen below (Fig.49).

Hellstrom et al. utilized *solid-state reaction* by mixing oxides and carbonates to synthesize their 2212 powder. Oxide Powder in Tube method was used to make tapes of 100μm x 3mm with a 35μm thick core. The tape samples were 2-3 cm long each and were crimped shut at the ends for sealing purposes.

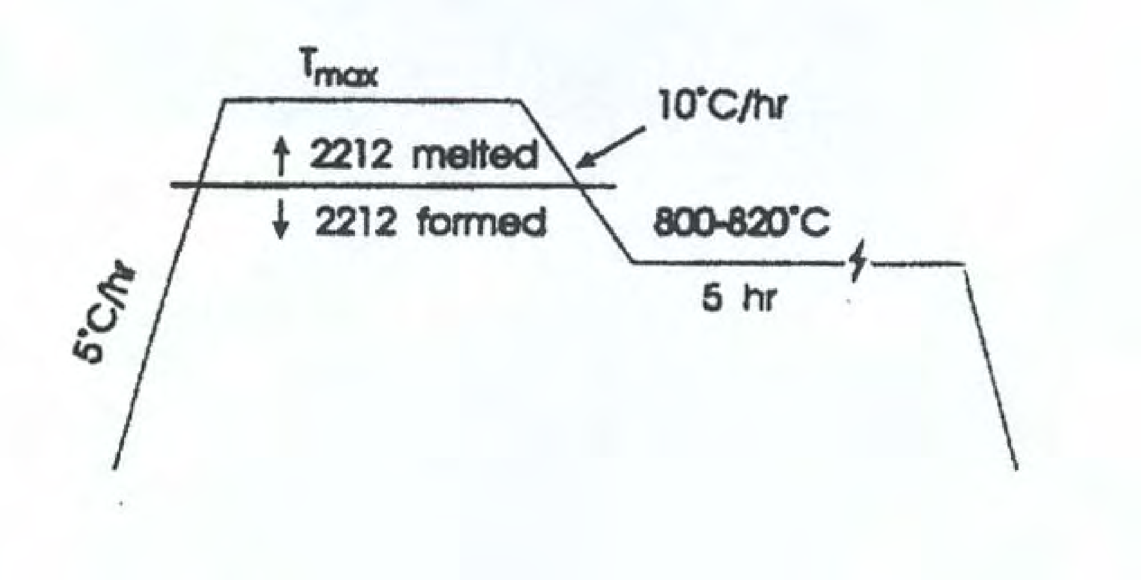

Fig.49 Heat treatment schedule for melt processing by Hellstrom et al. [34]. T_{max} varies with oxygen partial pressure.

In conclusion, Hellstrom et al. proclaimed that:

Ag sheathed 2212 tapes accommodate 1:1 AEC phase in the melt from which 2212 phase forms upon cooling under 1 and 7.5% oxygen purge. Going down from 21% oxygen content to 1%, the volume fraction of the 1:1 AEC phase decreased in the melt. However, this phase grew rapidly to very large sizes in the melt and remained large in the fully reacted tapes since they reacted slowly in the 2212 transform.

In the core, places where 2:1 phase $(Sr,Ca)_2CuO_3$ was present looked well aligned and homogeneous. Regions with large nonsuperconducting phases 1:1 AEC and CF were observed to consist of poorly aligned grains and represented with heterogeneous microstructure. Using reduced oxygen content in the atmosphere resulted in no gain for the microstructure of the core and pure oxygen was suggested to achieve better microstructure [34].

Motowidlo et al. [35] used *step solidification partial melt heat treatment* in air and in oxygen atmospheres to fully react 37 and 259 filaments OPIT method wires.

It has been reported that in contrast to 2223 superconductors, 2212 is melt processed and does not need multiple rolling and sintering steps. Therefore, they can be drawn, twisted, cabled and wound with ease before the reaction heat treatment of the wire.

Motowidlo et al. utilized Ag tubes (99.9% pure, 13.2 mm OD, 11.7 mm ID) to fill in the commercial 2212 powder (with a filling factor of 30%). Ag plugs were used and swaged at their places to seal the ends of the tubes. To make 37 filament wires, they drew monocore wires first and then stacked them in packs of 37. For the 37 filaments design, wires with 30, 60 and 100 μm filaments were heat treated. Only samples with 259 filaments design were given a twist pitch of four per inch for low loss operation and field uniformity free of large induced magnetic moments.

Step solidification melt processing was the heat treatment method employed by the authors. Its schematic can be seen in Fig.50, below. The maximum temperature was 885^{o}C, followed by cooling at 10 ^{o}C/h to 870^{o}C where the sample was held for 24 hours. The temperature steps were 24 hours, through 840^{o}C, after which the furnace was turned off for cooling down.

Image processing was carried out to find the superconducting fraction of the wires, which came out to be 35-40% for 37 filaments and 25-35% for 259 filaments wires.

The original step solidification process was done in air on tape samples by R.D. Ray. The main aim of this new heat treatment design was to reduce the size of the residual $(Sr,Ca)CuO_2$ (1:1 AEC) phase after full reaction.

The prevailing phases observed after the full reaction heat treatment in air seen in Fig.50 above were: *1:1 AEC* (*Alkaline Earth Cuprate*) $(Sr,Ca)CuO_2$, Bi2212 and *2:4 CF* (*Copper Free*) $Bi_2(Sr,Ca)_4O_x$. Under 50% oxygen, the phases turned out to be *14:24 AEC* $(Sr,Ca)_{14}Cu_{24}O_x$, Bi2212 and *2:4 CF* (*Copper Free*) $Bi_2(Sr,Ca)_4O_x$. Increasing oxygen content to 100% made a difference in pattern of the core characterized by significant melt texturing. The dominant phases in this case were Bi2212, Bi2201 and Sr-rich phases.

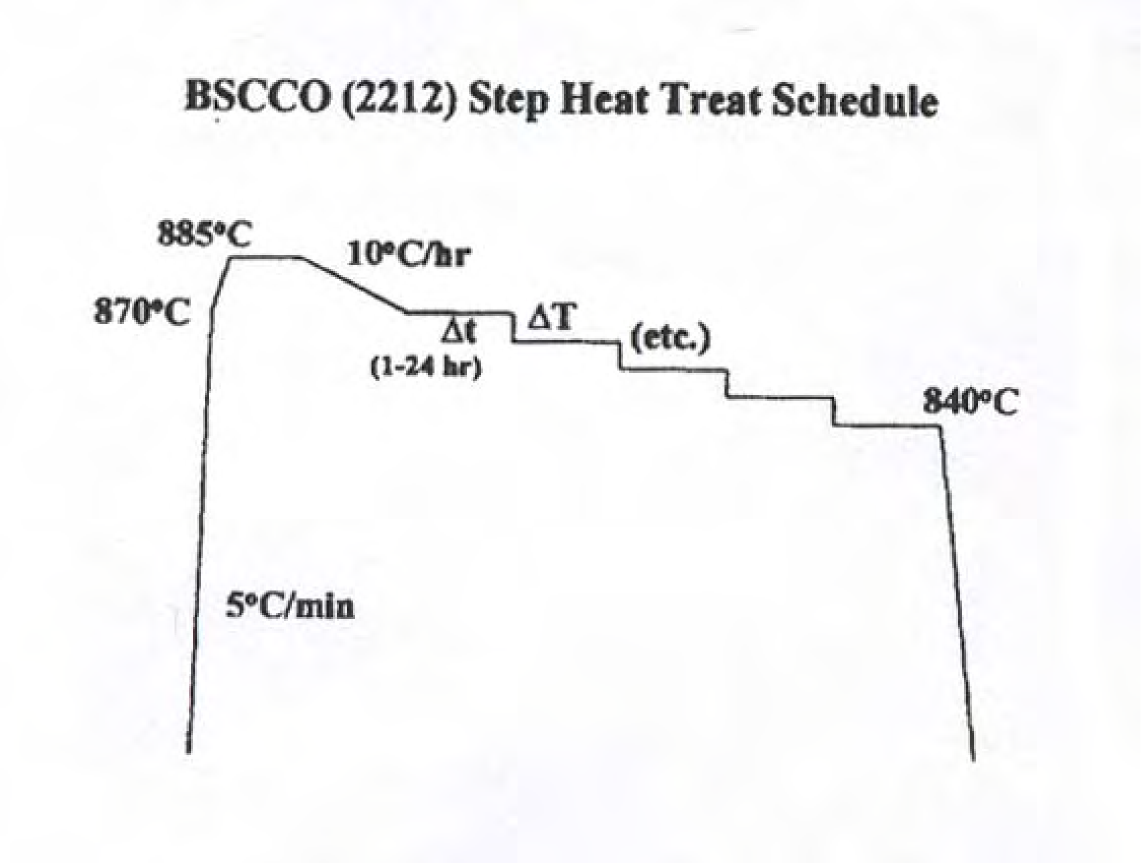

Fig.50 Heat treatment schedule for step solidification melt processing by Motowidlo et al. [35].

Regardless of filament size, wires that went under heat treatment in 100% oxygen ended up with the best J_c values. Furthermore, J_c was observed to increase with decreasing filament size [35].

Bi2212 has the advantage of melt processing applicability over Bi2223. However, having its T_c=106 K, 2223 looks advantageous over 2212 with T_c=85 K. For low temperature applications, there is not much difference cited between these two in terms of J_c under magnetic field. Cost of fabrication becomes an important factor for the selection of the right powder. Hu et al. [36] used OPIT method to manufacture multifilamentary Bi2212 tape. The stoichiometry of the commercial powder they employed was $Bi_{2.1}Sr_{1.7}Ca_{1.2}Cu_2O_x$. The sheath materials were pure Ag for inner and Ag-Mg alloy for outer tube. Final dimensions of the tape were 3 mm x 0.2 mm.

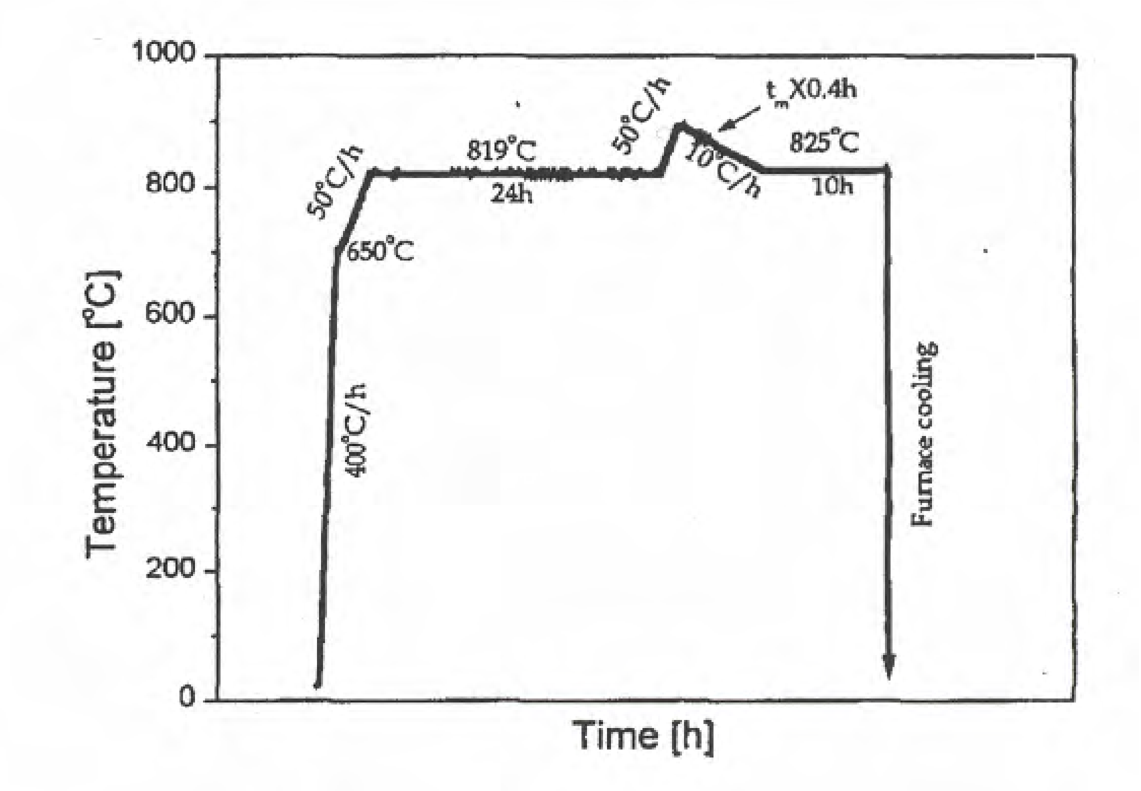

Fig.51 Heat treatment schedule by Hu et al. [36]

Fig.51 shown above represents the heat treatment schedule the researchers employed. It consists of pre-annealing, melting (peak temperature) and post annealing stages.

It is well known that Bi2212 consists of five different elements. The metallic elements that are considered in bound with oxygen are: Bi_2O3, SrO, CaO, CuO.

According to the Phase Rule,

$$F = C - P + 1 \tag{E.21}$$

Here, F is the degrees of freedom, C is the number of components, and P is the number of phases. For Bi2212 system, the maximum number of phases is:

$$P = C - F + 1 = 4 - 0 + 1 = 5$$

Since Bi2212 is ceramic, the mass transport phenomenon is poor during heat treatment. If a liquid phase were not present, the system would not be able to reach equilibrium. Therefore, the homogeneity of the core would be poor all over the tape. At a certain temperature, the real number of phases depends on the number of preexisting phases in the precursor powders; heating rate, heating duration and soaking time all affect the kinetic properties of the preexisting and intermediate phases.

The melting process is essential to mass transportation and therefore the homogeneity of the composition of the whole system.

Hu et al. found that existence of silver lowered the melting temperature of Bi2212 phase by 24°C. The melting temperature of the Bi2212 powder is known as 907°C, however, the same powder in the multifilamentary tape was observed to melt at 883°C in their experiments.

Another observation of theirs showed that a sample that was not melted at the peak temperature contained a substantial amount of secondary phases.

Bi2212 forms after a peritectic reaction:

$$\text{Bi2201} + (\text{Sr,Ca})\text{CuO}_2 + \text{Liquid} \rightarrow \text{Bi2212}$$

Here, if the liquid phase is off stoichiometry, the residual Bi2201 is mostly to remain unreacted. As a reminder, $(Sr,Ca)CuO_2$ is 1:1 AEC phase [36].

Zhang et al. [37] studied the effects of temperature and oxygen partial pressure on partial melt processing during Bi2212 forming. *Melt processing* was used to reach better critical current density, J_c, in Ag sheathed $Bi_2Sr_2CaCuO_x$ conductors. The 2212 precursor was heated until it melts incongruently and forms liquid and nonsuperconducting crystalline phases in this melt. On cooling, 2212 phase observed to arouse from the liquid and the crystalline phases. Therefore, the phase assemblage at this stage is of great importance to acquire a homogeneous and well-aligned microstructure in the core, thus supreme J_c.

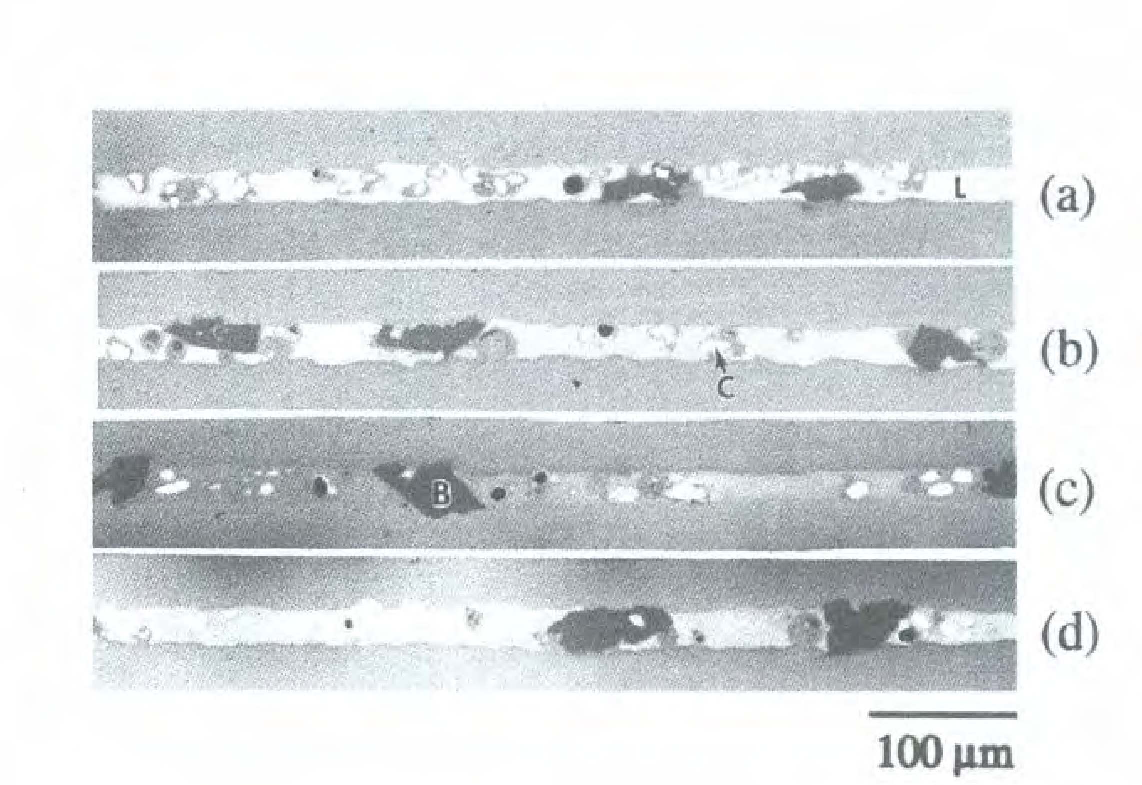

Fig.52 Tape melted in air at 890°C for (a) 0 min (b) 10 min (c) 30 min (d) 60 min. Heating rate 5°C/min. B= 1:1 AEC, C= 2:4 CF, L= Liquid [37].

The grains of nonsuperconducting phases in the melt should be small enough (1-10 µm) not to disturb the development of 2212 well alignment as much as possible. Besides, small grains are believed to react quickly and completely within the liquid.

The typical atmosphere for melt processing was air, i.e., (21% oxygen content in the purged gas mix) 0.21 atm partial pressure of oxygen. Under this atmosphere, 2212 melted incongruently into liquid, *1:1 AEC* (Alkaline Earth Cuprate) $(Sr,Ca)CuO_2$ and *2:4 CF* (Copper Free) $(Bi,Pb)_2(Sr,Ca)_4O_x$.

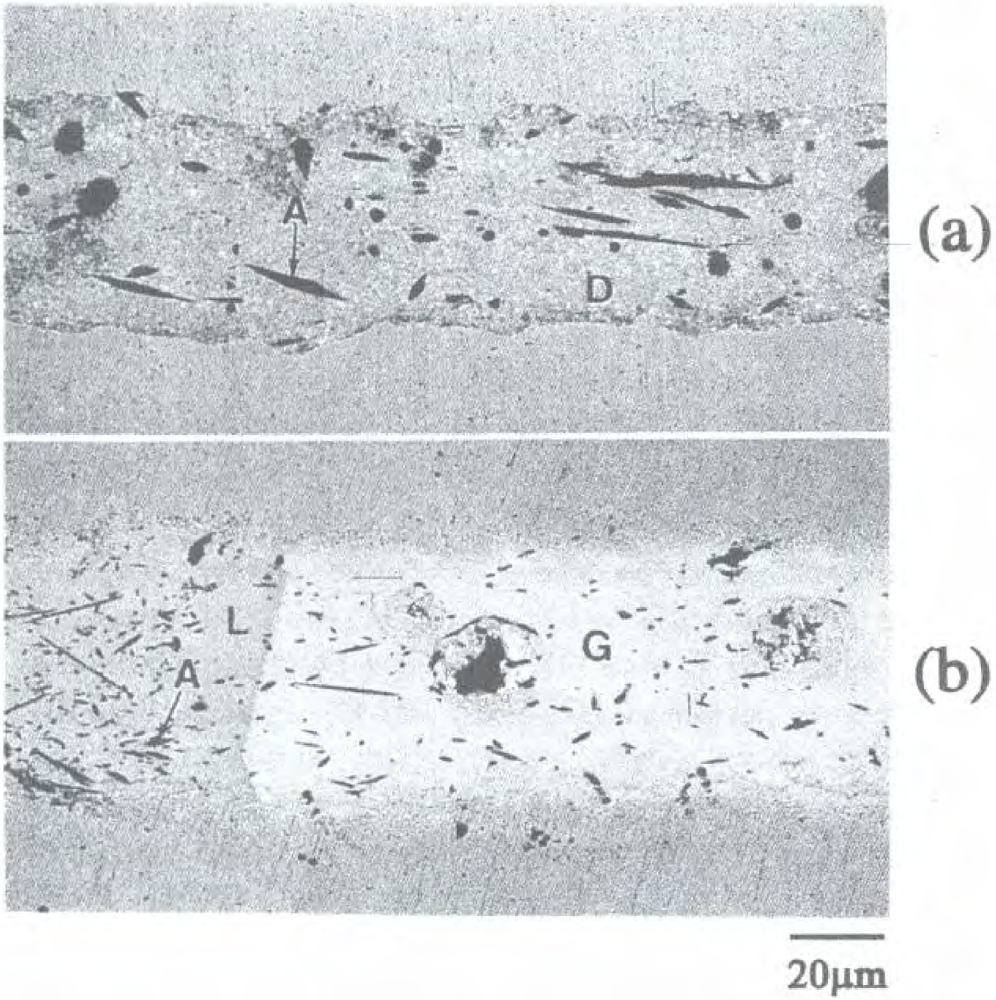

Fig.53 Tape melted in 0.01 atm for 10 min at (a) 840°C (b) 842°C. A= 2:1 AEC, D= 2212, G= 2:4 CF, L= Liquid [37].

The most common remnant phase seen in fully processed Bi2212 superconductors was 1:1 AEC. In the melt, this phase grows to a larger size rapidly and reacts slowly during cooling and annealing steps. It is a prominent barrier in front of homogeneous microstructure formation.

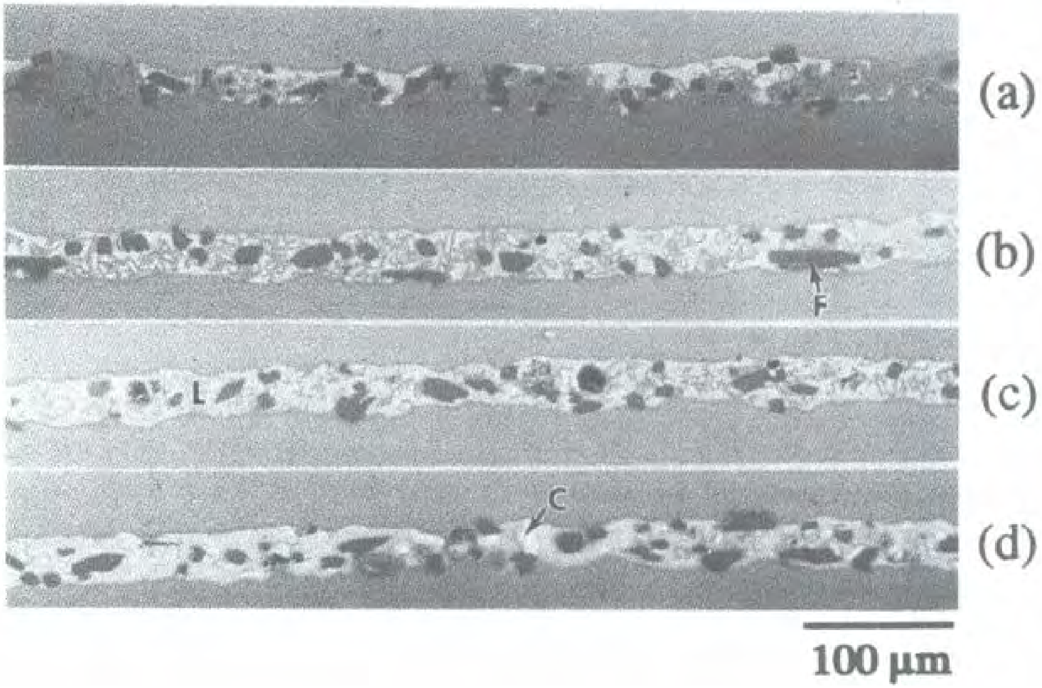

Fig.54 Tape melted in 1 atm at 900°C for (a) 0 min (b) 10 min (c) 30 min (d) 60 min. Heating rate 5°C/min. C= 2:4 CF, F= 12:24 AEC, L= Liquid. 14:24 AEC grains did not grow to large size [37].

Researchers [37] have shown that variation of oxygen partial pressure is effective on phase assemblage in the melt. It has also been reported that melt processing under 1 atm O_2 results in *14:24 AEC* $(Sr,Ca)_{14}Cu_{24}O_x$ instead of 1:1 AEC. Furthermore, volume fraction of 14:24 AEC nonsuperconducting phase under this condition appeared to be less than that of 1:1 AEC nonsuperconducting phase in tapes fully processed under air. On the other hand, atmospheres with low oxygen partial pressure like 0.01 atm were reported to yield *2:1 AEC* $(Sr,Ca)_2CuO_x$ and *2:3 CF* $Bi_2(Sr,Ca)_3O_x$ phases.

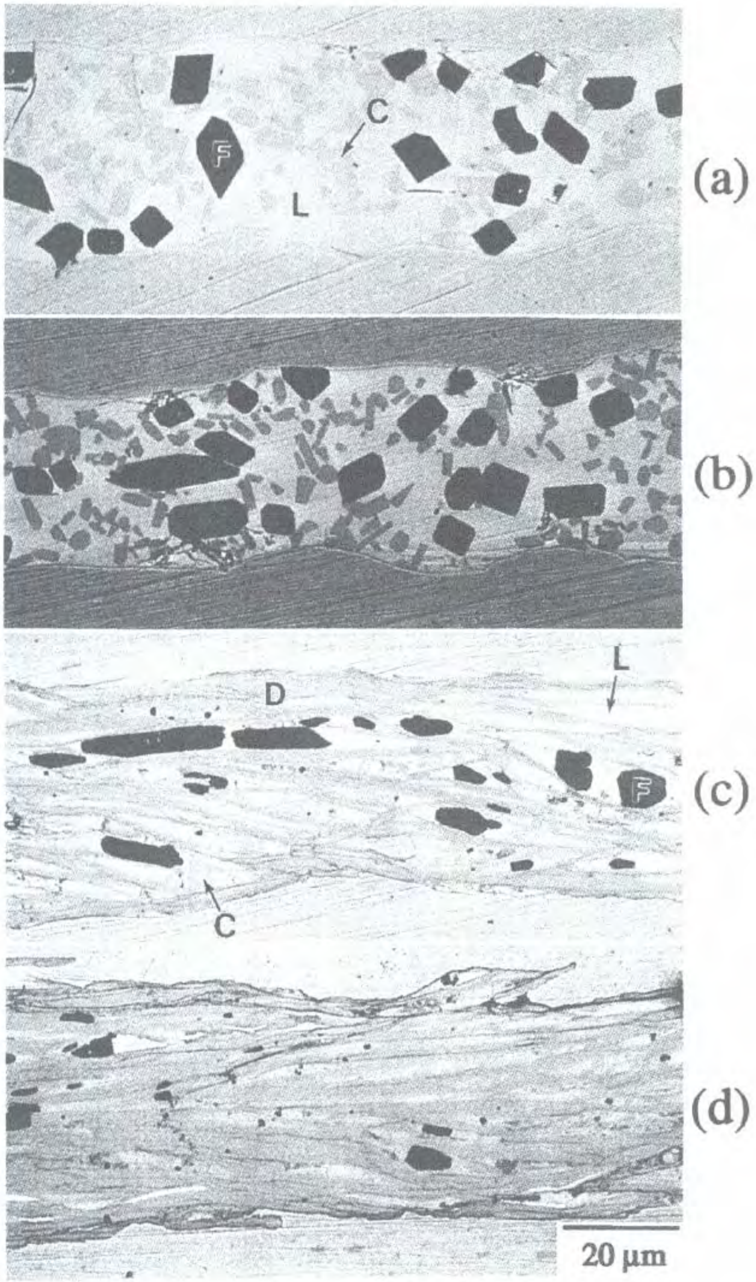

Fig.55 Cooling down states of tape melted in 1 atm starting from 900°C to (a) 890°C (b) 870°C (c) 860°C (d) 840°C. Cooling rate 10°C/hr. C= 2:4 CF, D= 2212, F= 12:24 AEC, L= Liquid. [37].

Zhang et al. used the same technique employed in this thesis work, *Solid State Synthesis*, by mixing the powders Bi_2O_3, $SrCO_3$, $CaCO_3$, CuO and sintering them at

800°C for 48 hours in air. Grinding and calcining for 12 hours at 600°C under O_2 completed the precursor preparation. Their Ag sheathed 2212 tape was made by the OPIT method utilizing a pure silver tube of 6.35mm OD x 4.35mm ID. The final thickness of the tapes was ~100μm with a core thickness of 40-50 μm. The ends of the tapes were hammered shut. The phase assemblages formed in the melt between 0.001 atm and 1 atm oxygen partial pressure were examined. Table 12 presents the results they achieved.

Table 12. Phase assemblages in Bi2212 melt under various atmospheres during cooling [37].

Oxygen partial pressure (atm)	***Phases in melt when 2212 forms***
0.5-1	Liquid, 14:24AEC, 2:4CF
0.21 (air)	Liquid, 1:1AEC, 2:4CF
0.075	Liquid, 1:1AEC, 2:1AEC, 2:4CF
0.01	Liquid, 1:1AEC, 2:1AEC, 2:3CF
0.001	Liquid, 2:1AEC, 2:3CF, (Sr,Ca)O

In 0.01, 0.075 and 0.001 atm oxygen partial pressures, the count of crystalline phases seemed to violate the phase rule. 2:4CF phase observed to be unstable in the melt during 2212 formation. Large 1:1 AEC grains occurred. Some 2:1 AEC grains were observed to be enclosed by larger 2:3 CF grains. Only a slight amount of (Sr,Ca)O was found in large 2:3 CF after Bi2212 formation.

AEC phase in the melt tended to shift from 2:1 to 1:1 AEC and from 1:1 AEC to 14:24 along with the increasing oxygen partial pressure.

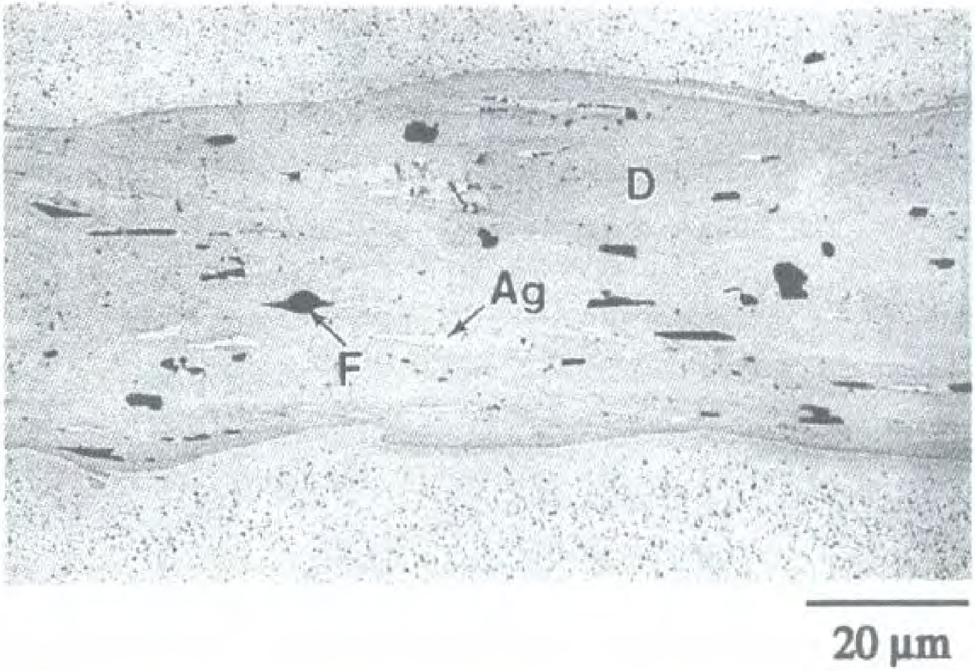

Fig.56 Fully processed tape in 1 atm O_2. D= 2212, F= 14:24 AEC [37].

According to the authors, higher J_c and smaller sized remnant grains that develop in the tape processed in 1 atm O_2 in comparison with 0.21 atm O_2 pressure suggest that Ag sheathed 2212 tape and wire should be melt processed in 1 atm O_2. However, they found that bubbling was a serious problem in their experiments. Bubbling is known to occur due to the O_2 released when Bi2212 melts. Since the melting temperature of the powder increases, and the strength of the Ag sheath decreases with increasing oxygen partial pressure, they first suggested to make use of lower partial pressures of oxygen for melting in order to keep the Ag sheath less vulnerable to bubbles. However, this idea proved inadequate because in 1 atm, 12:24 phase did not form. Therefore, it is inevitable to melt the powder where oxygen partial pressure is sufficient for 14:24 forming. The same authors showed in other research that it is better to process tapes in 0.40 atm O_2 rather than 1 atm O_2 for bubbling prevention [37].

It was discovered that Bi2212 powders provided ease in preparation compared to Bi2223. Formation of 2223 phase requires more time and precision than 2212. Thangaraj et al. [38] investigated the effect of atmosphere during heat treatment on 2212 phase formation, current transport properties and microstructure of the core. They employed *melt processing* to assure good connectivity and proper alignment of the 2212 grains.

It has been observed in previous research that upon heating, Bi2212 starts to decompose around 880°C by a peritectic reaction into a mix of liquid and alkaline earth cuprates of (Sr,Ca)CuO and copper free $Bi(SrCa)_2O_x$ phases. With further heating, the AEC phase decomposes such that the (Sr+Ca)/Cu ratio decreases following the completion of 2212 decomposition. It transforms from $(SrCa)Cu_2O_x$ (1:2 AEC) to $(SrCa)CuO_x$ (1:1 AEC) to $(SrCa)_2CuO_x$ (2:1 AEC) to $(SrCa)O_x$ (1:0 AEC). Ag sheath was suggested to decrease the melting temperature by 20°C, and accelerate the transformation of (Sr,Ca)CuO from a low (Sr+Ca)/Cu ratio to a higher one.

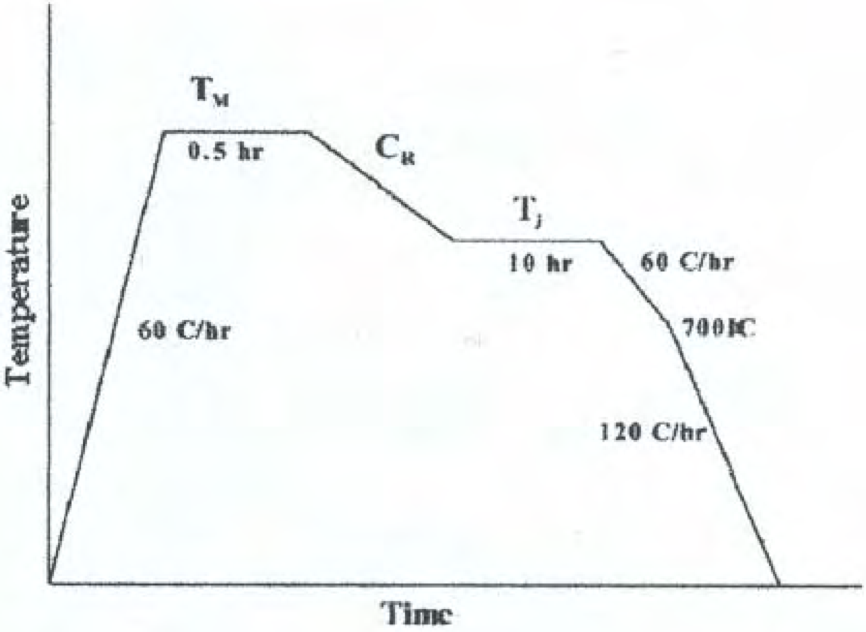

Fig.57 Schedule employed for partial melt heat treatment by Thangaraj et al. [38].

Upon cooling, the 2212 phase reforms by the peritectic reaction previously mentioned. It grows fast at around 850°C. It tends to crystallize with its a-b plane aligned along the Ag interface. This tendency gives way to c-axis textured grains, which are highly desirable for J_c enhancement.

In their study, Thangaraj et al. fabricated Bi2212 tapes by OPIT method using groove and flat rolling for deformation. BSCCO powder with the stoichiometry of $Bi_2Sr_{1.7}CaCu_2O$ was prepared by *spray combustion pyrolysis* method. The average particle size was measured as 1-2 μm. Mechanical agitation was used to pack the powder into pure Ag tubes with 6.35 mm OD and 1 mm wall thickness. The packing process was done carefully to uniformly consolidate the powder along the tube length. Packing density was found to be 30% of the 2212 theoretical density. By means of a two-high rolling mill and groove rolling technique, the packed tube was deformed into tapes with 2.1 x 2.0 mm rectangular cross section. Deformation per pass was controlled within 2% to assure homogeneity of the core and even stress distribution. Flat rollers were used to reach final form of 3.5 mm x 0.25 mm. These tapes were then heated to the partial melt temperature, T_m, and held there for 0.5 hour. Then, they were cooled to an intermediate temperature, T_i, and held there for 10 hours to complete the formation of 2212. T_m=890°C, T_i=855°C, cooling rate C_R=5-10°C/h are the conditions the authors claim to be optimum for melt processing.

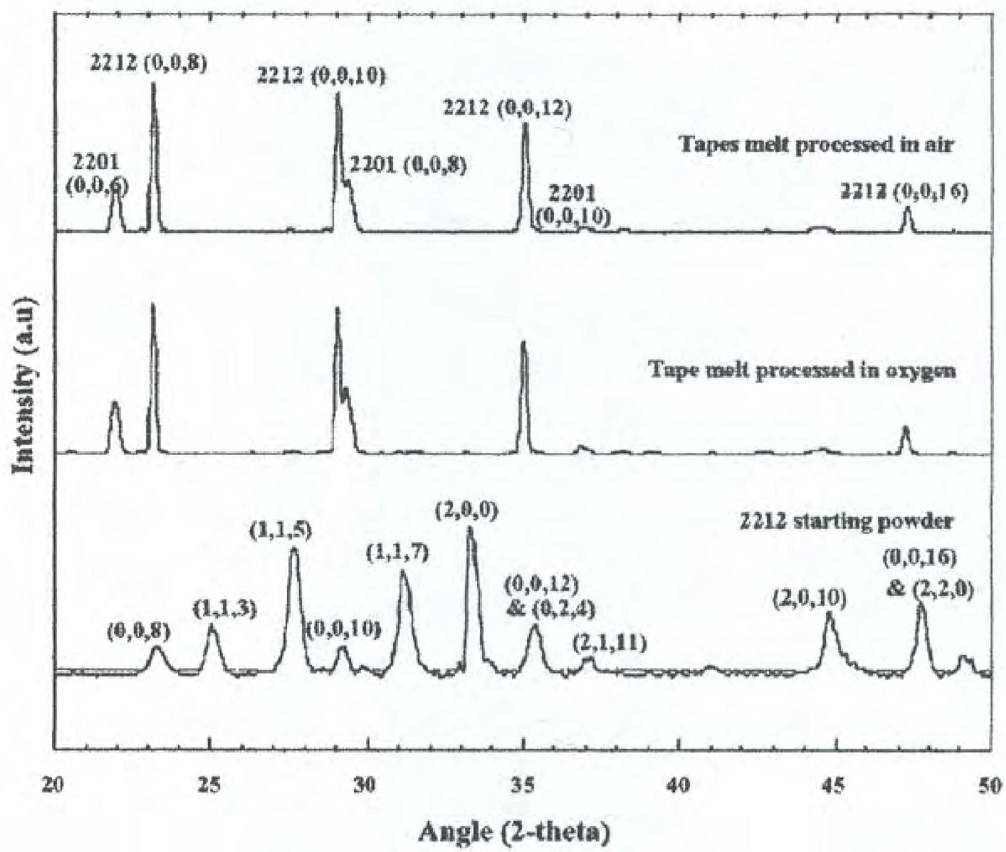

Fig.58 XRD results of the starting powder and the core from the heat-treated tapes under air and oxygen purge [38].

The XRD patterns show that heat treatment under oxygen and air did not make much difference in terms of phase variety. Bi2212, as the dominant phase, seems to be accompanied by a small amount of Bi2201 in each case.

Fig.59 below shows the backscattered electron image of the longitudinal cross section of the tape treated in air with the conditions of T_m= 890°C and C_R= 10°C/h by . After an examination by WDS (wave dispersive spectrum), the phases present are all indicated on the picture. 1:1 AEC grains look very large and disturbing the smooth alignment of the Bi2212 grains.

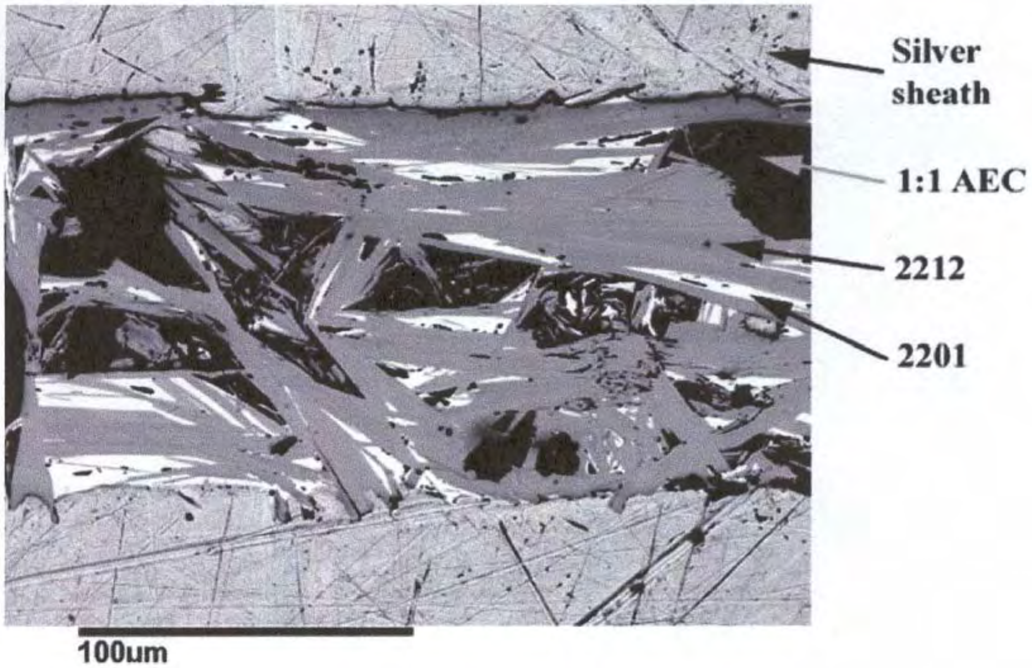

Fig.59 SEM image of tape core melt processed in air with the conditions of T_m= 890°C and C_R= 10°C/h [38].

In the following figures, longitudinal cross sections of the tapes treated in oxygen can be seen. Pose (a) shows the tape with conditions T_m= 890°C and C_R= 10°C/h and pose (b) shows T_m= 890°C and C_R= 5°C/h. Gray background is 2212 and bright needle-like grains are 2201. Dark small phases are 14:24 AEC; they don't seem to disturb the ordnance of the grain alignment much. Tapes with C_R= 10°C/h appear to have larger 2212 and 2201 grains than the other tape. However, small grains of C_R= 5°C/h tape appear to be more evenly distributed.

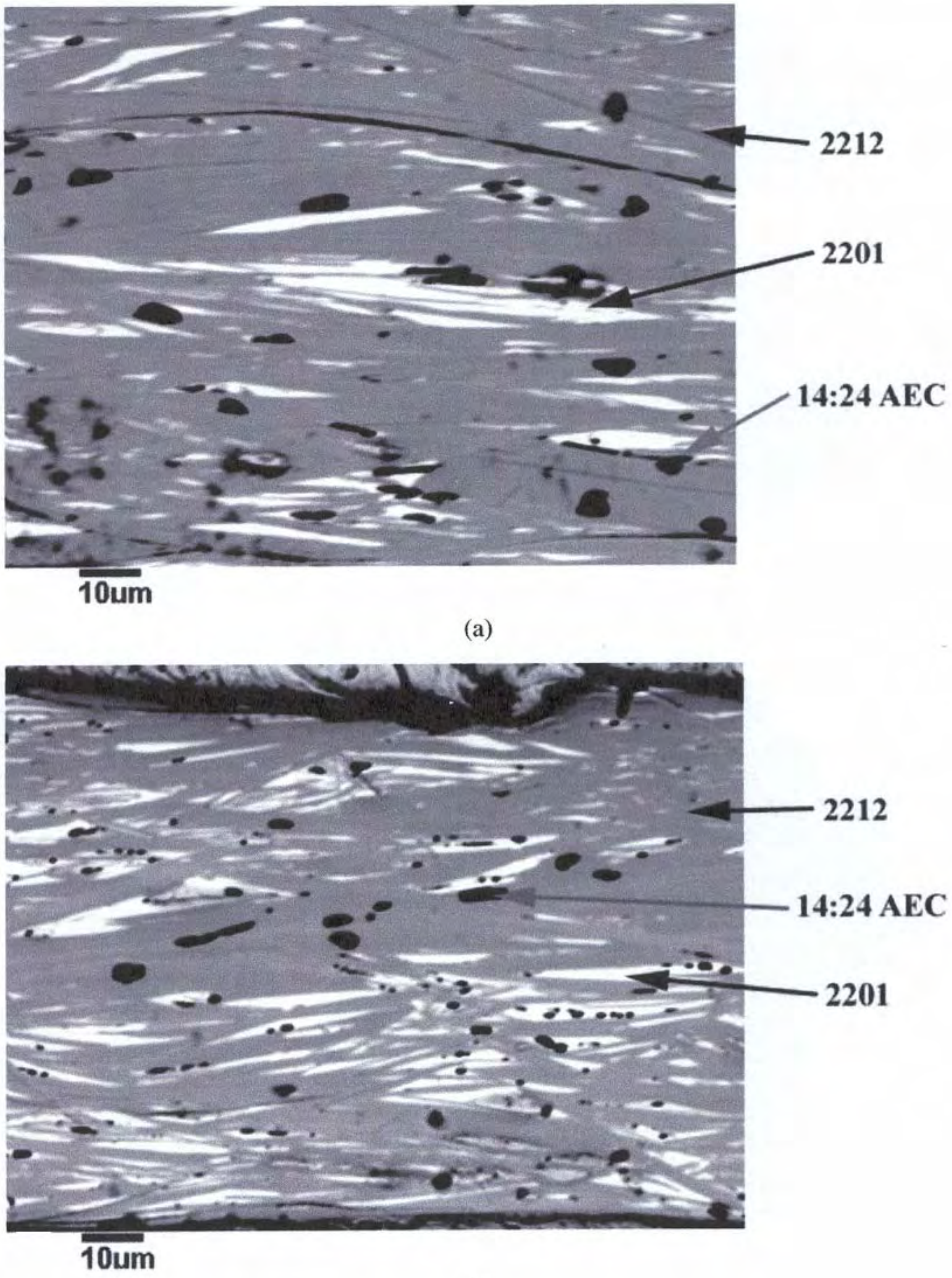

(a)

(b)

Fig.60 SEM image of melt processed tapes in oxygen (a) T_m= 890°C and C_R= 10°C/h (b) T_m= 890°C and C_R= 5°C/h [38].

There is an obvious distinction between the tapes treated in air and oxygen, which can be noticed in the pictures. During partial melting in the air, we know that a peritectic reaction takes place to form 1:1 AEC phase. This phase tends to grow larger and stay as remnant phase.

In the cooling process, conversion of the melt to 2212 could be considered incomplete by looking at these pictures. For the tapes melted in the oxygen, the 14:24 phase appears to be the major coexisting phase, and it remains as small grains.

Before, it was revealed that 14:24 AEC was highly oriented with respect to the silver interface. Moreover, it was stated that during cooling 2212 grains nucleated from both the Ag surface and the surface of the 14:24 phase. That seems to be the reason for better alignment in the core treated under oxygen compared to those treated in air.

14:24 AEC phase is known to react faster than 1:1 AEC at lower temperatures. This augments the conversion back to 2212. Besides, the tapes heat treated in oxygen were observed to display more uniform microstructure than the ones treated in air.

During melt processing, tapes could swell and thus form a deficient state of structural integrity. *Bubbling* is the common name given to this phenomenon. Size of the bubbles may vary. In the bubbled region, there is a void in the superconducting core, which is detrimental to the J_c. The cause for bubbling is the gas formation within the core during heat treatment. If the enclosed gas in the metal sheath exerts a bigger force than the thin tape clad can take on, it is inevitable to have bulging.

Thangaraj et al. encountered bubbling in their own experiments. They observed more of this phenomenon in the tapes that were exposed to higher temperatures and processed in oxygen than their counterparts treated under different conditions.

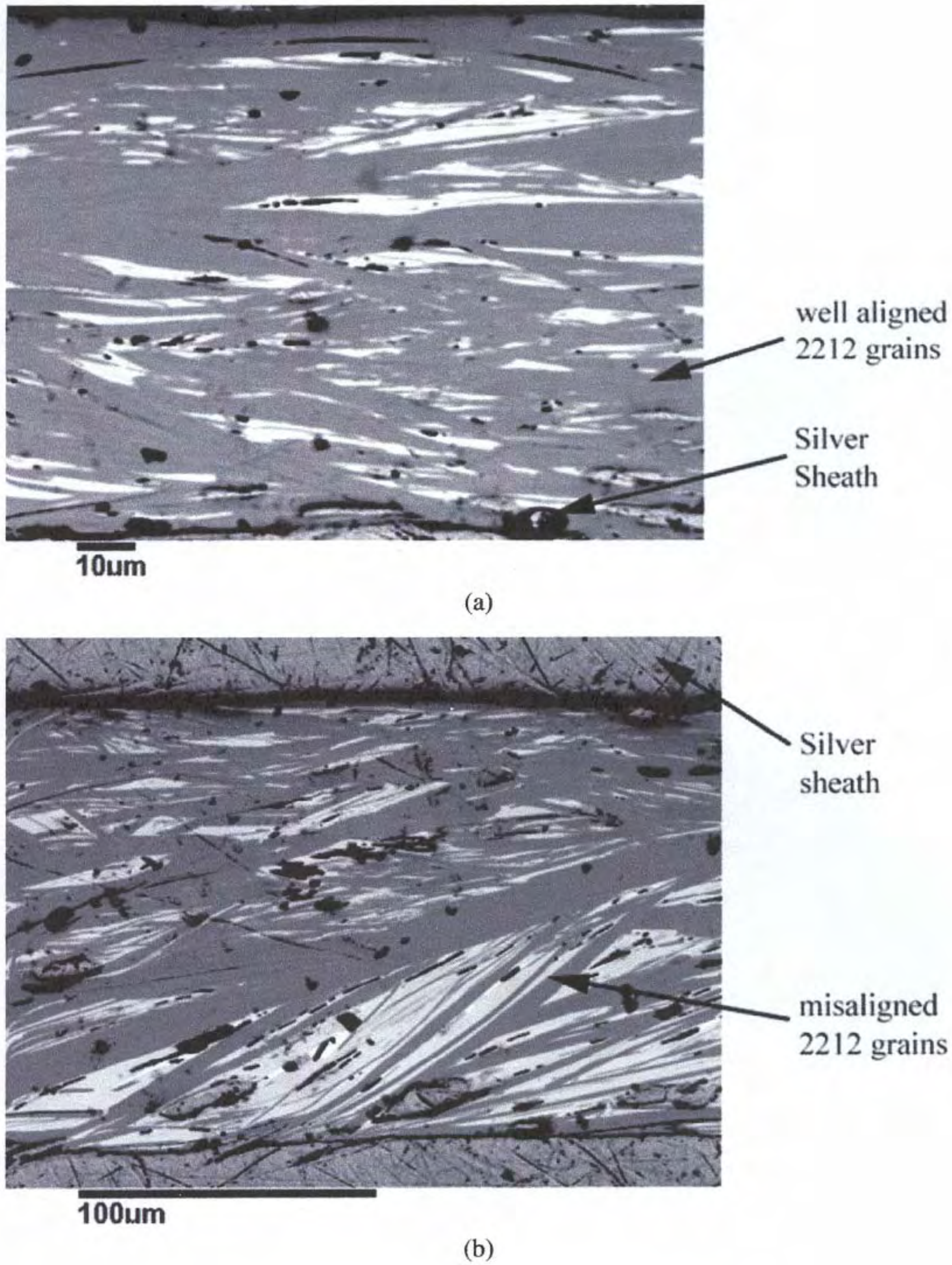

Fig.61 SEM images of tapes (a) in the flawless region (b) near the bubble defect [38].

As many research groups have reported, a minute segment of the supercurrent is transported through the bulk of the BSCCO tapes and most of it runs through a slim region close to the sheath-core interface. This non-uniform distribution of the flowing current has been related to almost perfect alignments of BSCCO grains located against the metal sheath. Researchers have also declared that in BSCCO 2212 tapes the grain boundaries are generally [001] *twist-boundaries*. The grains are plate-shaped yielding a microstructure composed of colonies of grains with almost parallel c-axes to each other. Within a colony, if a substantial misalignment of a-axis and b-axis appears, then it becomes possible to observe twist-boundaries between them [38].

In their study, Funahashi et al. [39] employed a variation of partial melting heat treatment named *Isothermal Partial Melting* (IPM), in which partial melting and solidification are carried out at the same temperature but in different atmospheric conditions. Because Bi2212 phase is an incongruent melting system, a liquid phase with Bi-rich composition and solid phases with Sr, Ca, Cu, O (Bi-free) and Bi, Sr, Ca, O (Cu-free) are formed initially inside. Bi2212 phase is precipitated and it grows by peritectic reaction between the liquid and the solid phases. If the peritectic reaction is not completed, Bi-free phase, Cu-free phase and Bi2201 (Bi_2Sr_2CuOx) phase appear as impurities in the liquid and remain in the composite degrading J_c. As being a polycrystalline ceramic, performance of Bi2212 superconductor is also affected regarding its grains' size and grains' coupling strength. In the *Conventional Partial Melting Method*, Bi2212 grains solidify through a slow cooling process; therefore, the optimum temperature range required for them to react can only be maintained for a short time. Thus, Bi2201, Bi-free and Cu-free phases remain as impurities.

Funahashi et al. proposed a modified heat treatment schedule to overcome the handicap of ample remnant nonsuperconducting phases. As they cited, at a given atmosphere, this method involves only two preparation parameters that are *melt processing temperature* and *solidification time*. They used the same temperature for partial melting and solidification but changed the melting point of the Bi2212 phase by oxygen partial pressure. The precursor they used had the stoichiometry of $Bi_{2.0}Sr_{2.4}Ca_{0.7}Cu_{2.0}O_x$. Under zero oxygen partial pressure (100% N_2), the melting temperature was determined as 810^{o}C and at 20% O_2 pressure (balanced with N_2) as 870^{o}C. The green tapes were heated at 500^{o}C and then partially melted at 830^{o}C or 865^{o}C for 5 min in N_2 purge. Solidification at the same temperature followed the partial melting. Solidification time, t_s, varied between 1-36 hours and oxygen partial pressure was 20%. The final stage of the whole process was to cool down the furnace to 750^{o}C. Grain size for Bi2212 phase was measured to be 65 and 130 μm in tapes solidified at 830^{o}C and 865^{o}C, respectively. Funahashi et al. also state that grain size was independent of solidification time. Other researchers have reported that Bi2212 grains increase with increasing melt-processing temperature. Fig.63 shows SEM images of grains at partially melted state at different melt temperatures.

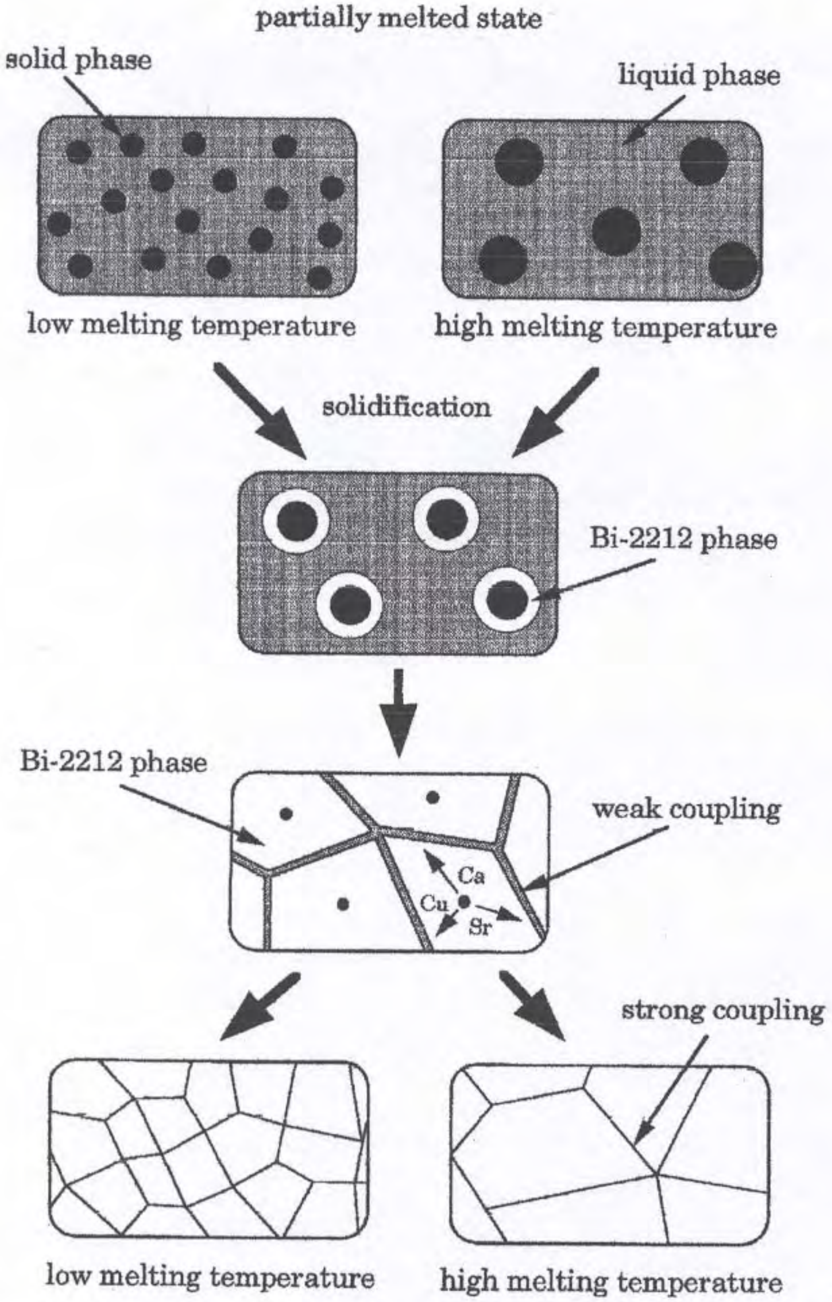

Fig.62 Schematic model of Bi2212 during cooling process [39].

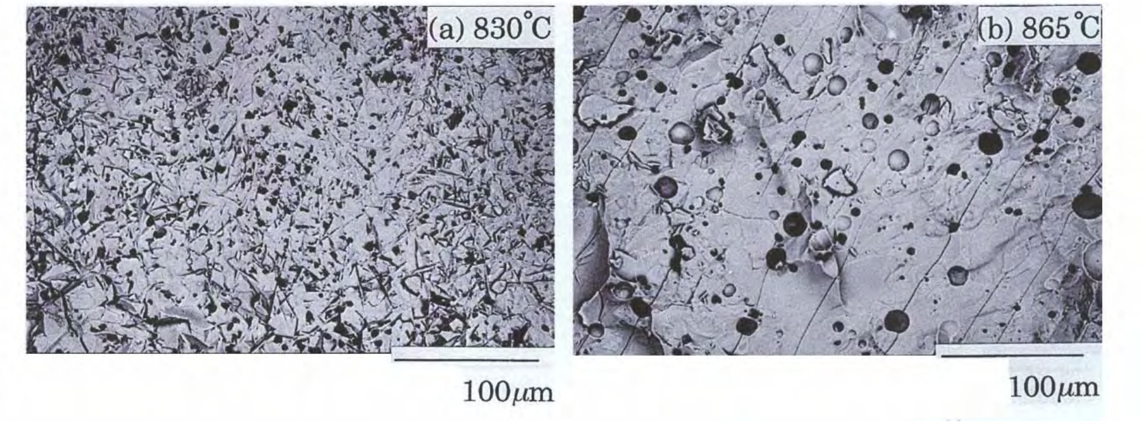

Fig.63 SEM images of tapes quenched from partially melted state at (a) 830°C (b) 865°C [39].

Dark spots in the figure represent the solid phases. Bi-free phases $(Sr,Ca)CuO_2$ and $(Sr,Ca)_2CuO_3$ as well as the Cu-free phase $Bi_2(Sr,Ca)_3O_6$ were mentioned to be present in both cases of temperatures. It is apparent that grains of the tape treated under lower melt temperature are smaller and dispersed in an orderly manner compared to the other one. This structure also implies earlier completion of peritectic reaction for the tape melted at 830°C.

Larger grains and the rough distribution of the solid phases in the second tape were suggested to lead to larger eventual size of Bi2212 phase grains by means of cation supply from the solid Bi-free and Cu-free phases.

The amount of the impurities, in other words remnant nonsuperconducting phases, was detected by means of XRD analysis. Bi-free phase $(Sr,Ca)CuO_2$ in the tape processed at 865°C reported to give a higher peak in density indicating that the amount of this phase was larger than the other tape processed at 830°C. However, it was also mentioned that size of Bi-free grains decreased with increased solidification time.

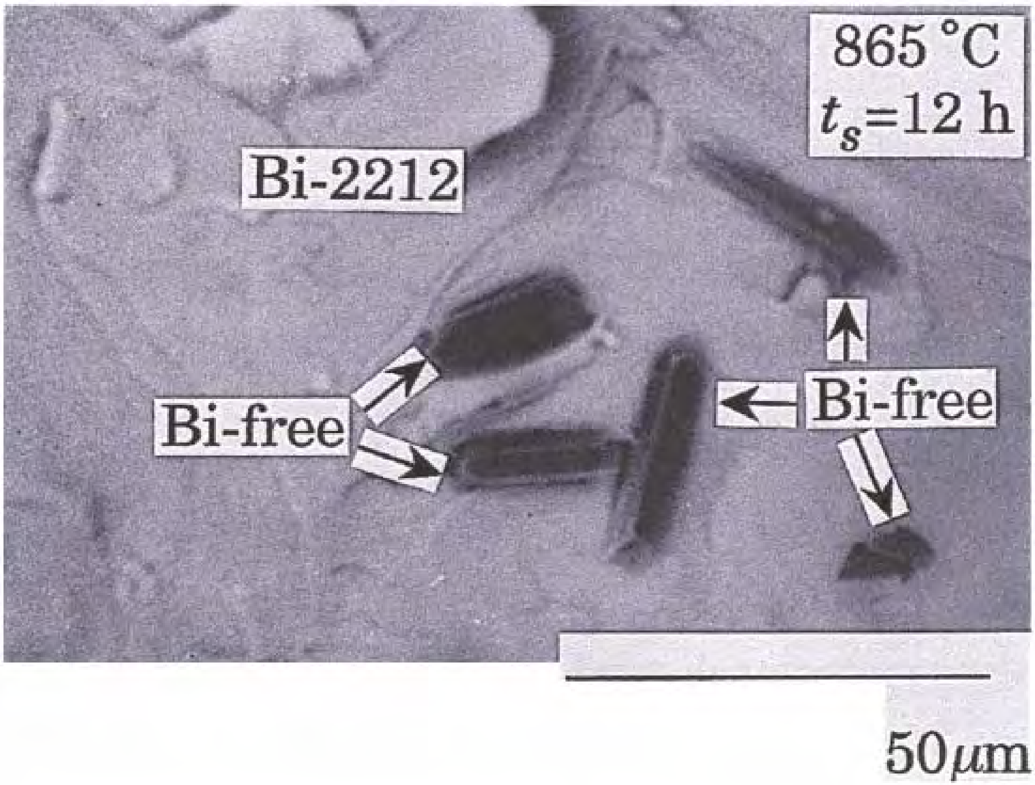

Fig.64 SEM image of tape solidified at 865°C for 12 hours of solidification time [39].

This suggests that it is possible to control the amount of impurities by adjusting the solidification duration. Fig.64 above shows the Bi-free grains and the Bi2212 grains around them.

Sr, Ca and Cu ions have to diffuse through the solid Bi2212 to react with the liquid phase at the edges of the Bi2212 grains. This is the reason for time demand by large 2212 phase formation. The authors stated that they did not observe any Bi-free grains in the tapes solidified at 830°C for 3 hours because the peritectic reaction was almost completed. The solidification duration that peritectic reaction is completed within depends on melt processing temperature and becomes longer with increasing grain size of the solid phases in the partial melt.

The amount of remaining Bi2201 phase is declared to be proportional to the amount of Bi-free phase remaining in the tapes in accord with the peritectic reaction. The authors found the diffraction peaks of Bi2201 phase to be weak and considered this as an uncertainty for the dependence of Bi2201 phase on solidification time (t_s). They also state that the amount of Bi2201 declines with increasing t_s.

Grain coupling was claimed to become stronger with increasing t_s. Since Bi2212 grows through the peritectic reaction;

$$\text{Bi2201} + \text{(Sr,Ca)CuO}_2 + \text{Liquid} \rightarrow \text{Bi2212}$$

the amount of remaining Bi-free and Cu-free phases is proportional to the amount of the liquid phase remaining at the grain boundaries. As the Bi2201 phase originates in the liquid surrounding Bi2212 grains, it appears to degrade the grain coupling.

It has also been reported that *Large Angle Tilt Boundaries* might take a role in making the grains coupling weaker. The authors state that through XRD, they found c-axis alignment comparable in the tapes treated at 865°C with solidification durations longer than 12 hours. This implies that t_s does not have much of an effect on grain boundary angle.

Schematic model of Bi2212 solidification during cooling process is given in Fig.62. As shown, Bi-free and Cu-free solid phases and liquid phase at first form in the partially melt incongruent phase assembly. The temperature of melt processing determines the composition of the solid phases previously mentioned. 1:1 AEC and 2:1 AEC and $Bi_2(Sr,Ca)_3O_6$ are the solid phases cited by the authors that were observed in both of the tapes. The grain size of solid phases increases with the melt processing temperature and larger solid grains eventually lead to larger Bi2212 grains. Solidification is triggered with increasing oxygen partial pressure and the Bi2212 precipitates and grows by the peritectic reaction mentioned earlier. The completion time for the peritectic reaction depends on the grain size of Bi-free and Cu-free solid phases in the partial melt. Naturally, more time is required for larger solid grains to react with the liquid completely. Optimization of powder precursor compositions also becomes crucial in removal of Bi-free grains and determination of the overall reaction period [39].

In their study, Ray et al. [40] stated that *Melt Processing* is a heat treatment method developed to replace *Solid-State Annealing* in order to further improve critical current density, J_c, of Ag clad BSCCO wires and tapes. It has been revealed that, to achieve highest electrical performance, 2212 grains need to be highly aligned within a homogeneous microstructure. The first models of melt processing were involved heating the Ag clad 2212 powders in air until the 2212 phase was completely melted and then cooling of the melt to reform the decomposed 2212 phase. However, the Bi2212 phase was discovered to melt incongruently at the maximum processing temperature (T_{max}) so that the melt would consist of liquid and nonsuperconducting "secondary" phases.

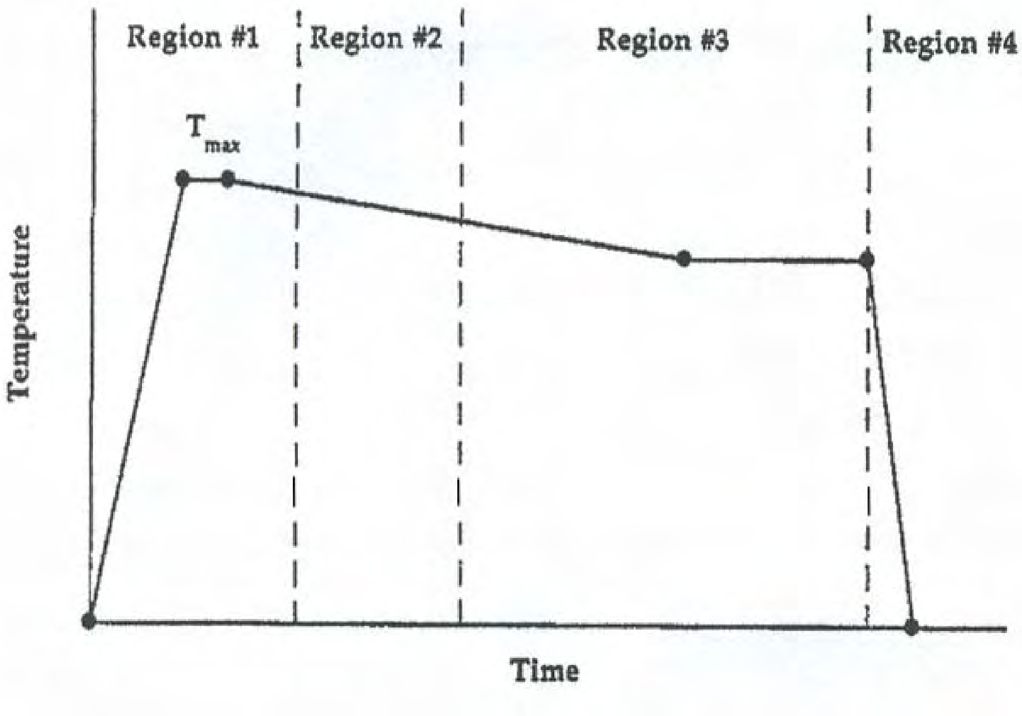

Fig.65 Schematic of a typical melt-process heat treatment divided into four regions [40].

These *secondary phases* were observed to remain in the core upon the completion of the reactions and disturb the alignment of 2212 grains in whose vicinity they were located. This disturbance was considered to yield blocking of supercurrent flow and tying up of cations so that a complete phase transformation of the melt into 2212 would be prevented. In theory, it is best to keep the secondary phases as small and dispersed as possible all over the core.

Melt processing has four main regions as shown in Fig.65 above. The *1st region* is the *incongruent melting of 2212* into liquid and secondary solid phases and subsequent cooling to the solidus temperature, which prevents formation of large Cu-free phases. The *2nd region* is the *initial precipitation of 2212* at ~ 860-870°C and AEC breakup, helps maximize 2212 alignment and minimize AEC grain size. The *3rd region* is the *formation of 2212* and *oxygen anneal*, which provides complete conversion of 2212 and maximizes critical temperature, T_c, of the superconductor by further reducing secondary phase size. The last one, the *4th region*, includes *cooling to room temperature*, which prevents decomposition of 2212 by its rapid rate.

The first two regions were considered decisive in the melt-process heat treatment in order to obtain well-aligned 2212 grains and small secondary phase grain size. Ray et al. revealed that the best microstructure achieved at the end of the 1st region was possible at $T_{max} \leq 895^{o}C$ by preventing formation of large Cu-free remnant grains, $Bi(Sr_{1-x}Ca_x)_2O_y$, that cannot be transformed on cooling. Other researchers have reported that 1:1 AEC phase could grow fast to larger size regardless of T_{max}. In the 2nd region, the core is an assembly of liquid, small Cu-free grains and large 1:1 AEC $(Sr_{1-x}Ca_x)CuO_2$ grains.

The authors prepared their 2212 powder by solid-state reaction of oxide and carbonate powders. OPIT method was utilized to fabricate tapes with 100 μm x 3 mm size. Core thickness was given as ~ 45 μm.

SEM observation of 2212 grains by Ray et al. revealed that these grains consisted of several plate-like 2212 grains with (001) *twist boundaries,* which were adjacent grains that have parallel *c-axes* with *ab-planes* rotated at some angle with respect to each other. They sought the valid 2212 grain alignment mechanism among these four possibilities:

Alignment due to density difference between liquid and 2212 phases,

Alignment due to aligned grains growing at the expense of unaligned grains, Alignment due to preferential nucleation on aligned surfaces such as the Ag sheath,

Alignment due to unimpeded grain growth of grains aligned within a range of angles that depend on the oxide core thickness.

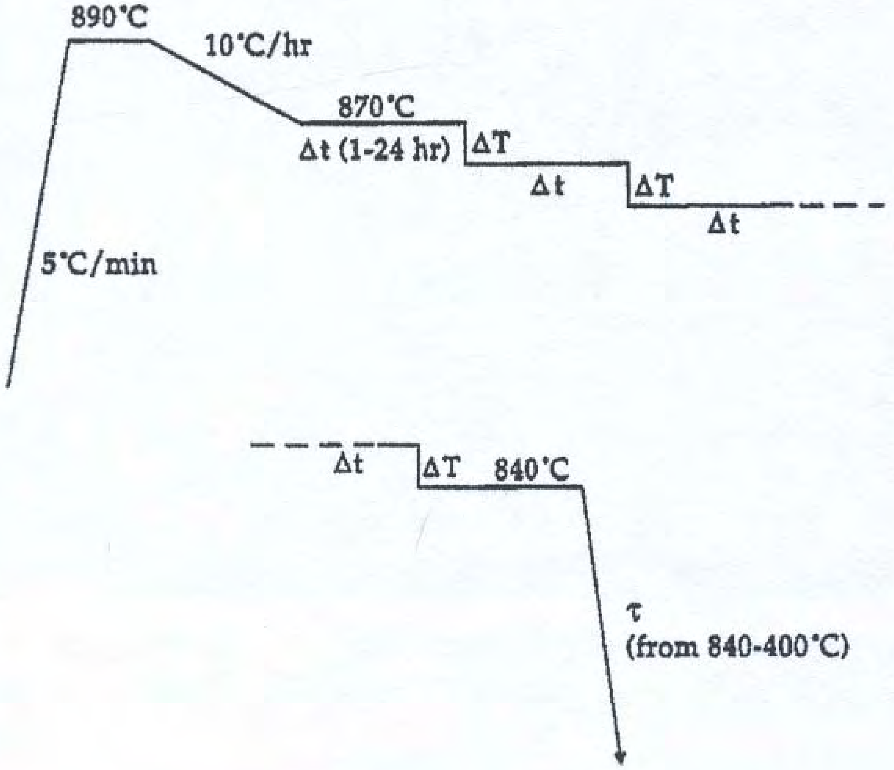

Fig.66 Step Solidification heat treatment original schedule by Ray et al. [40].

Authors studied the 2nd region (see Fig.65) extensively and came up with an alignment mechanism for 2212 grains called *Opportunistic Alignment* and developed a new heat treatment system, which they named *Step Solidification* (refer to Fig.66).
This heat treatment system, with some modification, is what was employed in this thesis work.

Ray et al.'s solidification melt processing heat treatment followed the schedule shown in Fig.66. Samples were heated at 5°C/min to 890°C, held for 10-30 min, then cooled at 10°C/h to 870°C for a certain period, *Δt*, after which the sample temperature was dropped a few degrees, ΔT, and held again for a certain length of time. This stepping and holding went on to 840°C where then the samples were cooled rapidly to 400°C at a certain rate, τ, to room temperature. They used ΔT= 5°C and Δt= 24h and τ =300°C/h in this study.

Upon sectioning and taking SEM pictures of the tapes, they found that the core showed highly aligned 2212 grains accompanied with small secondary phase grains. The number of large AEC phases was insignificant and no large Cu-free phase was observed. Very little residual liquid or 2201 phase was observed between 2212 grains. A few Ag regions could also be seen within the core of their tape.

The heat treatment schedule performed under the conditions cited above was reported to result in 1:1 AEC as the major and most detrimental remnant (secondary) phase in fully processed tape due to its size and permanency. Equilibrium phases below 2212 solidus line exclude 1:1 AEC. Therefore, kinetics of 1:1 AEC phase decomposition was considered slow at 840°C annealing temperature. Regarding their previous experiments, they conclude that with higher annealing temperatures, increased decomposition kinetics could improve size reduction of existing AEC. They also recount that 1:1 AEC began to decompose to 14:24 AEC near 864°C while these AEC phases broke up during cool down. They stated that this conversion was possibly due to dissolution of AEC phases into the liquid as 2212 formed.

It has been reported by researchers that 2212 developed between 890-850°C on cooling at an uncertain rate. Ray et al. observed that 2212 formed directly from the liquid at 870°C at a cooling rate of 10°C/h and continued to form until the temperature went down to 834°C. In solidification through peritectic reaction, direct formation of 2212 from the liquid is not the common case so far acknowledged.

$$\text{Bi2201} + (\text{Sr,Ca})\text{CuO}_2 + \text{Liquid} \rightarrow \text{Bi2212}$$

According to the well-known peritectic reaction above, 2212 formation is involved with solid phases as well as the liquid. 2212 forms plate-like grains, because the growth in the *a* and *b* directions is much faster than the growth in *c* direction. Important parameters for

2212 grain alignment were considered as the cooling rate, the soaking time at temperatures near the solidus line and the thickness of the oxide core in the tape.

Ray et al. also revealed that slow cooling yielded higher alignment compared to fast cooling, and different alignment mechanisms, which were mentioned before, appeared to work depending on the cooling rate. Their slow cooled samples were found to have highly aligned grains by 865°C. On the other hand, fast cooled samples displayed poorly aligned grains during the cooling period with most of the alignment occurring at around 840°C.

The amount of time spent in the forming of Bi2212 phase at temperatures near the solidus line appears as the second crucial parameter. For slow cooled (10°C/h) samples, substantial alignment was recorded in the first hour of the cooling process between 870-860°C. Extended anneals at 2212 solidus temperature (~ 870°C) seemed to provide the highest 2212 alignment. Decreasing the oxide core thickness in tapes has also been reported as another means to achieve highly aligned Bi2212 grains.

Alignment due to density differences takes place when density differences between 2212 and the liquid phase causes the 2212 grains to either float to the top or sink to the bottom of the melt. If these grains come across a horizontal surface adequate to align, then they align themselves accordingly. This mechanism yields the highest alignment with the horizontal plane of the tape.

Alignment due to aligned grains at the expense of unaligned grains happens if aligned 2212 grains tend to grow and the core has fewer grains overall and greater grain length. It is a slower mechanism and mostly favored during solid state processing.

Both *alignment due to preferred precipitation on the Ag sheath* (alternatively known as *preferred precipitation*) and *alignment due to unimpeded grain growth* (alternatively known as *opportunistic grain growth*) are the dominant mechanisms forming very similar final microstructures.

Within the melt-processed tapes, heterogeneous nucleation of Bi2212 phase is likely to occur on the Ag sheath, secondary phases, pores and even the Ag particles precipitated in the liquid. Decreasing the core thickness, i.e. overall thickness of the tape has been reported to increase the proper alignment in the core center.

Opportunistic grain growth mechanism makes use of any nucleation site possible among those cited above, provided grains of varying alignment grow within the melt; not absorb close 2212 grains. Initially, the grains must be apart from each other in order to allow mutual enlargement. Near the solidus temperature, the number of 2212 nuclei formed was observed to be minimized with maximized grains growth kinetics. Moreover, slow cooling is also known to contribute grain growth in the process of nucleation. Therefore, with isothermal annealing near the solidus line or with slow cooling, fewer and larger grains could initially form in the melt.

Preferential alignment takes place when grain growth is favored in certain directions by the influence of morphology of both the environment and the grains themselves. Grains oriented without any hindrance on their borders by their environment naturally grow larger while the ones faced with obstruction remain smaller. The authors observed that grains with their *ab-plane* initially parallel to the tape plane were the largest, while unaligned grains stopped growing further due to encroachment on the Ag sheath. With increasing time, due to the larger fraction of surface area of the newly developed grains, epitaxial (*the growth on a crystalline substrate of a crystalline substance that mimics the orientation of the substrate*) growth in *c direction* on *ab-planes* of existing grains was discovered to be very likely to occur. Consequently, extended annealing was suggested to yield the greatest alignment near the solidus temperature for any core thickness. Opportunistic grain growth mechanism has been intensely observed at ~ 870°C.

Ray et al. suggested *opportunistic grain growth mechanism* is the best explanation for high alignment of Bi2212 grains in melt processed tapes.

The best microstructure obtained after the 1st region (see Fig.65) in partial melt heat treatment was said to be possible with $T_{max} \leq 895^oC$. This schedule was observed to prevent formation of large Cu-free grains. Upon cooling, the microstructure was reported to consist of liquid, small Cu–free grains and large 1:1 AEC grains at temperatures slightly above solidus. In the 2nd heat treatment region (see Fig.65), high alignment of Bi2212 grains and reduction of secondary phases, especially 1:1 AEC, were selected as the main priorities. Utilizing isothermal annealing close to the solidus temperature, 870°C well alignment of grains was found to be achievable through the opportunistic grains growth mechanism. Nonetheless, the authors stated that 1:1 AEC grains at 870°C accompanying the Bi2212 grain alignment did not exhibit breakup and they decomposed into 14:24 AEC following loss in size at temperatures below 864°C. This suggested that reduction in secondary grain size should have been achieved as Bi2212 grains initially formed from the liquid; because the smaller the second phase grains the less likely they are to impede alignment of Bi2212. Moreover, even as the substantial amount of liquid containing fewer large secondary phase grains transformed into 2212, there might be less chance for significant non-uniformities to exist in the core composition since large nonsuperconducting grains are known to transform slowly into 2212 by solid state diffusion at 840°C. Therefore, it was declared a necessity to achieve 2212 alignment first, and then second phase grain size reduction.

Although extended annealing at 870°C was employed, a huge amount of liquid was still observed to exist. In order to complete the transformation, further processing at lower temperatures was required. Since the new 2212 grains were observed to be as highly aligned as possible at 870°C, then through the opportunistic grain alignment mechanism, the best alignment could be expected to occur with the following generation of 2212 grains then allowed to grow larger and larger. This phenomenon was considered to be possible by dropping the temperature slightly below 870°C and holding it there.

In time, volume fraction of 2212 grains would require further decrease in temperature followed by holds as they reached equilibrium. Below 865^{o}C this “step” heat treatment proved to reduce 1:1 AEC grain size. Given the most appropriate step height, ΔT, and step time, Δt, desired 2212 alignment and 1:1 AEC grain size reduction were achieved by this step wise process between 870-860^{o}C.

The annealing in the 3rd region (refer to Fig.65) for complete transformation into 2212 was applied next.

In the 4th region, at temperatures below 840^{o}C, 2212 was observed to decompose to 2201 at around 730^{o}C. Researchers have reported that slow cooling rates (20-30^{o}C/h) from 836 to 400^{o}C degraded superconductivity of the tapes. It was also revealed that 2212 grain boundaries were decomposing into 2201, BiSrCaCuO and CuO phases due to oxygen absorption. Therefore, fast-cooling rates seemed to be required below 400^{o}C to conserve 2212 phase in hand. Utilization of a fast quench rate (τ) down to at least 400^{o}C was suggested in order to avoid 2212 grain boundary degradation. However, it should not be as fast to cause thermal stress and introduce fractures in the core [40].

Heat Treatment of Bi(Pb)2212 Wires and Tapes: Step Solidification Partial Melt

After a broad literature survey and a profound examination of the available partial melt heat treatment procedure for 2212 superconductors, *Step Solidification Method* of Ray and Hellstrom [40] was considered the most appropriate for the scope of our thesis work. Based on the schedule they published, the heat treatment process employed in our experiments is given in Fig.69, below.

The schedule consists of 16 sections and furnace cool down to room temperature. During all experiments, the ambient temperature was 22^{o}C.

Step 01 was heat up ramp at a rate of 5^{o}C/min, then followed by step 02, a soaking of 30 min at T_{max}= 890^{o}C. Step 03 was slow cool down to 870^{o}C at 10^{o}C/h. The next stage was the 24 hour total process of "step solidification", consisting of six soaking steps; 04,06,08,10,12 and 14, each with a step time Δt= 4 h. The step height was ΔT= 5^{o}C and designated with 05,07,09,11,13 and 15. Furnace cool down lasted for approximately 6-7 hours.

The first wires processed with step solidification heat treatment were sealed at their ends by clamping. After the heat treatment, it was observed that the molten ceramic leaked out of the wires and contaminated the sample holder and the tube of the furnace which were both, made of quartz. After a quick research, it was revealed that Alkali Earth Metals, such as Ca, Sr and Mg, become highly aggressive on quartz at elevated temperatures. Dark brown, penetrating spots were observed on the inner surface of the quartz tube, which then acted as initiation points of a crack system that eventually caused discarding. The quartz sample holder was also devastated through a transformation due to Alkali Metal attack by the leak. The clear quartz turned into a dull, whitish/indigo blue ceramic like very brittle material, which shattered into pieces at first touch.

Upon this costly experience, TIG welding was employed to seal the ends of the wires, and it worked very well.

In order to seal the end of the tapes, the lateral face of a cylindrical metal piece was utilized under press and the tape ends were cleanly impressed. This method was sufficient in prevention of molten superconductor leak through the ends of the tapes.

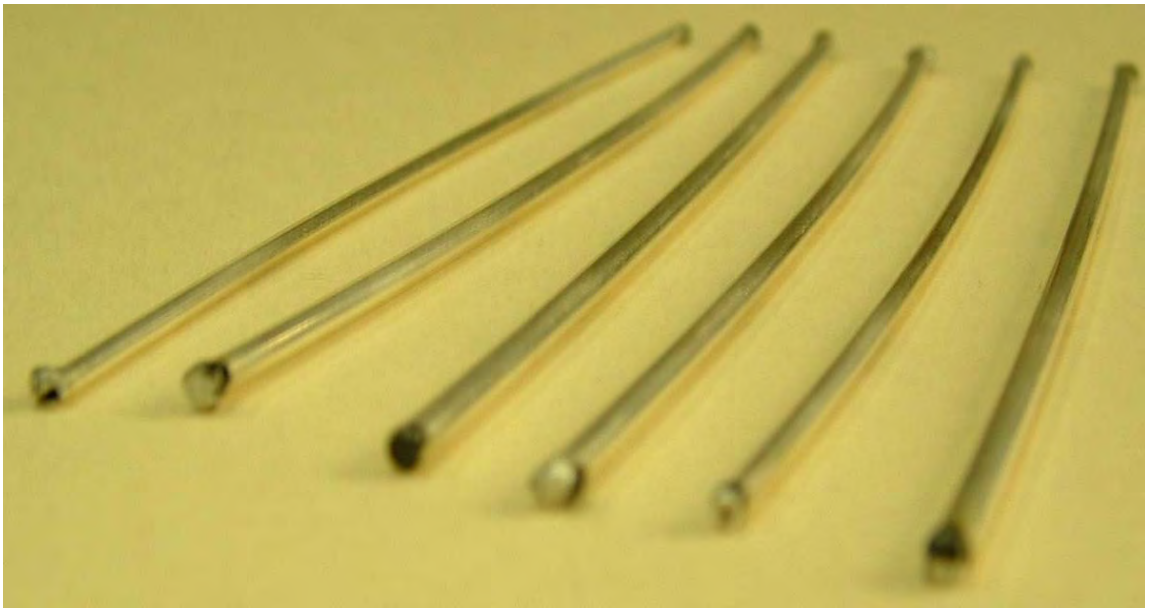

Fig.67 TIG welded mono and multifilament wire specimens before heat treatment.

Bubbling Problem with Tapes: Reasons and Prevention

Throughout the tape heat treatments, *bubbling* was a big concern (see Fig.68). However, there was no visible deterioration observed due to bubbling on any wire processed.

As cited in the previous section, Thangaraj et al. [38] also observed similar problems with their tapes. In his broad work, Hellstrom [3] declared bubbling as a serious problem, which causes dimensional non-uniformity in the conductor and degradation, or even complete loss of J_c in the bubbled region. Bubbles are bulges in the Ag sheath of the composite due to high internal gas pressure that develops at elevated temperatures. It occurs when a condensed material alters to a gas, building up pressure that deforms the Ag sheath.

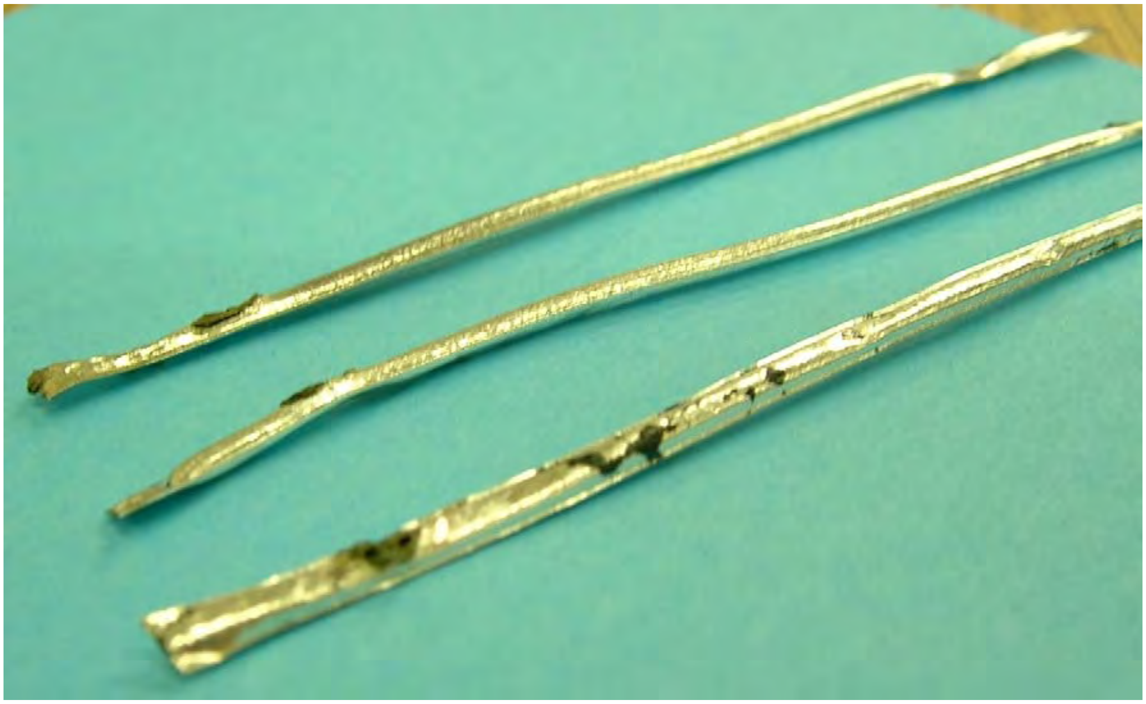

Fig.68 Tapes severely deformed due to bubbling formation following step solidification melt processing.

Three chemical materials are known to cause bubbling: H_2O, CO_2 and O_2.

Water is likely to be caught by the superconductor through absorption on the surface of the precursor powder or as $Ca(OH)_2$ or $Sr(OH)_2$. CO_2 may enter to the superconductor as carbonate or even from the atmosphere. In order to eliminate water and CO_2, Hellstrom advises heating the powder in flowing oxygen or inert gas at ~800^{o}C for ~8-48 hours.

Bubbling caused by water was observed to happen typically at 400-600^{o}C; by CO_2 it occurs just below the melting point of 2212 and by O_2 at the 2212 melting point. The O_2 release that takes place on melting is considered to be caused by the Cu reduced in the melt. Despite readily diffusion of O_2 through Ag, when a tape or wire is rapidly heated up close to the melting point of 2212, O_2 may form so quickly that it builds up high pressure before it finds a chance to diffuse through Ag.

So far, researchers proposed several different methods to prevent bubbling. One of them involves *piercing the tape* before heat treatment to release the gas.

This method was employed in our experiments as well. However, even several tiny punctures made in an orderly manner did not help very much. To the contrary, they acted as leak passages, and the melt was lost through these holes.

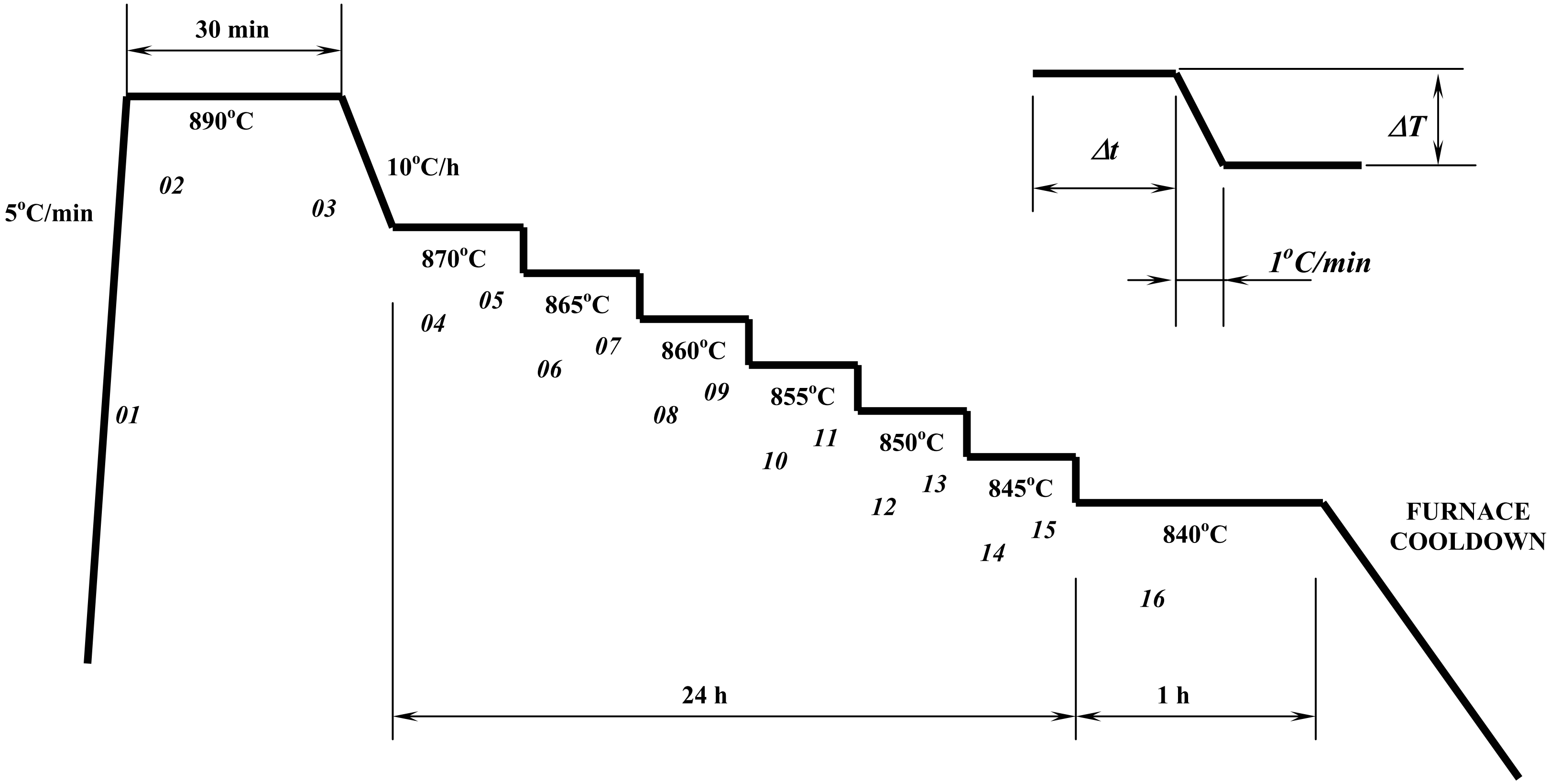

Fig.69 Step solidification partial melt heat treatment. Intervals 05,07,09,11,13,15 are cooling ramps for smooth temperature gradient between steps, each 1°C/min, and detail view shown upper right hand side of schematic. ΔT= 5°C, Δt= 4 h.

Another method suggested is *reduction of the heating rate* when passing through the 2212 melting point and reduction of the rate of O_2 formation. This method introduces the risk of 1:1 AEC grains growing larger than anticipated.

The third method cited is *heating the powder close to the melting point in air* at a lower temperature in vacuum. In other words, melt processing in reduced oxygen partial pressure (1% O_2) and holding the tape below the melting temperature allowing oxygen to diffuse out through the Ag sheath before 2212 melts [3].

Material properties limitations of our quartz tube furnace did not allow us to reach gage pressures around 1 atm. Therefore, none of the oxygen partial pressure atmospheres previously mentioned was available.

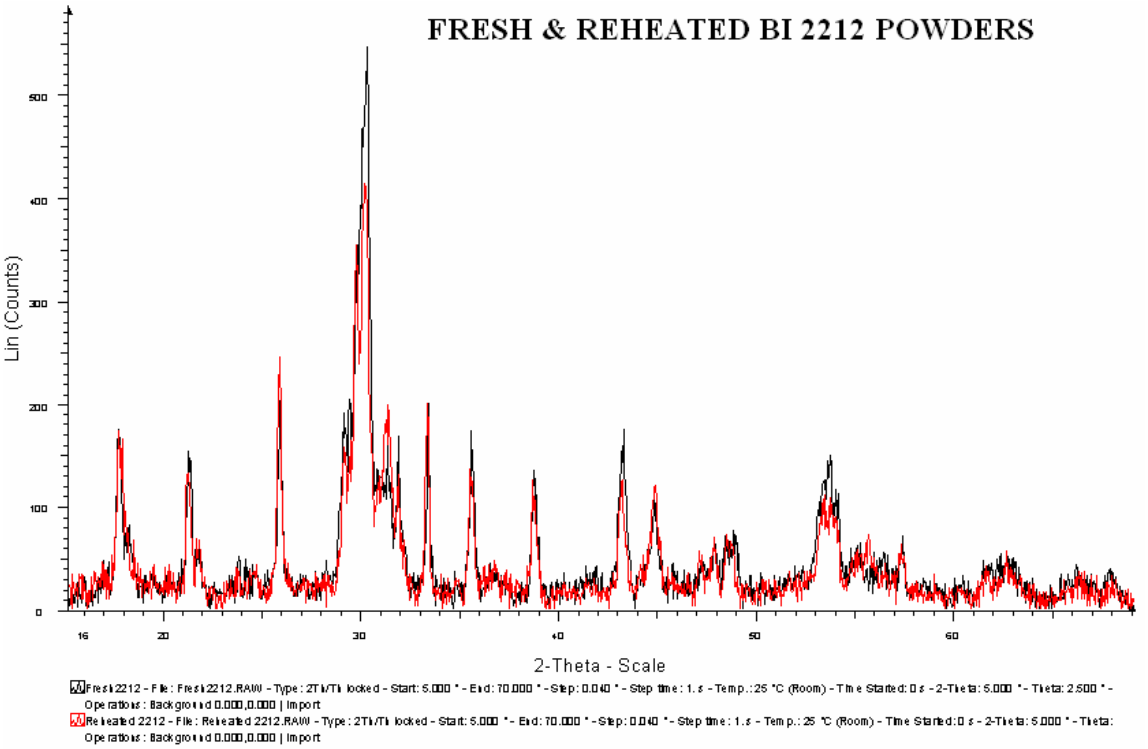

Fig.70 XRD graphs of original (fresh) and reheated precursor powders together. Red line represents reheated powder; black line represents the fresh batch.

Carbon remnant in the superconductor core has also been reported to cause bubbling as CO_2 and alter the melting point of 2212. It is considered effective on phase assemblage as for increase in C content in the powder yielded Sr-rich phase to appear and among of Cu-free phase to decrease in the melt. However, it is still not certain how much C can be tolerated in powders used to manufacture tape and wire superconductors with good performance.

After getting unsatisfactory results with the tapes due to bubbling, our precursor powder with the stoichiometry (see section Bi2212 Powder Preparation for detailed discussion) $Bi_{1.6}(Pb_{0.6})Sr_{1.8}Ca_{1.0}Cu_{2.0}O_{8+x}$ was decided to be reheated along the schedule as described above by Hellstrom [3].

XRD merged graph of original and reheated precursor powders can be seen in Fig.70. There was not much of a change noticed in the characteristic peak locations and intensities between two graphs; in other words, the reheating schedule employed did not seem to work for C decrement in reheated powder compared to the original one used with the tapes that experienced bubbling.

EVALUATION OF STRUCTURAL AND CHEMICAL INTEGRITY OF WIRES AND TAPES

Image Analysis and Results

Image analysis comprised of two main stages: The first stage involved utilization of a scanning electron microscope (SEM), Cameca SX 50, for BSE (back scattered electron) micro photography, WDS (wave dispersive spectrum) and EDS (energy dispersive spectrum) analyses. The second stage included conversion of the SEM pictures into binary images and performing dimension measurements and area calculations by means of *NIH Image 1.61* image processing and analysis program.

BSE micro photographs of tape and wire cross sections (transverse/longitudinal) were taken to observe the outcome of the employed deformation procedures and verify the structural integrity of the composites afterwards (see Appendices 3-6 for all the BSE and binary images processed).

Transverse cross section pictures of wires helped calculate the compaction of powder for drawing operations, thus the filling factor of the precursor powders used in OPIT method. Axial cross section photos showed sausaging effect at different stages of drawing operations on wires with various diameters and sheath material combinations; these will be presented under the subtitle of Investigation of Interface and Filament Pattern for Sausaging.

Integrity of flattening deformation regimes, in other words, the accuracy of rolling processes used to fabricate tapes out of mono and multifilament wires was evaluated by investigating transverse cross section photos of tapes. Axial cross section pictures helped exhibit the monocore/multifilament pattern and the sausaging effect inside.

Both tape and wire BSE pictures with 63x or 100x magnification factors were converted into binary images for evaluation of core to metal sheath ratio on the transverse cross sections. This analysis provided a comparison among the rolling schedules of mono and multi filament tapes with various metal sheath combinations deformed by various reduction-per-pass regimes. The tapes and the deformation schedules applied can be seen in Table 9.

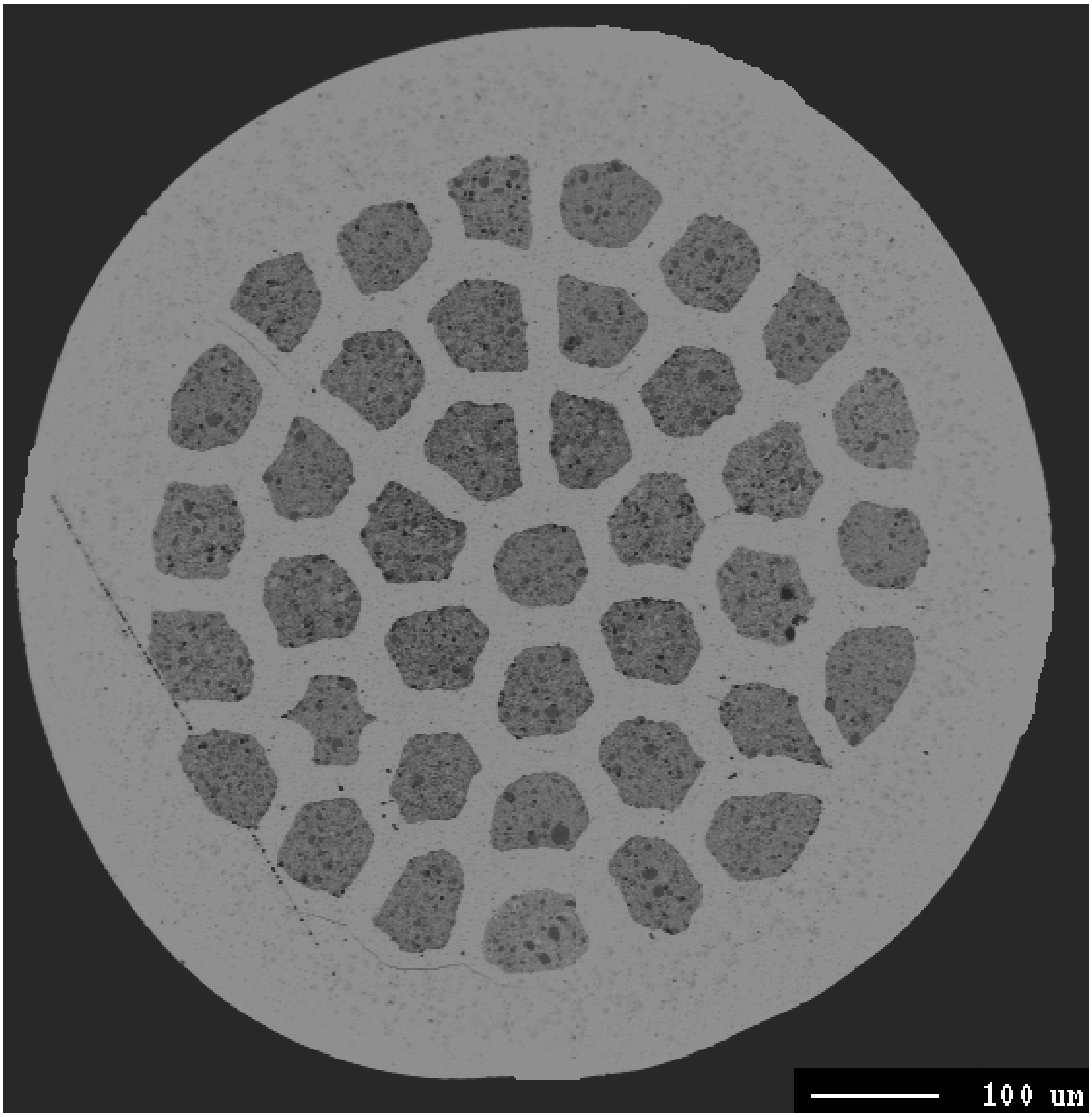

Fig.71 BSE image of *Mg filament-Mg tube* wire with 38 filaments, 0.0600” (1.52 mm) diameter, BB4_m60_63x

The parameters evaluated in the binary image calculations by means of NIH Image software included *total cross sectional area, core area, sheath area, width* and *thickness* of the tape samples. Results for all are presented in Tables 13-24. Example explanations to names of some tables are as follows:

Title, *BB1_monoAg_25% reduction_100xBSE* represents one part of the SEM sample #1 prepared with mono filament Ag sheath tapes fabricated using 25% constant reduction per pass starting with a wire of diameter 0.0500 inch.

Title, *BB2b_multi_Agfilament_Agtube_25% reduction_dia600_63xBSE* means one part of the SEM sample #2 prepared with multi filament (Ag filament-Ag tube) tapes fabricated using 25% constant reduction per pass starting with a wire of diameter 0.0600 inch.

Title, *BB8_multi_Agfilament_Mgtube_IR1 reduction_dia500_63xBSE* is one part of the SEM sample #8 prepared with multi filament (Ag filament/Mg tube) tapes fabricated using IR1 type increasing reduction per pass starting with a wire of diameter 0.0500 inch

For instance, *BB1_Ag16_100xBSE* is the code for the "100x zoom factor BSE tape picture" corresponding to the pass by *roller reduction-scale-step #16* and *BB1_Ag37_100xBSE* corresponds to *roller reduction-scale-step #37*.

In the tables, all the tapes are given in accordance with the roller scale used for the deformation procedures, from the thinnest (#16) to the thickest step. Each row contains the parameters' values, which were evaluated by image processing except the *mean thickness* (given in mills). Mean thickness was measured by micrometer after each pass for every tape as a reference dimension for the deformation process. Some deviations related to photography accuracy and zoom factors were then corrected with respect to this absolute measurement.

Table 13. Image analysis results for tape, BB1_monoAg_25% reduction_dia500_100xBSE

TAPE BB1_monoAg_25% reduction_100xBSE (all dimensions in microns)

Name	***Roller Scale***	***Total cross sectional Area***	***Core Area***	***Sheath Area***	***Filling Factor (core area/total area)***	***Width***	***Thickness***	***Mean Thickness (Mills)***	***Aspect Ratio [Width/Thickness] Normalized***
BB1_Ag16dp_100xBSE	16	478352.69	251158.15	227194.54	1.88	3224.16	149.86	0.0059	100.00
BB1_Ag16_100xBSE	16	508908.03	369054.11	139853.92	2.17	3117.85	165.1	0.0065	87.78
BB1_Ag18_100xBSE	18	632658.02	384092.95	248565.07	2.00	3011.00	213.36	0.0084	65.59
BB1_Ag22_100xBSE	22	773385.76	439540.18	333845.58	1.98	2710.36	292.1	0.0115	43.13
BB1_Ag25_100xBSE	25	872809.59	535315.76	337493.84	2.13	2530.78	355.6	0.0140	33.08
BB1_Ag31_100xBSE	31	989573.42	519679.79	469893.63	1.93	2094.57	497.84	0.0196	19.56
BB1_Ag37_100xBSE	37	1090429.89	595678.08	494751.82	2.01	1866.24	629.92	0.0248	13.77
BB1_Ag46_100xBSE	46	1209518.80	639166.83	570351.98	2.01	1630.58	833.12	0.0328	9.10

Table 14. Image analysis results for tape, BB1_monoMg_25% reduction_dia500_100xBSE

TAPE BB1_monoMg_25% reduction_100xBSE (all dimensions in microns)

Name	***Roller Scale***	***Total cross sectional Area***	***Core Area***	***Sheath Area***	***Filling Factor (core area/total area)***	***Width***	***Thickness***	***Mean Thickness (Mills)***	***Aspect Ratio [Width/Thickness] Normalized***
BB1_Mg16tp_100xBSE	16	508803.06	258487.76	250315.31	1.70	3213.96	160.02	0.0063	100.00
BB1_Mg16_100xBSE	16	534248.77	237624.00	296624.77	1.68	3085.93	175.26	0.0069	87.67
BB1_Mg18_100xBSE	18	621902.29	341259.79	280642.50	1.77	2926.84	215.90	0.0085	67.50
BB1_Mg22_100xBSE	22	739013.95	384623.99	354389.97	1.76	2490.00	304.80	0.0120	40.67
BB1_Mg25_100xBSE	25	869184.33	381958.97	487225.36	1.74	2487.25	360.68	0.0142	34.33
BB1_Mg31_100xBSE	31	1001142.50	591019.52	410122.98	1.87	2089.13	505.46	0.0199	20.58
BB1_Mg37_100xBSE	37	1112989.76	528819.11	584170.65	1.66	1833.01	657.86	0.0259	13.87
BB1_Mg46_100xBSE	46	1203502.02	562953.98	640548.04	1.65	1589.69	855.98	0.0337	9.25

Table 15. Image analysis results for tape, BB2a_multi_Agfilament_Agtube_25% reduction_dia500_63xBSE

TAPE BB2a_multi_Ag filament_Ag tube_25% reduction_dia500_63xBSE (all dimensions in microns)									
Name	***Roller Scale***	***Total cross sectional Area***	***Core Area***	***Sheath Area***	***Filling Factor (core area/total area)***	***Width***	***Thickness***	***Mean Thickness (Mills)***	***Aspect Ratio [Width/Thickness] Normalized***
BB2a_Ag16_63xBSE	16	645838.13	280903.46	364934.68	0.43	4007.81	162.56	0.0064	100.00
BB2a_Ag18_63xBSE	18	639393.33	198315.71	441077.63	0.31	3229.51	200.66	0.0079	65.28
BB2a_Ag22_ 3xBSE	22	789893.37	254848.51	535044.86	0.32	2790.05	289.56	0.0114	39.08
BB2a_Ag25_63xBSE	25	899025.98	301262.63	597763.35	0.34	2622.15	353.06	0.0139	30.12
BB2a_Ag31_ 3xBSE	31	821226.89	314346.67	506880.23	0.38	2294.09	370.84	0.0146	25.09
BB2a_Ag37_ 3xBSE	37	1121361.14	308792.84	812568.30	0.28	1928.73	624.84	0.0246	12.52
BB2a_Ag46_ 3xBSE	46	1275753.55	324872.87	950880.68	0.25	1710.09	833.12	0.0328	8.33

Table 16. Image analysis results for tape, BB2b_multi_Agfilament_Agtube_25% reduction_dia600_63xBSE

TAPE BB2b_multi_Ag filament_Ag tube_25% reduction_dia600_63xBSE (all dimensions in microns)									
Name	***Roller Scale***	***Total cross sectional Area***	***Core Area***	***Sheath Area***	***Filling Factor (core area/total area)***	***Width***	***Thickness***	***Mean Thickness (Mills)***	***Aspect Ratio [Width/Thickness] Normalized***
BB2b_Ag16T_63xBSE	16	528873.94	186344.83	342529.12	0.35	3446.66	154.94	0.0061	100.00
BB2b_Ag16_63xBSE	16	587261.92	128312.16	458949.76	0.22	3487.35	170.18	0.0067	92.12
BB2b_Ag18_63xBSE	18	620422.93	165590.67	454832.26	0.27	2855.02	220.98	0.0087	58.08
BB2b_Ag22_ 63xBSE	22	951232.44	350934.24	600298.20	0.37	3211.93	302.26	0.0119	47.77
BB2b_Ag25_ 63xBSE	25	1061091.71	250119.50	810972.21	0.24	2940.90	370.84	0.0146	35.65
BB2b_Ag31_ 63xBSE	31	1246065.42	351755.51	894309.91	0.28	2561.90	508.00	0.0200	22.67
BB2b_Ag37_ 63xBSE	37	1427918.51	352514.47	1075404.04	0.25	2351.73	645.16	0.0254	16.39
BB2b_Ag46_ 63xBSE	46	1525332.81	375046.41	1150286.39	0.25	1965.67	855.98	0.0337	10.32

Table 17. Image analysis results for tape, BB6_multi_Agfilament_Mgtube_25% reduction_dia500_63xBSE

TAPE BB6_multi_Ag filament_Mg tube_25% reduction_dia500_63xBSE (all dimensions in microns)

Name	***Roller Scale***	***Total cross sectional Area***	***Core Area***	***Sheath Area***	***Filling Factor (core area/total area)***	***Width***	***Thickness***	***Mean Thickness (Mills)***	***Aspect Ratio [Width/Thickness] Normalized***
BB6_Ag16T_63xBSE	16	489646.39	200608.49	200608.49	0.41	3299.52	149.86	0.0059	100.00
BB6_Ag16_63xBSE	16	536707.33	193803.16	193803.16	0.36	3388.34	160.02	0.0063	96.17
BB6_Ag18_63xBSE	18	651562.06	325734.61	325734.61	0.50	3211.07	205.74	0.0081	70.89
BB6_Ag22_ 63xBSE	22	786942.72	317555.53	317555.53	0.40	2827.30	284.48	0.0112	45.14
BB6_Ag25_ 63xBSE	25	907814.50	323827.65	323827.65	0.36	2665.13	350.52	0.0138	34.53
BB6_Ag31_ 63xBSE	31	1069154.20	397439.21	397439.21	0.37	2264.89	495.30	0.0195	20.77
BB6_Ag37_ 63xBSE	37	1114176.09	344957.69	344957.69	0.31	1930.76	619.76	0.0244	14.15
BB6_Ag46_ 63xBSE	46	1230846.66	375414.54	375414.54	0.31	1672.24	822.96	0.0324	9.23

Table 18. Image analysis results for tape, BB6_multi_Mgfilament_Mgtube_25% reduction_dia500_63xBSE

TAPE BB6_multi_Mg filament_Mg tube_25% reduction_dia500_63xBSE (all dimensions in microns)

Name	***Roller Scale***	***Total cross sectional Area***	***Core Area***	***Sheath Area***	***Filling Factor (core area/total area)***	***Width***	***Thickness***	***Mean Thickness (Mills)***	***Aspect Ratio [Width/Thickness] Normalized***
BB6_Mg16_63xBSE	16	361745.96	72625.58	289120.37	0.20	2368.00	154.94	0.0061	100.00
BB6_Mg18_63xBSE	18	358098.08	127574.42	230523.65	0.36	2140.75	170.18	0.0067	82.31
BB6_Mg22_63xBSE	22	448823.79	200204.96	248618.82	0.45	2078.48	220.98	0.0087	61.54
BB6_Mg25_63xBSE	25	552693.46	217714.01	334979.46	0.39	1893.40	302.26	0.0119	40.99
BB6_Mg31_63xBSE	31	583257.07	245121.84	338135.23	0.42	1652.38	370.84	0.0146	29.15
BB6_Mg37_63xBSE	37	651936.17	180348.19	471587.98	0.28	1392.36	508.00	0.0200	17.93
BB6_Mg46_63xBSE	46	698569.89	190000.37	508569.52	0.27	1221.24	645.16	0.0254	12.39

Table 19. Image analysis results for tape, BB8_multi_Agfilament_Mgtube_IR1 reduction_dia500_63xBSE

TAPE BB8_multi_Ag filament_Mg tube_IR1 reduction_dia500_63xBSE (all dimensions in microns)									
Name	***Roller Scale***	***Total cross sectional Area***	***Core Area***	***Sheath Area***	***Filling Factor (core area/total area)***	***Width***	***Thickness***	***Mean Thickness (Mills)***	***Aspect Ratio [Width/Thickness] Normalized***
BB8_Ag16T_63xBSE	16	504888.11	392540.13	112347.98	0.78	3291.85	154.94	0.0061	100.00
BB8_Ag16_63xBSE	16	510372.58	297171.19	213201.39	0.58	3080.43	167.64	0.0066	86.49
BB8_Ag19_63xBSE	19	637185.70	335727.64	301458.06	0.53	2930.88	220.98	0.0087	62.43
BB8_Ag25_63xBSE	25	790696.17	377707.63	412988.54	0.48	2363.09	345.44	0.0136	32.20
BB8_Ag32_63xBSE	32	933447.81	310400.13	623047.68	0.33	1929.41	513.08	0.0202	17.70
BB8_Ag38_63xBSE	38	1011165.06	297980.93	713184.13	0.29	1711.41	642.62	0.0253	12.53
BB8_Ag45_63xBSE	45	1152512.93	338012.63	814500.30	0.29	1612.16	800.10	0.0315	9.48
BB8_Ag53_63xBSE	53	1166765.56	354681.19	812084.36	0.30	1410.73	970.28	0.0382	6.84
BB8_Ag58_63xBSE	58	1186609.22	372568.37	814040.85	0.31	1349.76	1056.64	0.0416	6.01
BB8_Ag60_63xBSE	60	1214258.80	365384.66	848874.13	0.78	1334.11	1107.44	0.0436	5.67

Table 20. Image analysis results for tape, BB8_multi_Mgfilament_Mgtube_IR1 reduction_dia500 _63xBSE

TAPE BB8_multi_Mg filament_Mg tube_IR1 reduction_dia500_63xBSE (all dimensions in microns)									
Name	***Roller Scale***	***Total cross sectional Area***	***Core Area***	***Sheath Area***	***Filling Factor (core area/total area)***	***Width***	***Thickness***	***Mean Thickness (Mills)***	***Aspect Ratio [Width/Thickness] Normalized***
BB8_Mg16_63xBSE	16	534419.95	278606.65	255813.30	0.52	3374.05	160.02	0.0063	100.00
BB8_Mg19_63xBSE	19	664723.62	313460.96	351262.66	0.47	3125.18	215.90	0.0085	68.65
BB8_Mg25_63xBSE	25	818077.72	479040.19	339037.53	0.59	2425.61	347.98	0.0137	33.06
BB8_Mg32_63xBSE	32	1000094.68	298572.21	701522.46	0.30	2087.06	505.46	0.0199	19.58
BB8_Mg38_63xBSE	38	1155398.16	362112.70	793285.46	0.31	1969.38	629.92	0.0248	14.83
BB8_Mg45_63xBSE	45	1288440.40	360328.71	928111.69	0.28	1772.98	805.18	0.0317	10.44
BB8_Mg53_63xBSE	53	1294151.36	373737.15	920414.20	0.29	1547.95	965.20	0.0380	7.61
BB8_Mg58_63xBSE	58	1289648.67	389491.55	900157.12	0.30	1459.40	1043.94	0.0411	6.63

Table 20. (continued)

Name	*Roller Scale*	*Total cross sectional Area*	*Core Area*	*Sheath Area*	*Filling Factor (core area/total area)*	*Width*	*Thickness*	*Mean Thickness (Mills)*	*Aspect Ratio [Width/Thickness] Normalized*
BB8_Mg60_63xBSE	60	1333409.75	398181.67	935228.08	0.30	1450.67	1097.28	0.0432	6.27

Table 21. Image analysis results for tape, BB3_monoMg_5% reduction_dia500_63xBSE

TAPE BB3_monoMg_5% reduction_63xBSE (all dimensions in microns)									
Name	*Roller Scale*	*Total cross sectional Area*	*Core Area*	*Sheath Area*	*Filling Factor (core area/total area)*	*Width*	*Thickness*	*Mean Thickness (Mills)*	*Aspect Ratio [Width/Thickness] Normalized*
BB3_Mg16_63xBSE	16	424798.51	172330.11	252468.40	0.41	2866.80	149.86	0.0059	100.00
BB3_Mg17_63xBSE	17	454614.25	176647.22	277967.03	0.39	2789.00	165.10	0.0065	88.31
BB3_Mg18_63xBSE	18	501759.92	240283.39	261476.53	0.48	2782.90	182.88	0.0072	79.55
BB3_Mg19_63xBSE	19	534569.52	263763.85	270805.67	0.49	2642.43	205.74	0.0081	67.14
BB3_Mg20_63xBSE	20	566874.89	297732.27	269142.62	0.53	2556.14	226.06	0.0089	59.11
BB3_Mg21_63xBSE	21	593063.01	345736.35	247326.66	0.58	2459.98	246.38	0.0097	52.19
BB3_Mg22_63xBSE	22	643357.78	342336.87	301020.91	0.53	2447.31	269.24	0.0106	47.52
BB3_Mg23_63xBSE	23	716899.26	362571.27	354328.00	0.51	2516.98	292.10	0.0115	45.04
BB3_Mg24_63xBSE	24	855840.11	239368.87	616471.24	0.28	2806.44	312.42	0.0123	46.96
BB3_Mg25_63xBSE	25	774944.16	406780.45	368163.71	0.52	2383.29	335.28	0.0132	37.16
BB3_Mg26_63xBSE	26	818001.00	361730.92	456270.08	0.44	2330.03	363.22	0.0143	33.53
BB3_Mg27_63xBSE	27	840499.08	433333.97	407165.11	0.52	2273.73	383.54	0.0151	30.99
BB3_Mg28_63xBSE	28	887080.72	441276.13	445804.59	0.50	2269.99	406.40	0.016	29.20
BB3_Mg29_63xBSE	29	908791.53	404415.94	504375.60	0.45	2197.32	431.80	0.017	26.60
BB3_Mg30_63xBSE	30	929862.69	515424.97	414437.72	0.55	2100.23	464.82	0.0183	23.62
BB3_Mg32_63xBSE	32	1009067.50	574760.49	434307.01	0.57	2104.81	505.46	0.0199	21.77
BB3_Mg34_63xBSE	34	1007862.27	556486.97	451375.30	0.55	1979.00	541.02	0.0213	19.12
BB3_Mg35_63xBSE	35	1043044.63	586607.82	456436.80	0.56	1986.50	558.80	0.022	18.58

Table 21. (continued)

Name	*Roller Scale*	*Total cross sectional Area*	*Core Area*	*Sheath Area*	*Filling Factor (core area/total area)*	*Width*	*Thickness*	*Mean Thickness (Mills)*	*Aspect Ratio [Width/Thickness] Normalized*
BB3_Mg36_63xBSE	36	1068491.60	581669.92	486821.68	0.54	1939.68	589.28	0.0232	17.21
BB3_Mg39_63xBSE	39	1094602.43	566856.20	527746.23	0.52	1799.21	660.40	0.026	14.24
BB3_Mg41_63xBSE	41	1142533.52	575493.19	567040.33	0.50	1780.21	701.04	0.0276	13.27
BB3_Mg42_63xBSE	42	1150471.03	593553.94	556917.09	0.52	1739.61	726.44	0.0286	12.52
BB3_Mg43_63xBSE	43	1172890.44	595599.35	577291.10	0.51	1721.37	751.84	0.0296	11.97
BB3_Mg45_63xBSE	45	1178877.75	607225.84	571651.91	0.52	1636.91	805.18	0.0317	10.63
BB3_Mg48_63xBSE	48	1190330.17	599044.21	591285.96	0.50	1553.25	871.22	0.0343	9.32
BB3_Mg50_63xBSE	50	1205511.87	617643.26	587868.60	0.51	1508.40	919.48	0.0362	8.58
BB3_Mg53_63xBSE	53	1223244.40	628135.22	595109.18	0.51	1460.75	977.90	0.0385	7.81
BB3_Mg58_63xBSE	58	1270459.58	652448.09	618011.49	0.51	1424.45	1061.72	0.0418	7.01

Table 22. Image analysis results for tape, BB5_multi_Mgfilament_Mgtube_5% reduction_dia500_63xBSE

TAPE BB5_multi_Mg filament_Mg tube_5% reduction_dia500_63xBSE (all dimensions in microns)									
Name	*Roller Scale*	*Total cross sectional Area*	*Core Area*	*Sheath Area*	*Filling Factor (core area/total area)*	*Width*	*Thickness*	*Mean Thickness (Mills)*	*Aspect Ratio [Width/Thickness] Normalized*
BB5_Mg17_63xBSE	17	439309.07	79579.75	359729.32	0.18	2963.62	149.86	0.0059	100.00
BB5_Mg18_63xBSE	18	462404.42	125626.25	336778.17	0.27	2753.67	170.18	0.0067	81.82
BB5_Mg19_63xBSE	19	481248.36	127633.70	353614.66	0.27	2635.24	185.42	0.0073	71.87
BB5_Mg20_63xBSE	20	554661.76	115597.23	439064.53	0.21	2676.22	210.82	0.0083	64.19
BB5_Mg21_63xBSE	21	601366.13	137512.17	463853.97	0.23	2623.61	233.68	0.0092	56.77
BB5_Mg22_63xBSE	22	641718.26	146989.14	494729.12	0.23	2580.96	254.00	0.01	51.38
BB5_Mg23_63xBSE	23	668449.84	180580.90	487868.95	0.27	2495.62	274.32	0.0108	46.00
BB5_Mg24_63xBSE	24	726849.28	197995.78	528853.50	0.27	2509.60	297.18	0.0117	42.70

Table 22. (continued)

Name	***Roller Scale***	***Total cross sectional Area***	***Core Area***	***Sheath Area***	***Filling Factor (core area/total area)***	***Width***	***Thickness***	***Mean Thickness (Mills)***	***Aspect Ratio [Width/Thickness] Normalized***
BB5_Mg25_63xBSE	25	754646.51	188895.24	565751.27	0.25	2444.98	317.50	0.0125	38.94
BB5_Mg26_63xBSE	26	800455.02	200630.60	599824.42	0.25	2424.83	340.36	0.0134	36.03
BB5_Mg27_63xBSE	27	827227.36	228409.07	598818.29	0.28	2355.43	363.22	0.0143	32.79
BB5_Mg28_63xBSE	28	806633.32	245246.79	561386.54	0.30	2159.03	388.62	0.0153	28.09
BB5_Mg29_63xBSE	29	890876.08	247245.90	643630.18	0.28	2253.36	411.48	0.0162	27.69
BB5_Mg30_63xBSE	30	923797.95	257057.41	666740.54	0.28	2208.29	436.88	0.0172	25.56
BB5_Mg32_63xBSE	32	1004677.31	276488.15	728189.17	0.28	2195.84	480.06	0.0189	23.13
BB5_Mg34_63xBSE	34	1073296.67	279056.05	794240.62	0.26	2144.91	528.32	0.0208	20.53
BB5_Mg35_63xBSE	35	1067657.62	294789.64	772867.98	0.28	2046.98	553.72	0.0218	18.69
BB5_Mg36_63xBSE	36	1097853.32	305077.97	792775.35	0.28	2012.27	581.66	0.0229	17.49
BB5_Mg39_63xBSE	39	1117621.33	308239.72	809381.61	0.28	1870.77	645.16	0.0254	14.66
BB5_Mg41_63xBSE	41	1168208.04	315249.17	852958.87	0.27	1839.16	690.88	0.0272	13.46
BB5_Mg42_63xBSE	42	1215480.28	319540.17	895940.11	0.26	1845.20	718.82	0.0283	12.98
BB5_Mg43_63xBSE	43	1191336.39	322509.56	868826.83	0.27	1755.60	746.76	0.0294	11.89
BB5_Mg45_63xBSE	45	1207764.69	338586.09	869178.59	0.28	1689.78	795.02	0.0313	10.75
BB5_Mg48_63xBSE	48	1219458.02	335733.79	883724.23	0.28	1597.39	863.60	0.034	9.35
BB5_Mg50_63xBSE	50	1246615.14	338435.54	908179.60	0.27	1566.07	909.32	0.0358	8.71
BB5_Mg53_63xBSE	53	1204178.13	395556.60	808621.52	0.33	1443.91	975.36	0.0384	7.49
BB5_Mg58_63xBSE	58	1245152.80	393181.09	851971.71	0.32	1393.89	1069.34	0.0421	6.59

Table 23. Image analysis results for tape, BB7_multi_Agfilament_Mgtube_5% reduction_dia500_63xBSE

TAPE BB7_multi_Ag filament_Mg tube_5% reduction_dia500_63xBSE (all dimensions in microns)									
Name	Roller Scale	Total cross sectional Area	Core Area	Sheath Area	Filling Factor (core area/total area)	Width	Thickness	Mean Thickness (Mills)	Aspect Ratio [Width/Thickness] Normalized
BB7_Ag16_63xBSE	16	441863.28	124408.00	317455.29	0.28	3030.96	147.32	0.0058	100.00
BB7_Ag17_63xBSE	17	448997.05	119157.19	329839.87	0.27	2884.93	157.48	0.0062	89.04
BB7_Ag18_63xBSE	18	501767.78	111344.77	390423.01	0.22	2782.95	182.88	0.0072	73.96
BB7_Ag19_63xBSE	19	544061.20	176086.41	367974.80	0.32	2721.07	203.20	0.008	65.09
BB7_Ag20_63xBSE	20	586923.87	210663.68	376260.19	0.36	2733.77	218.44	0.0086	60.83
BB7_Ag21_63xBSE	21	648968.96	224293.52	424675.45	0.35	2769.32	238.76	0.0094	56.38
BB7_Ag22_63xBSE	22	691720.26	224979.80	466740.47	0.33	2626.94	269.24	0.0106	47.42
BB7_Ag23_63xBSE	23	719490.41	214462.17	505028.24	0.30	2568.36	287.02	0.0113	43.49
BB7_Ag24_63xBSE	24	767536.04	223256.12	544279.93	0.29	2543.38	309.88	0.0122	39.89
BB7_Ag25_63xBSE	25	827130.58	226551.87	600578.71	0.27	2520.93	337.82	0.0133	36.27
BB7_Ag26_63xBSE	26	820103.79	236207.64	583896.15	0.29	2431.43	347.98	0.0137	33.96
BB7_Ag27_63xBSE	27	874703.98	292203.19	582500.79	0.33	2438.29	370.84	0.0146	31.96
BB7_Ag28_63xBSE	28	912249.78	250108.75	662141.03	0.27	2387.30	396.24	0.0156	29.28
BB7_Ag29_63xBSE	29	929431.24	291500.98	637930.26	0.31	2294.81	421.64	0.0166	26.45
BB7_Ag30_63xBSE	30	968592.27	300941.30	667650.97	0.31	2250.92	449.58	0.0177	24.34
BB7_Ag32_63xBSE	32	1084333.34	339771.89	744561.45	0.31	2295.54	495.30	0.0195	22.53
BB7_Ag34_63xBSE	34	1045878.57	326904.06	718974.51	0.31	2066.50	535.94	0.0211	18.74
BB7_Ag35_63xBSE	35	1033881.24	331783.97	702097.27	0.32	1970.10	558.80	0.022	17.14
BB7_Ag36_63xBSE	36	1109563.06	390724.15	718838.91	0.35	2009.37	589.28	0.0232	16.57
BB7_Ag39_63xBSE	39	1097006.94	386438.87	710568.07	0.35	1814.63	655.32	0.0258	13.46
BB7_Ag41_63xBSE	41	1140691.42	328623.86	812067.56	0.29	1777.59	701.04	0.0276	12.32
BB7_Ag42_63xBSE	42	1159316.57	303407.10	855909.47	0.26	1756.84	723.90	0.0285	11.80
BB7_Ag43_63xBSE	43	1187884.37	304332.79	883551.58	0.26	1746.13	749.30	0.0295	11.33
BB7_Ag45_63xBSE	45	1147497.20	337848.73	809648.47	0.29	1605.90	800.10	0.0315	9.76

Table 23. (continued)

Name	***Roller Scale***	***Total cross sectional Area***	***Core Area***	***Sheath Area***	***Filling Factor (core area/total area)***	***Width***	***Thickness***	***Mean Thickness (Mills)***	***Aspect Ratio [Width/Thickness] Normalized***
BB7_Ag48_63xBSE	48	1231510.57	341812.70	889697.87	0.28	1604.10	868.68	0.0342	8.98
BB7_Ag50_63xBSE	50	1168906.27	382616.45	786289.82	0.33	1410.33	972.82	0.0383	7.05
BB7_Ag53_63xBSE	53	1195981.38	371947.22	824034.16	0.31	1412.33	998.22	0.0393	6.88
BB7_Ag58_63xBSE	58	1247250.04	386909.70	860340.33	0.31	1400.33	1064.26	0.0419	6.40

Table 24. Image analysis results for wires

WIRES BB4_TRANSVERSE CROSS SECTION (all dimensions in microns)						
Name	***Total cross sectional Area***	***Core Area***	***Sheath Area***	***Filling Factor (core area/total area)***	***Diameter***	***Diameter (Mills)***
BB4_A50_63xBSE_monoAg_dia500	1256647.04	560987.63	695659.41	0.45	1270.00	0.0500
BB4_A54_63xBSE_multi_Agfilament_Mgtube_dia540	1460907.90	526988.57	933919.32	0.36	1371.60	0.0540
BB4_A60_63xBSE_multi_Agfilament_Mgtube_dia600	1778614.98	670278.39	1108336.59	0.38	1524.00	0.0600
BB4_A68_63xBSE_multi_Agfilament_Mgtube_dia680	2308589.47	879618.49	1428970.98	0.38	1727.20	0.0680
BB4_A76_63xBSE_multi_Agfilament_Mgtube_dia760	2851110.29	1135374.30	1715735.99	0.40	1930.40	0.0760
BB4_M50_63xBSE_monoMg_dia500	1240101.46	585132.75	654968.72	0.47	1270.00	0.0500
BB4_M60_63xBSE_multiMg_dia600	1817034.53	564083.61	1252950.92	0.31	1524.00	0.0600
BB4_M76_63xBSE_multiMg_dia760	2873444.92	805029.82	2068415.11	0.28	1930.40	0.0760
BB4_M86_63xBSE_multi_Mgfilament_Agtube_dia860	3607813.46	1083584.20	2524229.27	0.30	2184.40	0.0860
BB4_M96_63xBSE_multi_Mgfilament_Agtube_dia960	4658795.10	1334906.92	3323888.18	0.29	2438.40	0.0960
BB4_H48_63xBSE_monoAg_hexagonalfilament	1093785.93	465920.42	627865.51	0.43	1219.20	0.0480

Graphic depiction of change of tape parameters (in tables above) evaluated by binary image analysis can be all seen in Appendix 4, and the following five plots are given as examples:

For *B1_monoAg_25% reduction*, i.e., mono filament Ag sheath tape with 25% constant reduction ratio, Fig.72 exhibits the change in cross sectional area. From the first step of rolling operation scaled as #46 to the last step #16, the cross section showed a very smooth transition. Until the middle deformation step, the overall area chance looks linear. Starting with step #31 down to the final step, reduction of tape area shows acceleration. The area of the mono core is always greater than that of the surrounding Ag sheath and both diminish along a soft transition in accord.

Fig.73 demonstrates a very similar reduction for the overall cross sectional area of *B1_monoMg_25% reduction* tape. Because of the work hardening nature of the 0.02%Mg-Ag alloy, deformations of the sheath and the mono core do not look in harmony as much as that of the Ag sheath tape despite the same rolling schedule applied. However, when taken into account one by one, the reduction curves of Mg and Ag metal sheaths are found quite similar.

For both of the sheaths the tape width shows an almost linear variation, stable increase from the first step to the last. Tape thickness is also observed to change consistently in a linear manner (Figures 74-75).

In terms of all area related changes and thickness/width variations, the same deformation regime resulted in almost the same dimensions for mono core Ag and Mg sheaths. The normalized aspect ratio plot seen in Fig.76 is a nice submission for this statement.

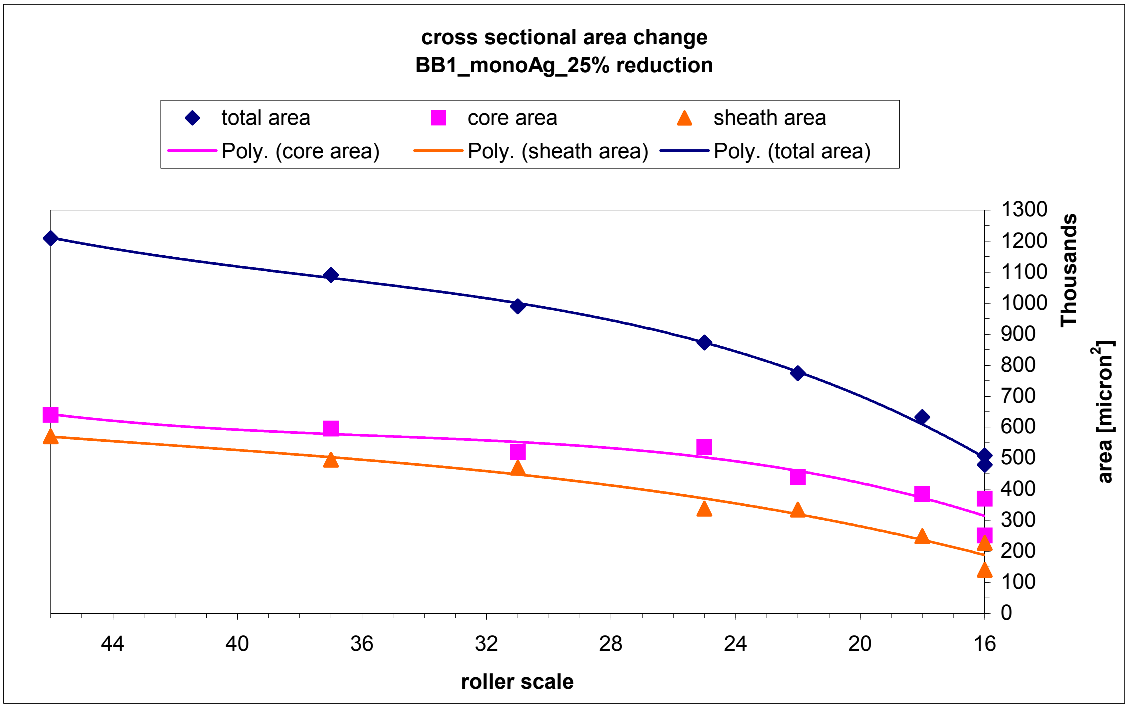

Fig.72 Area change for BB1 monofilament Ag sheath tape, 25% constant reduction/pass, 0.0500” dia.

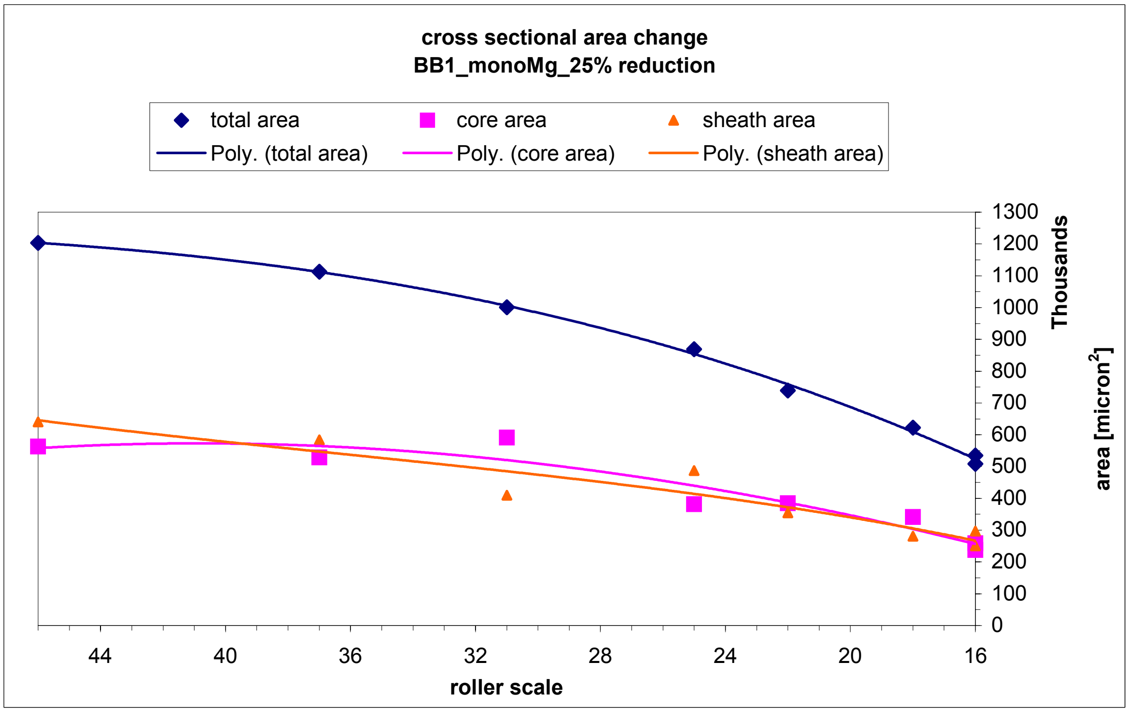

Fig.73 Area change for BB1 monofilament Mg sheath tape, 25% constant reduction/pass, 0.0500” dia.

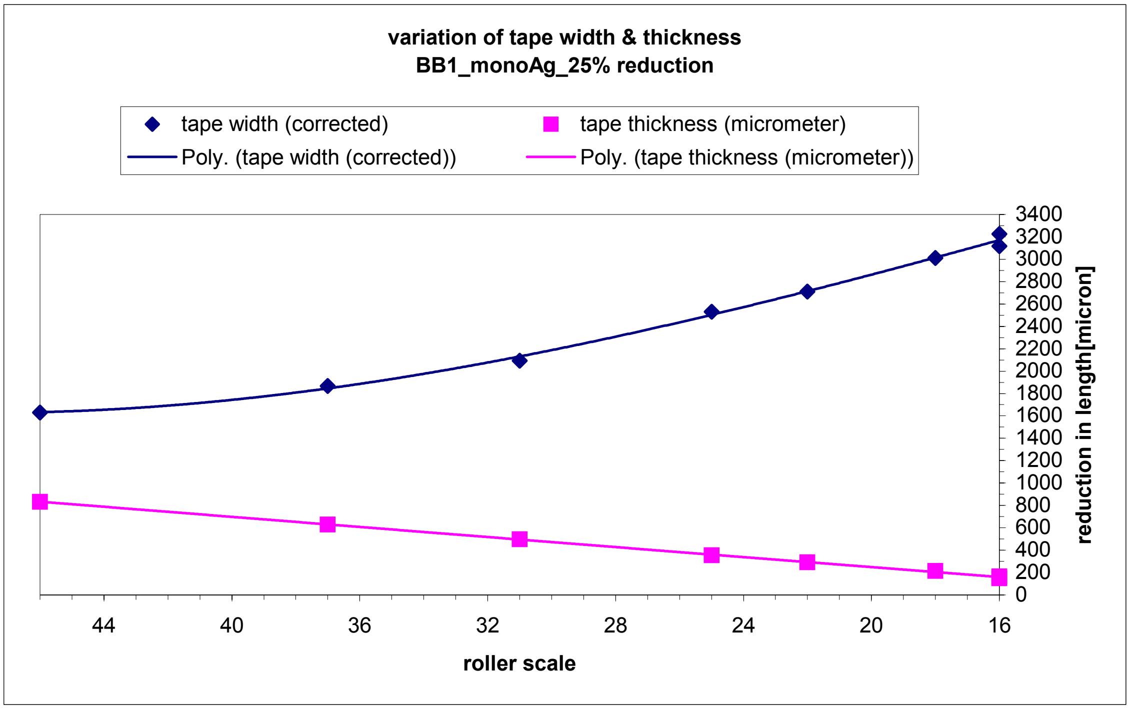

Fig.74 Width and thickness change for BB1 monofilament Ag sheath tape, 25% constant reduction/pass, 0.0500” dia.

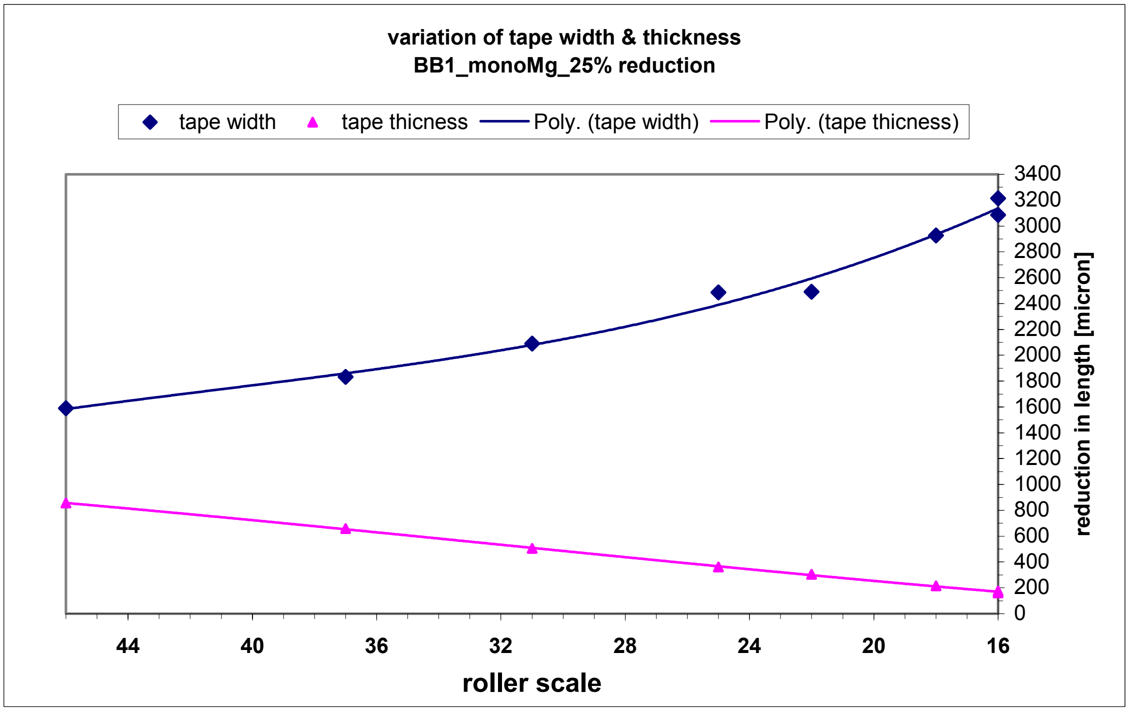

Fig.75 Width and thickness change for BB1 monofilament Mg sheath tape, 25% constant reduction/pass, 0.0500” dia.

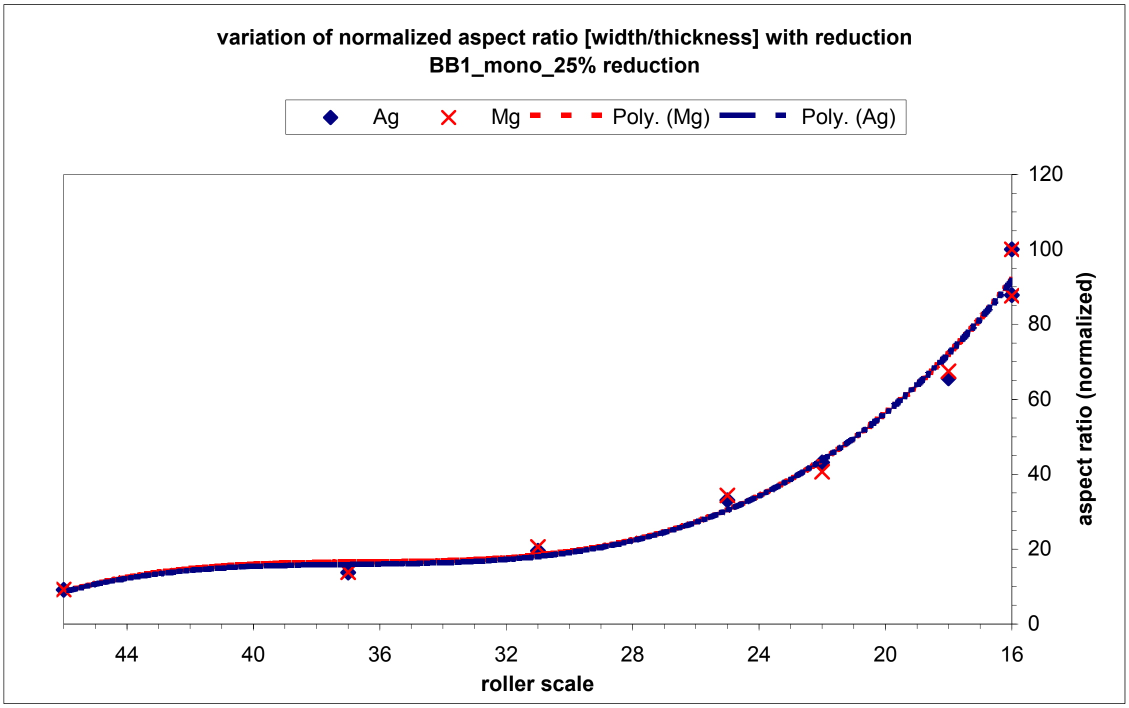

Fig.76 Normalized aspect ratio for BB1 monofilament Ag and Mg sheath tapes, 25% constant reduction/pass, 0.0500” dia.

When the rest of the plots for the other tapes with distinct sheath material composition deformed through various deformation regimes (refer to Table 8 and Appendix 2) are verified, these conclusions can be reached:

Ag filament-Ag tube, Ag filament-Mg tube and *Mg filament-Mg tube* multifilament tapes deformed with *25% constant reduction* per pass regime (*BB2a, BB6*) results are given in Figures A2.6-8, and A2.17-21, respectively. Having the advantage of malleable pure silver filaments and outer tube, Ag filament-Ag tube tape exhibits a linear reduction in overall cross sectional area. While the core area seems to remain almost the same throughout the whole deformation procedure, pure Ag sheath reduction curve looks in accord with the total area curve. Ag filament-Mg tube multifilament tape also displays a similar curve for the total area and sheath area values. Only, core area makes a slight drop at the last rolling step. This could be due to image processing vagueness. Having different materials for filament cladding and outer tube, this multifilament tape was hard to draw.

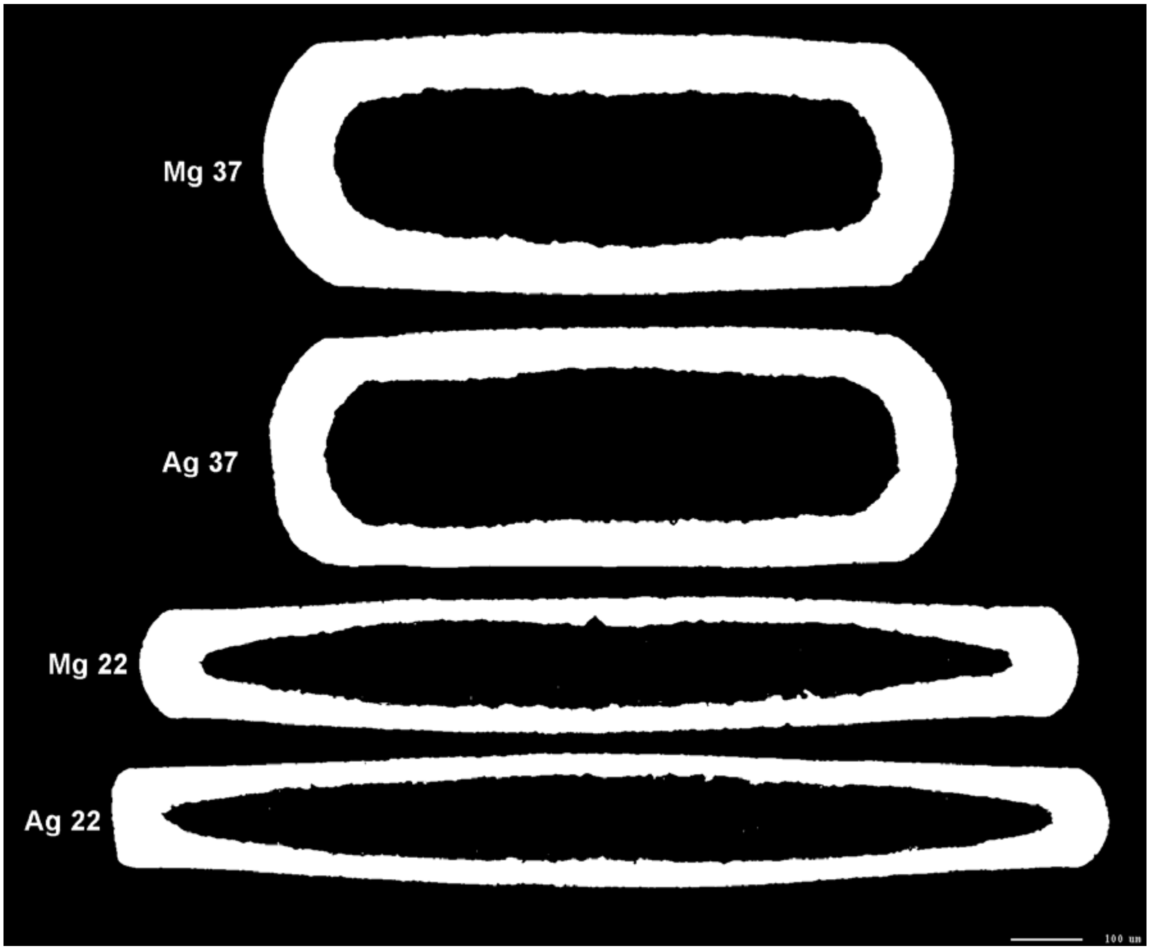

Fig.77 Binary image comparison for aspect ratio variation of monofilament tapes (*BB1*) with pure silver and Mg/Ag alloy sheaths deformed by 25% constant reduction per pass. Rolling steps corresponding to the images are denoted by numbers.

Mg filament-Mg tube tape shows a similar deformation trend as those of the latter two, but there is a fluctuation in the core area curve, most probably because of image processing ambiguity. For this tape, the sheath area also rises and falls, getting closer to core area at the steps #22 and #25. Normalized aspect ratio (width/thickness) curves of Ag filament-Mg tube and Ag filament-Ag tube multifilament tapes are almost the same. By roller reduction-scale-step #25, the aspect ratio curve shows an increasing slope, i.e., noticeable increase in width with respect to thickness. Intermediate steps demonstrate a constant slope, no change in the dimensions ratio. Meanwhile, Mg filament-Mg tube tape has greater aspect ratio values at every reduction step compared to the other tapes mentioned. This means, Mg filament-Mg tube tape deformed into wider shapes at the same order of thickness compared to the latter two.

The final diameters of mono and multifilament superconductor wires did not seem to follow a standard according to the broad literature survey. Thus, the tapes fabricated out of these wires so far all had a different starting dimension (diameter). The effects of various deformation regimes (rolling and drawing) were put under investigation by many researchers; however, nobody came up with research regarding final size of wires before tape fabrication and final size of tapes for better superconductor properties. Therefore, two multifilament wires with the same composition (*BB2a* and *BB2b*, *Ag filament-Ag tube*) having *0.0500”* and *0.0600” diameters* were rolled through the same deformation regime (*25% constant reduction per pass*) to observe if it made any difference, eventually. Tapes, *BB2a-0.0500” dia* and *BB2b-0.0600” dia*, display similar deformation trend in all curves (Figures. A2.6-10). In 0.0500” dia tape, the final ratio of core area to total area is 2:5, whilst, in 0.0600” tape this ratio is 1:5. This can be inferred as more freedom for the powder inside the larger wire to deform and contour itself along with the silver sheath as the rolling procedure furthered. On the other hand, the resistance of the powder to deformation must have been already greater in the thinner wire and this resulted in the sheath taking larger part of the simultaneous deformation. The 0.0500” dia tape also ended up with a larger cross section for the same final thickness as the other one. Fig.A2.10 is a good indication of width/thickness variation for different dia wires rolled under same deformation rate. Starting with the step #37 down to #18, the tape with 0.0500” seems to expand less than the tape with 0.0600” due to its more compact initial state before rolling.

Ag filament-Mg tube and *Mg filament-Mg tube* multifilament tapes deformed with *5% constant reduction* per pass regime (*BB7* and *BB5*, respectively) results are given in Figures A2.22-24 and A2.14-16 (Appendix 2), respectively. Their deformation results all look alike; almost the same fashion for the curves. The core areas show linear variation with a minute slope and the areas for sheath and total cross section display a stable decrease. Looking at the normalized aspect ratio plots (Figures A2.16 and A2.24), it can be said that having Mg tube outside and, either Ag or Mg filaments inside did not make too much of a difference under 5% reduction per pass.

Ag filament-Mg tube and *Mg filament-Mg tube* multifilament tapes deformed with *IR1 varying reduction* per pass regime (*BB8*) results are demonstrated in Figures A2.25-29 (Appendix 2), respectively. As a reminder, IR1 (increasing rolling 1) varying reduction per pass schedule was built up applying different reduction rates consecutively as 5, 10, 15, 20, 25, 30, 35, 40% of the preceding rolling step, instead of keeping the rate constant. It was aimed to see the distinction between the results of a constant reduction rate and a regularly increasing reduction rate for the same type of sheath material.

Both tapes looked akin concerning their total area reduction. However, Ag filament-Mg tube tape winded up with slightly smaller sheath area. The variations of core areas also look comparable to each other. The fluctuation in the core area curve for the Mg filament-Mg tube tape is thought to be due to lack of clarity of a few data points in image processing. As for the aspect ratio, Fig.A2.29 displays very close results for both of the tapes, having the Mg filament-Mg tube one with a slightly wider shape than the other at almost every reduction step of rolling.

If *mono core* tape (*BB3*) is compared to *multifilament* ones (*BB5, BB7*) all deformed with *5% constant reduction per pass*, the first remarkable difference noticed is having larger sheath area than core area in multifilament tapes. On the contrary, mono core tape has a close but nevertheless, smaller sheath area then its core area. The reduction fashion of total area looks very similar on both multifilament tapes and the mono core tape with very close values. Changes in aspect ratio in all tapes also seem very much alike. That is, regardless of being mono or multifilament core, the same deformation regime resulted in almost the same size at every rolling step in terms of tape width/thickness ratio.

If *mono core* tapes (*BB1, Ag and Mg sheath*) are compared to multifilament tapes (*BB2a, BB2b, BB6*) all deformed with *25% constant reduction per pass*, total area reduction looks similar for all, major differences are not seen. The most prominent difference noticed is that, in mono core tapes, the core area is greater than the sheath area, but in multifilament tapes it is the other way around. This can be attributed to the ‘extra sheath’ that naturally came with filament cladding metal in multifilament tapes. As for the aspect ratio, all the tapes exhibit a resembling tendency. The mono core ones display slightly bigger aspect ratio compared to Ag filament-Mg tube and Ag filament-Ag tube multifilament tapes. That is, either the mono core tapes had slightly larger shapes at the same thickness levels as the multifilament ones or the multifilament tapes experienced less deformation at the same rolling steps because of their filaments making them tougher to deform inside.

If *multifilament* tapes (*BB5, BB7*) deformed with *5% constant reduction per pass* are compared to multifilament tapes (*BB8*) deformed with *IR1 varying reduction per pass*, the general view of the area changes appears alike. Ag filament-Mg tube deformed with IR1 reduction (Fig.A2.25) indicates a larger final total area value compared to the tape deformed with 5% reduction (Figures A2.22 and A2.14). Although in 5% reduction tape the core area always remains smaller than the sheath area, in the IR1 reduction tape, the sheath area looks smaller than that of the core. Mg filament-Mg tube tapes display similar curves with each other, as well. 5% reduction tape ends up with smaller total area then its IR1 reduction counterpart. IR1 reduction tape also displays smaller sheath area than its core area corresponding the last two rolling steps opposed to those of 5% reduction tape. As for the aspect ratio for the Ag filament-Mg tube tapes (Figures A2.24, A2.29), starting by the middle rolling steps and going down to the last ones, the width/thickness ratio of IR1 reduction tape always looks smaller than that of 5% reduction tape. This means, under the ideal deformation condition of having the same thickness at the same rolling step, 5% tapes acquired larger width than the IR1 tapes did. Just the same aspect ratio drift is observed between the 5% and IR1 tapes with Mg filament-Mg tube composition (Figures A2.29, A2.16).

If *multifilament* tapes (*BB6*) deformed with *25% constant reduction per pass* are compared to multifilament tapes (*BB8*) deformed with *IR1 varying reduction per pass*, all the curves show variations akin to themselves. There is no distinctive detail seen but the greatness of the core area over sheath for the last two steps of rolling in IR1 tapes. Regarding the aspect ratio, Mg filament-Mg tube tape with IR1 reduction appears to have a steeper slope then its counterpart for 25% reduction tape. That is, after rolling step #38, there was a rapid increase in width in the IR1 tape compared to 25% tape. The same tendency can also be stated for the Ag filament-Mg tube tapes with 25% and IR1 reduction regimes, respectively.

Another aspect of the image processing by means of SEM included the qualitative analysis through BSE pictures and EDS diffraction pattern graphs to identify the elements present in the superconductor core samples analyzed. Fig.78, taken on tape sample *BB2_Mg32*, acts as a guide or a map to the points where EDS search took place. Several points, attributed to as *Dark gray phase, Medium gray phase, Lighter gray phase, Brighter phase, Brightest phase, 250 micron diameter area, Higher Pb phase* can all be seen on the map picture. Bi, Sr, Ca, Cu, Pb elements were traced and matching of their appearances in the core picture was attempted.

Dark (dk) gray phase (Fig.79) corresponds to point *A* on the guide picture and Cu was observed as the dominant element, probably as part of some CuO. *Medium (med) gray phase* (Fig.80) corresponds to point *B* on the guide picture. Bi appeared as the dominant element at this spot, and Sr was found to be almost plentiful. *Brightest phase* (Fig.81) corresponds to point *C* on the guide picture. Bi was recognized as the dominant element.

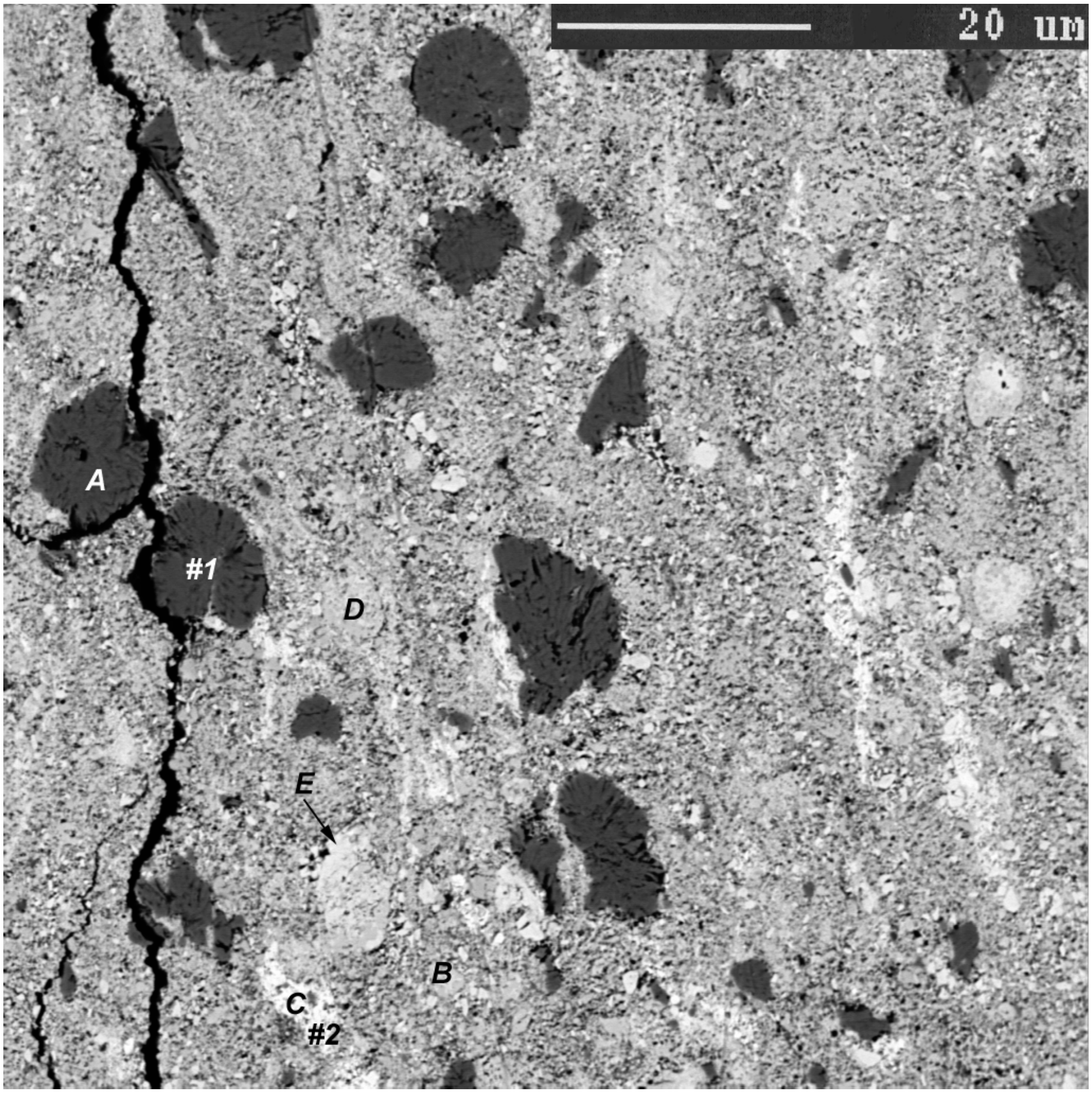

Fig.78 Guide picture for points where EDS and WDS analysis took place on tape sample BB2_Mg32. Point *A* is the *dk gray phase,* point *B* is the *med gray phase,* point *C* is the *brightest phase,* point *D* is the *lighter gray phase,* point *E* is the *brighter phase*.

Lighter gray phase (Fig.82) corresponds to point *D* on the guide picture. Bi found as the dominant element, Sr was almost as abundant. *Brighter phase* (Fig.83) corresponds to point *E* on the guide picture. Bi appeared to be the dominant element, Sr was also present. *250-micron diameter area* (Fig.84) corresponds to lighter gray phase point somewhere in the background on the guide picture. Bi was present as the dominant element, Pb and Sr also showed up as the other major elements. *Higher Pb phase*

(Fig.85) corresponds to lighter gray phase point somewhere in the 250-micron diameter area. As clear from the name, Pb was the dominant element, accompanied by Sr.

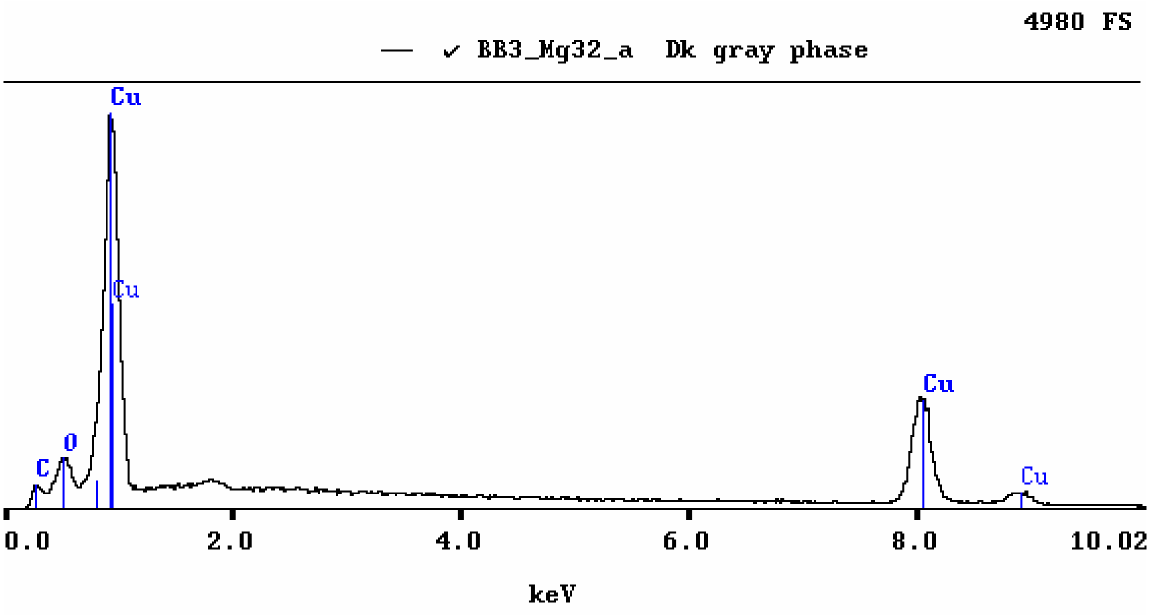

Fig.79 EDS diffraction pattern for *dark (dk) gray phase.* Corresponds to point *A* on the guide picture. Cu is the dominant element.

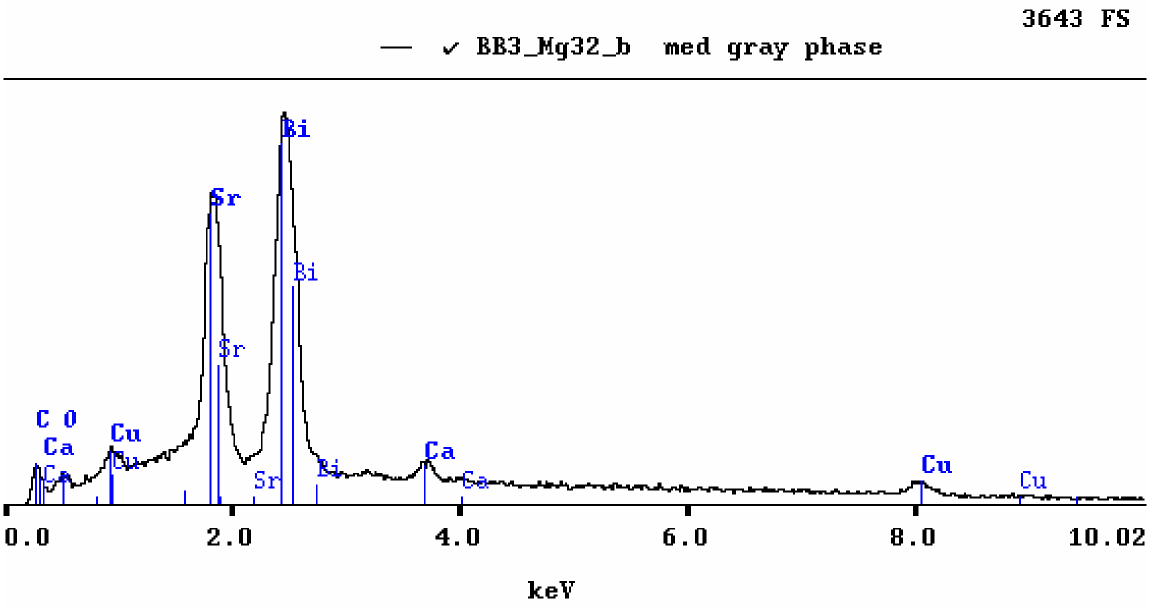

Fig.80 EDS diffraction pattern for *medium (med) gray phase.* Corresponds to point *B* on the guide picture. Bi is the dominant element, Sr comes next.

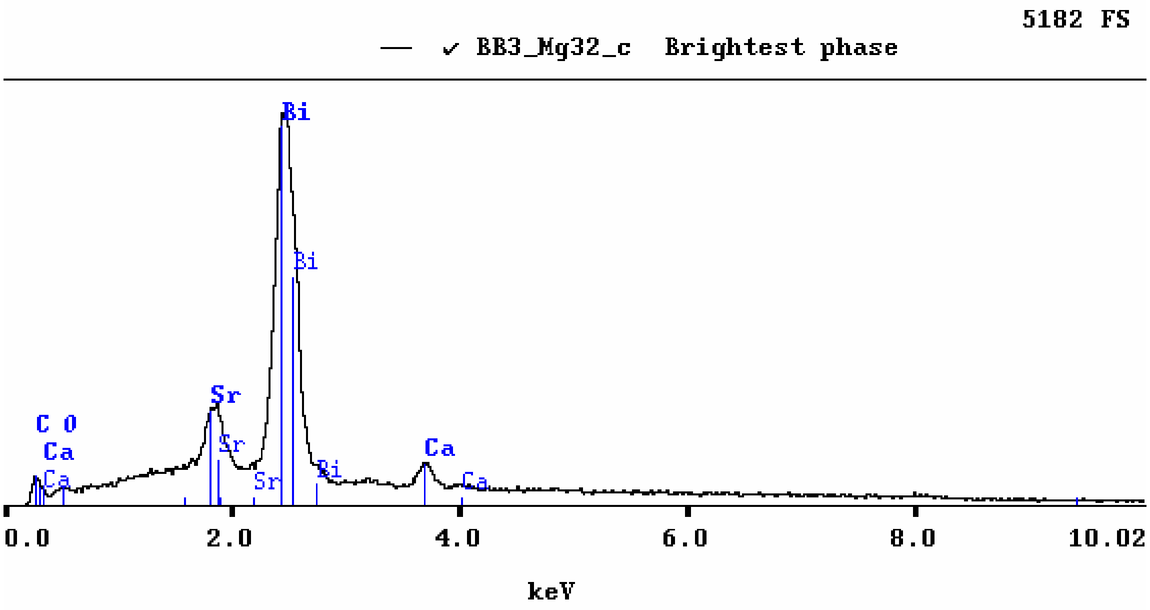

Fig.81 EDS diffraction pattern for *brightest phase.* Corresponds to point *C* on the guide picture. Bi is the dominant element.

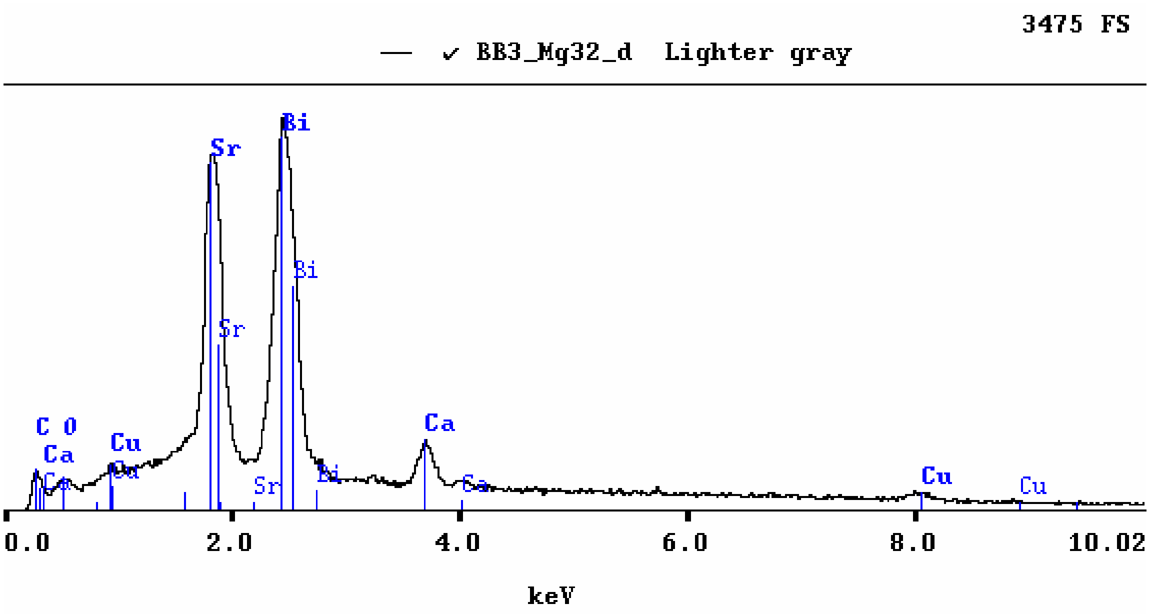

Fig.82 EDS diffraction pattern for *lighter gray phase.* Corresponds to point *D* on the guide picture. Bi is the dominant element, Sr is almost as abundant.

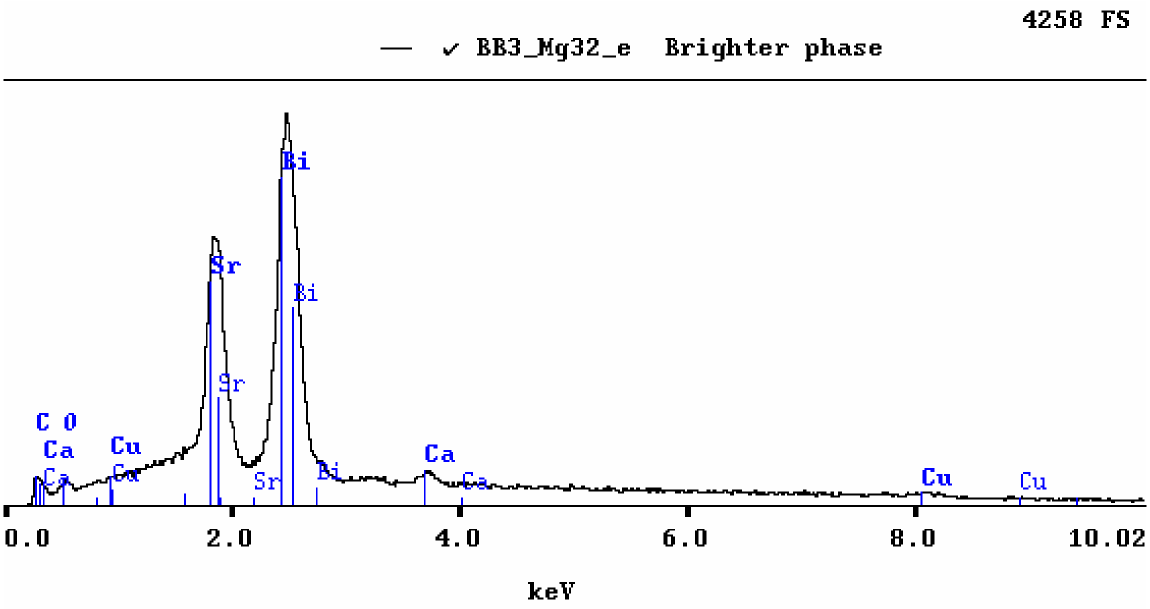

Fig.83 EDS diffraction pattern for *brighter phase.* Corresponds to point *E* on the guide picture. Bi is the dominant element, Sr also present.

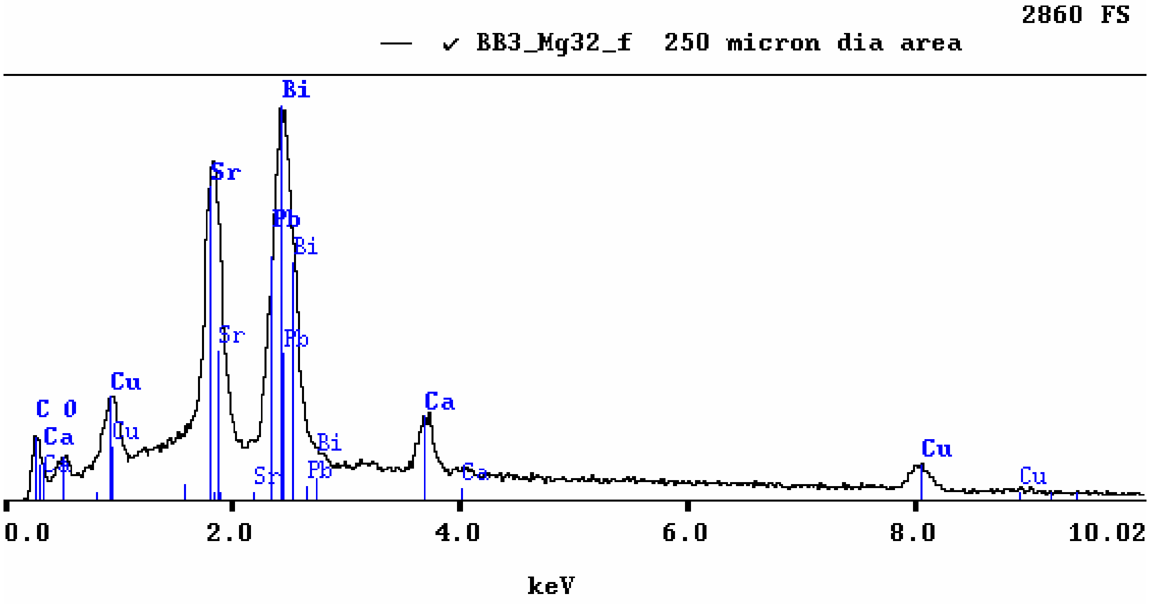

Fig.84 EDS diffraction pattern for *250 micron diameter area.* Corresponds to lighter gray phase point somewhere in the background on the guide picture. Bi is the dominant element; Pb and Sr also show up as the other major elements.

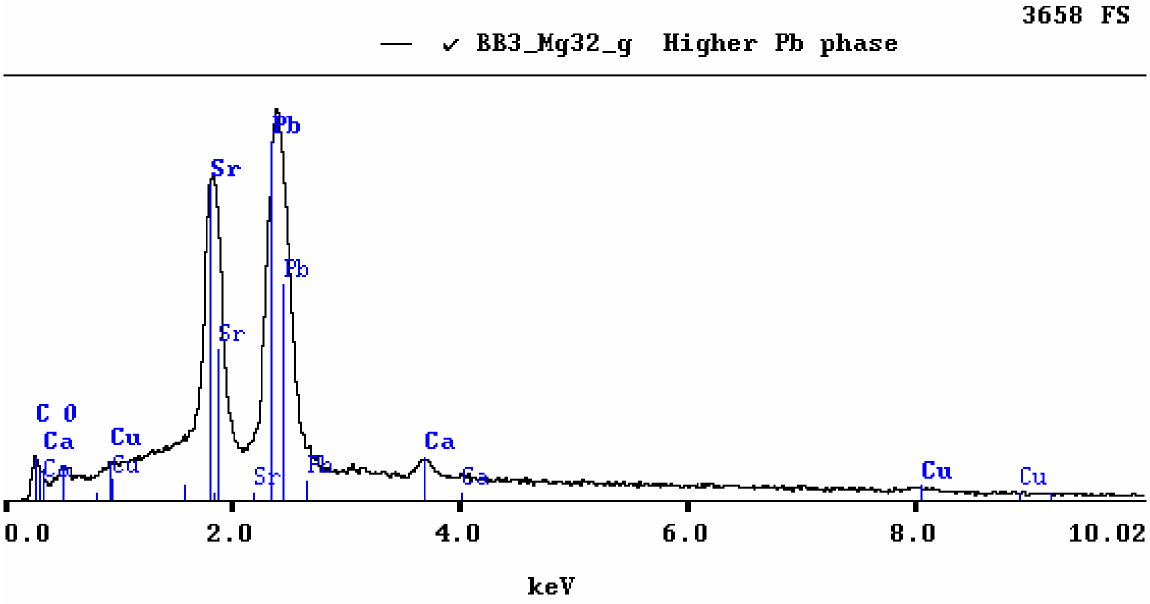

Fig.85 EDS diffraction pattern for *higher Pb phase.* Corresponds to lighter gray phase point somewhere in the 250-micron diameter area. Pb is the dominant element, Sr also present.

For WDS analysis, the standards used were Cu, $CaSiO_3$, $SrTiO_3$, PbS, Bi_2O_3. X ray maps shown below were all taken at the same region with 4000x zoom factor to clarify the distribution of elements in the background. As an example, the second square on the upper row shows where Cu is most rich on the whole picture.

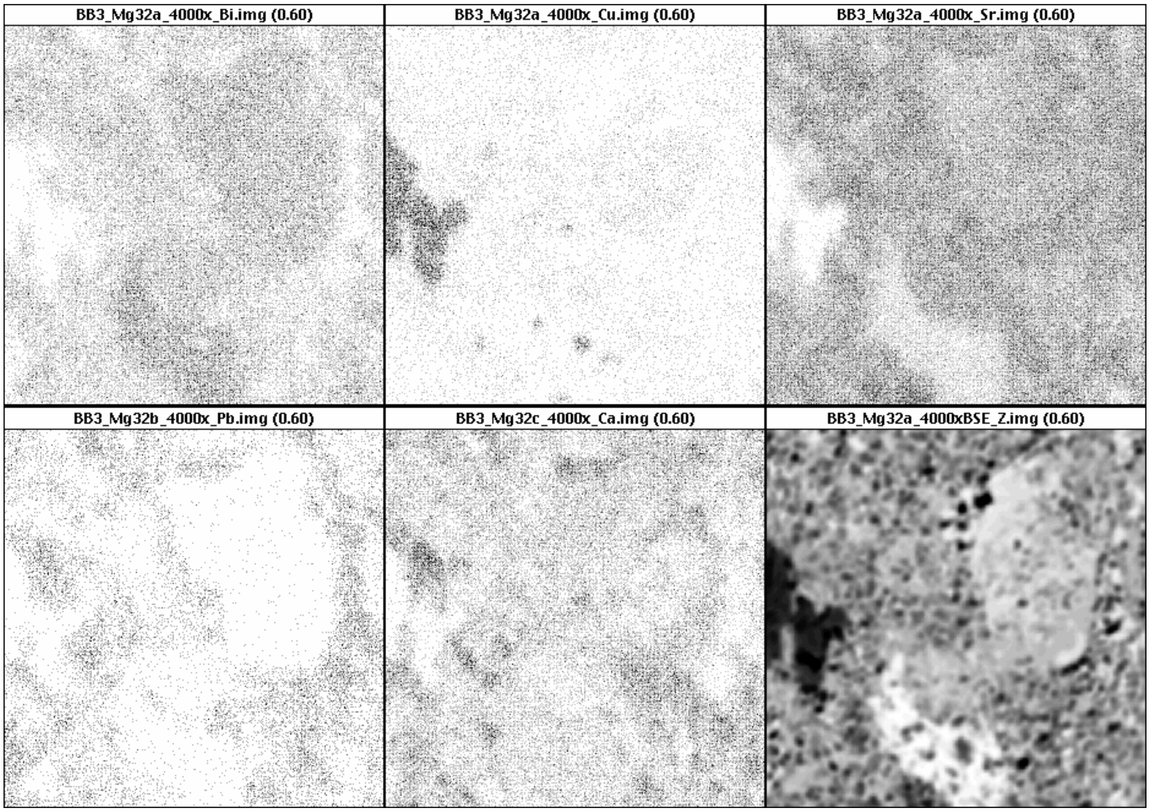

Fig.86 X ray maps for distribution of elements in the background. The areas of cumulated dark spots represent Bi, Cu, Sr, Pb or Ca as the abundant element at that specific part of the background. The square at the right bottom corner is the actual picture with 4000x.

XRD Analysis and Results

XRD (x-ray diffraction) was used to determine the stoichiometry of the powders and the core after heat treatment. XRD standards and their diffraction pattern compatibility plots with respect to our Bi2212 fully reacted powder both under air and oxygen purge were investigated. As an example of matching, standard 46-0431; Calcium Copper Strontium Bismuth Oxide (Bi2212 without Pb doped) plot is given below.

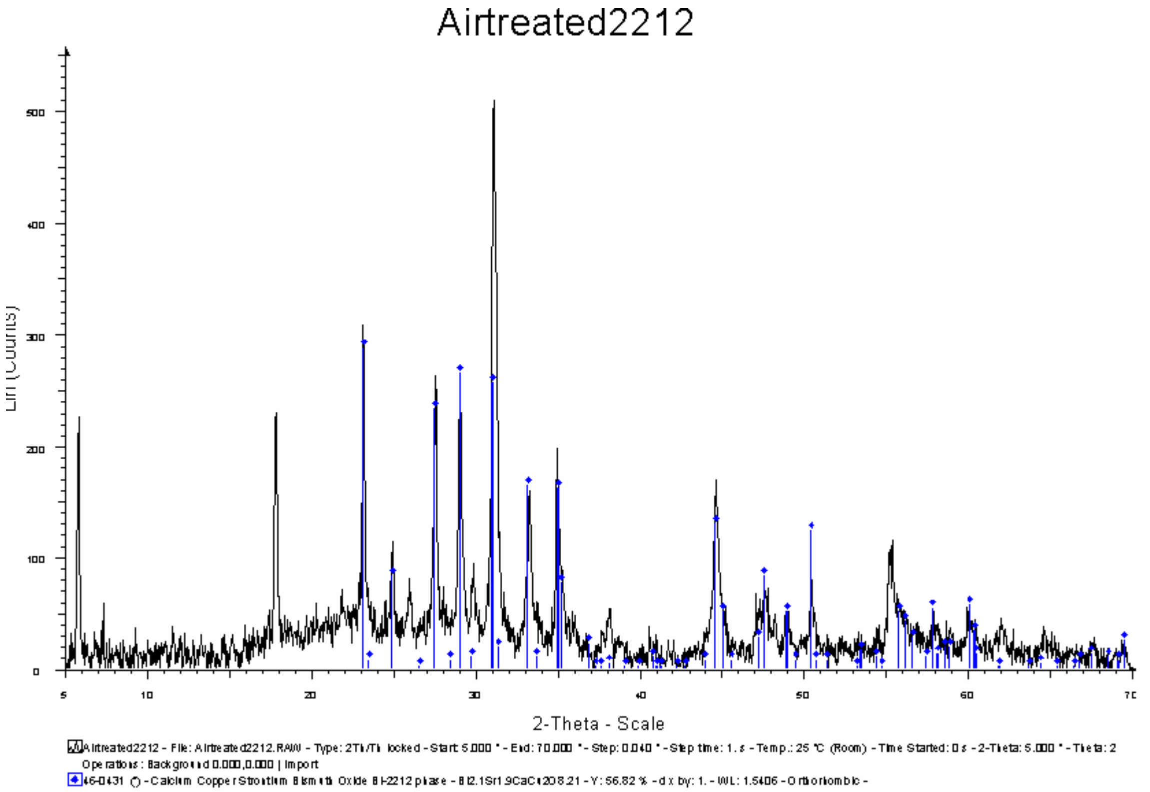

Fig.87 XRD pattern comparison of Bi(Pb)2212 fully reacted powder (black line) and standard 46-0431 Calcium Copper Strontium Bismuth Oxide (blue line).

XRD results comparison of our superconducting core material $Bi_{1.6}(Pb_{0.6})Sr_{1.8}Ca_{1.0}Cu_{2.0}O_{8+x}$ after *Step Solidification Partial Melt* heat treatment revealed very close values with $Bi_{1.72}(Pb_{0.34})Sr_{1.83}Ca_{0.97}Cu_{1.13}O_y$ core material partial melt heat treated in air at 860°C by Jeremie and Flukiger [33].

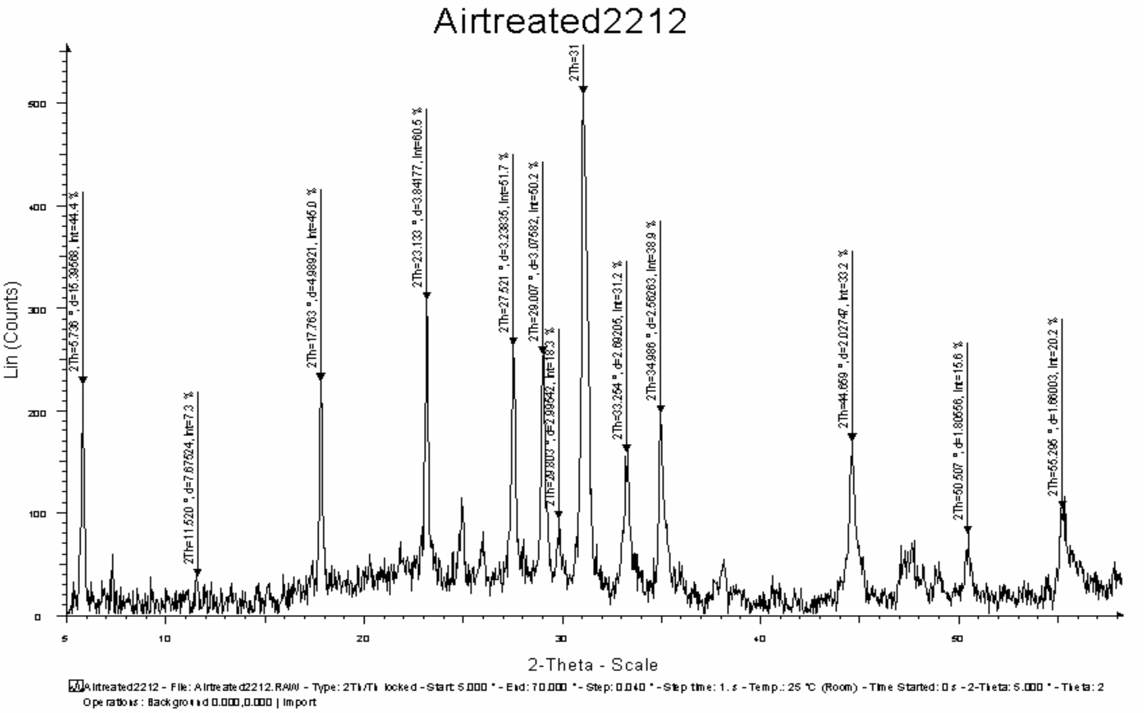

Fig.88 XRD pattern for Bi2212 core after step solidification heat treatment under air purge.

Figures 88 and 48 represent XRD patterns of these samples, respectively. According to XRD results by Jeremie, at 860^{o}C the patterns demonstrated characteristic (Bi,Pb)-2212 with (020) and (200) peaks clearly separated. This was considered as a sign of Pb addition to induce the formation of orthorhombic phase.

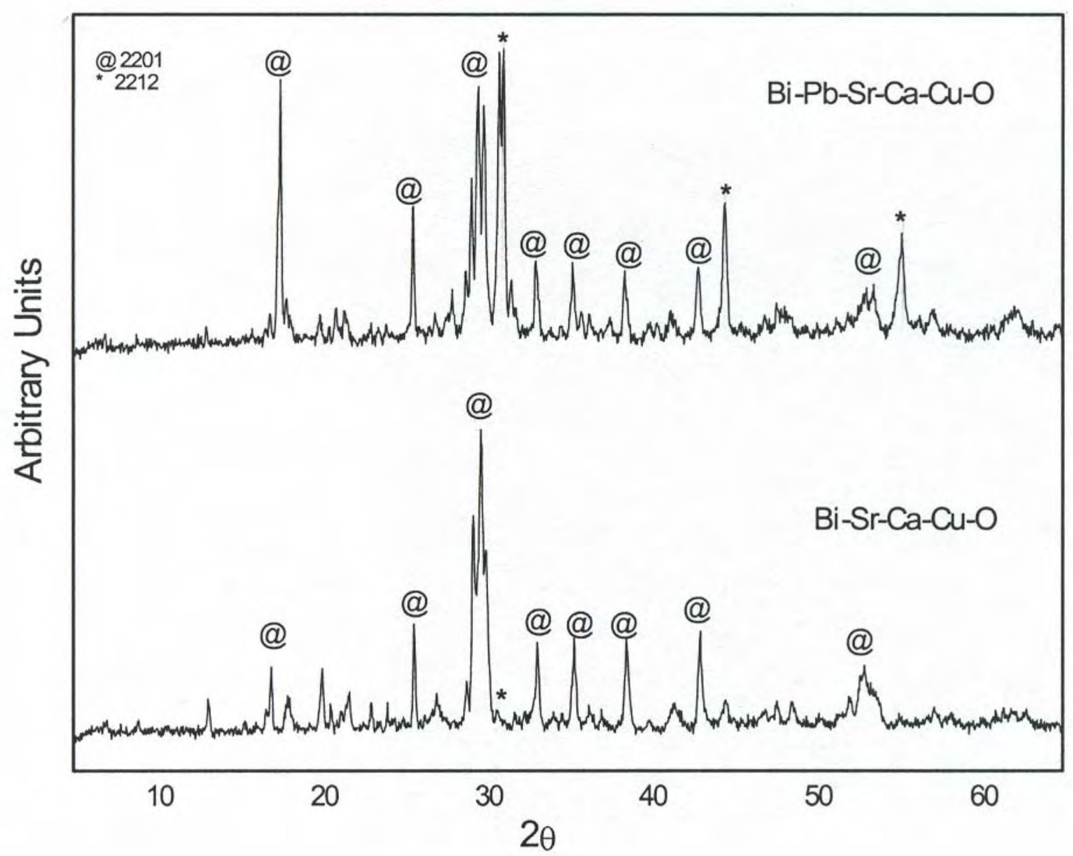

Fig.89 XRD patterns of BiPbSrCaCuO and BiSrCaCuO polycrystalline precursor powders for comparison with XRD pattern for our Bi2212 powder precursor after second calcination [41].

At 840°C, the XRD patterns did not show the same trend for (020) and (200) peaks but the characteristic peaks for Ca_2PbO_4. The researchers found it more beneficial to have the heat treatment at 860°C rather than at 840°C in order to get higher content of Pb dissolved. This dissolving is known by the structural transformation from tetragonal to orthorhombic [33].Analysis of precursor Bi2212 powders preparation, which is narrated in detail under subtitle Bi(Pb)-2212 Powder Preparation, covered four samples.

The first and the second samples were taken after completion of the calcining steps. Both calcining steps took place under air, lasted 10 hours each and were at 600°C and 700°C for first and second steps, respectively. 30 min intermediate grinding followed each step. Table 25 presents the results of analysis in numbers and Fig.90 displays the diffraction peaks for the fist calcination. The plots are drawn for 2θ angle vs. intensity.

XRD analysis results of Ertekin [41] for his Bi(Pb)2212 precursor powder before full heat treatment (Fig.89) shows great similarity to our precursor powder after second calcination (Fig.91).

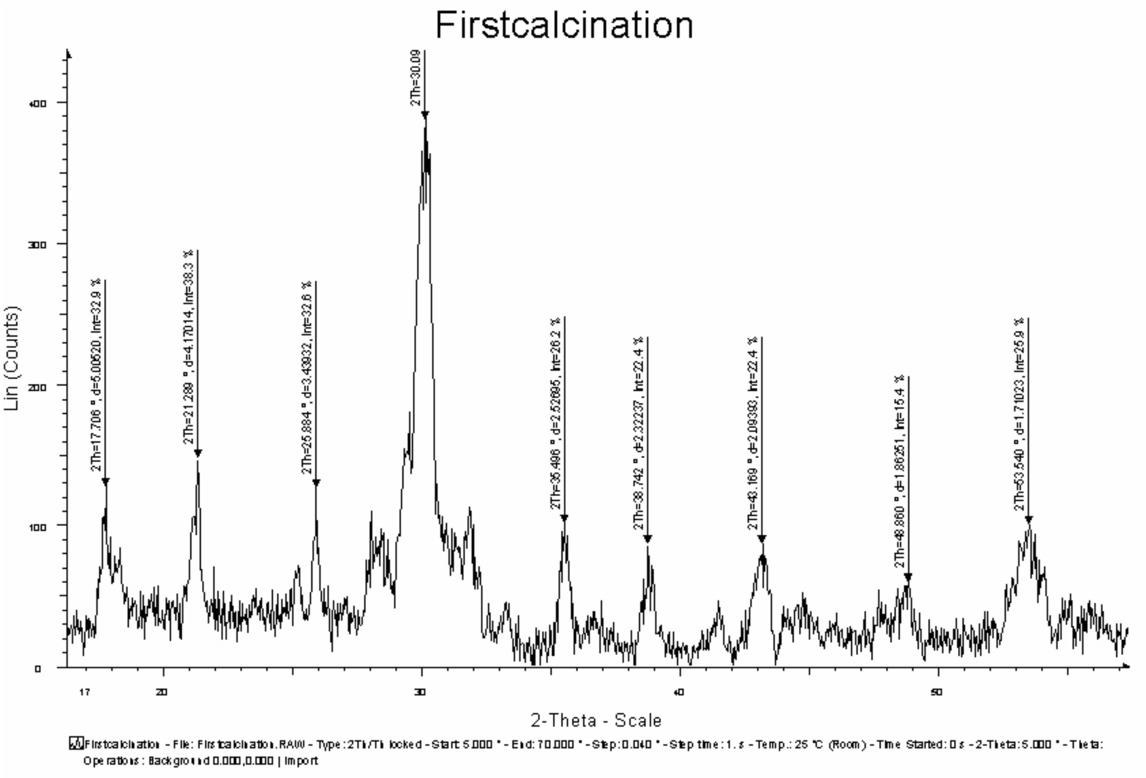

Fig.90 XRD pattern for Bi2212 powder precursor after first calcination.

Table 25. XRD analysis results for Bi2212 powder (after first calcination, not fully reacted).

FIRST CALCINATION Bi 2212 POWDER XRD ANALYSIS RESULTS						
Angle 2-Theta °	***d value angstrom***	***Intensity Count %***	***Intensity %***	***h***	***k***	***l***
30.098	2.96674	100.0	30.098	2.96674	389	100.0
17.706	5.00520	32.9	17.706	5.00520	128	32.9
21.289	4.17014	38.3	21.289	4.17014	149	38.3
25.884	3.43932	32.6	25.884	3.43932	127	32.6
35.496	2.52695	26.2	35.496	2.52695	102	26.2
38.742	2.32237	22.4	38.742	2.32237	87.0	22.4
43.169	2.09393	22.4	43.169	2.09393	87.0	22.4
48.860	1.86251	15.4	48.860	1.86251	59.7	15.4
53.540	1.71023	25.9	53.540	1.71023	101	25.9

Results of the second calcination step are shown in Table 25 and Fig.91.

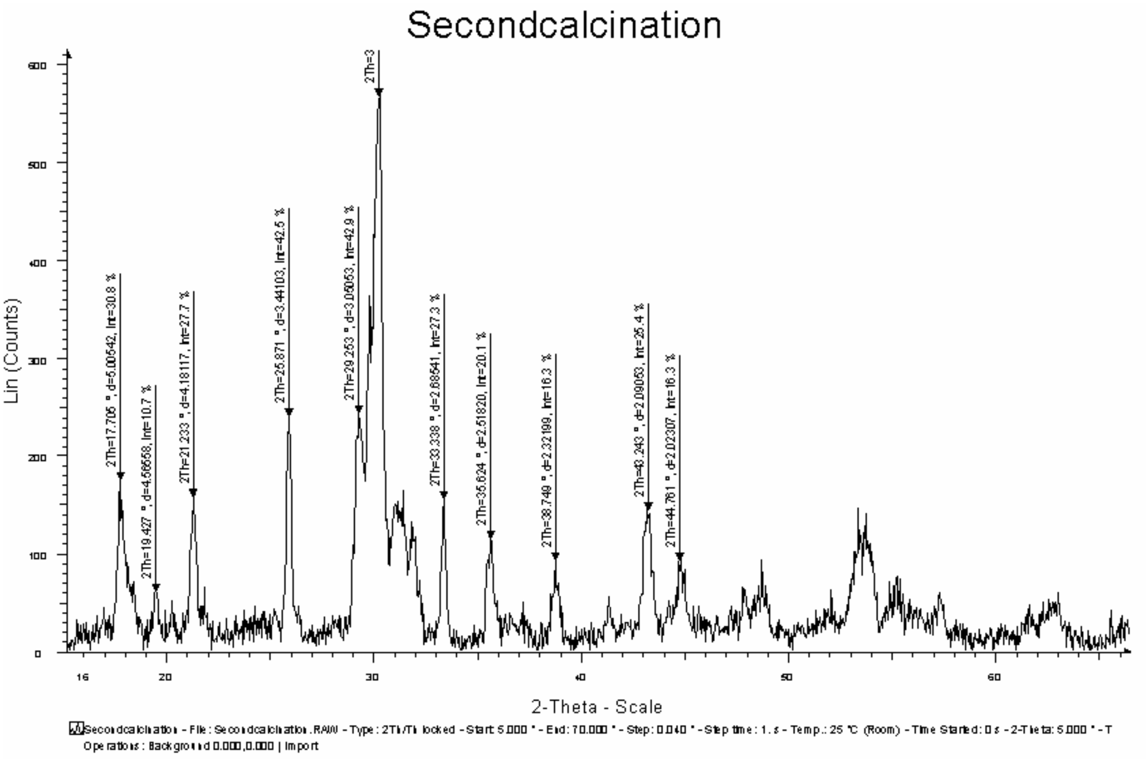

Fig.91 XRD pattern for Bi2212 powder precursor after second calcination.

Table 26. XRD analysis results for Bi2212 powder (after second calcination, not fully reacted).

SECOND CALCINATION Bi 2212 POWDER XRD ANALYSIS RESULTS						
Angle 2-Theta	***d value angstrom***	***Intensity Count %***	***Intensity %***	***h***	***k***	***l***
17.705	5.00542	30.8	17.705	5.00542	175	30.8
19.427	4.56558	10.7	19.427	4.56558	60.7	10.7
21.233	4.18117	27.7	21.233	4.18117	158	27.7
25.871	3.44103	42.5	25.871	3.44103	242	42.5
29.253	3.05053	42.9	29.253	3.05053	244	42.9
30.197	2.95728	100.0	30.197	2.95728	569	100.0
33.338	2.68541	27.3	33.338	2.68541	155	27.3
35.624	2.51820	20.1	35.624	2.51820	114	20.1
38.749	2.32199	16.3	38.749	2.32199	92.6	16.3
43.243	2.09053	25.4	43.243	2.09053	144	25.4
44.761	2.02307	16.3	44.761	2.02307	92.5	16.3

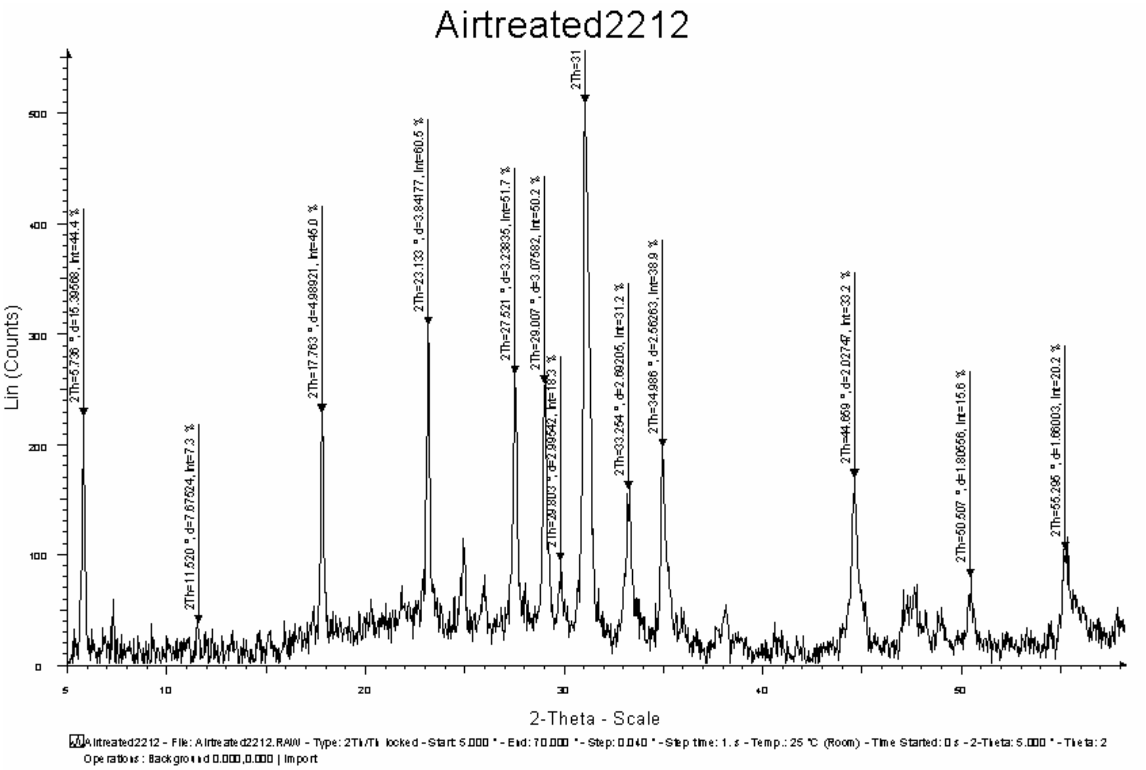

Fig.92 XRD pattern for Bi2212 core after step solidification heat treatment under air purge.

Table 27. XRD analysis results for Bi2212 powder (core) fully reacted (heat treated) under air flow.

AIR TREATED Bi 2212 POWDER (core) XRD ANALYSIS RESULTS						
Angle 2-Theta °	***d value angstrom***	***Intensity Count %***	***Intensity %***	***h***	***k***	***l***
11.520	7.67524	7.3	11.520	7.67524	37.5	7.3
17.763	4.98921	45.0	17.763	4.98921	230	45
23.133	3.84177	60.5	23.133	3.84177	309	60.5
27.521	3.23835	51.7	27.521	3.23835	264	51.7
29.007	3.07582	50.2	29.007	3.07582	256	50.2
29.803	2.99542	18.3	29.803	2.99542	93.7	18.3
31.060	2.87701	100.0	31.060	2.87701	511	100.0
33.254	2.69205	31.2	33.254	2.69205	159	31.2
34.986	2.56263	38.9	34.986	2.56263	198	38.9
44.659	2.02747	33.2	44.659	2.02747	169	33.2
50.507	1.80556	15.6	50.507	1.80556	79.5	15.6
55.295	1.66003	20.2	55.295	1.66003	103	20.2

In order to see the effects of different atmospheres on the full reaction of powders, metal sheath of tapes and wires had to be etched. In order to reveal the reacted cores from tapes and wires, it is the safest way to submerge the composite into a 2.5:1 mixture of NH_2OH and H_2O_2 (30%) [42]. This chemical etched the metal sheaths of a few mm long wires within a couple of hours. After extraction, the cores were collected, dried in air and grounded to prepare XRD samples. For the superconductor core treated under air purge, results are presented in Table 27 and Fig.92.

For the superconductor core treated under oxygen purge, results can be seen in Table 28 and Fig.94.

Fig.93 Close view of a bubbling burst on Bi2212 tape after step solidification heat treatment under oxygen purge.

Bubbling during heat treatment has been cited as a serious problem standing in the way of achieving good quality superconductor core and our experience (Fig.93) was discussed with all the specifics in the related major section. In order to diminish the carbon content of the precursors in hand they were reheated following a schedule suggested by Hellstrom [2]. Tables 29 and 30 along with Figures 95 and 96 give a comparative representation of XRD analysis for fresh and reheated precursor powders in terms of C content. XRD merged graph of original and reheated precursor powders is available in Fig.70. There was not much of a change noticed in the characteristic peak locations and intensities between the two graphs; in other words, the reheating schedule employed did not seem to work for C decrement in reheated powder compared to the original one used with the tapes that experienced bubbling.

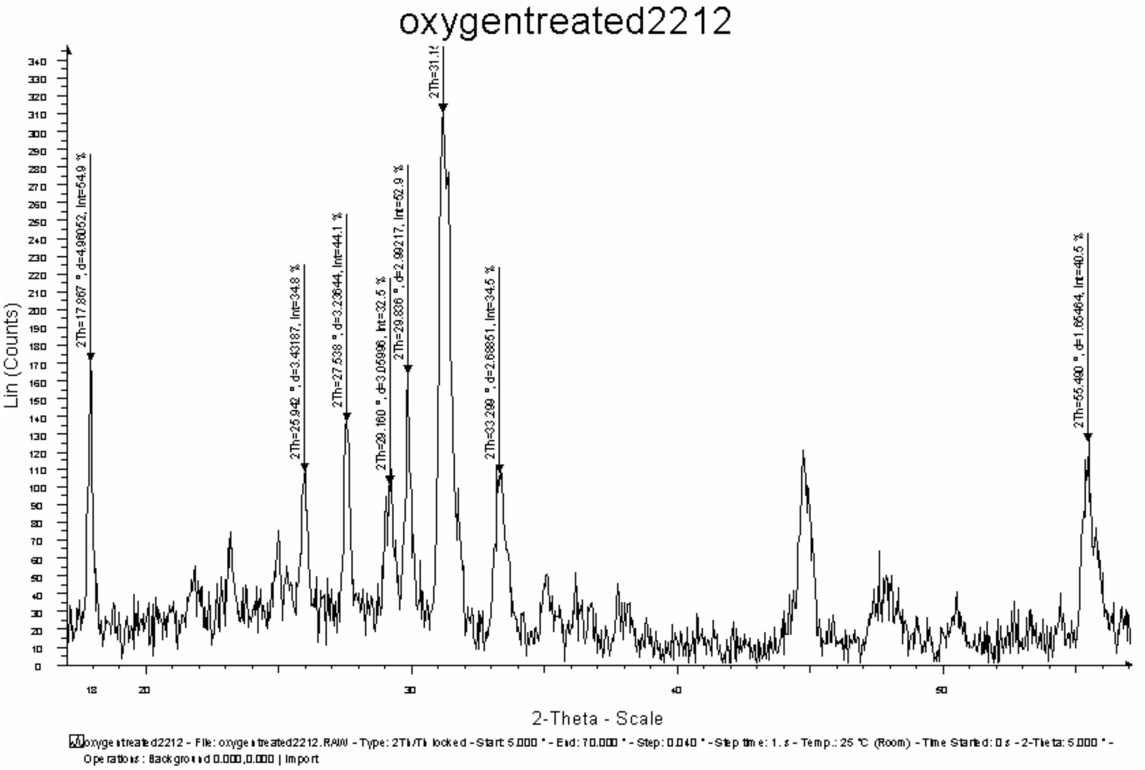

Fig.94 XRD pattern for Bi2212 core after step solidification heat treatment under oxygen purge.

Table 28. XRD analysis results for Bi2212 powder fully reacted (heat treated) under oxygen flow.

OXYGEN TREATED Bi 2212 POWDER (core) XRD ANALYSIS RESULTS						
Angle 2-Theta °	***d value angstrom***	***Intensity Count %***	***Intensity %***	***h***	***k***	***l***
17.867	4.96052	54.9	17.867	4.96052	171	54.9
25.942	3.43187	34.8	25.942	3.43187	108	34.8
27.538	3.23644	44.1	27.538	3.23644	137	44.1
29.160	3.05996	32.5	29.160	3.05996	101	32.5
29.836	2.99217	52.9	29.836	2.99217	165	52.9
31.157	2.86827	100.0	31.157	2.86827	311	100.0
33.299	2.68851	34.5	33.299	2.68851	108	34.5
55.490	1.65464	40.5	55.490	1.65464	126	40.5

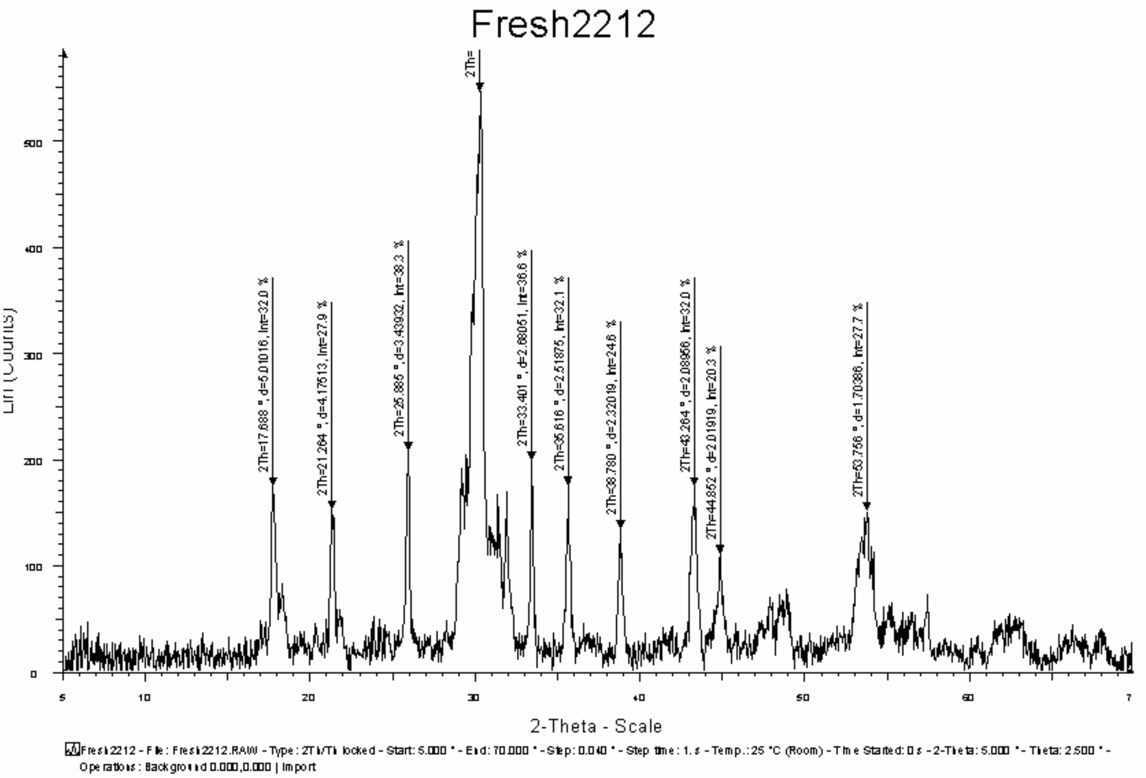

Fig.95 XRD pattern for Bi2212 precursor powder after second calcination step under air.

Table 29. XRD analysis results for Bi2212 powder (before packed in tube; not fully reacted).

FRESH Bi 2212 POWDER XRD ANALYSIS RESULTS						
Angle 2-Theta °	***d value angstrom***	***Intensity Count %***	***Intensity %***	***h***	***k***	***l***
17.688	5.01016	32.0	17.688	5.01016	175	32.0
21.264	4.17513	27.9	21.264	4.17513	153	27.9
25.885	3.43932	38.3	25.885	3.43932	210	38.3
30.257	2.95147	100.0	30.257	2.95147	547	100.0
33.401	2.68051	36.6	33.401	2.68051	201	36.6
38.780	2.32019	24.6	38.780	2.32019	135	24.6
43.264	2.08956	32.0	43.264	2.08956	175	32.0
35.616	2.51875	32.1	35.616	2.51875	176	32.1
44.852	2.01919	20.3	44.852	2.01919	111	20.3
53.756	1.70386	27.7	53.756	1.70386	152	27.7

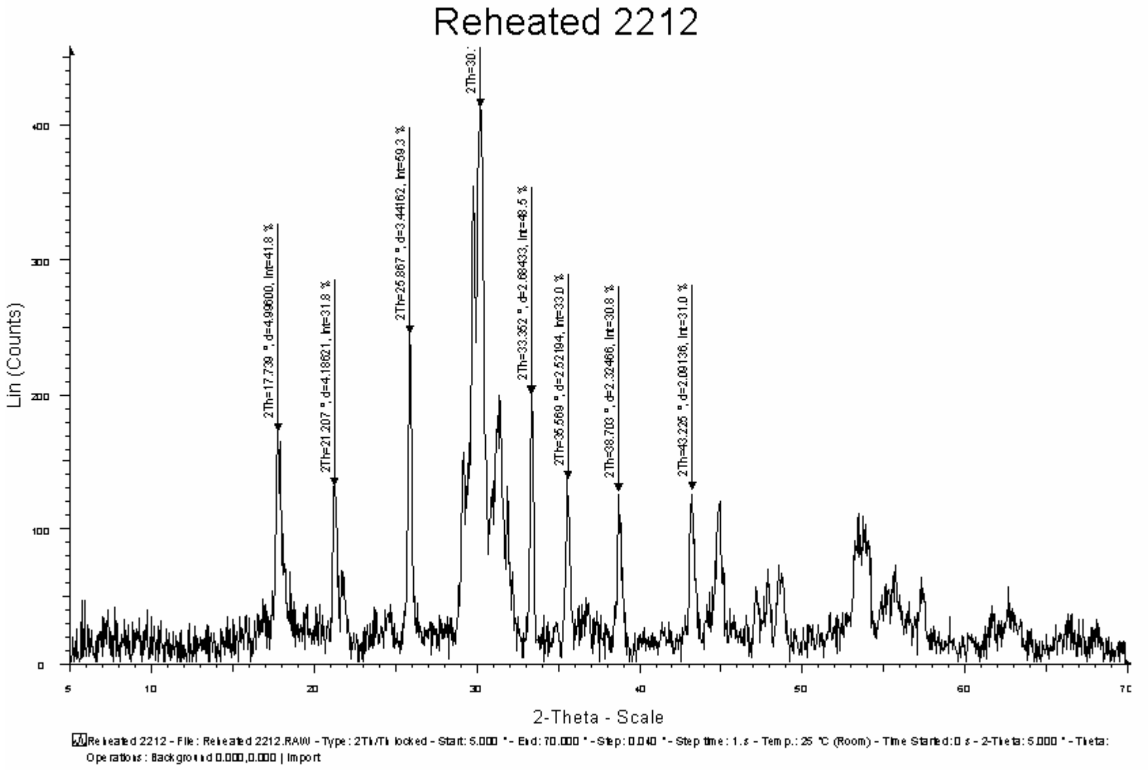

Fig.96 XRD pattern for Bi2212 precursor powder after reheating process under air.

Table 30. XRD analysis results for Bi2212 powder (before packed in tube; reheated to prevent excessive carbon content, not fully reacted).

REHEATED BI 2212 POWDER XRD ANALYSIS RESULTS						
Angle 2-Theta °	***d value angstrom***	**Intensity Count %**	***Intensity %***	***h***	***k***	***l***
17.739	4.99600	41.8	17.739	4.99600	173	41.8
21.207	4.18621	31.8	21.207	4.18621	132	31.8
25.867	3.44162	59.3	25.867	3.44162	246	59.3
30.196	2.95734	100.0	30.196	2.95734	414	100.0
33.352	2.68433	48.5	33.352	2.68433	201	48.5
35.569	2.52194	33.0	35.569	2.52194	137	33.0
38.703	2.32466	30.8	38.703	2.32466	127	30.8
43.225	2.09136	31.0	43.225	2.09136	129	31.0

Investigation of Interface and Filament Pattern for Sausaging and Cracks

As it was mentioned several times in previous sections, homogeneity is a very important criterion for the quality of the wire and tape superconductors. The wavy interface between the oxide core and the Ag sheath, referred to as “sausaging”, occurs due to the mechanical deformation and the narrow sections of the sausage decrease the actual cross sectional area, thus reducing I_c. Sausaging has also been observed to be detrimental for bending and tension capabilities of tapes.

Microcracks can be cited as another very serious fault, limiting J_c or even blocking the supercurrent.

Some important parameters effective on sausage and crack formation include powder packing method (initial powder density), drawing die geometry, and reduction ratio for both drawing and rolling processes, all of which were cited before in detail in literature survey. Hardness was also mentioned as an indicator for densification of powder during deformation processes.

Ag sheath promotes the alignment of 2212 crystals along the interface as a malleable metal. During rolling, if the freedom of the powder is larger, i.e. the diameter of the rollers is smaller, the sausaging (at least the repetition of bulges) and the density of the core is expected to reduce. The drawing process usually does not cause much sausaging.

It was claimed that [5] small reduction ratio per pass (around 10%) is another remedy to diminish sausaging possibility during the rolling process. It gives more freedom to silver in length direction. Without doubt, the core density achieved in this way will be lower compared to use of bigger rollers and/or larger reduction ratio per pass.

Post pressing after rolling can be beneficial to suppress sausaging and crack formation, and help grain alignment to promote texture of the core and lead less J_c degradation.

Very high filling factor yields to poor workability and large sausaging in filaments along their longitudinal direction. A non-uniform shape of filaments in a cross-section-view generally corresponds to strong sausaging in the longitudinal direction of the tapes. Tapes with filling factor of 35% found to have poor workability since higher filling factor leads to higher deformation force and lower ductility in the composite and it has been concluded that a smaller filament with less sausaging is the key for better conductive performance [17].

Pure Ag is soft, HV=33, in comparison to ceramic core, HV=120. This difference is the reason for sausaging formation at the interface, material wise. It was reported that Mg in the $Ag_{0.999}Mg_{0.001}$ alloy and the ceramic core was considered helpful in reducing internally oxidized during heat treatment under air and dispersed as MgO particles. Compared to Mg alloy, pure silver sheathed tapes were found to display more sausaging. Matching the hardness of sheath material and the ceramic core was considered helpful in reducing the sausaging effect or rolling process; even the sheath materials could be annealed before deformation [19].

Smaller approach angle for drawing dies was claimed to reduce sausaging in multifilament wires [22].

Setting the thickness reduction to 10% for rolling operations reduced sausaging of the monofilament tapes. Optimum core thickness for monofilament tapes was targeted as 40 μm for best J_c [24].

The sausaging effect has also been claimed reduced by cut in annealing temperature and time, which brings up the concept of increased sheath strength by work hardening. IR deformation path let the authors increase the applied shear stress gradually on the core and allowed the powder to flow freely. Introducing no intermediate annealing in between rolling steps improved strength of the silver sheath due to work hardening. Therefore, IR deformed multifilament tapes seemed to fulfill the requirements of high density, homogeneous deformation and good grain alignment (texture) much better than CR deformed ones [26].

It has also been claimed that by using harder cladding sheaths it could be possible to reduce the roughness of the core/sheath interface (sausaging) and increase powder filling factor [27].

Below, seen in Fig. 97 is the longitudinal cross section of Ag filament-Ag tube tape with 38 filaments. Here, the deformation regime was constant 25% reduction per pass, and the diameter of the starting wire product was 0.0600” (1.5 mm). This wire was rolled down to a thickness of 0.006” (~0.15 mm). Although the filaments looked continuous, the massive irregularity in the core/Ag interface is obvious.

The large, dark dots interrupting the filament continuity are Cu particles as discovered during our SEM investigations.

Another noticeable feature is the long crack running throughout the whole tape, from one end to the other. As discussed before, other researchers declared that crack formation during rolling took place in the width direction of the tape (see Fig.16). Here, what we observe is contradictory to this opinion and favors as if the deformation process were pressing, instead.

On this sample, there was no apparent sign of fracture. Such a considerable internal crack, for sure, is unacceptable in terms of the structural integrity if the tape is to be shaped with respect to the needs of any future applications. However, it also looks like the border between the sheath of one filament and the tube, which did not diffuse into each other.

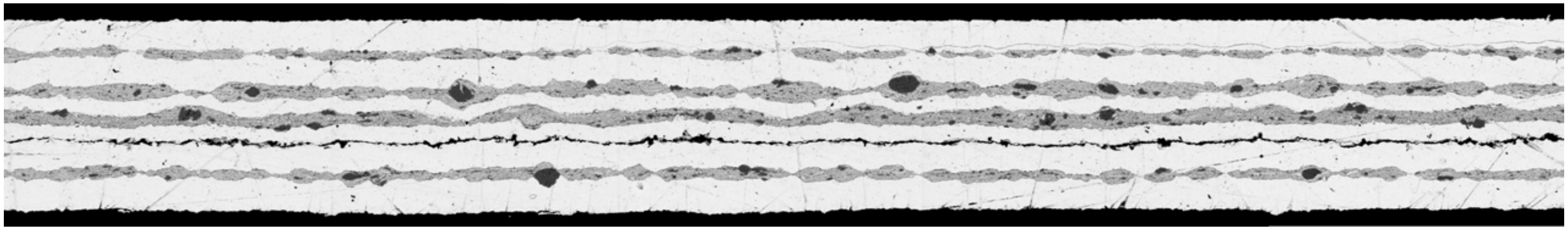

Fig.97 Merged longitudinal cross sectional view Ag filament-Ag tube tape with 38 filaments, 25% reduction per pass, starting wire diameter 0.0600”, AgT600_300x.

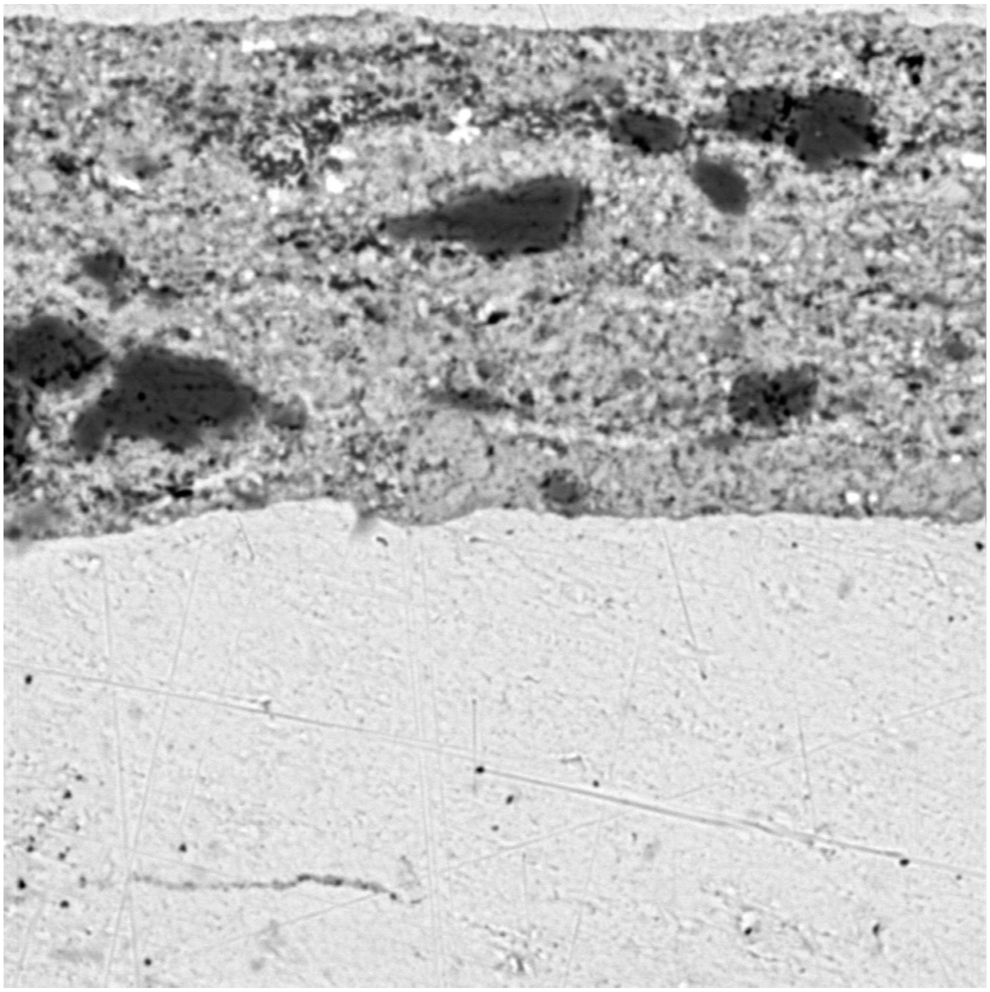

Fig.98 Close look at core/Ag interface in longitudinal cross section of Ag filament-Mg tube tape with thickness larger than final tape thickness, starting diameter 0.0500", AgT25_2000x.

In Fig.98 above, core/pure Ag interface in longitudinal cross section of Ag filament-Mg tube multifilament tape with a thickness of 0.0130" (~0.33 mm) is shown at a magnification of 2000x.

In order to find the optimum tape thickness that will give the best interface and filament configuration after deformation, a few samples were prepared at rolling reduction step #25.

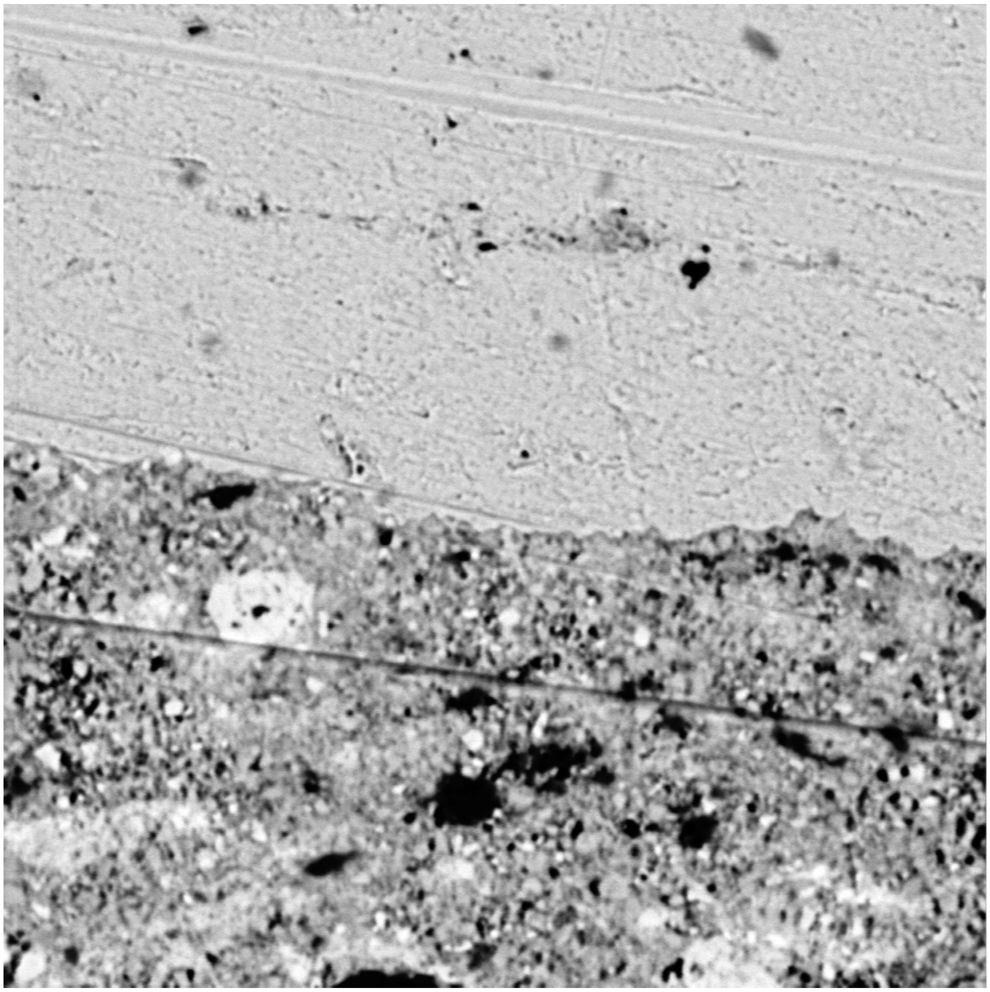

Fig.99 Close look at core/Ag interface in longitudinal cross section of Mg filament-Mg tube tape with thickness larger than final tape thickness, starting diameter 0.0500”) MgT25_2000x.

In Fig.99 above, core/pure Ag interface in longitudinal cross section of Mg filament-Mg tube multifilament tape with a thickness of 0.0130” (~0.33 mm) is shown at a magnification of 2000x. Compared with Fig.98, the core of Mg filament composite looked more porous although the geometric and deformation related properties of both tape samples were identical. However, harder clad material of the latter multifilament tape might have affected the compaction level of the powder inside despite cooperative the outer pure silver tube in terms of conveying the rolling force through.

Fig.100 is another picture from the same, thicker sample with Ag filament_Mg tube, which emphasizes the integrity and the continuity of the filaments compared to the thinner one in Fig.97. It was mentioned earlier that the BSCCO powder was required to be as compact as possible.

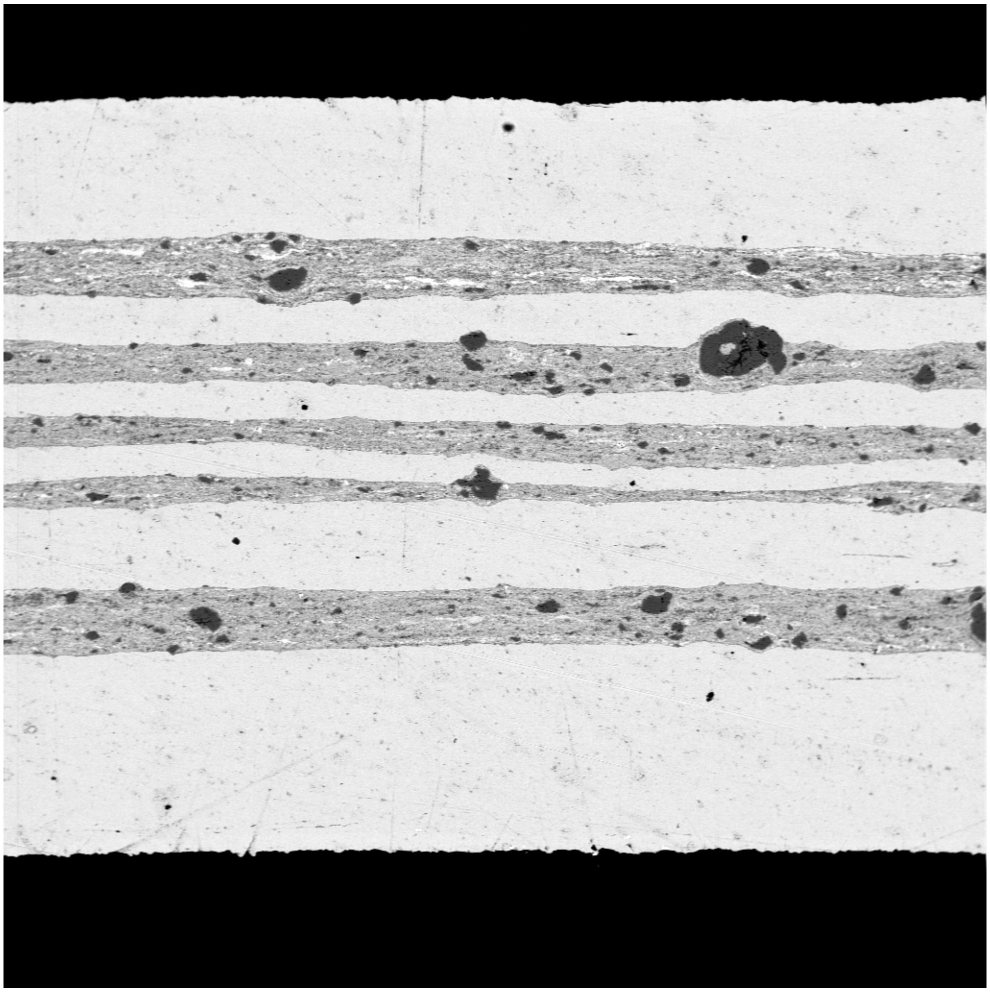

Fig.100 A general look at longitudinal cross section of Ag filament-Mg tube tape with thickness (0.0135”) greater than final tape thickness (0.0060”), starting wire diameter 0.0500”, AgT25_200x.

However, there must be a trade off between filament size and interface irregularity. That is, the recommended thickness of 0.0060” by several research groups did not work regarding the experience gained through our project. As long as the tape can be bent over the required radius by the application, it is better to keep it as thick as possible.

In Fig.100, the filaments closer to the tape center seemed thinner, thus we can conclude that they must have undergone more substantial deformation compared to the filaments nearer to the upper and lower surfaces of the tape. This issue was also brought up in the literature survey section (refer to Fig.25).

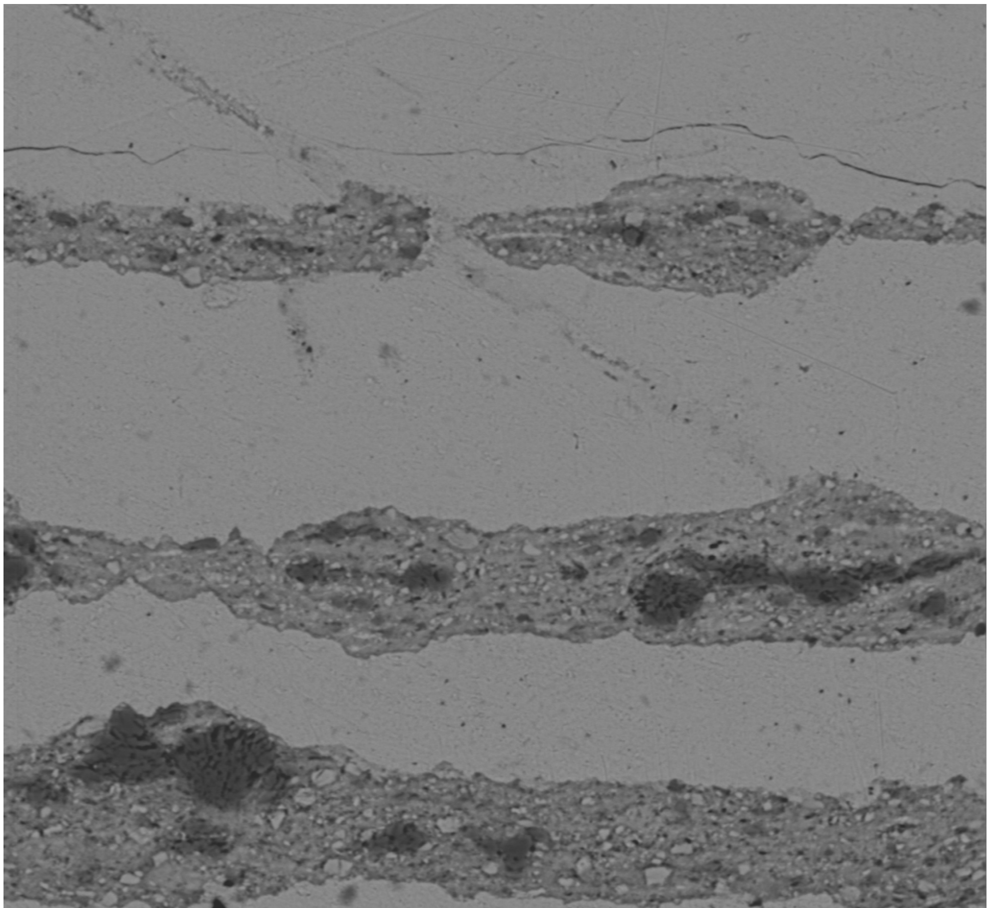

Fig.101 A closer look at filament discontinuity in-Ag filament-Ag tube tape with thickness 0.0060”, starting wire diameter 0.0600”, AgT600_1000x.

In Fig.101, the discontinuity in a filament can be seen in detail. The crack located just above the discontinuity is the border between the filament and the surrounding tube. This discontinuity can be due to a fault inherited by the filament during the drawing process since it looks as if the powder was not there at the point of breaking. Moreover, there is no clear sign of collapsing or any other kind of metal sheath disturbance due to severe deformation**.**

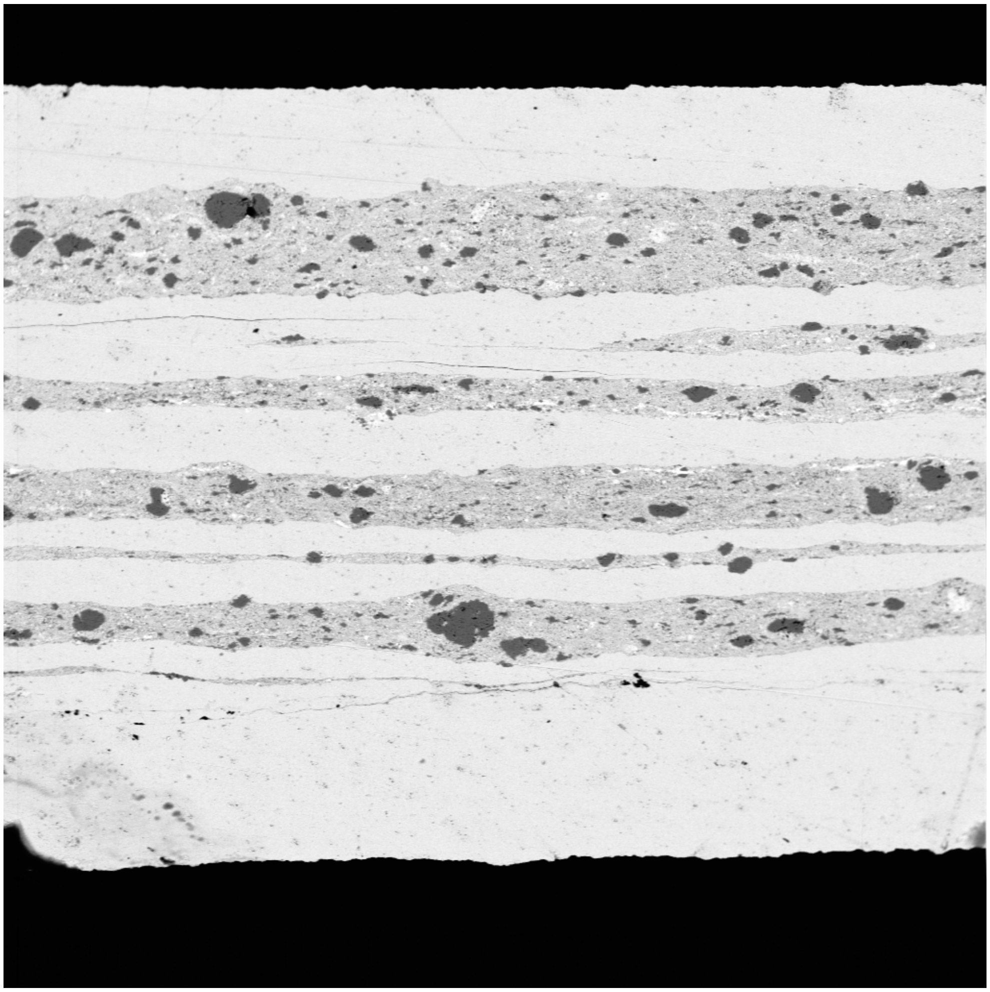

Fig.102 A general look at longitudinal cross section of Mg filament-Mg tube tape with thickness (0.0135”) greater than final tape thickness (0.0060”), starting wire diameter 0.0500”, MgT25_200x.

When compared with the tape with Ag filaments, i.e. Fig.100, Fig.102 obviously seemed more disturbed as for its Mg sheathed filaments. Having Mg as clad sheath for both on its filaments and outer tube, this multifilament composite had a tougher deformation due to strain hardening. Although some researchers declared their favor for harder sheath metal alloys to avoid sausaging, depending on the experience acquired throughout our project, pure Ag was witnessed as almost always more workable. SEM images of more regular interfaces of Ag filaments also confirm this observation of ours.

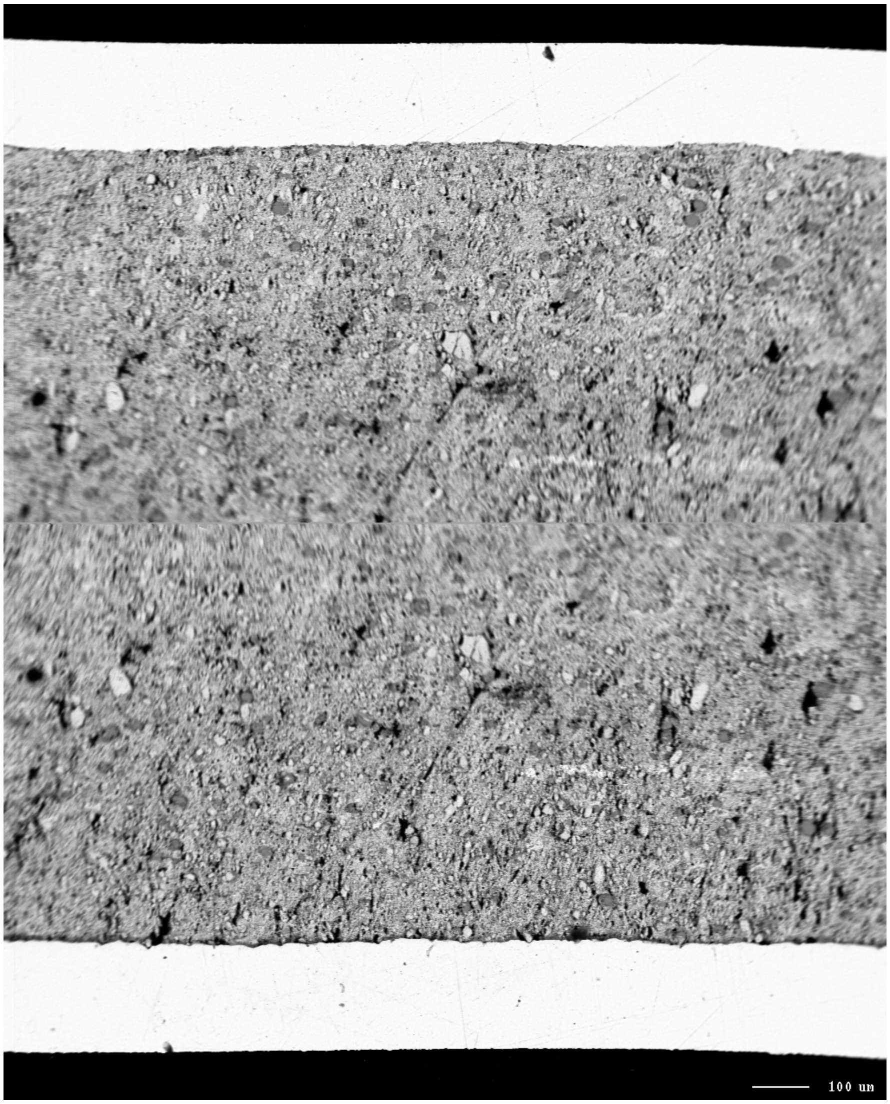

Fig.103 Merged BSE image of longitudinal cross section of monofilament wire with 0.0450” (1.143 mm) diameter, BB9_mono45_63x.

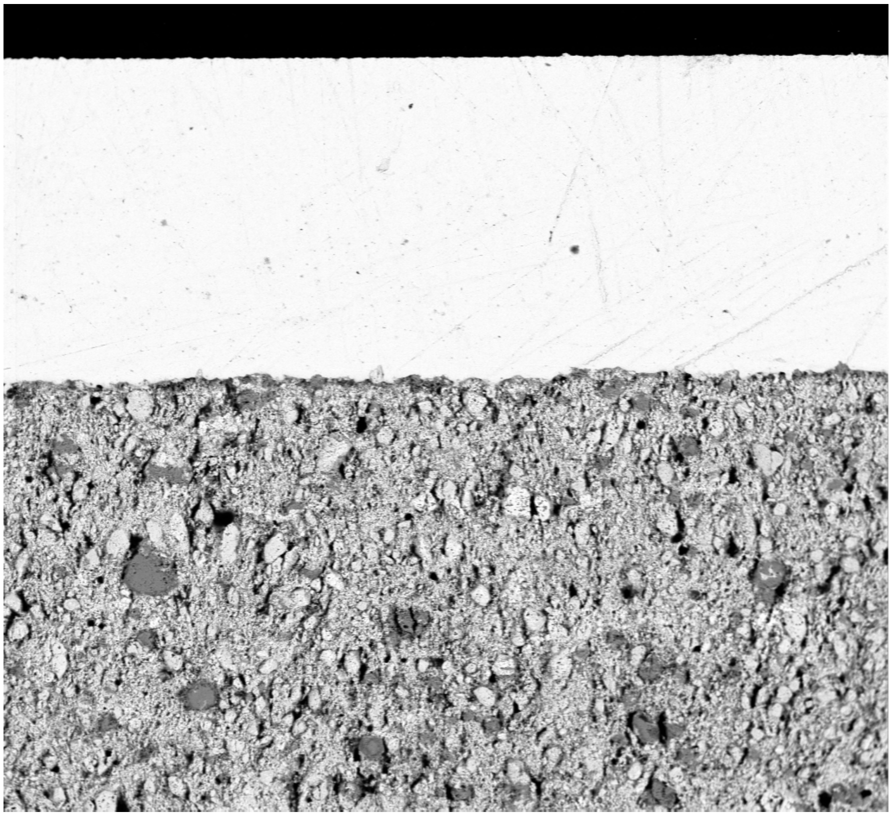

Fig.104 Closer look of core/pure Ag interface monofilament wire with 0.0450” (1.143 mm) diameter, mono45up200x.

As an example of good reduction regime employed for drawing operations, the rather regular interface and dense core in Fig.103 can be put forward. A wire diameter in the range of 0.0450-0.0500” was ideal to get optimum inner structure for our mono and multifilament wires in the light of SEM images and electrical performance tests.

In our opinion, a good wire is also a good start for multi and monofilament tapes with superior electrical performance, provided the optimum deformation conditions of rolling are secured. The initial filling factor for the starting billets was calculated and the result was also reported in section named Fabrication of Mono and Multifilament Wire. By looking at the straight interface of our wires, it can be concluded that our drawing reduction regime, drawing die and lubricant selections were appropriate. The next major section will present the ultimate decision maker of the optimization search of our project, which is the electrical performance test.

ELECTRICAL PERFORMANCE EVALUATION OF Bi2212 MONO AND MULTIFILAMENT WIRES

Electrical performance evaluation testing of our successfully fabricated mono and multi filament wires with 0.0500" (1.27 mm) diameter was the last step of this thesis work.

All the experiments were done by means of a self and custom-made testing rig at our laboratories. Fig.105 shows the *top-head* of the test setup to hold the samples in the cryogenic liquid as they perform.

Fig.105 Top-head of the test setup with wire samples and all cables attached ready to be immersed into cryogenic liquid.

With a small alteration in structure, the top-head allowed us to run three wire samples together at a time. This saved time and considerable amount of liquefied He.

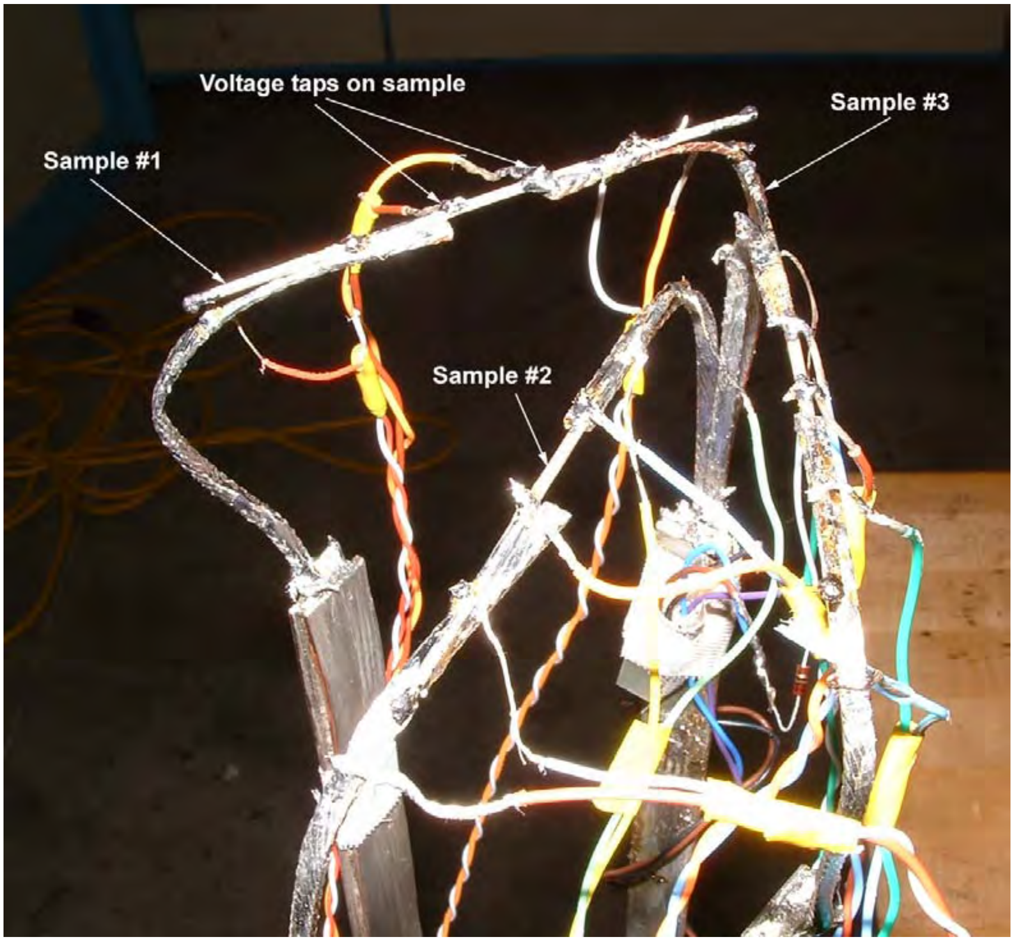

Fig.106 Closer view of the end of the top-head where the samples are attached with all cable connections ready.

Fig.107 shows the overall schematic of the test setup used for performance tests. The power supply used was a Hewlett-Packard 6680A DC 0-5V/0-875A integrated with two Hewlett-Packard 3458A multimeters. The tests were conducted by means of a computer program that commanded the electronic devices cited above to get to the current level flowing through each sample at a certain rate. The program also allowed setting of a quench voltage, which saved the samples from burning by shutting the current off.

The samples were first precooled in liquid N. Under nitrogen, all the samples displayed normal state resistance, i.e., it was not cold enough for them to switch to superconducting state.

Two carbon resistors were attached to the copper leads in order to indicate the level of the cryogenic coolant left in the dewar.

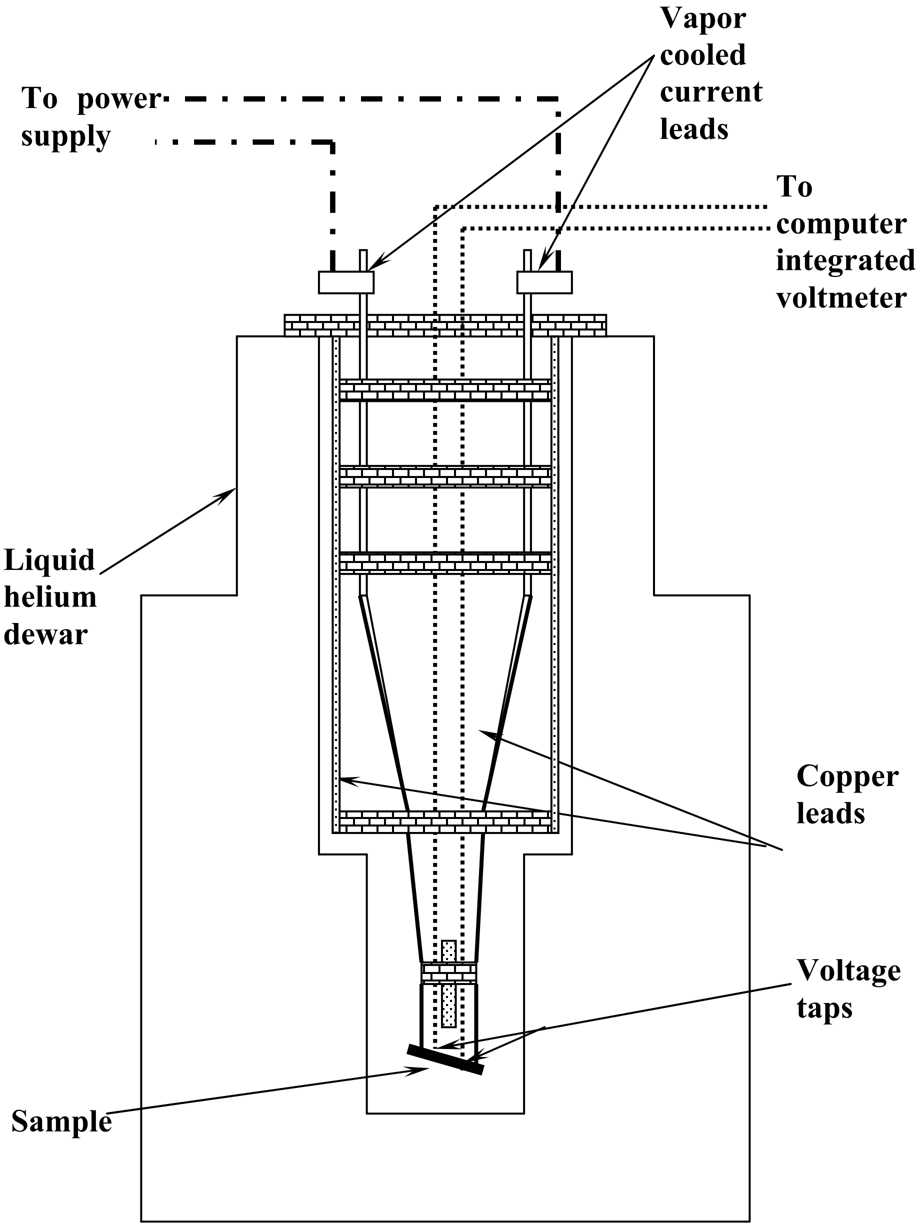

Fig.107 Schematic of the test setup with the top-head immersed into dewar.

Table 31. Results of electrical performance evaluation test for 0.0500” diameter wire samples under liquid He with respect to 1μV criteria.

	Electrical Performance Test Results for Wire Samples with 0.0500”(1.27 mm) diameter					
	Mg filament -Ag tube	***Ag filament -Ag tube***	***Mg filament -Mg tube***	***Ag filament -Mg tube***	***Mg sheath monofilament***	***Ag sheath monofilament***
Power supply current setting (Ampere)	770	710	350	750	455	690
Max Sample current (Ampere)	741.807	689.60	340.13	740.51	445.43	671.35
Critical current with respect to 1μV criteria (Ampere)	449.70	399.81	300.18	NA	265.19	NA
Corresponding volts (Volts)	8.9E-5	3.62E-5	5.84E-4	6.66E-6	6.41E-6	6.04E-6
Critical current density (Ampere/cm^2)	97760.87	86915.22	65256.52	NA	57560.00	NA

Results of the performance tests are presented in Table 31.

Except *Ag filament_Mg tube multifilament wire* and *Ag sheath monofilament wire,* all the samples quenched at some voltage, thus it was possible to find their critical currents with respect to *1μV criteria*. This criteria was employed by means of graphics and the concerning plots can be found in Appendix 7.

Figures 108 through 114 show the I-V curves (performance curves) for each sample under liquid He.

Fig.111 is given as a comparison for performance of *Ag filament-Mg tube, 38-filament wire*, in liquid N.

Compared to the results published in other papers, electrical performance results of our wires appeared very promising.

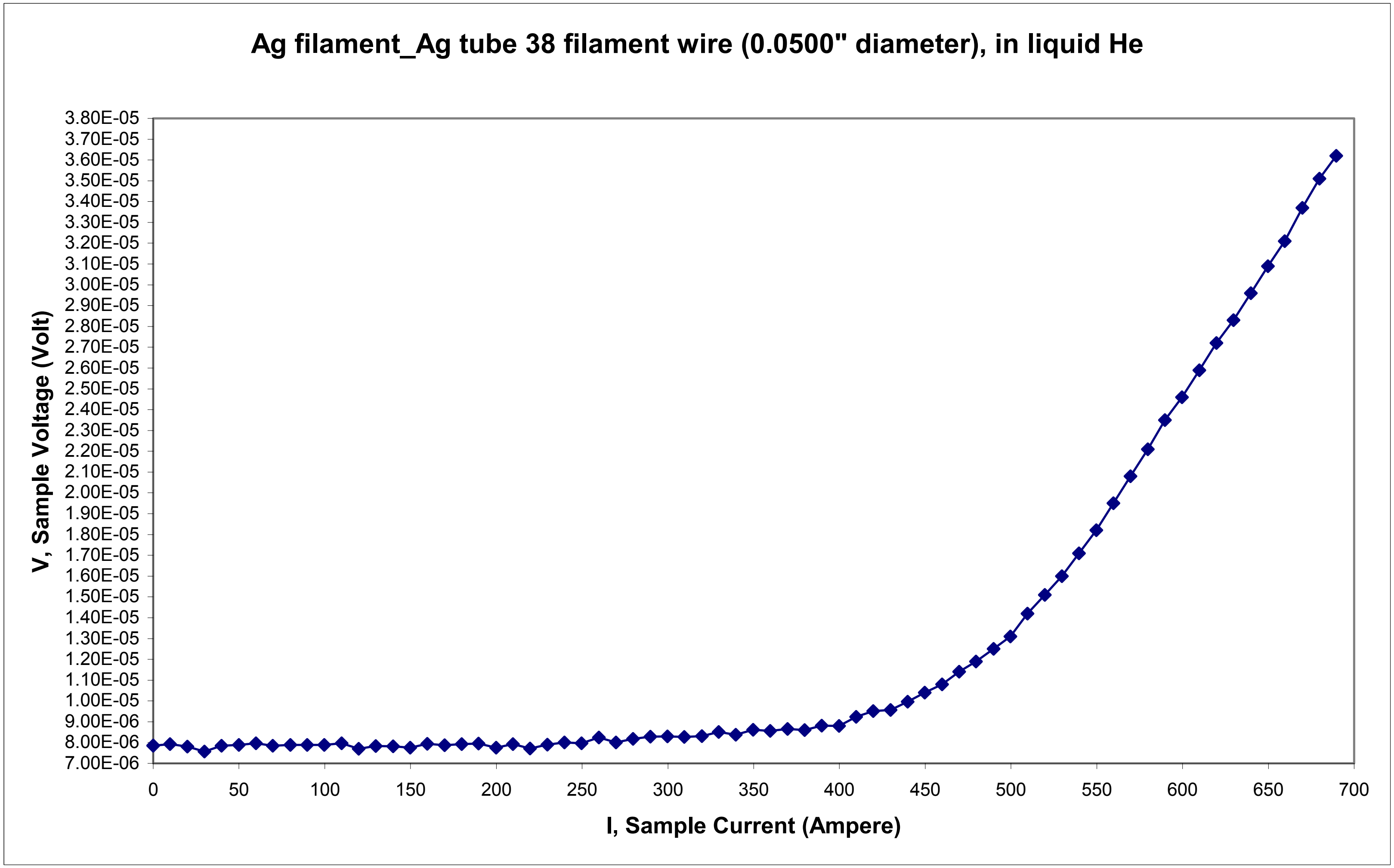

Fig.108 I-V (Current-Voltage) graph for Ag filament-Ag tube, 38 filament wire, 0.0500” diameter, in liquid He.

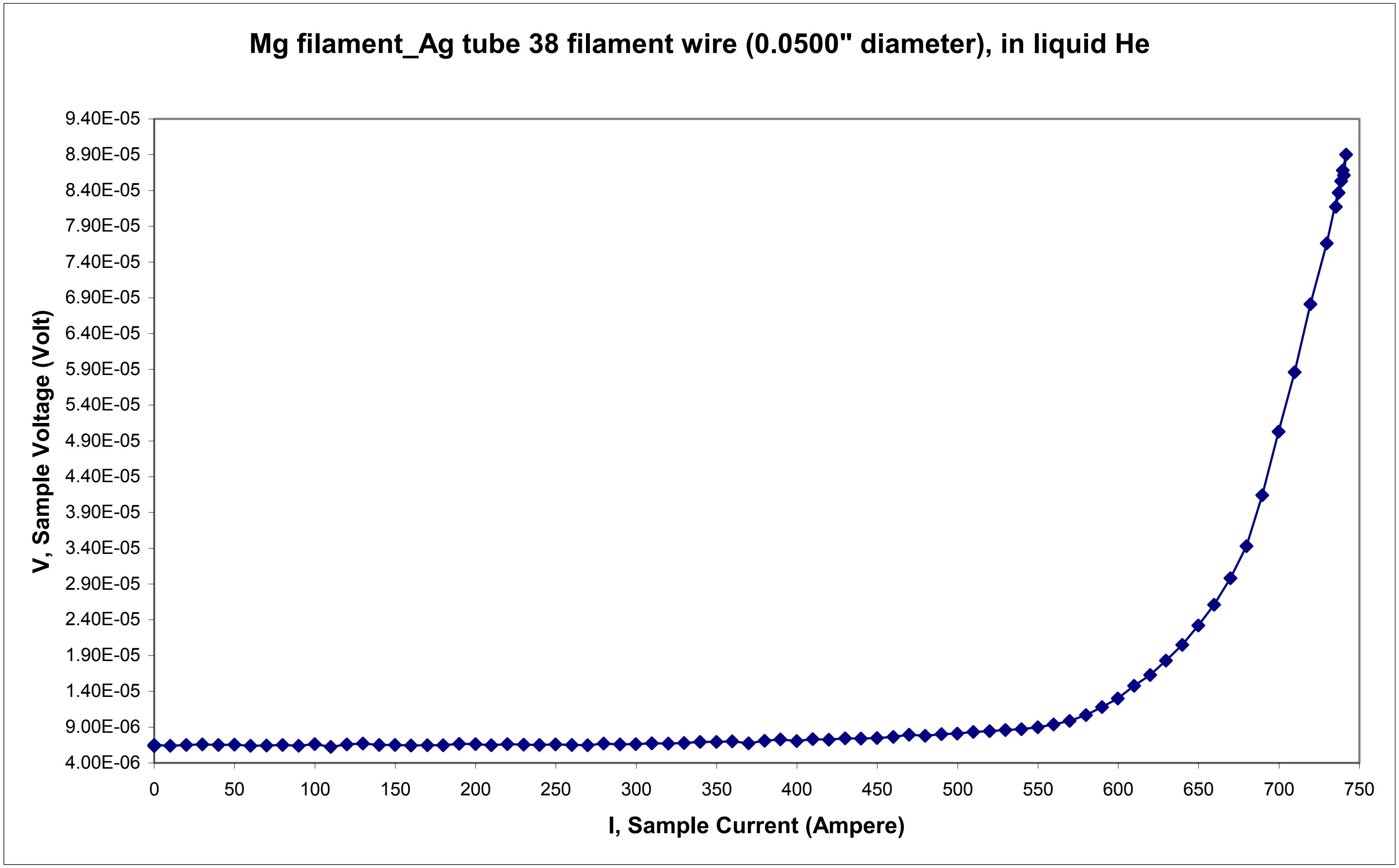

Fig.109 I-V (Current-Voltage) graph for Mg filament-Ag tube, 38 filament wire, 0.0500” diameter, in liquid He.

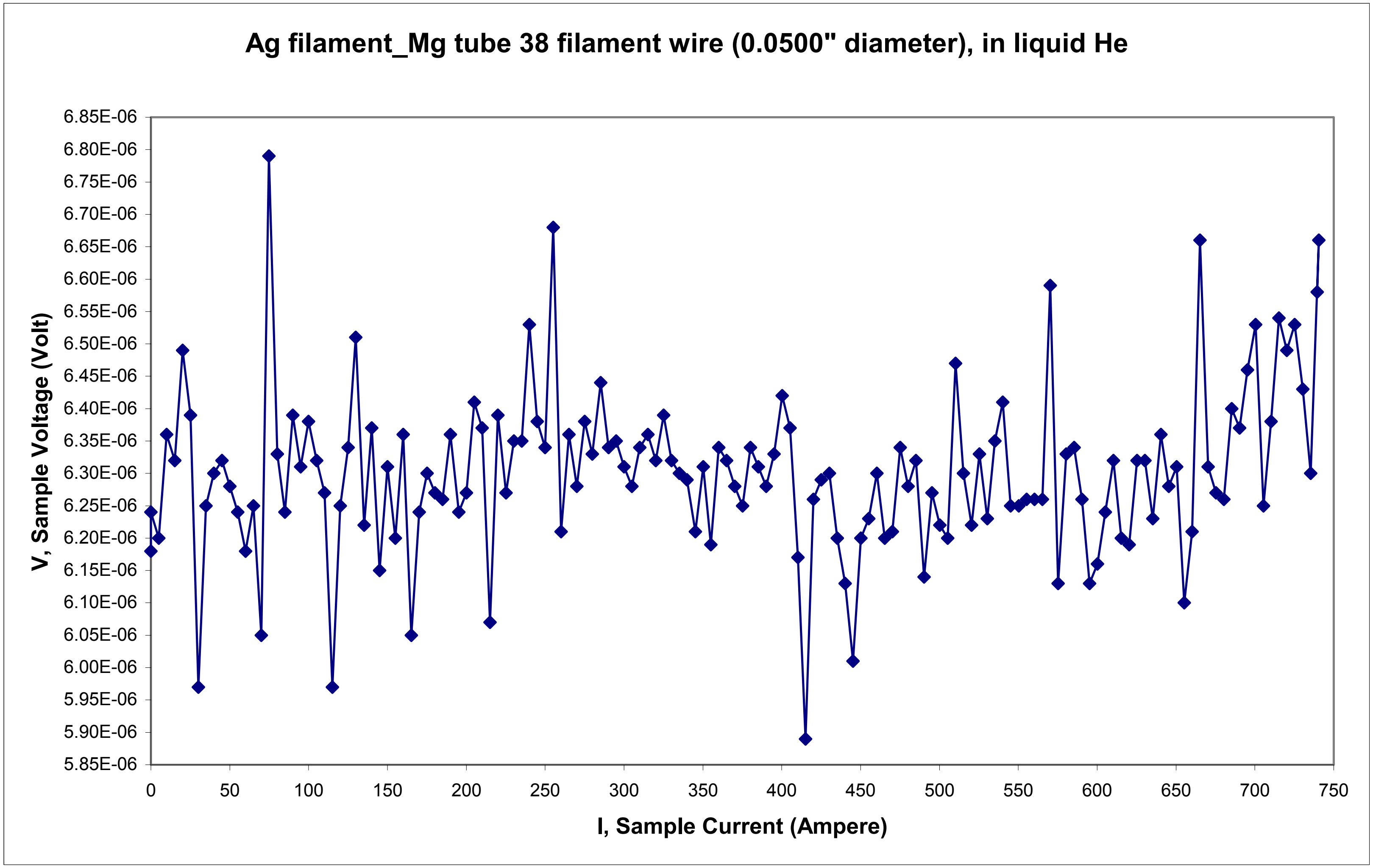

Fig.110 I-V (Current-Voltage) graph for Ag filament-Mg tube, 38 filament wire, 0.0500” diameter, in liquid He.

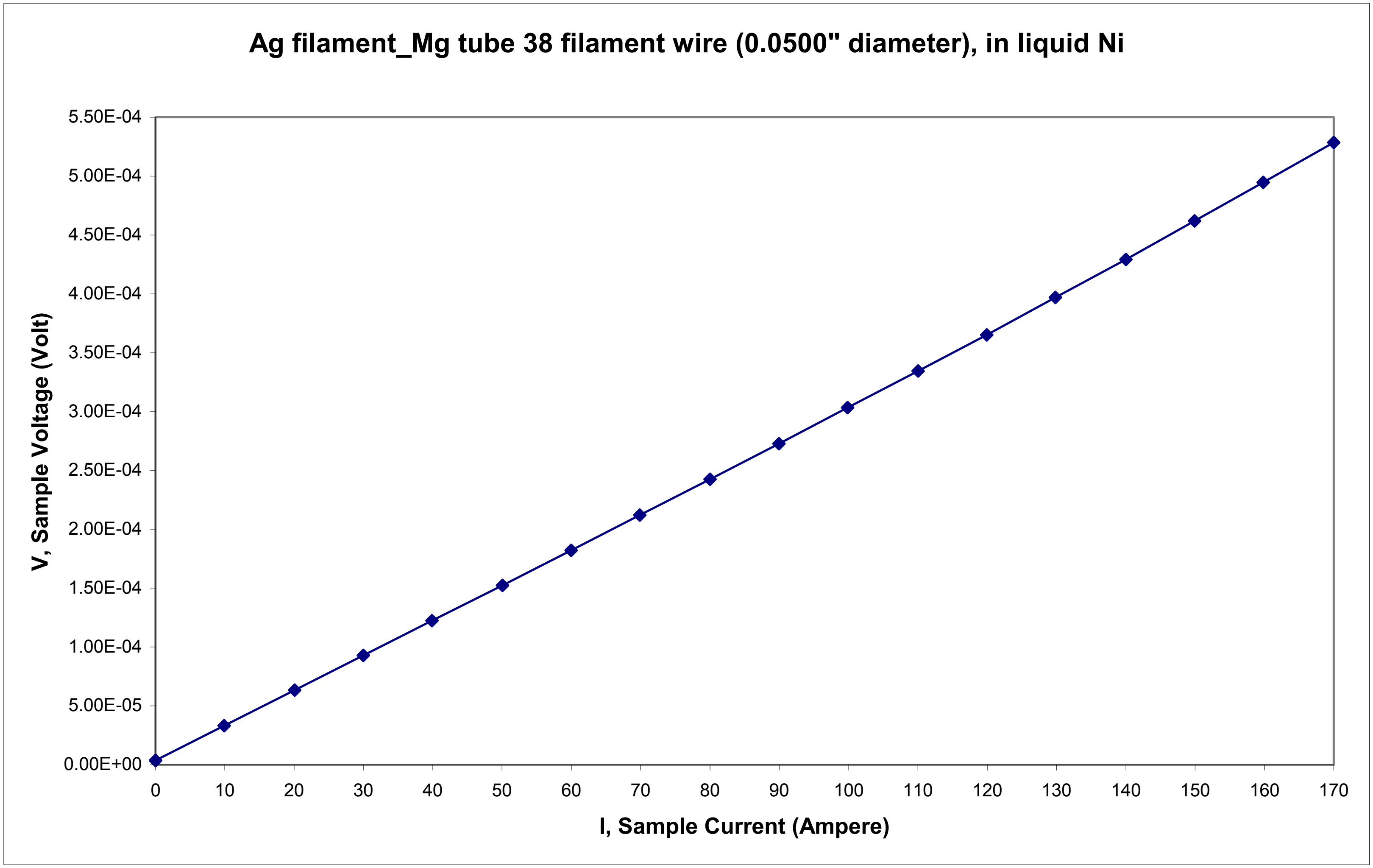

Fig.111 I-V (Current-Voltage) graph for Ag filament-Mg tube, 38-filament wire, 0.0500” diameter, in liquid N.

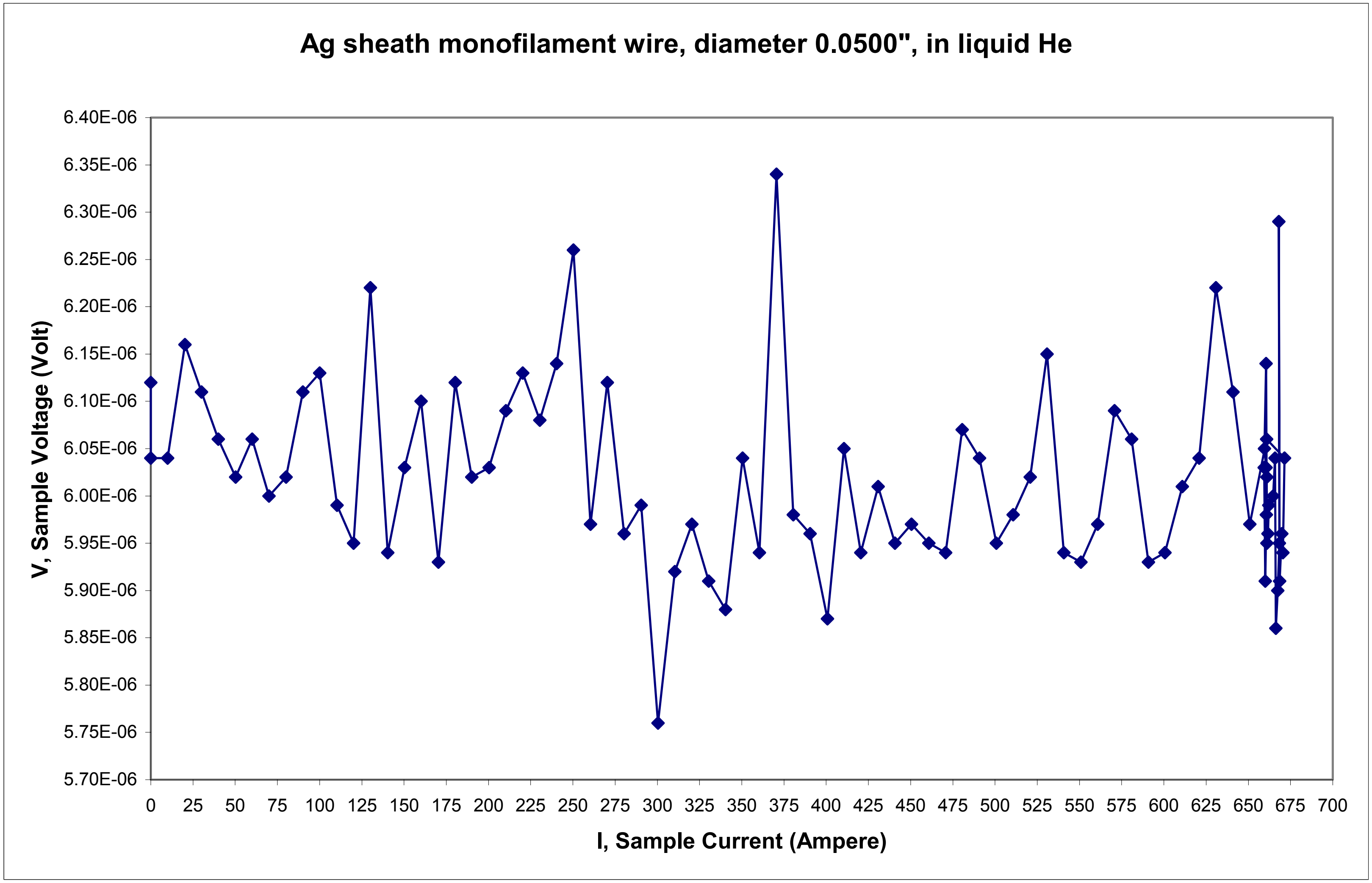

Fig.112 I-V (Current-Voltage) graph for Ag sheath, monofilament wire, 0.0500” diameter, in liquid He.

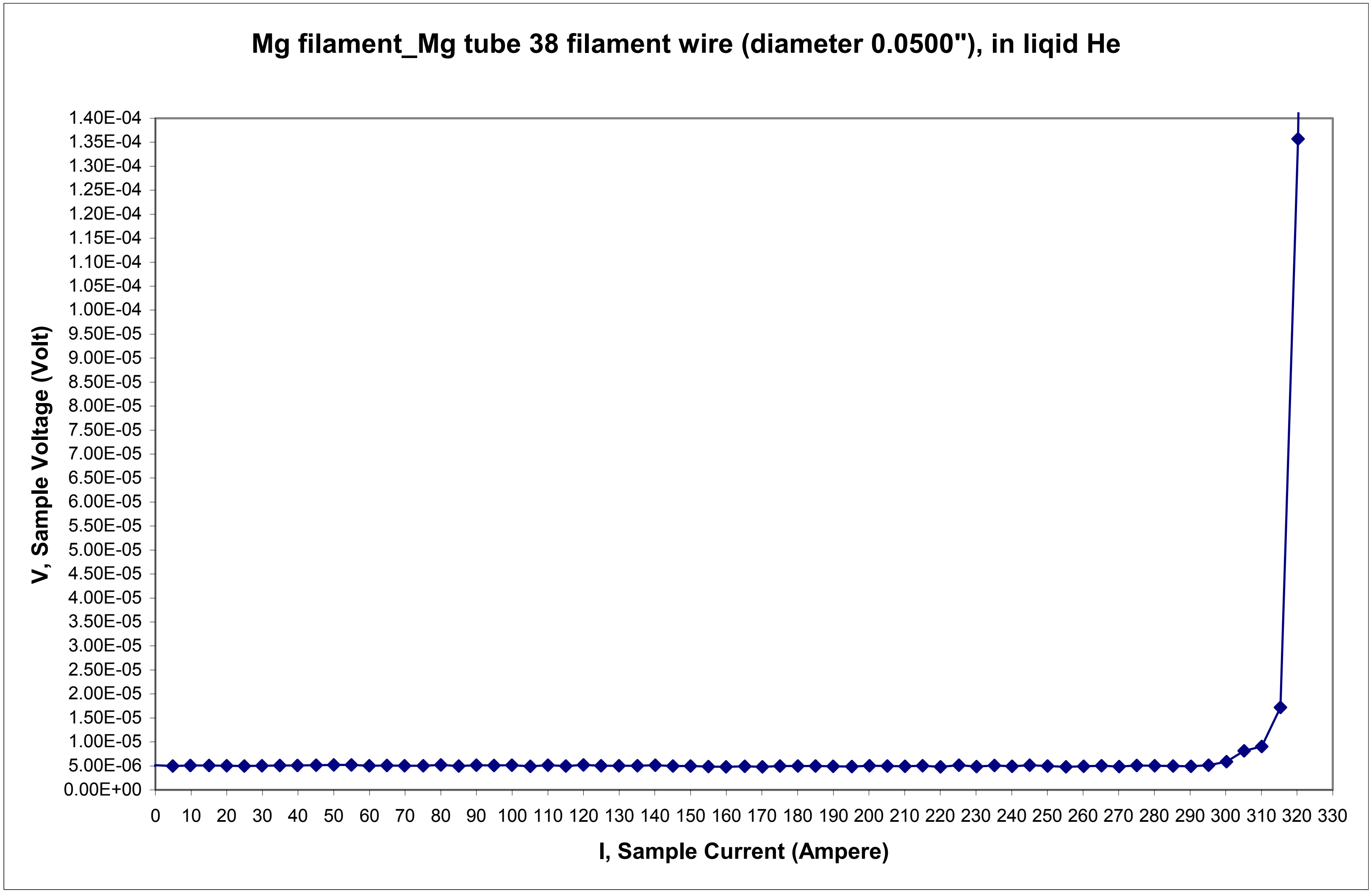

Fig.113 I-V (Current-Voltage) graph for Mg filament-Mg tube, 38 filament wire, 0.0500” diameter, in liquid He.

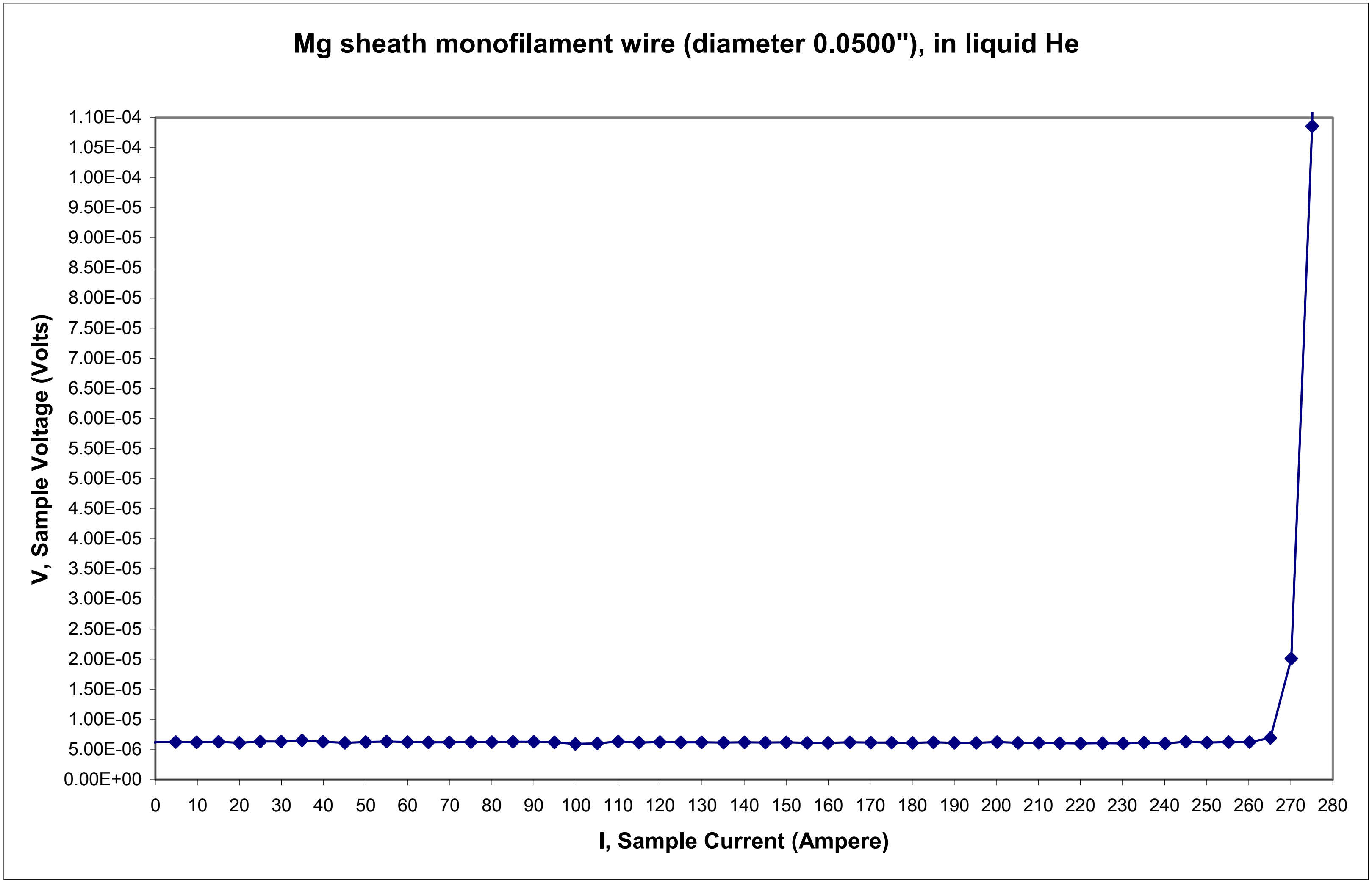

Fig.114 I-V (Current-Voltage) graph for Mg sheath, monofilament wire, 0.0500” diameter, in liquid He.

SUMMARY, COMPARISON AND CONCLUSIONS

It is well known that assessment of satisfactory performance for ceramic-based superconductor composites is a very difficult task. The parameters involved in the fabrication process were previously cited in detail in related sections. Until the present time, researchers have been working on optimization of these parameters and have reported many challenging handicaps associated with materials, plastic deformation processes and heat treatment schedules. However, each of them had different combinations of parameters to investigate at once, thus almost all came up with different solutions for the same problems regarding the different conditions under which their research was conducted.

In this project, it was aimed to combine all necessary parameters that claimed to be optimized before. In this regard, our effort comprised of four stages:

Employment of the best and most pragmatic method of Bi2212 powder synthesis utilizing the standard, inexpensive chemicals available in the market,

Use of standard size and composition pure silver and silver-magnesium alloy tubing available in the market,

Use of standard and inexpensive drawing dies, a common drawing bench and rolling mill calibrated according to deformation process requirements,

Employment of a simplified version of an optimized heat treatment schedule by means of a regular tubular furnace with modest modification.

Eventually, for the first time at our institution, Texas A&M, fabrication of ceramic based mono and multifilament superconductor composite wires was very successfully accomplished without the use of any custom made, prefabricated components. Everything necessary was manufactured by the degree candidate.

The electrical performance tests, also conducted at our own lab using our own custom-made test setup, brought about promising results in comparison with those published by national research labs and professional companies.

A detailed study of image processing was conducted on our wires and tapes made with different metal clad sheath and filament structure to reveal the effects of various deformation regimes at intermediate and final stages. XRD analysis of precursor and reacted powders was carried out to see the effects of our powder synthesis method and efficiency of the heat treatment schedule employed.

Finally, the electrical performance tests registered the success of our optimized parameters combination.

The biggest problem faced was bubbling of tapes during heat treatment. Although there observed no bubbling with any of the wires, all tape samples were devastated due to severe gas release. Despite the measures taken chemically, it was found impossible to prevent this phenomenon. Furthermore, in light of our XRD evaluation, not much of difference in the results was found when the advice and know-how on chemical issues by the most prominent researchers were employed. Taking the intact, thicker clad sheaths around the wires as a model, an effort was made to heat treat tape samples thicker than the final size. Unfortunately, the shattered quartz tube of our furnace disturbed this attempt. It was understood that quartz happened to be very susceptible to react with alkali metals at elevated temperatures. Thus, the almost invulnerable glass was cracked.

In my opinion, if thicker tape samples could be put under heat treatment, satisfactory results might be achieved like our wires.

The ideal size of mono/multifilament wire prior to rolling process and the final size for mono/multifilament tape depends on the powder particle size, wall thickness of the tubes, heat treatment (bubbling) and the requirements of the application in which the superconductors will be utilized. In my opinion, a thickness value around 0.0060” was too thin to have structurally stable tape. Regarding the observations on tape transverse cross sections, I think that a diameter around 0.0500” is appropriate to start rolling. Intuitively, a good pre-production, i.e. wire, is expected to result in better tape provided a suitable deformation regime was used. Since our wires proved their agility and integrity, the final size could be declared as good.

As for the drawing process, pure silver was easier to work with compared to Mg alloy. The images of wire cross sectional areas also gave us positive feed-back about the wall thickness selection of our tubes. In terms of sausaging, I don’t think the two different metals we employed differed too much. However, interfaces of ceramic core/pure silver looked smoother despite the claims of other researchers favoring harder sheath materials.

Following is a brief comparison of fabrication parameters used by various researchers:

Korzekwa et al. [6] packed their powders into tubes by tapping or inserting a cold isostatically pressed and machined powder rod (78% of theoretical density) in order to have 2.0 to 4.8 g/cm^3 initial packing density. The theoretical density of Bi2223 powders they used was proclaimed as 6.1 g/cm^3. The drawing die angle utilized was 20^o and drawing reduction per pass was 5%. At the end they observed that regardless of the initial packing density, both samples winded up with 4.5 g/cm^3, i.e., 75% of the theoretical density for 2223 [6].

Willen et al. [7] used pure Ag tube with 6.25 mm OD and 1 mm wall thickness. The final wire diameter was 1 mm. The diameter of the rollers they used was 20 mm. The area reductions were confined with 10% per pass and they did not use any lubricant due to the risk of core contamination through possible cracks in the Ag sheath. Final thickness of the tapes was 80-85 μm. The core was measured around 25 μm thick [7].

Yuan et al. [11] used two different powder particle sizes to see its effect. The particle size of the Bi2212 powder prepared by spray pyrolysis method was 2.8 μm and that of the other one prepared by melt casting process was 14.7 μm. Theoretical densities of the powders were given as 6.45 g/cm^3 and 6.41 g/cm^3, respectively. 99.9% pure silver tubes with 6.35 mm OD, having 1 mm and 0.25 mm wall thicknesses were utilized. Initial powder densities were also two folds; 30% and 40%. They made use of a ramrod. The lubricant employed for drawing operations was zinc stearate. The cross sectional areas deformation routine consisted of a constant reduction of 20.7% per pass. Final diameter of the wire products was measured as 1.62 mm (~0.0638”) [11].

Yuan et al. [4] annealed the 99.9% pure silver as received tubes for 1 hr at 400^{o}C to improve workability. Packing density was 30% with density of 2212 as 6.43 g/cm^3. Their final wire product had 1.62 mm (0.0638”) OD. Diameters of the rolls used were

21.27 mm and 6.35 mm. 10% and 25 % rolling reduction per pass regimes were employed. Final tape thickness was 160 μm (0.0063”) [4].

Ha et al. [22] used 20 mm OD pure silver tubing for OPIT method to achieve monofilament wires with 2.69 mm diameter. The die geometry they employed changed with approach angle (half angle of entrance), reduction ratios and bearing lengths. Then, they made hexagonal filaments out of these wires and bundled 37 of these filaments into a silver alloy outer tube with 20 mm diameter. This assembly was then drawn down to 1.4 mm. Flat rolling was employed to deform the multifilament wire into a tape with 0.25 mm final thickness through 30% reduction ratio [22].

Grasso et al. [24] avowed that a reduction per pass of 10% for wire drawing process seemed ideal. The final wire diameter after drawing determines the tape width and it is considerably important for current transport properties, as well. As a trade off between high J_c and sufficient mechanical strength, the authors chose to fabricate tapes from wires with 1-2 mm diameter. Setting the thickness reduction to 10% for rolling operations reduced sausaging of the monofilament tapes. Optimum core thickness for monofilament tapes was targeted as 40 μm for best J_c [24].

Kajuch et al. [25] used Bi2212 precursors with particle size of 2-5 μm prepared by spray pyrolysis method. They employed 99.9% pure silver tubes with 6.35 mm OD and 1 mm wall thickness to fabricate wires by OPIT method. Prior to drawing, each sample was weighed and measured to determine the initial powder packing density. The diameter for their final wire product was 1.63 mm (0.0642”). The drawing dies had a semi die angle of 8^o. The corresponding reduction of area per pass was 16, 20.7 and 25.2%, respectively, for the three different deformation schedules they carried out. Packing densities of the wire samples with 10 cm length were cut and amount of Bi2212 powder in these samples was calculated by subtracting the mass of silver from the total weight. Dimensions of the silver tube were already determined. Theoretical density of Bi2212 powder was taken as 6.45 g/cm^3 [25].

Zeng et al. [26] used a powder with an average particle size of 2-4 μm. The silver tubes used for OPIT method had 10 mm OD and 8.5 mm ID. The packing density of the powder as filled in tube was 2.5 g/cm^3. The drawing operation was carried out at 5%

reduction per pass. Final outer diameter of the monofilament wires was 2 mm. They used two different deformation routes for flat rolling process. The first one was defined as constant rolling per pass (CR) and the second as increasing rolling per pass (IR). Comparing these two procedures, CR reduction was of the order of 5% per pass and IR reduction increased gradually from 3 to 30% per pass. Authors fabricated 81 filament multifilament wires and deformed them into tapes starting from 2 mm (0.0787”) diameter wire and ending up with 0.16mm (0.0063”) thick tape [26].

Thangaraj et al. [38] fabricated Bi2212 tapes by OPIT method using groove and flat rolling for deformation. BSCCO powder with the stoichiometry of $Bi_2Sr_{1.7}CaCu_2O$ was prepared by spray combustion pyrolysis method. The average particle size was measured as 1-2 μm. Mechanical agitation was used to pack the powder into pure Ag tubes with 6.35 mm OD and 1 mm wall thickness. The packing process was done carefully to uniformly consolidate the powder along the tube length. The packing density was found to be 30% of the 2212 theoretical density. By means of a two-high rolling mill and groove rolling technique, packed tube was deformed into tapes with 2.1 x 2.0 mm rectangular cross section. Deformation per pass was controlled within 2% to assure homogeneity of the core and even stress distribution. Flat rollers were used to reach final form of 3.5 mm x 0.25 mm [38].

Zhang et al.’s [37] Ag sheathed 2212 tape was made by the OPIT method utilizing a pure silver tube of 6.35mm OD x 4.35mm ID. The final thickness of the tapes was ~100μm with a core thickness of 40-50 μm. Ends of the tapes were hammered shut [37].

Shinkawa et al. [43] used silver tubes with 4 mm inner diameter and 6 mm outer diameter to pack their $Bi_{1.8}Pb_{0.4}Sr_{2.0}Ca_{2.2}Cu_3O_x$ powder. The outer diameter of the tube then was reduced to 3 mm by 4-pass swaging. The final diameter of the oxide core was measured 1.33 mm. They rolled these wires into 0.3 mm thick tapes by 50-pass operations. 4.5% reduction-per-pass was employed to prevent sausaging. The authors reported the width of their as rolled tapes as 4.2 mm [43].

REFERENCES

[1] T. P. Sheahen, *Introduction to High-Temperature Superconductivity*, New York: Plenum Press, 1994

[2] E. E. Hellstrom, "Processing Bi-based high-T_c superconducting tapes, wires and thick films for conductor applications," in *High Temperature Superconducting Materials Science and Engineering*, D. L. Shi, Ed., New York: Pergamon, 1994, pp.383-436

[3] M. Yavuz, "Powder processing of Bi-Pb-Sr-Ca-Cu-O superconducting ceramic composites," Ph.D. dissertation, University of Wollongong, Wollongong, Australia, 1996

[4] D. W. Yuan, M. K. Pollock and J. Kajuch, "Effect of rolling properties of monofilamentary Bi-2212 superconductor tapes," *Physica C*, vol.302, pp.1-9, 1998

[5] Z. Han, P. Skov-Hansen and T. Freltoft, "The mechanical deformation of superconducting BiSrCaCuO/Ag composites," *Supercond. Sci. Technol.*, vol.10, pp.371-387, 1997

[6] D. A. Korzekwa, J. F. Bingert, E. J. Podtburg and P. Miles, "Deformation processing of wires and tapes using the oxide powder in tube method," *IEEE Trans. Applied Supercond.*, vol.2, no.3/4, pp.261-270, 1994

[7] D. W. A. Willen, W. Zhu and R. Nadi, "Fabrication of thin-filament Bi2223 superconducting tapes," *IEEE Trans. Applied Supercond.*, vol.7, no.2, pp.2079-2082, 1997

[8] I. Husek, P. Kovac and W. Pachla, “Microhardness profiles in BSCCO/Ag composites made by various technological steps,” *Supercond. Sci. Technol.*, vol.8, pp.617-625, 1995

[9] M. T. Malachevsky and D. A. Esparza, “Metal-ceramics interface response to bending and fatigue cycles in superconducting Ag-Bi2223 composites,” *Physica C*, vol.324, pp.153-160, 1999

[10] Z. Han and T. Freltoft, “The mechanical deformation process for preparing Ag-sheathed BiSrCaCuO superconducting tapes,” *IEEE Trans. Applied Superconductivity*, vol.2, no.3/4, pp.201-215, 1994

[11] D-W Yuan, M. K. Pollock and J. Kajuch, “Drawing of Ag-clad $Bi_2Sr_2CaCu_2O_8$ superconductor wires,” *Supercond. Sci. Technol.*, vol.10, pp.52-57, 1997

[12] T. Sakai, H. Utsunomiya and Y. Saito “Effect of intermediate rolling condition on the critical current density of silver-sheathed Bi(2223) superconducting tapes,” *Physica C*, vol.277, pp.189-195, 1997

[13] L. Bigoni, F. Barberis and R. Berti, “Development of Bi2223/Ag-alloy tapes,” *IEEE Trans. Applied Supercond.*, vol.9, no.2, pp.2597-2600, 1999

[14] A. Oota and K. Kawano, “Influence of rolling pressure on microstructure and current path evolution,” *IEEE Trans. Applied Supercond.*, vol.9, no.2, pp.2529-2532, 1999

[15] E. C. L. Chesneau, B. A. Glowacki and I. MacDougall, “Residual stress and the critical current in superconducting tapes,” *Cryogenics*, vol.37, pp.615-618, 1997

[16] G. Grasso and B. Hensel, "Transport properties of long monofilamentary Bi(2223) tapes," *IEEE Trans. Applied Supercond.*, vol.5, no.2, pp.1255-1258, 1995

[17] Y. B. Huang, F. Marti and G. Witz, "Enhancing the engineering J_c of Bi-2223 multifilamentary tapes by two-axial rolling and periodic pressing," *IEEE Trans. Applied Supercond.*, vol.9, no.2, pp.2722-2725, 1999

[18] W. L. Carter, G. N. Riley and A. Otto, "Advances in the development of silver sheathed (Bi, Pb)2223 composite conductors," *IEEE Trans. Applied Supercond.*, vol.5, no.2, pp.1145-1149, 1995

[19] J. Yoo, H. Chung and J. Ko, "Long length processing of BSCCO-2223 tapes made by using Ag alloys sheath," *IEEE Trans. Applied Supercond.*, vol.7, no.2, pp.1837-1840, 1997

[20] O. O. Olusoji and O. Oduleye, "Thermal cycling, critical current vs. strain and finite element modeling of 1, 7, 19 and 37 filament Ag/Bi-Sr-Ca-Cu-O (BSCCO) tapes," *IEEE Trans. Applied Supercond.*, vol.9, no.2, pp.2621-2624, 1999

[21] W. G. Wang, B. Seifi and Y. L. Liu, "Engineering critical current density of Ag-Bi2223 tapes," *IEEE Trans. Applied Supercond.*, vol.11, no.1, pp.2983-2986, 2001

[22] H. S. Ha, S. S. Oh and D. W. Ha, "The effects of drawing parameters on sausaging and critical current density of Bi-2223/Ag HTS wires," *IEEE Trans. Applied Supercond.*, vol.11, no.1, pp.3748-3751, 2001

[23] M. Malberg, J. Bech and N. Bay, "Influence of process parameters in drawing of superconducting wire," *IEEE Trans. Applied Supercond.*, vol.9, no.2, pp.2577-2580, 1999

[24] G. Grasso, A. Jeremie and R. Flukiger, “Optimization of the preparation parameters of monofilamentary Bi(2223) tapes and the effect of the rolling pressure on J_c,” *Supercond. Sci. Technol.*, vol.8, pp.827-832, 1995

[25] J. Kajuch, D. W. Yuan and M. J. Pollock, “On the manufacture of silver-sheathed Bi-2212 high temperature superconducting wires,” *J. Electronic Materials*, vol.24, no.12, pp.1773-1780, 1995

[26] R. Zeng, T. P. Beales and H. K. Liu, “Optimal reduction in rolling Ag-sheathed Bi2223 multifilamentary tapes,” *Supercond. Sci. Technol.*, vol.11, pp.299-303, 1998

[27] R. Navarro, “Silver alloys used in composite BSCCO tapes: development of electrical and mechanical properties,” *Supercond. Sci. Technol.*, vol.13, pp.R147-170, 2000

[28] A. McInturff, *Personal communication*, Supercon/LBNL, Berkeley, CA, 2003

[29] R. C. Weast, Ed., *Handbook of Chemistry and Physics*, 57th ed., Cleveland, OH: CRC Press, 1976-1977

[30] W. D. Callister, *Material Science and Engineering*, 5th ed., New York: John Wiley and Sons, 2000

[31] P. Strobel and T. Fournier, “Phase diagram studies in the Bi(Pb)SrCaCuO system,” *Journal of the Less Common Metals.*, vol.164 and 165, pp.519-525, 1990

[32] W. Zhang, E. E. Hellstrom and M. Polak, “A study of Ag sheathed $(Bi,Pb)_2Sr_2CaCuO_x$ tape,” *Supercond. Sci. Technol.*, vol.9, pp.971-977, 1996

[33] A. Jeremie, K. Alami-Yadri, J-C Grivel and R. Flukiger, “Bi,Pb(2212) and Bi(2223) formation in the Bi-Pb-Sr-Ca-Cu-O system,” *Supercond. Sci. Technol.*, vol.6, pp.730-735, 1993

[34] E. E. Hellstrom and W. Zhang, “Phase assemblages in the melt state in Ag-sheathed Bi-2212 tape in 1% and 7.5% O_2,” in *Advances in Superconductivity 6, Proc. 6th Int. Symp. Superconductivity* (ISS 93), pp.615-620, Hiroshima, Japan, 1993

[35] L. Motowidlo, G. Galinski, G. Ozeryansky, W. Zhang, E. E. Hellstrom, M. Sumption and T. Collings, “Influence of filament size and atmosphere on the microstructure and J_c of round multifilament $Bi_2Sr_2Ca_1Cu_2O_x$ wires,” *IEEE Trans. Applied Supercond.*, vol.5, no.2, pp.1162-1166, 1995

[36] W. Hu, P.V.P.S.S. Sastry, U. P. Trociewitz and J. Schwartz, “Microstructure and critical currents in AgMg-sheathed multifilamentary $Bi_2Sr_2CaCu_2O_8$ tapes,” *IEEE Trans. Applied Supercond.*, vol.9, no.2, pp.1876-1879, 1999

[37] W. Zhang and E. E. Hellstrom, “The effects of oxygen on melt processing Ag-sheathed $Bi_2Sr_2CaCuO_x$ conductors,” *Supercond. Sci. Technol.*, vol.8, pp.430-438, 1995

[38] K. Thangaraj, A. N. Iyer, L. Zhang and K. Salama, “Heat treatment studies on Bi-2212/Ag tapes fabricated using a powder-in-tube technique,” *Supercond. Sci. Technol.*, vol.13, pp.1035-1041, 2000

[39] R. Funahashi, I. Matsubara and K. Ueno, “Preparation parameters governing microstructure and grain coupling of $Bi_2Sr_2CaCu_2O_x$/Ag tapes prepared by partial melting,” *Physica C*, vol.295, pp.39-46, 1998

[40] R. D. Ray II and E. E. Hellstrom, "Microstructurally optimized heat treatment for melt-processed Ag clad $Bi_2Sr_2CaCu_2O_y$ tape, step solidification melt processing," *Physica C*, vol.251, pp.27-49, 1995

[41] A. Erkekin, "Effect of doping in Bi-Pb-Sr-Ca-Cu-O superconductor composites," M.S. thesis, Texas A&M University, College Station, TX, 2001

[42] J. Jiang, D. C. Larbalestier and X. Y. Cai, "Through-process study of factors controlling the critical current density of Ag sheathed $(Bi,Pb)_2Sr_2Ca_2Cu_3O_x$ tapes," *Supercond. Sci. Technol.*, vol.14, pp.548-556, 2001

[43] M. Shinkawa, H. Utsunomiya, T. Sakai and Y. Saito, "Critical current density of Ag-sheathed (Bi,Pb)2223 tapes produced by various thermo-mechanical treatment patterns," *Physica C*, vol.281, pp.64-68, 1997

APPENDIX 1

CONTROL CALIBRATION OF FURNACE HOTZONE

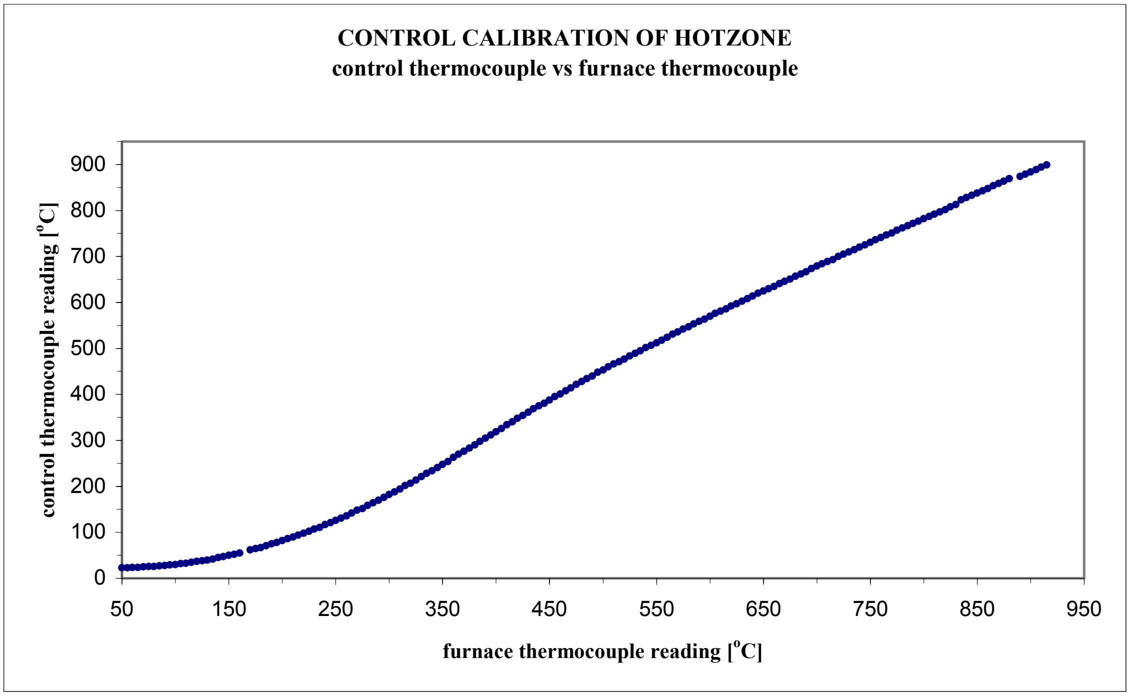

Fig.A1.1 Control calibration of tubular furnace hotzone (ceramic tube).

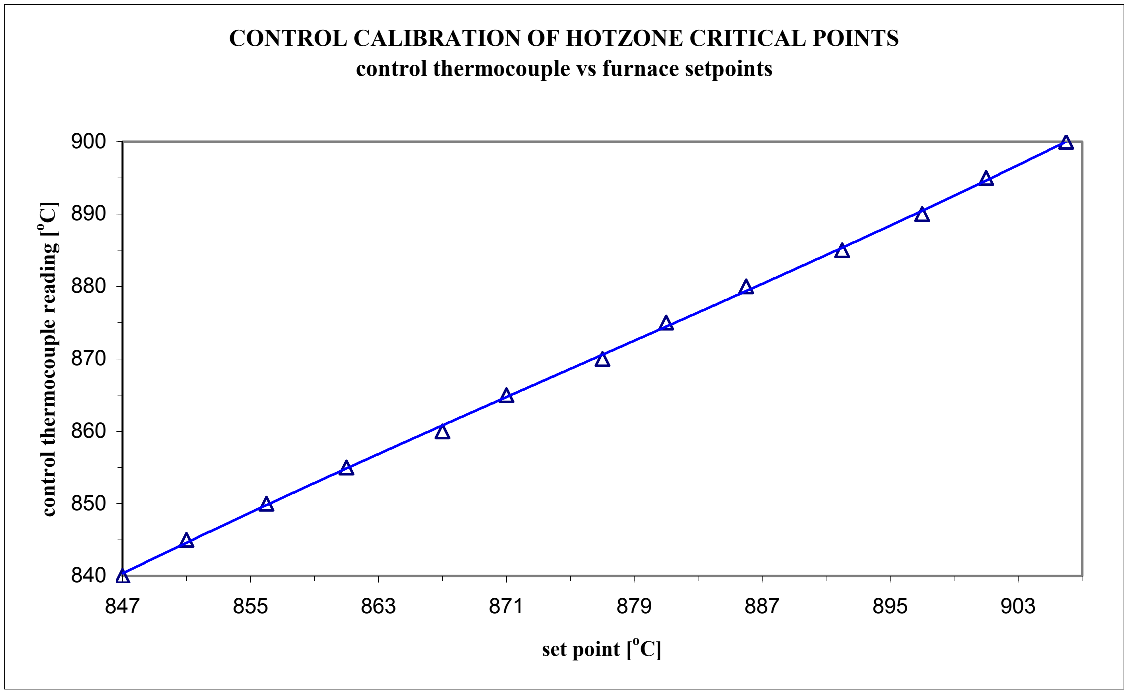

Fig.A1.2 Critical setpoints for control calibration of tubular furnace hotzone (ceramic tube).

APPENDIX 2

GRAPHICAL REPRESENTATION OF TAPE IMAGE ANAYLSIS RESULTS (ROLLING DEFORMATION)

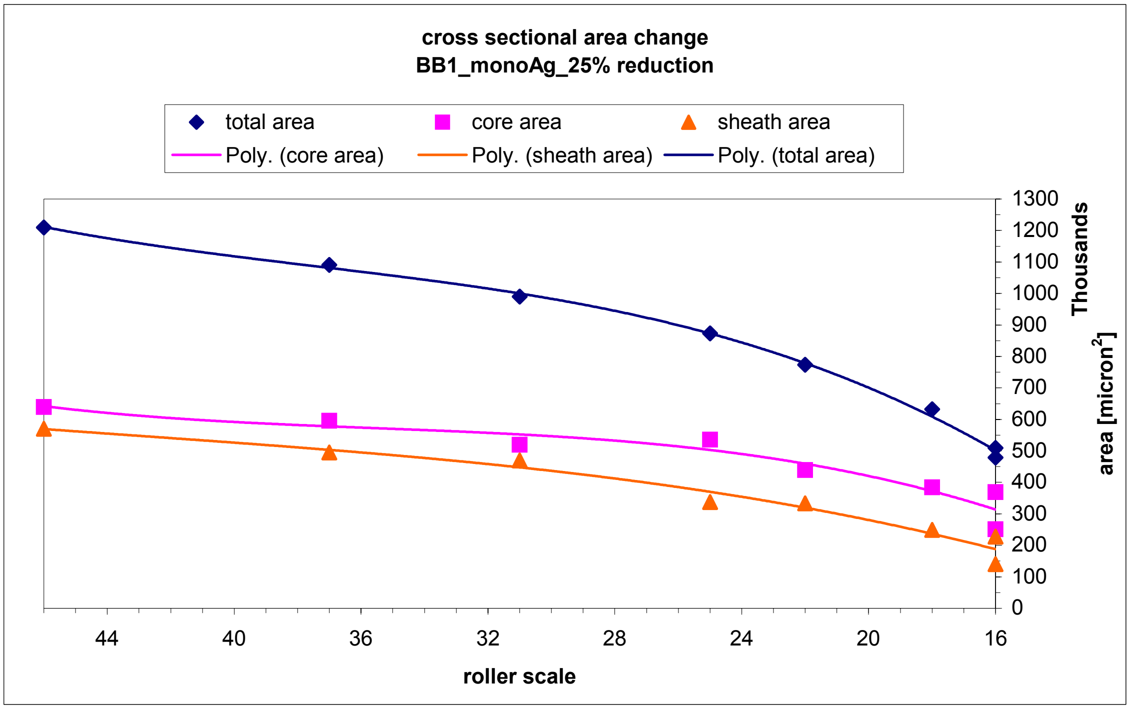

Fig.A2.1 Area change for BB1 monofilament Ag sheath tape, 25% constant reduction/pass, 0.0500” dia.

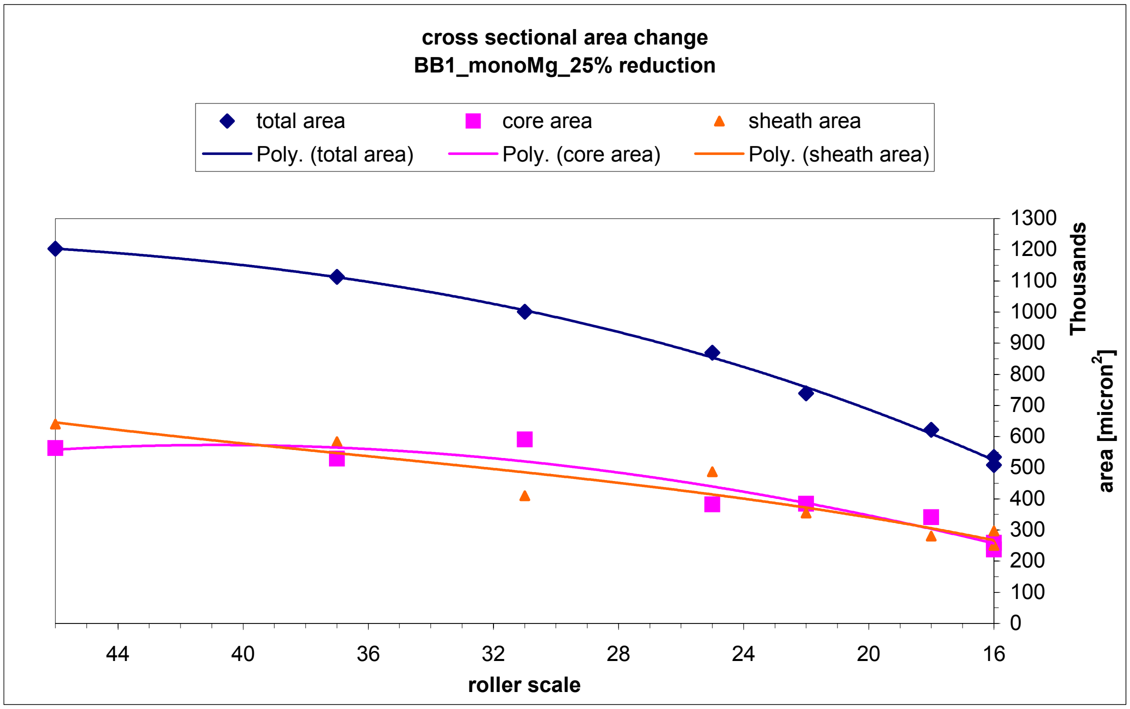

Fig.A2.2 Area change for BB1 monofilament Mg sheath tape, 25% constant reduction/pass, 0.0500” dia.

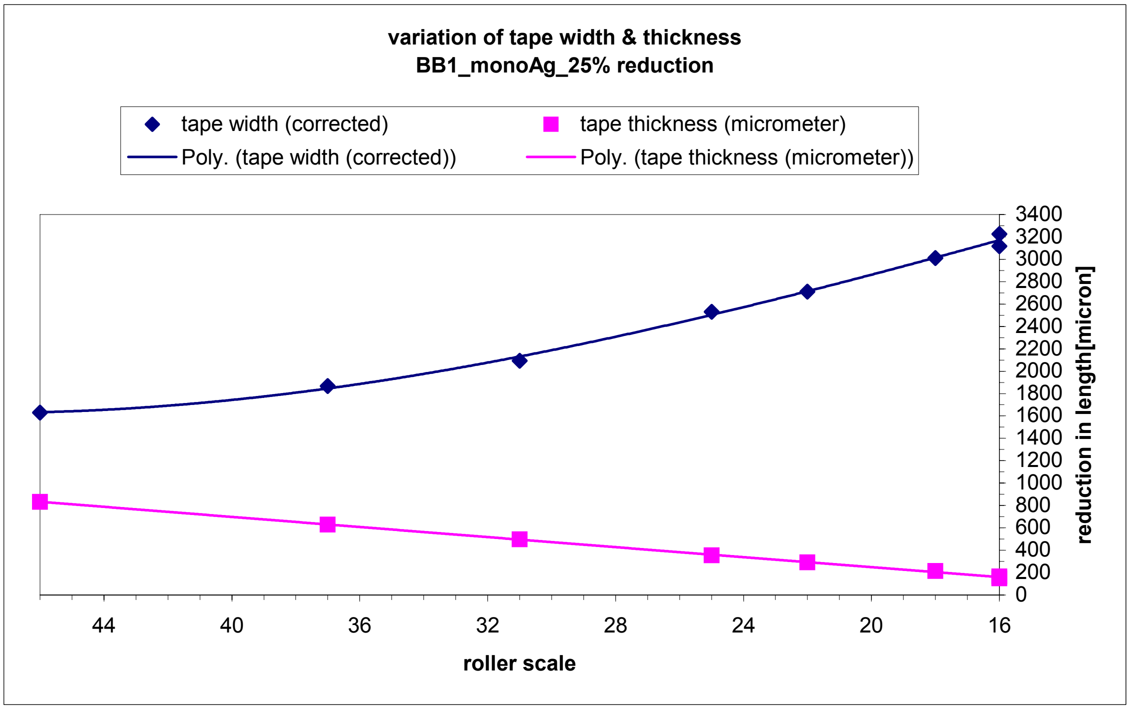

Fig.A2.3 Width and thickness change for BB1 monofilament Ag sheath tape, 25% constant reduction/pass, 0.0500” dia.

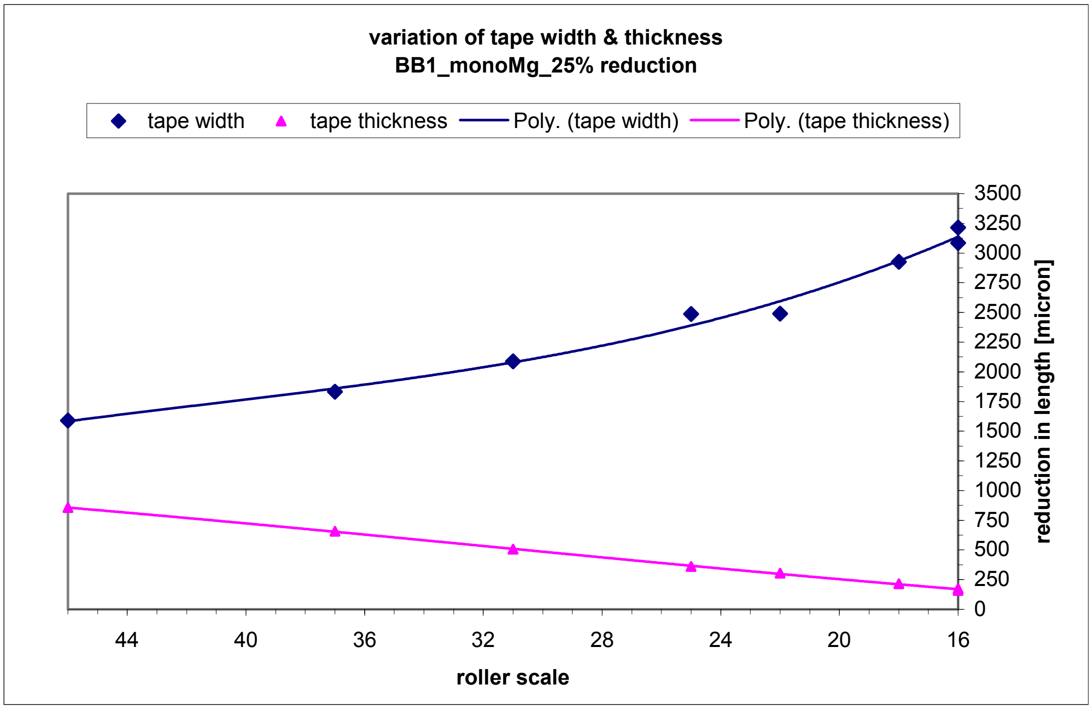

Fig.A2.4 Width and thickness change for BB1 monofilament Mg sheath tape, 25% constant reduction/pass, 0.0500” dia.

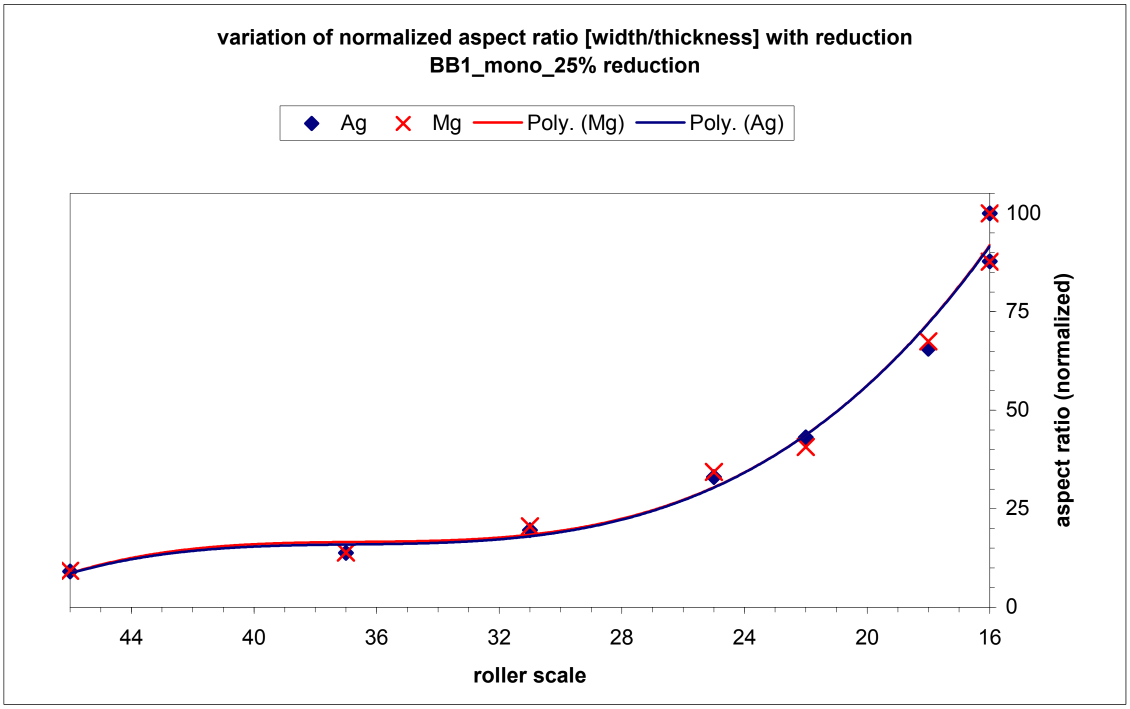

Fig.A2.5 Normalized aspect ratio for BB1 monofilament Ag and Mg sheath tapes, 25% constant reduction/pass, 0.0500” dia.

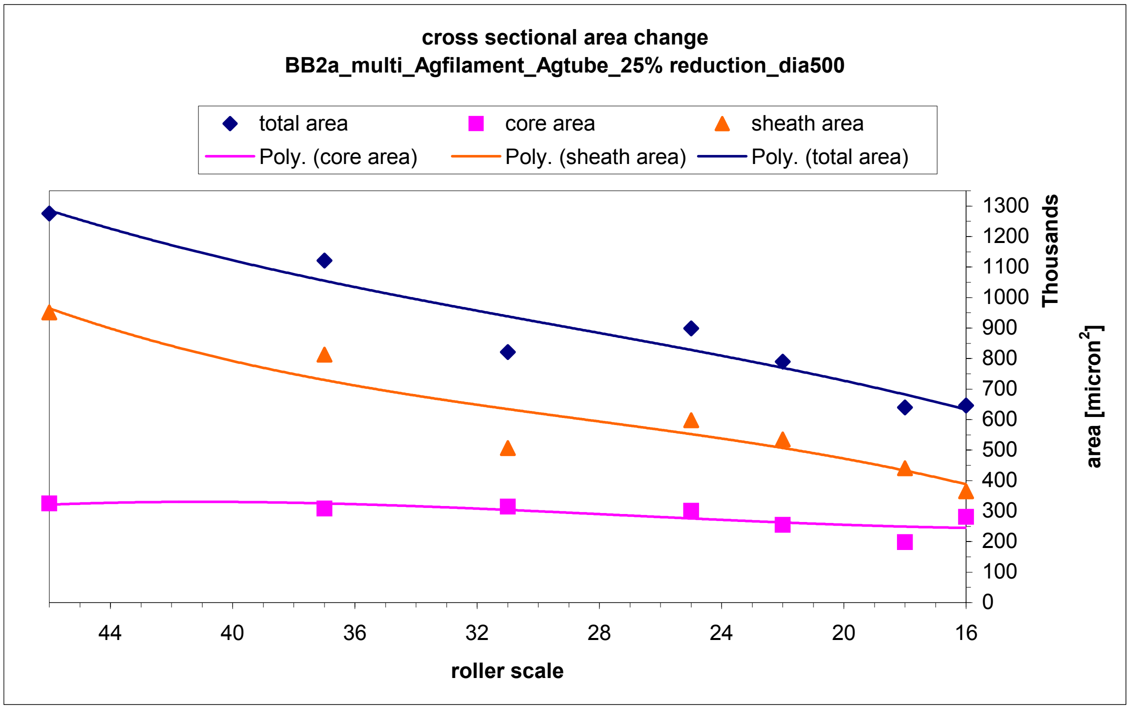

Fig.A2.6 Area change for BB2a multifilament (Ag filament-Ag tube) tape, 25% constant reduction/pass, 0.0500” dia.

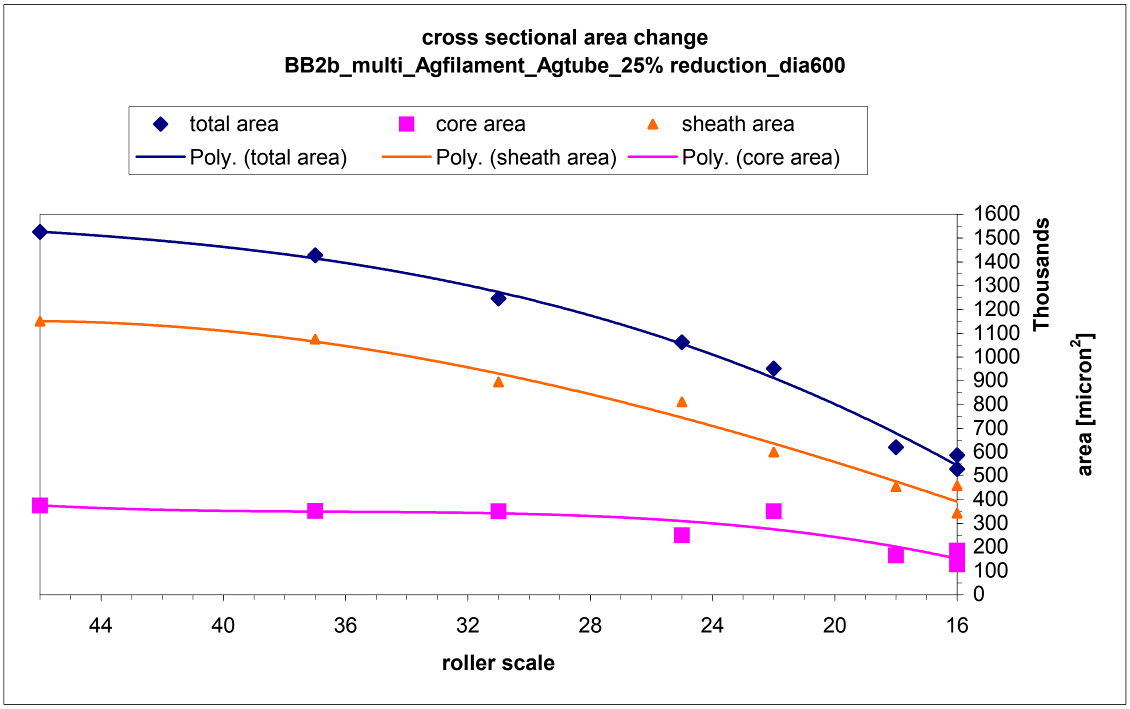

Fig.A2.7 Area change for BB2b multifilament (Ag filament-Ag tube) tape, 25% constant reduction/pass, 0.0600” dia.

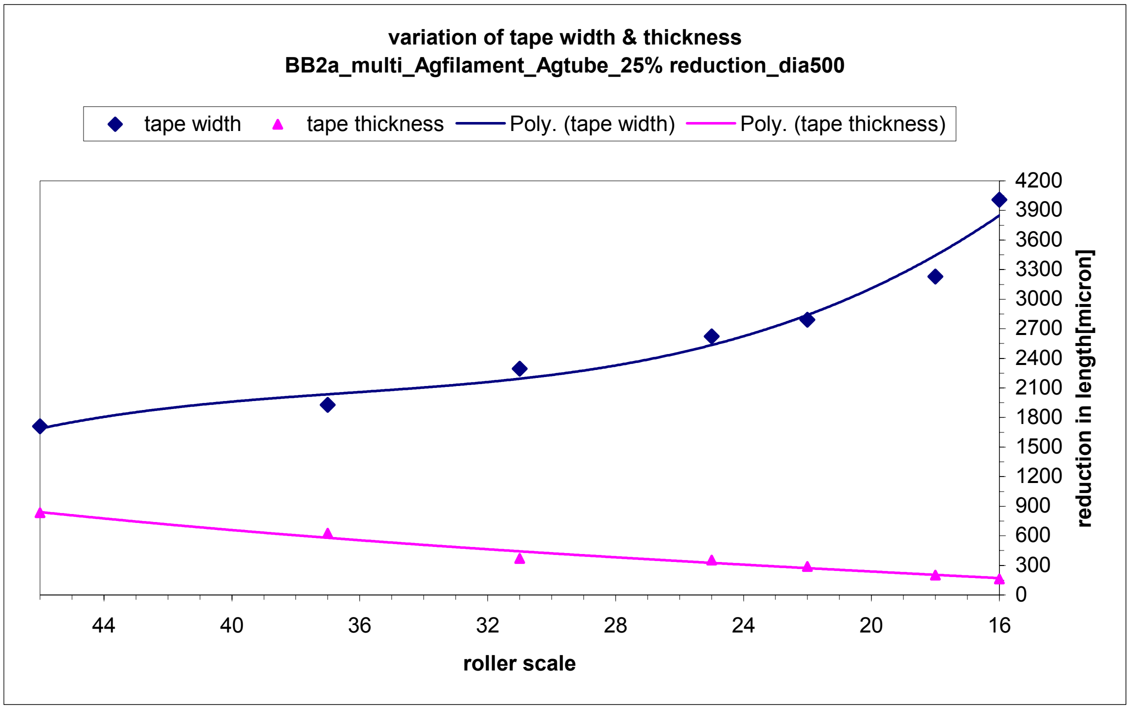

Fig.A2.8 Width and thickness change for BB2a multifilament (Ag filament-Ag tube) tape, 25% CR/P, 0.0500" dia.

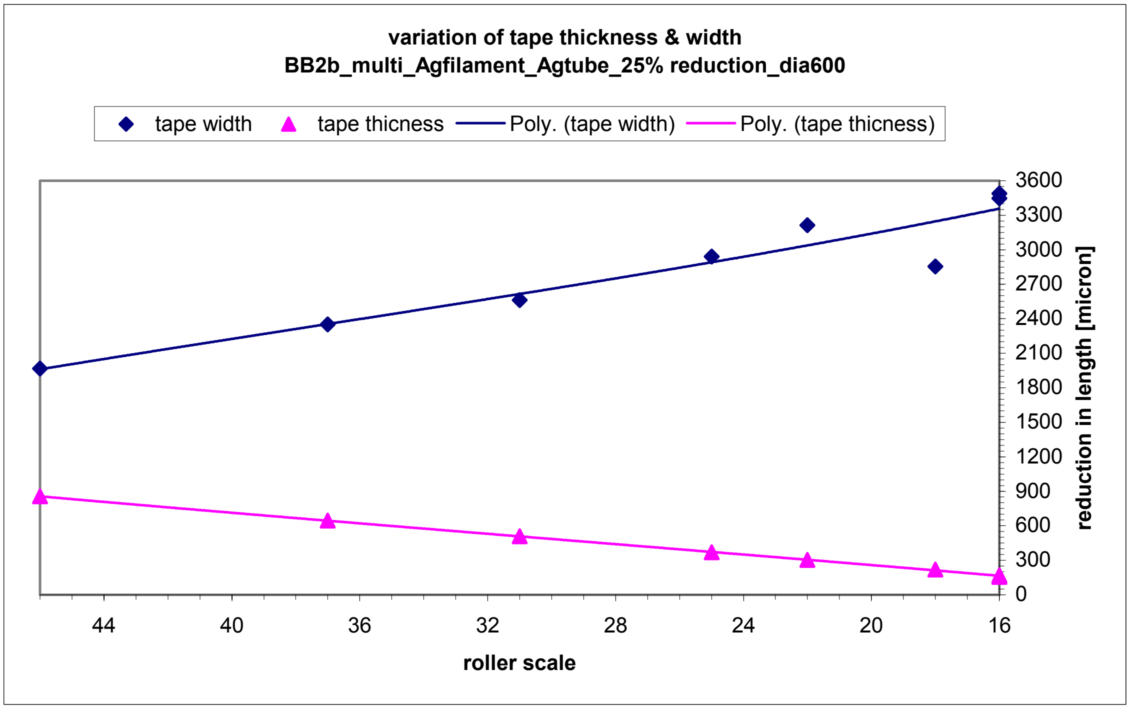

Fig.A2.9 Width and thickness change for BB2b multifilament (Ag filament-Ag tube) tape, 25% CR/P, 0.0600" dia.

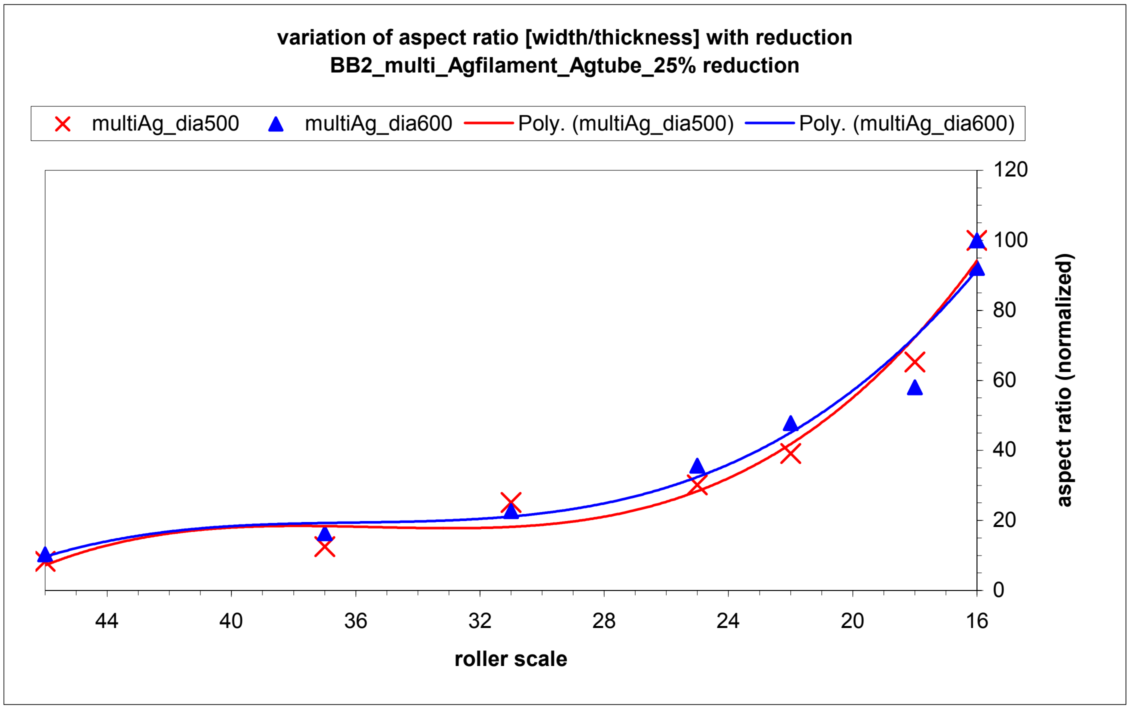

Fig.A2.10 Normalized aspect ratio for BB2 multifilament (Ag filament-Ag tube tapes), 25% CR/P, 0.0500" and 0.0600" dia

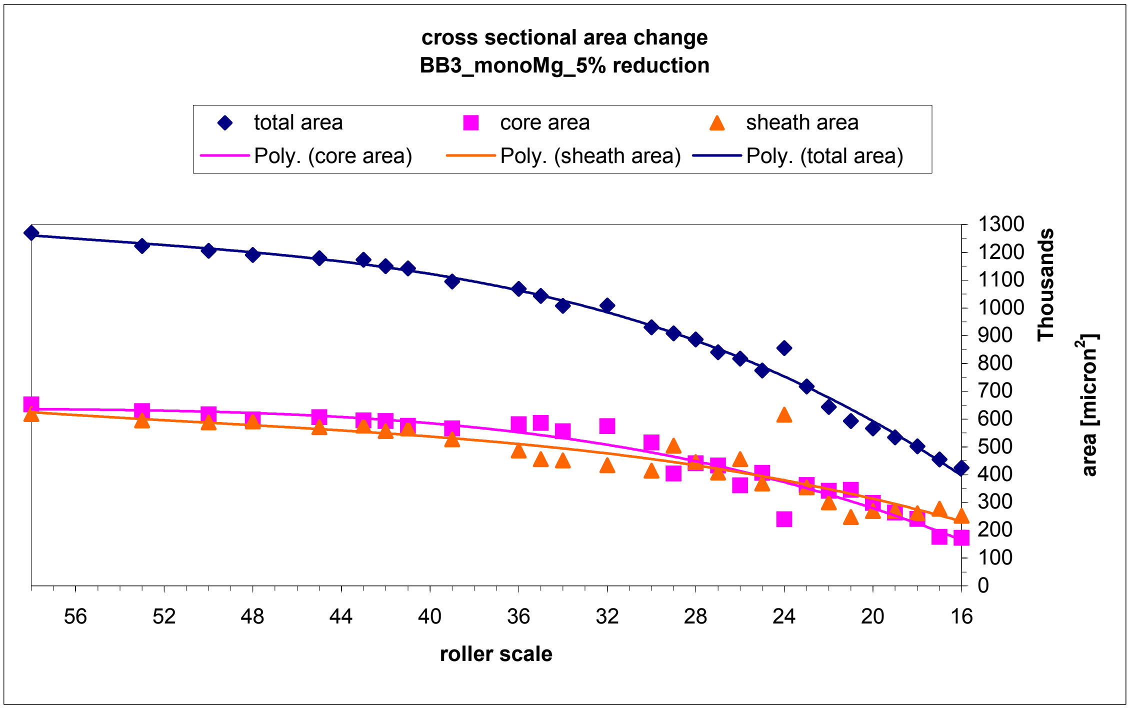

Fig.A2.11 Area change for BB3 monofilament Mg sheath tape, 5% constant reduction/pass, 0.0500" dia.

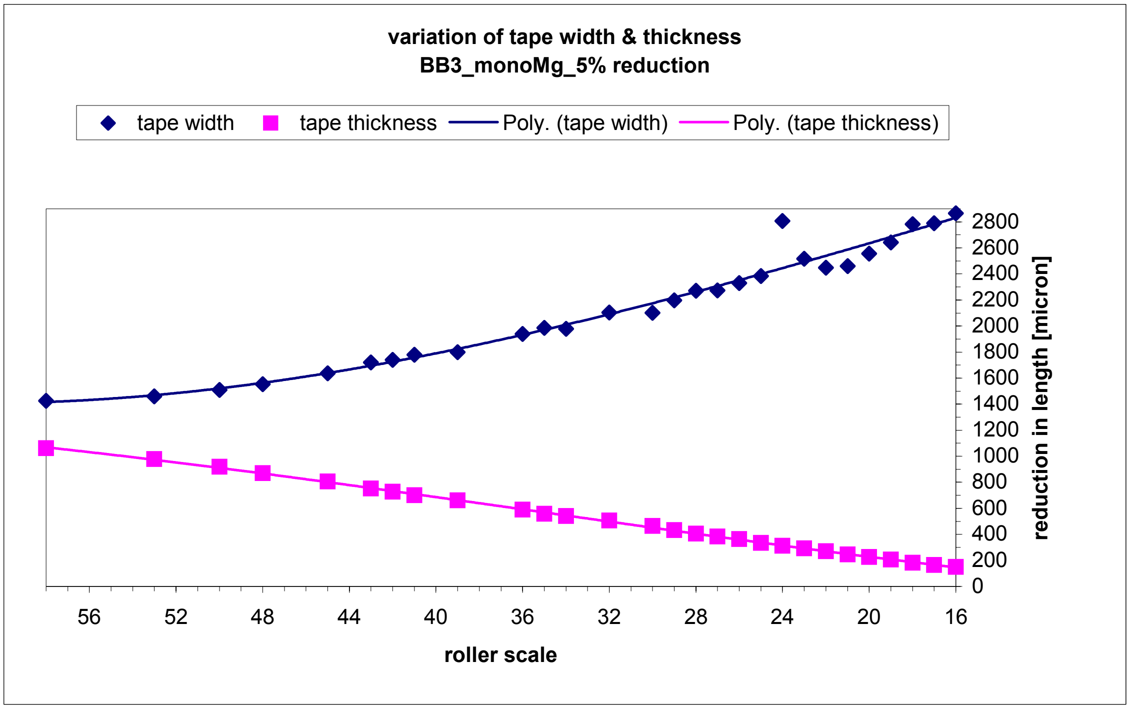

Fig.A2.12 Width and thickness change for BB3 monofilament Mg sheath tape, 5% constant reduction/pass, 0.0500" dia.

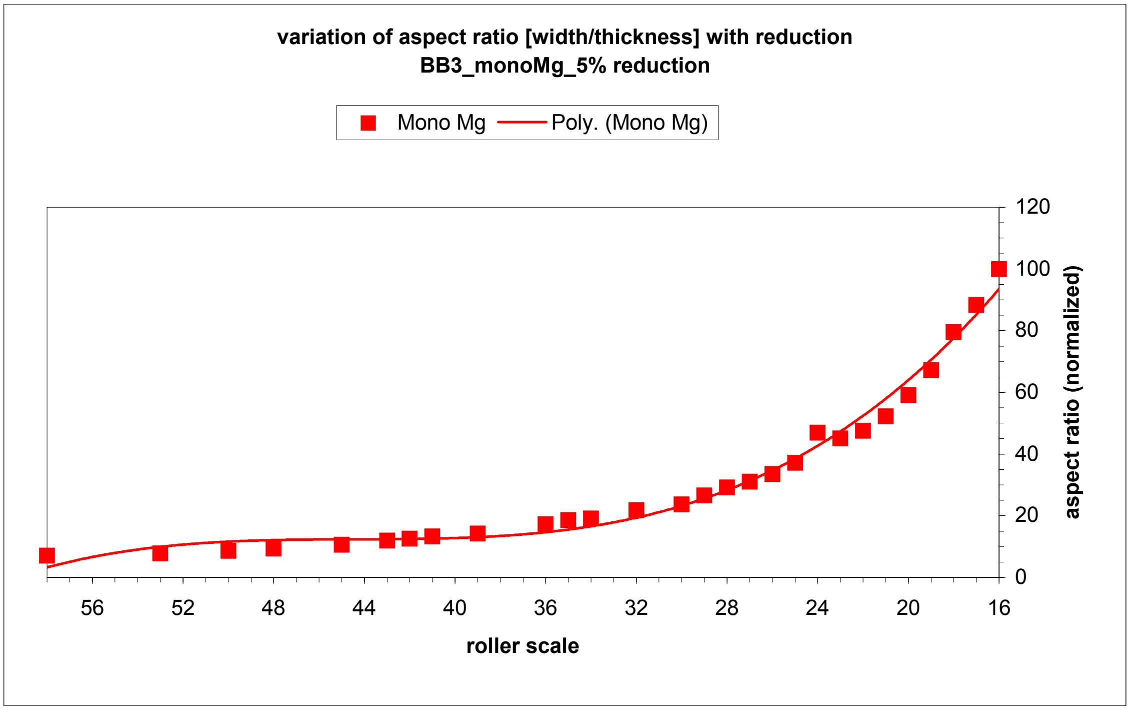

Fig.A2.13 Normalized aspect ratio for BB3 monofilament Mg sheath tape, 5% constant reduction/pass, 0.0500" dia.

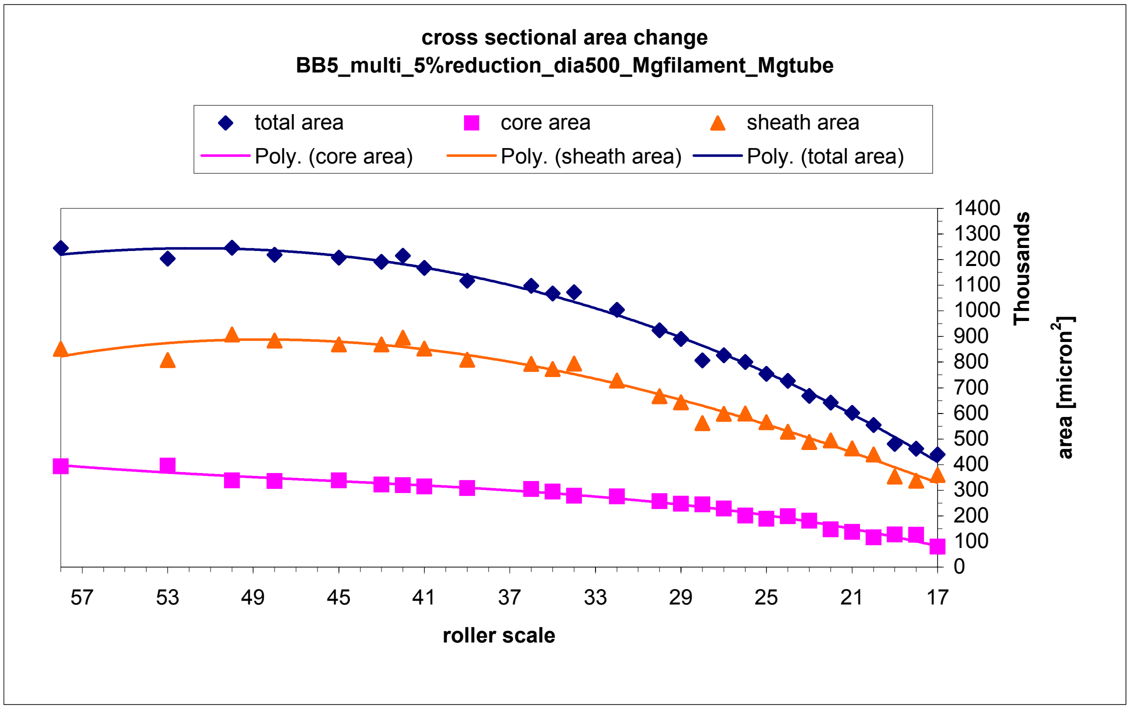

Fig.A2.14 Area change for BB5 multifilament (Mg filament-Mg tube) tape, 5% constant reduction/pass, 0.0500" dia.

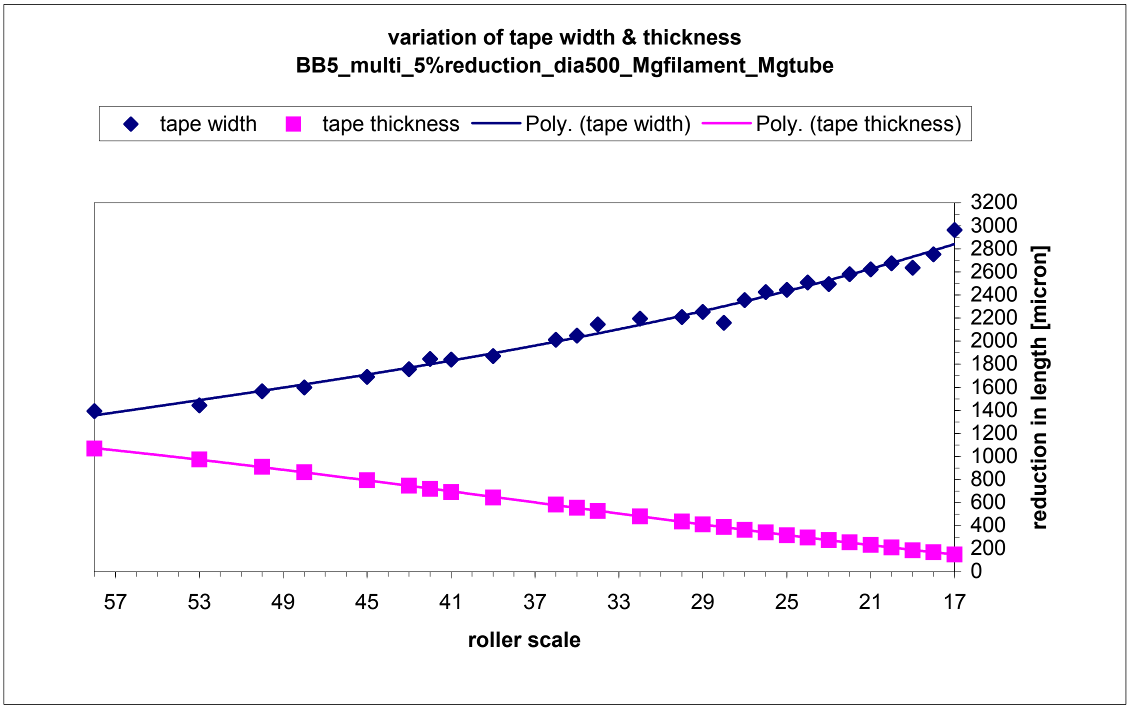

Fig.A2.15 Width and thickness change for BB5 multifilament (Mg filament-Mg tube) tape, 5% constant reduction/pass, 0.0500" dia.

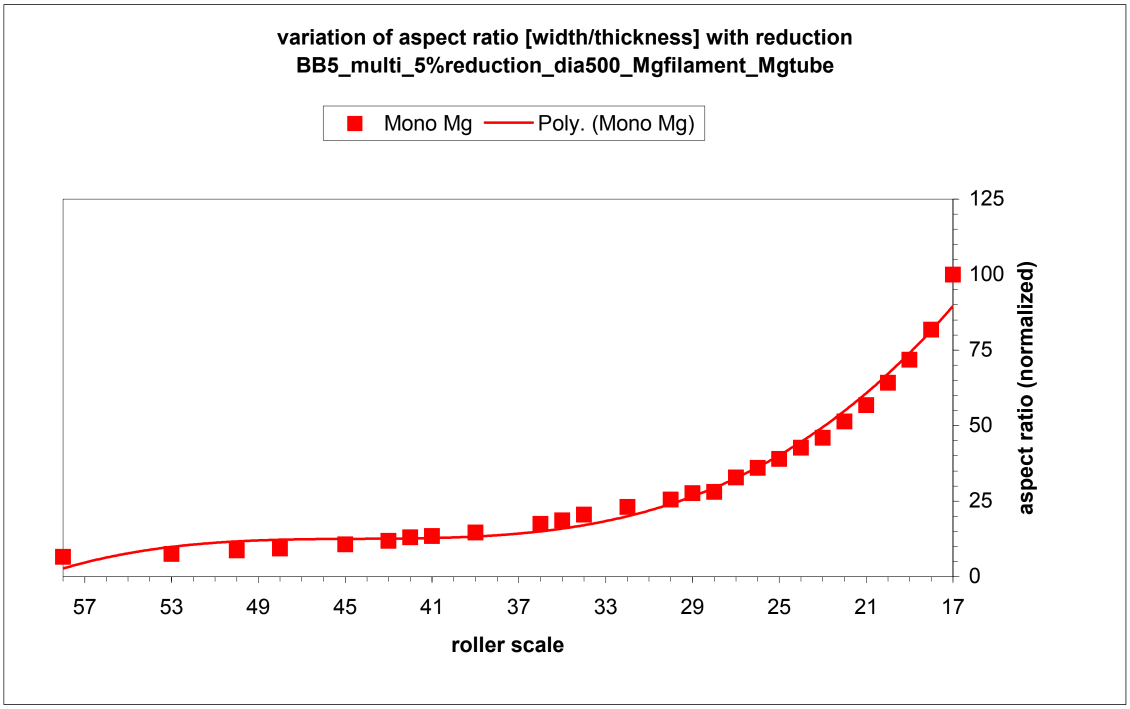

Fig.A2.16 Normalized aspect ratio for BB5 multifilament (Mg filament-Mg tube) tape, 5% constant reduction/pass, 0.0500” dia.

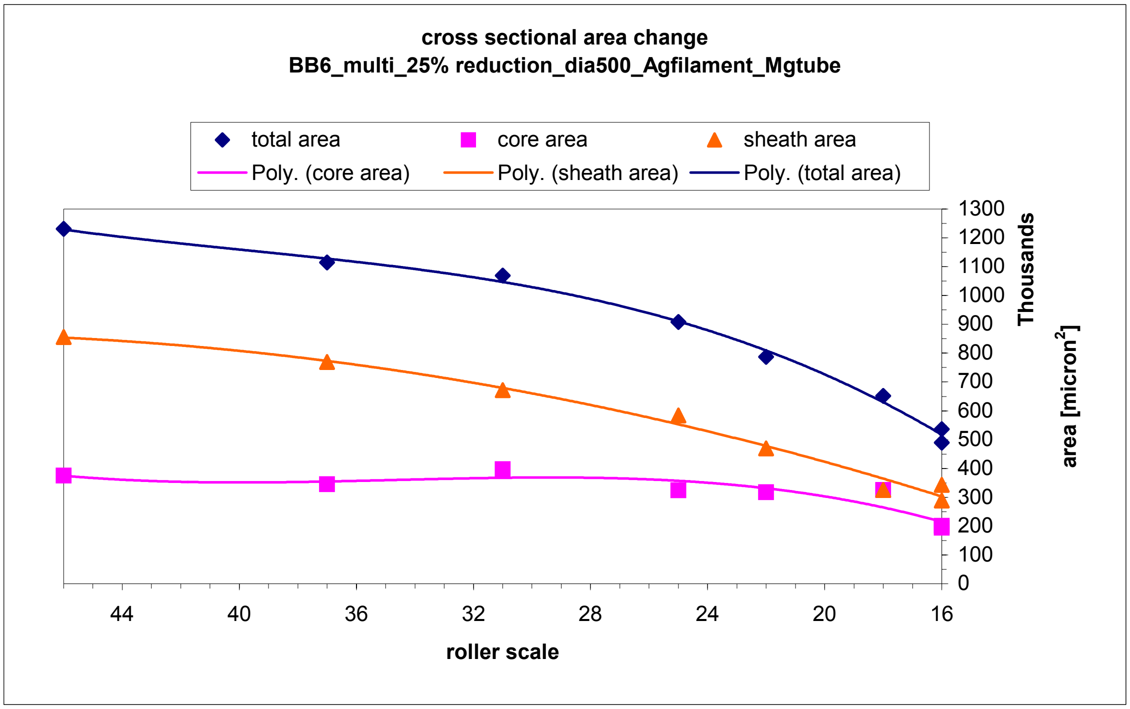

Fig.A2.17 Area change for BB6 multifilament (Ag filament-Mg tube) tape, 25% constant reduction/pass, 0.0500” dia.

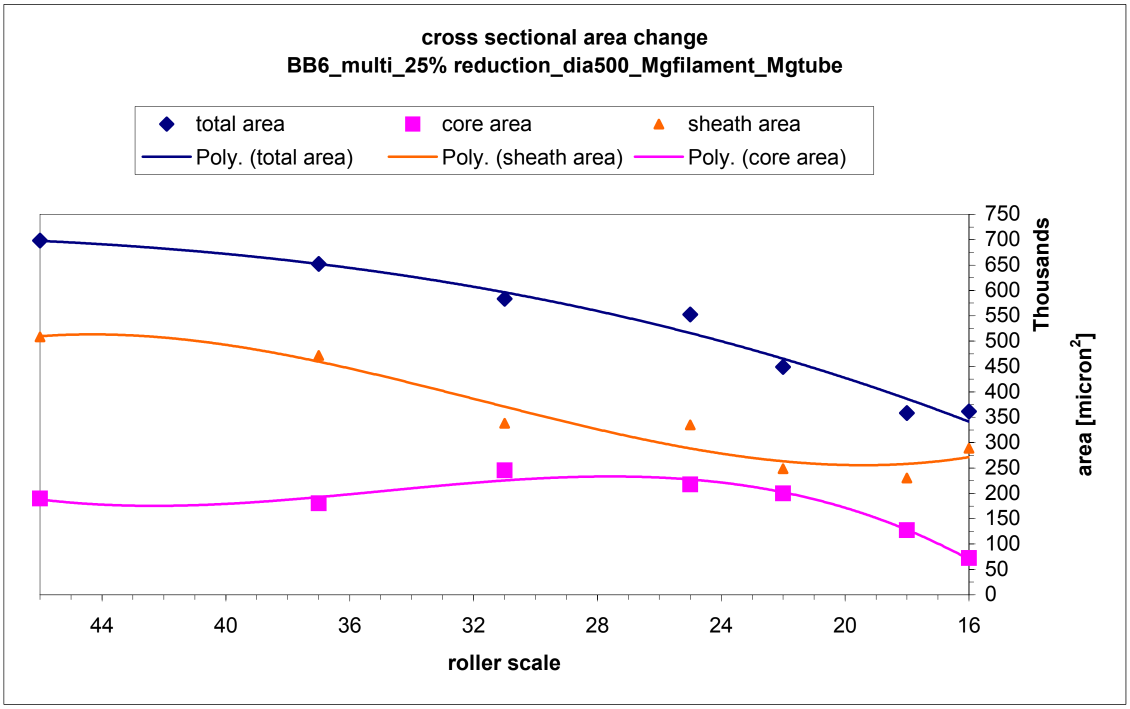

Fig.A2.18 Area change for BB6 multifilament (Mg filament-Mg tube) tape, 25% constant reduction/pass, 0.0500” dia.

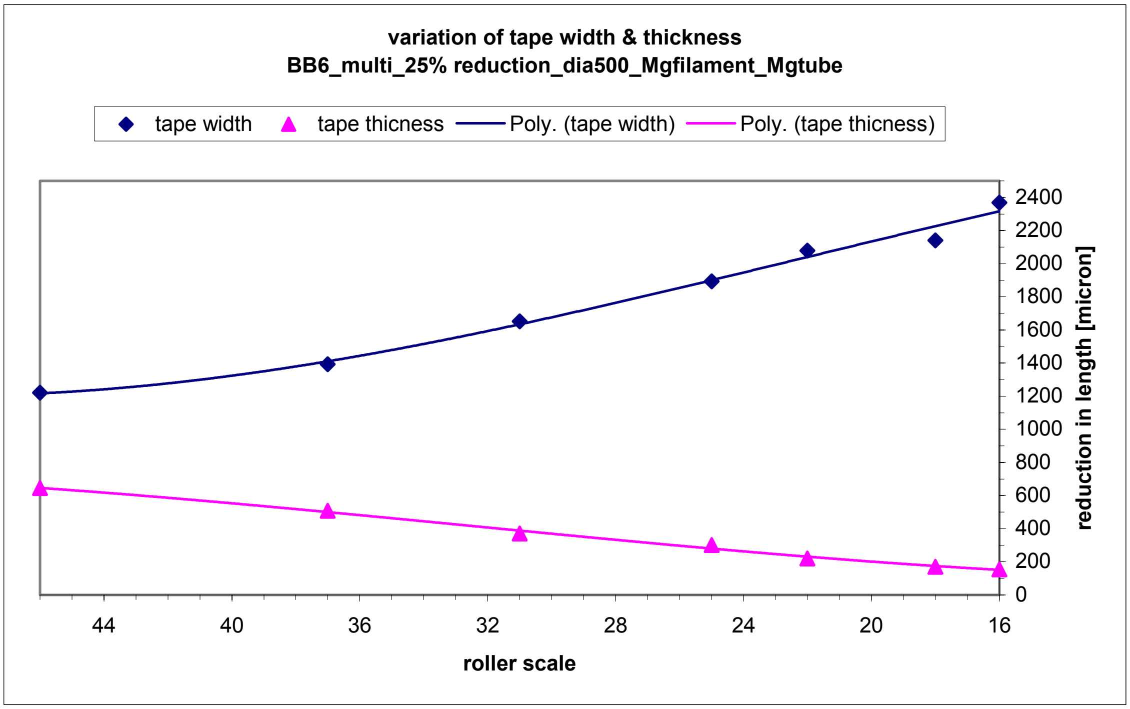

Fig.A2.19 Width and thickness change for BB6 multifilament (Mg filament-Mg tube) tape, 25% constant reduction/pass, 0.0500” dia.

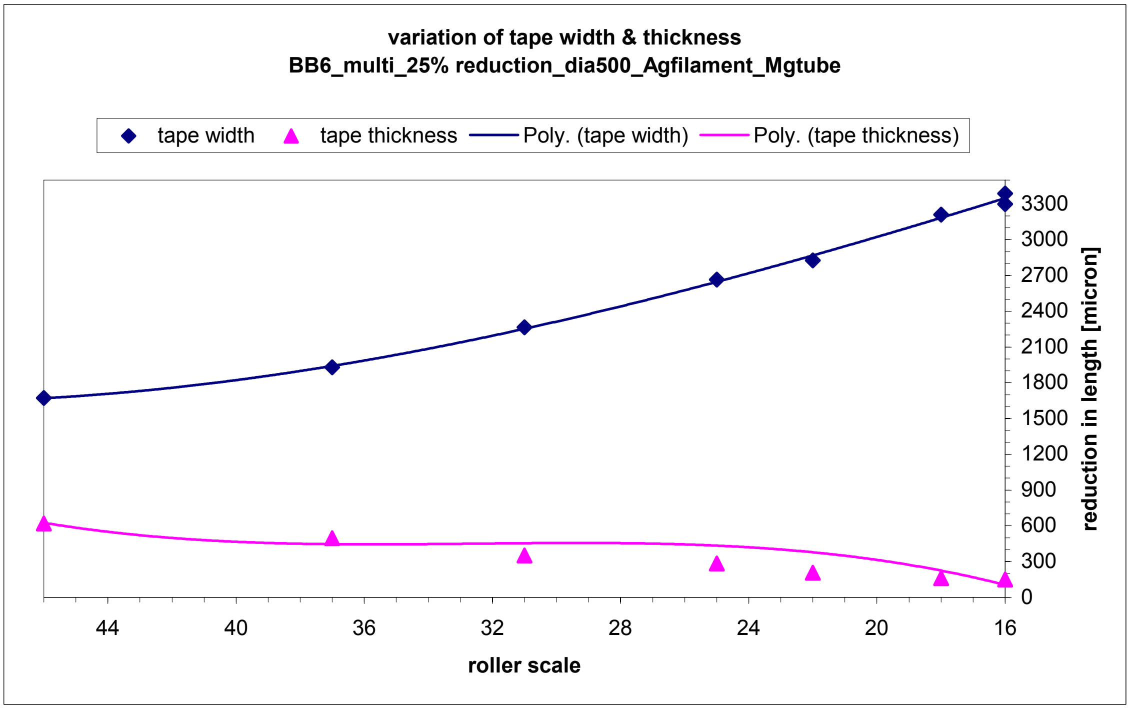

Fig.A2.20 Width and thickness change for BB6 multifilament (Ag filament-Mg tube) tape, 25% constant reduction/pass, 0.0500” dia.

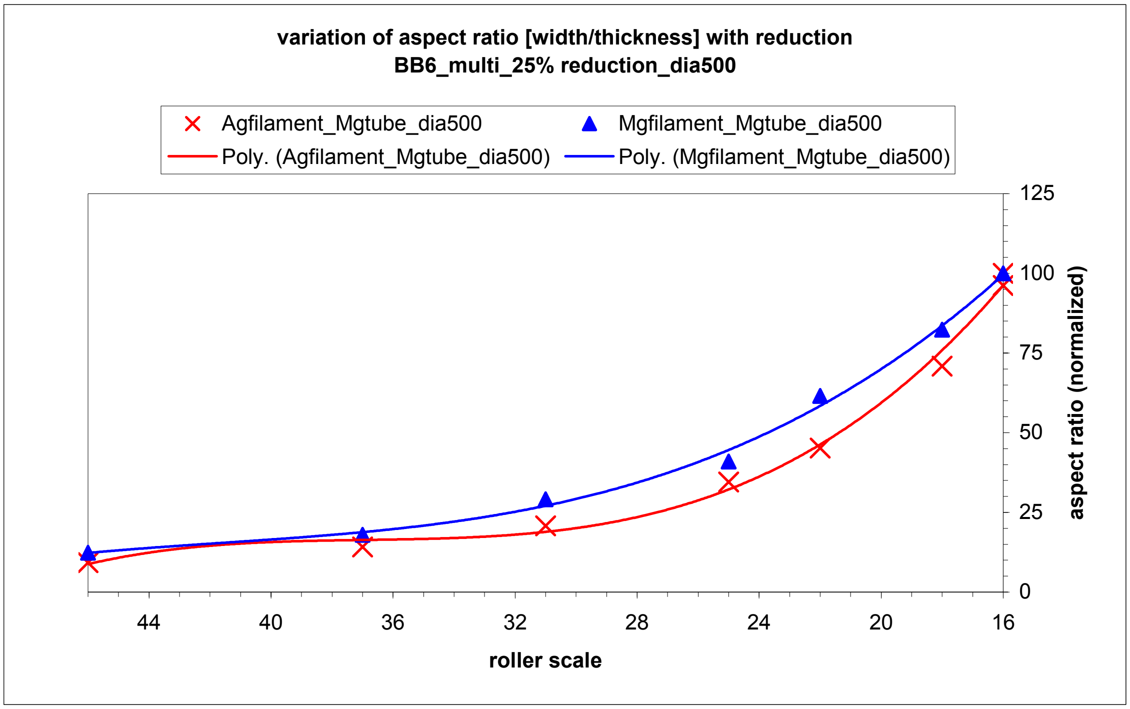

Fig.A2.21Normalized aspect ratio for BB6 multifilament (Ag filament-Mg tube and Mg filament-Mg tube) tapes, 25% constant reduction/pass, 0.0500” dia.

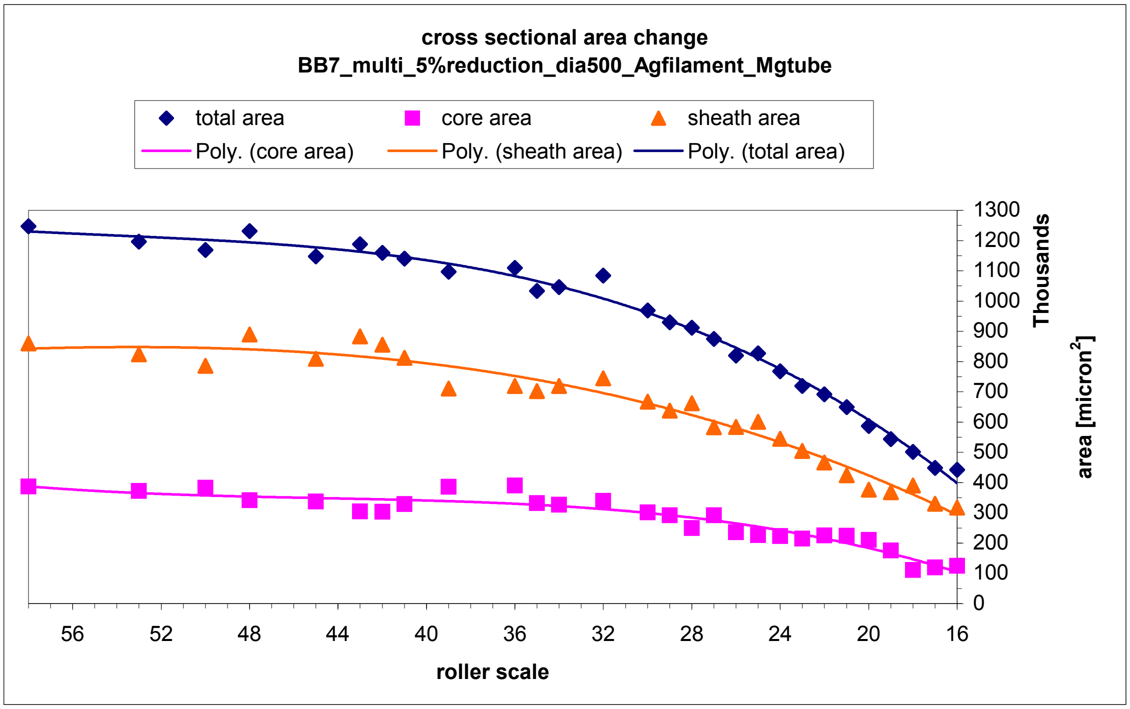

Fig.A2.22 Area change for BB7 multifilament (Ag filament-Mg tube) tape, 5% constant reduction/pass, 0.0500" dia.

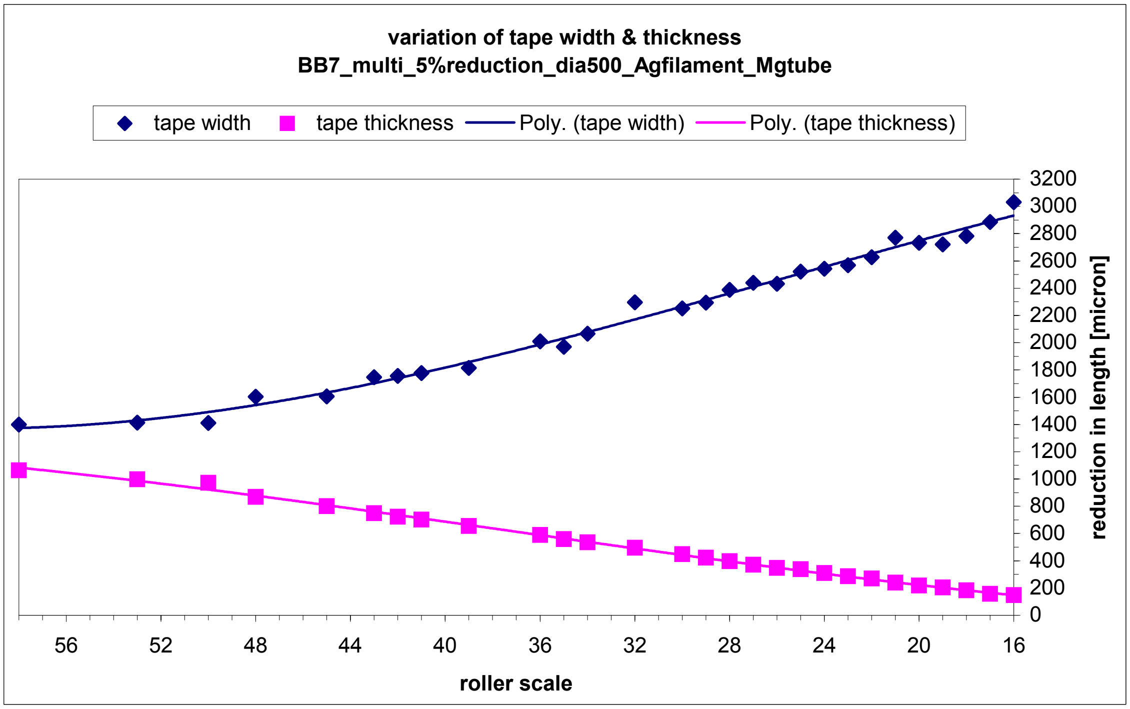

Fig.A2.23 Width and thickness change for BB7 multifilament (Ag filament-Mg tube) tape, 5% constant reduction/pass, 0.0500" dia.

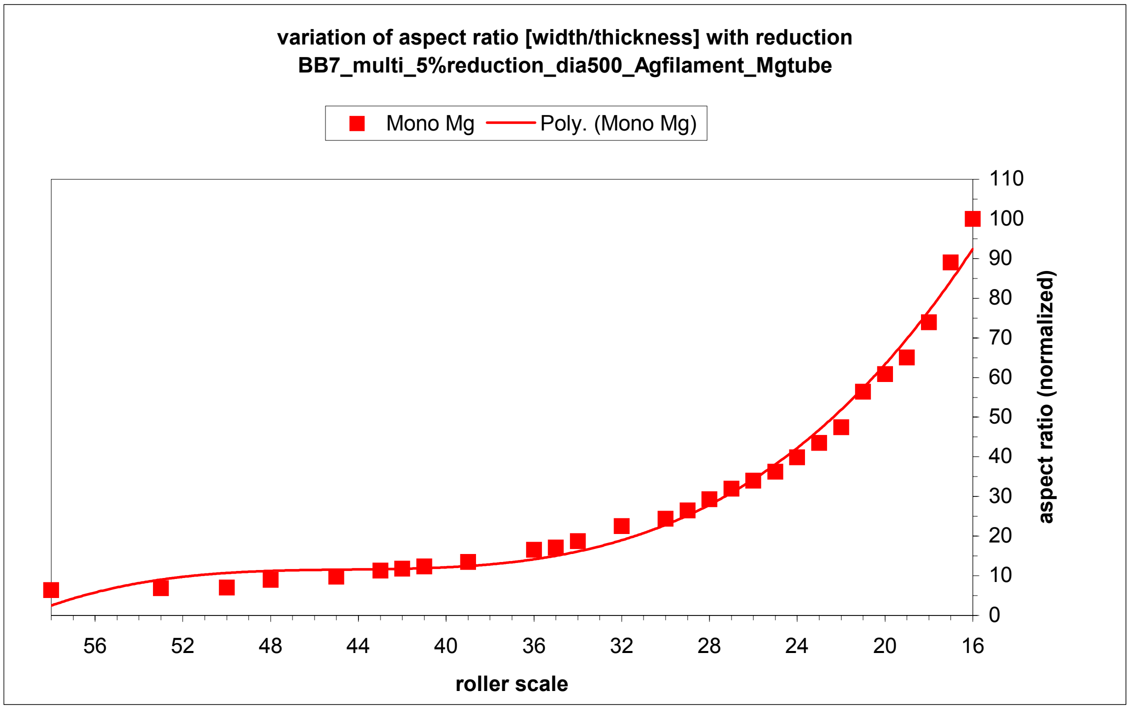

Fig.A2.24 Normalized aspect ratio for BB7 multifilament (Ag filament-Mg tube) tape, 5% constant reduction/pass, 0.0500” dia.

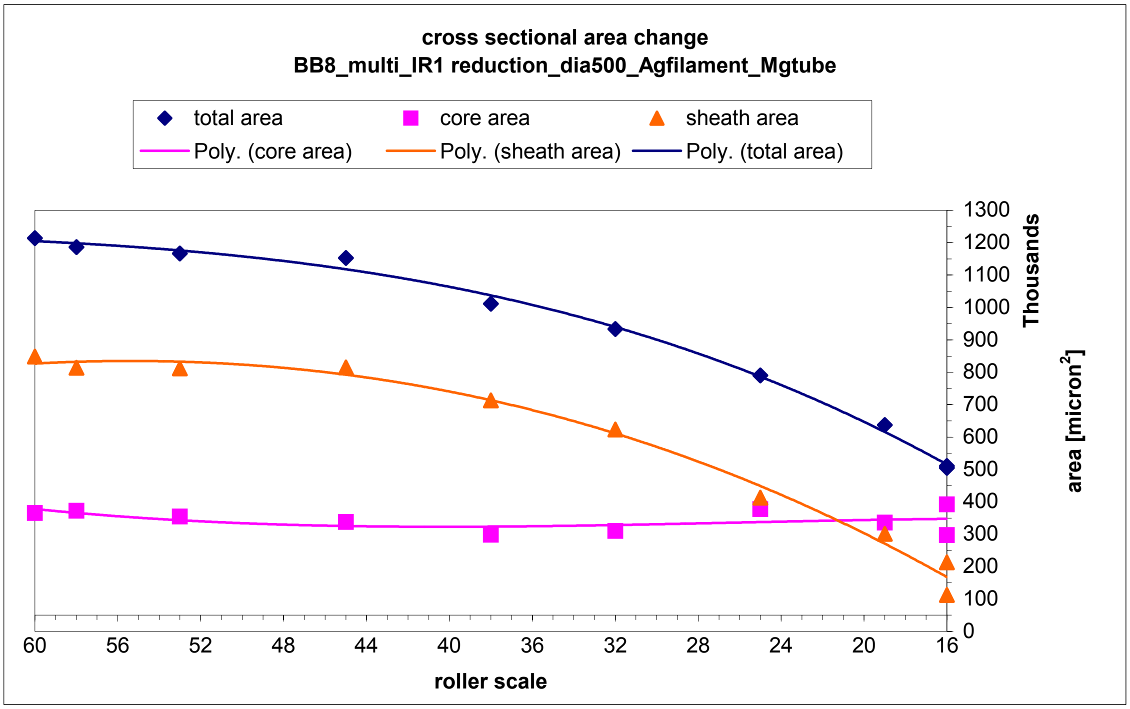

Fig.A2.25 Area change for BB8 multifilament (Ag filament-Mg tube) tape, IR1 varying reduction/pass, 0.0500" dia.

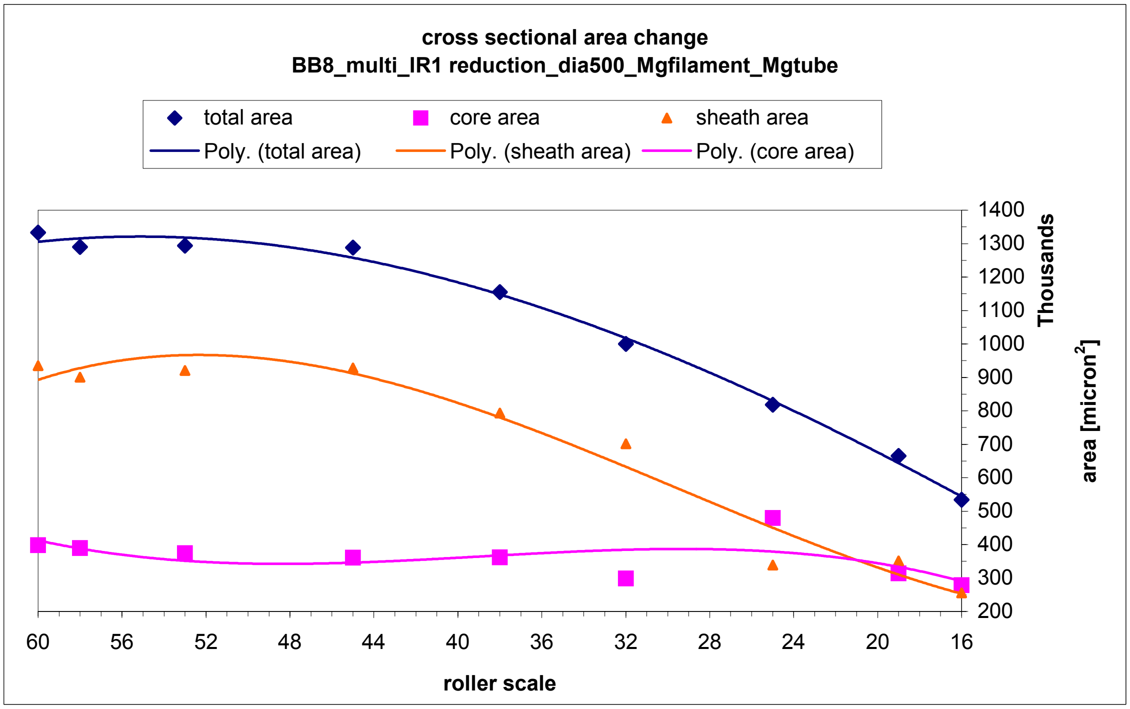

Fig.A2.26 Area change for BB8 multifilament (Mg filament-Mg tube) tape, IR1 varying reduction/pass, 0.0500" dia.

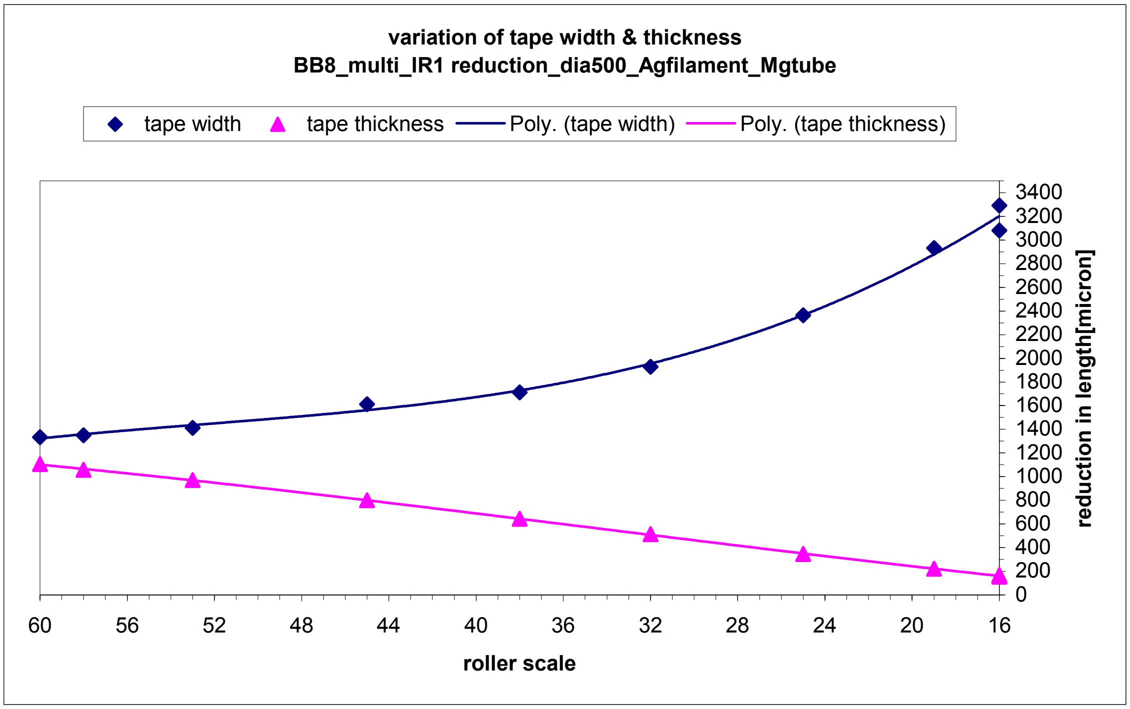

Fig.A2.27 Width and thickness change for BB8 multifilament (Ag filament-Mg tube) tape, IR1 varying reduction/pass, 0.0500” dia.

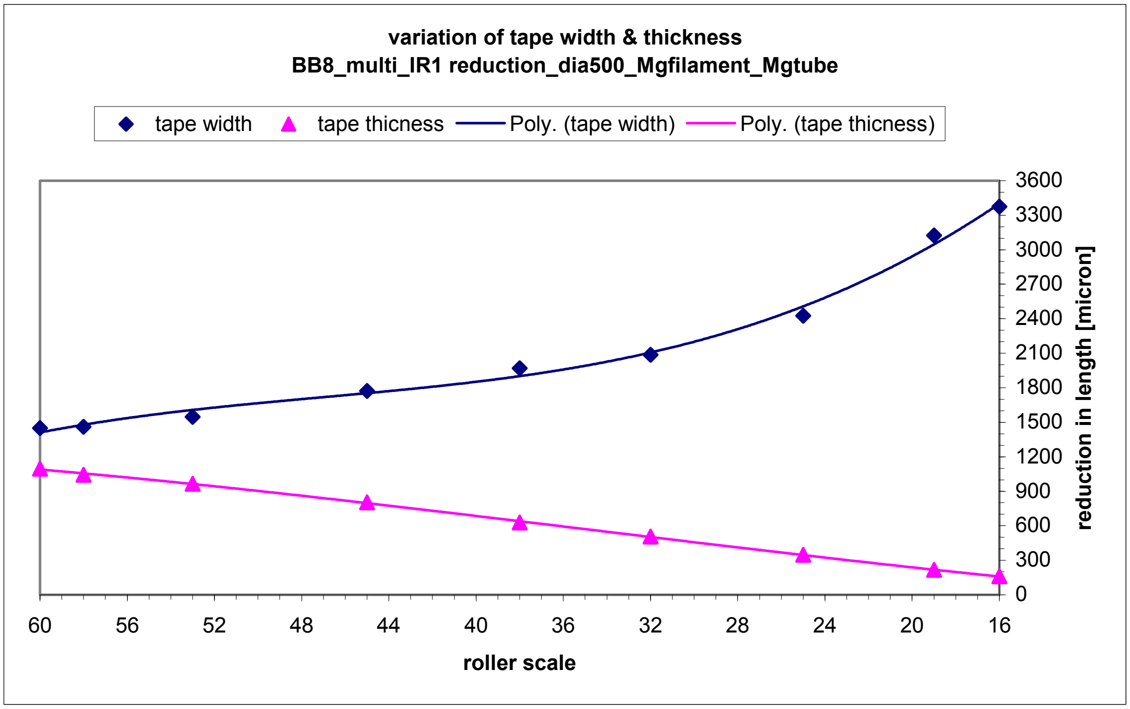

Fig.A2.28 Width and thickness change for BB8 multifilament (Mg filament-Mg tube) tape, IR1 varying reduction/pass, 0.0500” dia.

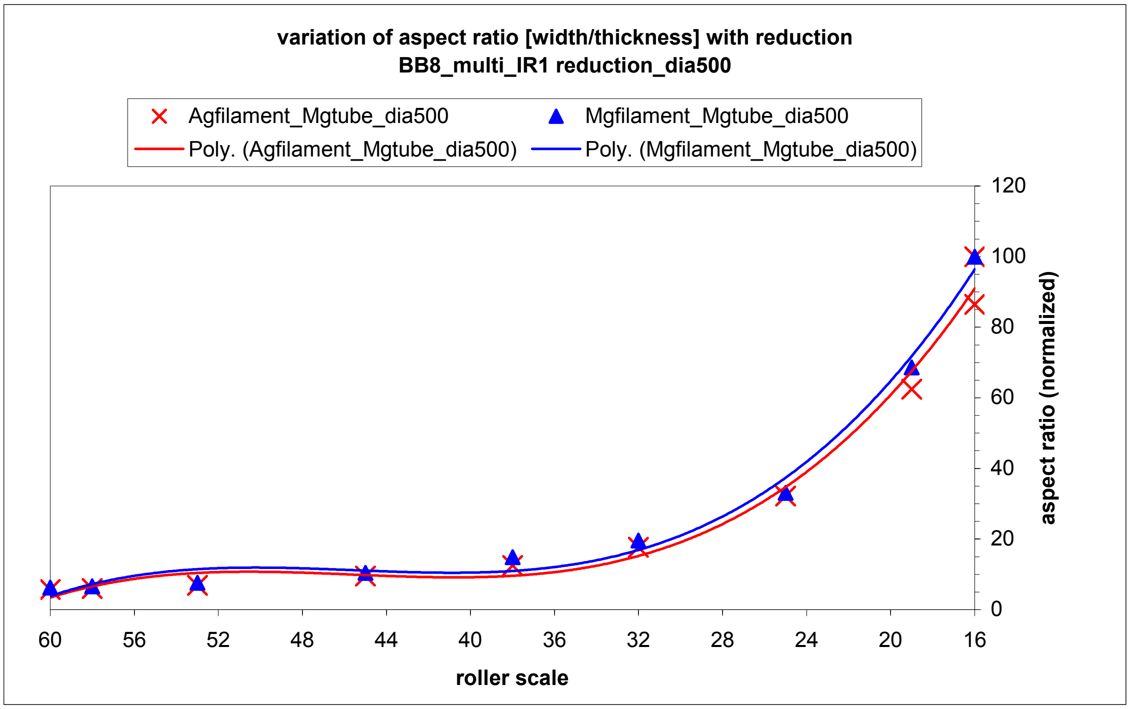

Fig.A2.29 Normalized aspect ratio for BB8 multifilament (Ag filament-Mg tube and Mg filament-Mg tube) tapes, IR1 varying reduction/pass, 0.0500" dia.

APPENDIX 3

SEM (BSE) IMAGES OF MONO AND MUTIFILAMENT WIRES TRANSVERSE CROSS SECTIONS/CORE-SHEATH INTERFACE

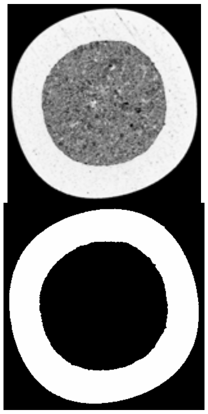

Fig.A3.1 BB4_a50_63xBSE and binary image, Ag monofilament wire with 0.0500” diameter

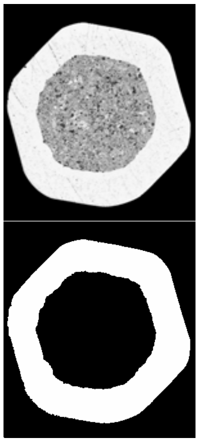

Fig.A33 BB4_h48_63xBSE and binary image, Ag monofilament hexagonal wire with 0.0480” diameter

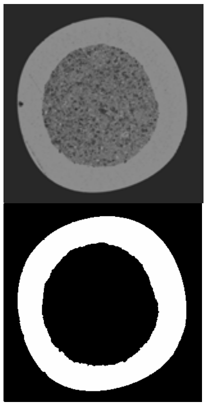

Fig.A3.2 BB4_m50_63xBSE and binary image, Mg monofilament wire with 0.0500” diameter

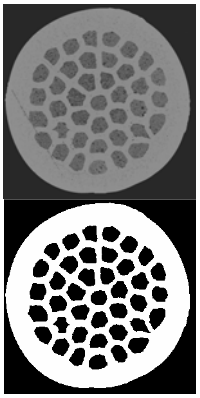

Fig.A3.4 BB4_m60_63xBSE and binary image, Mg FILAMENT-Mg TUBE multifilament wire with 0.0600” diameter

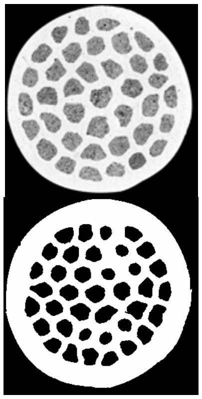

Fig.A3.5 BB4_m76_63xBSE and binary image, Mg FILAMENT-Mg TUBE multifilament wire with 0.0760” diameter

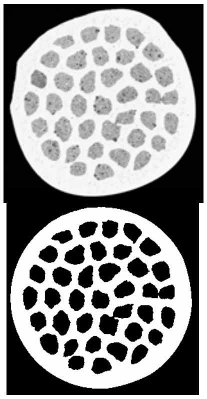

Fig.A3.6 BB4_a54_63xBSE and binary image, Ag FILAMENT-Mg TUBE multifilament wire with 0.0540” diameter

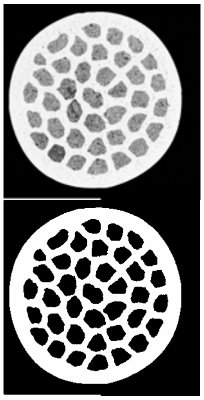

Fig.A3.7 BB4_a60_63xBSE and binary image, Ag FILAMENT-Mg TUBE multifilament wire with 0.0600” diameter

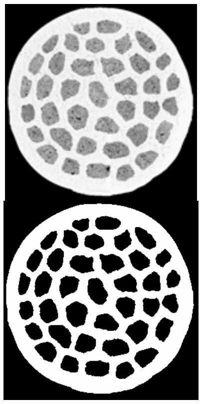

Fig.A3.8 BB4_a68_63xBSE and binary image, Ag FILAMENT-Mg TUBE multifilament wire with 0.0680” diameter

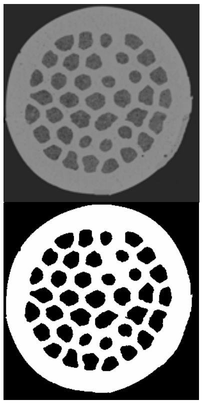

Fig.A3.9 BB4_a76_63xBSE and binary image, Ag FILAMENT-Mg TUBE multifilament wire with 0.0760” diameter

Fig.A3.10 BB4_a86_63xBSE and binary image, Mg FILAMENT-Ag TUBE multifilament wire with 0.0860” diameter

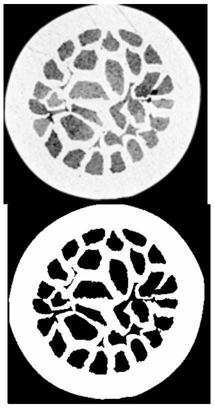

Fig.A3.11 BB4_a96_63xBSE and binary image, Mg FILAMENT-Ag TUBE multifilament wire with 0.0960” diamete

APPENDIX 4

SEM (BSE) IMAGES OF 25% REDUCTION 0.0500" DIAMETER Ag TUBE MONOFILAMENT TAPES

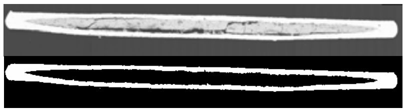
Fig.A4.1 BB1_Ag16dp_100xBSE and binary image


Fig.A4.2 BB1_Ag16_100xBSE and binary image


Fig.A4.3 BB1_Ag18_100xBSE and binary image


Fig.A4.4 BB1_Ag22_100xBSE and binary image


Fig.A4.5 BB1_Ag25_100xBSE and binary image

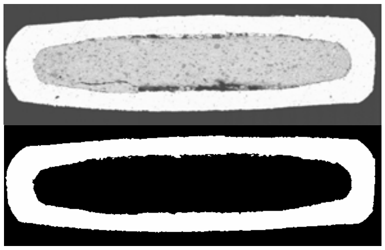
Fig.A4.6 BB1_Ag31_100xBSE and binary image

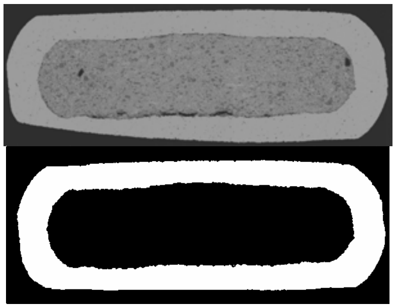
Fig.A4.7 BB1_Ag37_100xBSE and binary image

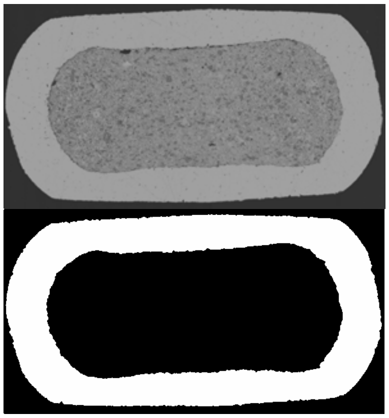
Fig.A4.8 BB1_Ag46_100xBSE and binary image

SEM (BSE) IMAGES OF 25% REDUCTION 0.0500” DIAMETER Mg TUBE MONOFILAMENT TAPES

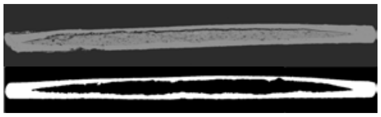

Fig.A4.9 BB1_Mg16tp_100xBSE and binary image

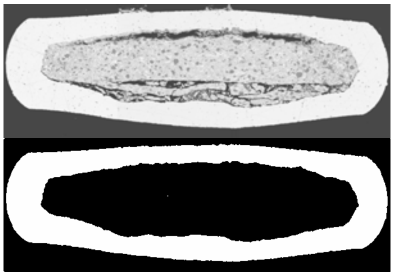

Fig.A4.13 BB1_Mg31_100xBSE and binary image

Fig.A4.10 BB1_Mg18_100xBSE and binary image

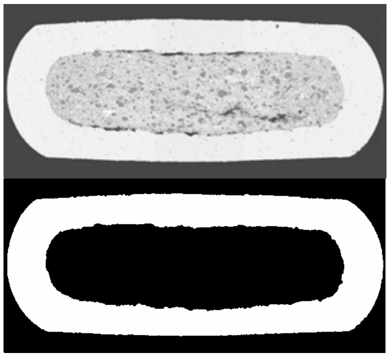

Fig.A4.14 BB1_Mg37_100xBSE and binary image

Fig.A4.11 BB1_Mg22_100xBSE and binary image

Fig.A4.12 BB1_Mg25_100xBSE and binary image

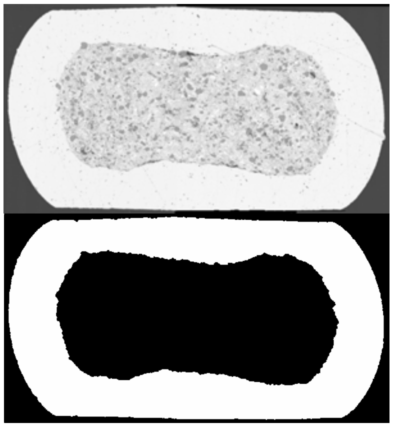

Fig.A4.15 BB1_Mg46_100xBSE and binary image

SEM (BSE) IMAGES OF 25% REDUCTION 0.0500” DIAMETER Ag FILAMENT-Ag TUBE MUTIFILAMENT TAPES

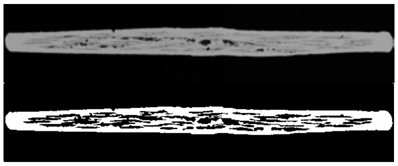

Fig.A4.16 BB2a_Ag16_63xBSE and binary image

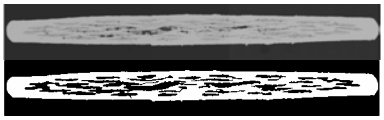

Fig.A4.17 BB2a_Ag18_63xBSE and binary image

Fig.A4.18 BB2a_Ag22_63xBSE and binary image

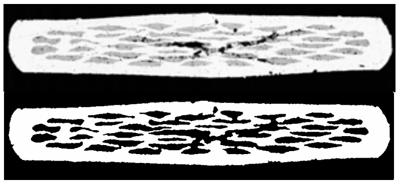

Fig.A4.19 BB2a_Ag25_63xBSE and binary image

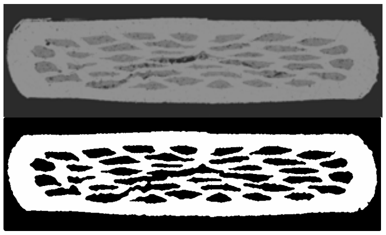

Fig.A4.20 BB2a_Ag31_63xBSE and binary image

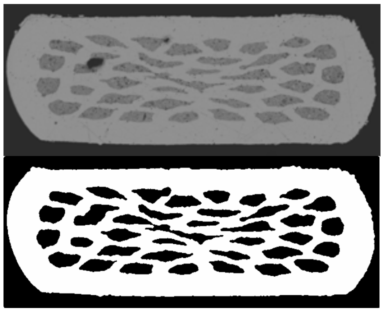

Fig.A4.21 BB2a_Ag37_63xBSE and binary image

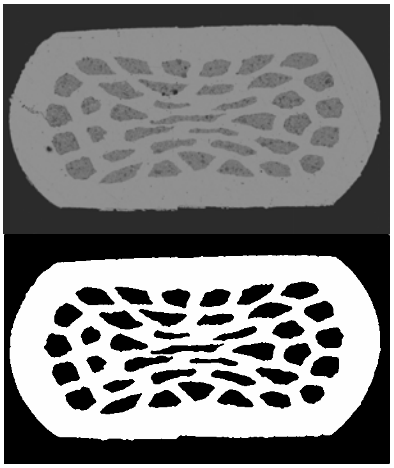

Fig.A4.22 BB2a_Ag46_63xBSE and binary image

SEM (BSE) IMAGES OF 25% REDUCTION 0.0600” DIAMETER Ag FILAMENT-Ag TUBE MUTIFILAMENT TAPES

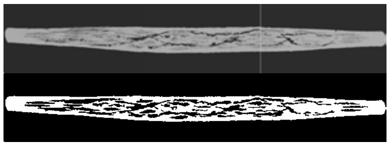

Fig.A4.23 BB2b_Ag16T_63xBSE and binary image

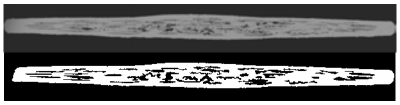

Fig.A4.24 BB2b_Ag16_63xBSE and binary image

Fig.A4.25 BB2b_Ag18_63xBSE and binary image

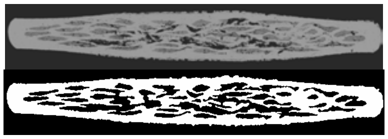

Fig.A4.26 BB2b_Ag22_63xBSE and binary image

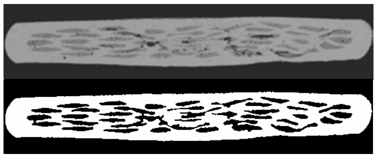

Fig.A4.27 BB2b_Ag25_63xBSE and binary image

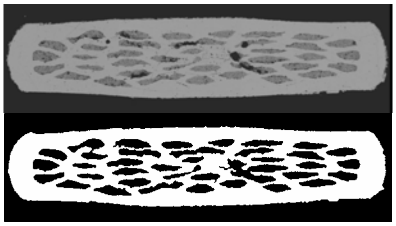

Fig.A4.28 BB2b_Ag31_63xBSE and binary image

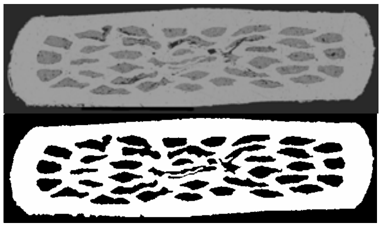

Fig.A4.29 BB2b_Ag37_63xBSE and binary image

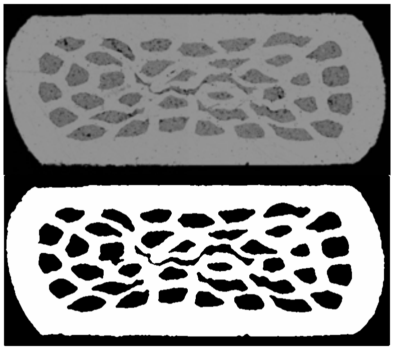

Fig.A4.30 BB2b_Ag46_63xBSE and binary image

SEM (BSE) IMAGES OF 5% REDUCTION 0.0500" DIAMETER Mg TUBE MONOFILAMENT TAPE

Fig.A4.31 BB3_Mg16_63xBSE and binary image

Fig.A4.32 BB3_Mg17_63xBSE and binary image

Fig.A4.33 BB3_Mg18_63xBSE and binary image

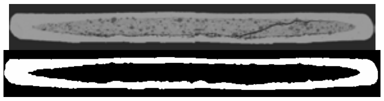

Fig.A4.34 BB3_Mg19_63xBSE and binary image

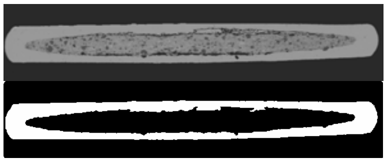

Fig.A4.35 BB3_Mg20_63xBSE and binary image

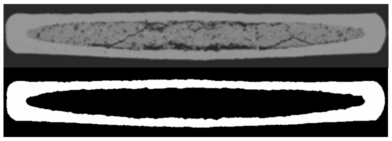

Fig.A4.36 BB3_Mg21_63xBSE and binary image

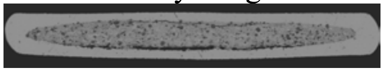

Fig.A4.37 BB3_Mg22_63xBSE and binary image

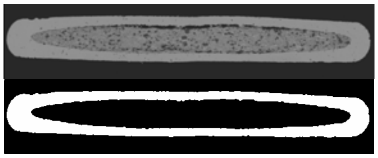

Fig.A4.38 BB3_Mg23_63xBSE and binary image

Fig.A4.39 BB3_Mg24_63xBSE and binary image

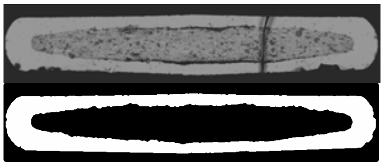

Fig.A4.40 BB3_Mg25_63xBSE and binary image

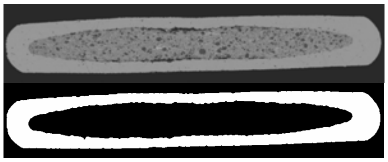

Fig.A4.41 BB3_Mg26_63xBSE and binary image

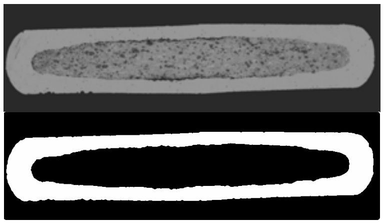

Fig.A4.42 BB3_Mg27_63xBSE and binary image

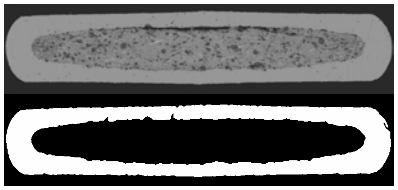

Fig.A4.43 BB3_Mg28_63xBSE and binary image

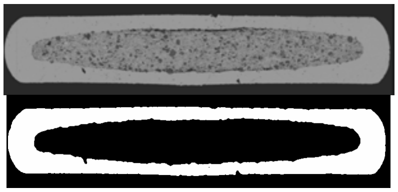

Fig.A4.44 BB3_Mg29_63xBSE and binary image

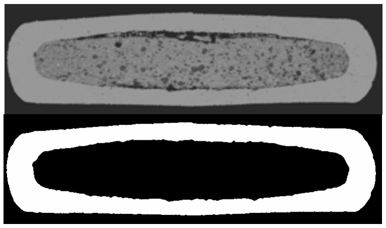

Fig.A4.45 BB3_Mg30_63xBSE and binary image

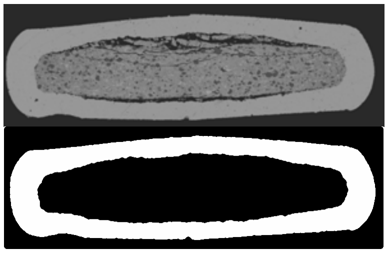

Fig.A4.46 BB3_Mg32_63xBSE and binary image

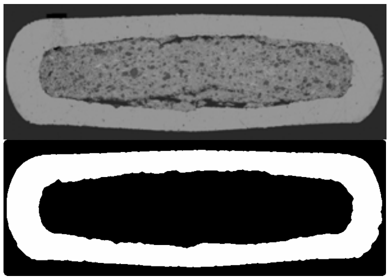

Fig.A4.47 BB3_Mg34_63xBSE and binary image

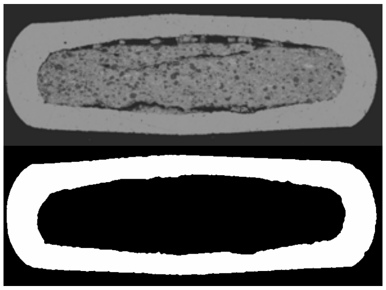

Fig.A4.48 BB3_Mg35_63xBSE and binary image

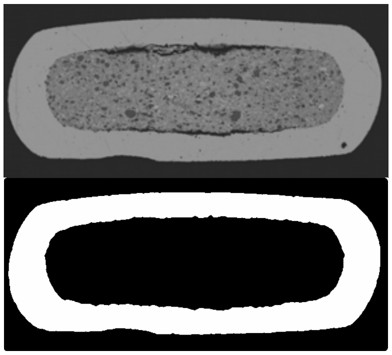
Fig.A4.49 BB3_Mg39_63xBSE and binary image

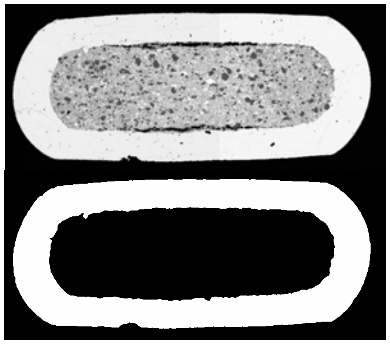
Fig.A4.50 BB3_Mg41_63xBSE and binary image

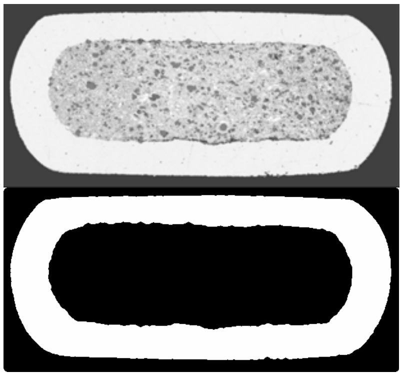
Fig.A4.51 BB3_Mg42_63xBSE and binary image

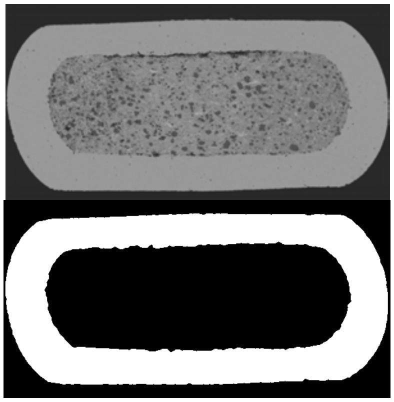
Fig.A4.52 BB3_Mg43_63xBSE and binary image

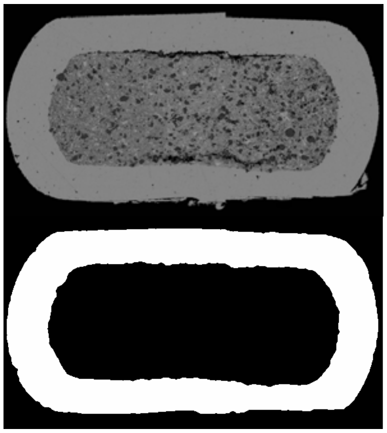
Fig.A4.53 BB3_Mg45_63xBSE and binary image

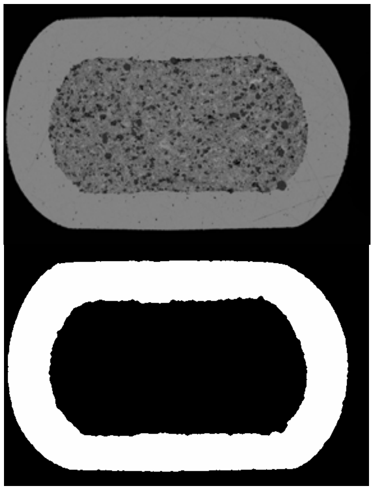

Fig.A4.54 BB3_Mg50_63xBSE and binary image

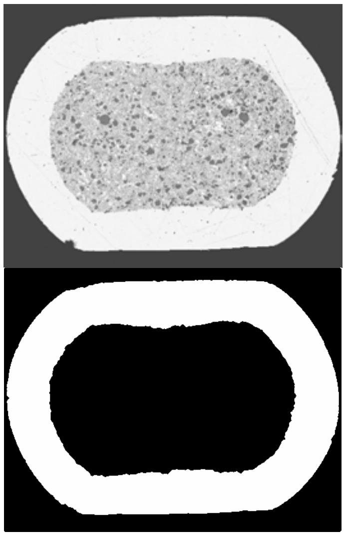

Fig.A4.55 BB3_Mg58_63xBSE and binary image

SEM (BSE) IMAGES OF 5% REDUCTION 0.0500” DIAMETER Mg FILAMENT-Mg TUBE MUTIFILAMENT TAPES

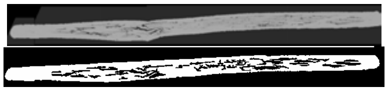
Fig.A4.56 BB5_Mg17_63xBSE and binary image


Fig.A4.57 BB5_Mg18_63xBSE and binary image


Fig.A4.58 BB5_Mg19_63xBSE and binary image

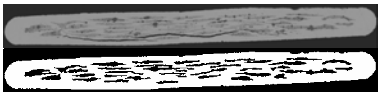
Fig.A4.59 BB5_Mg20_63xBSE and binary image

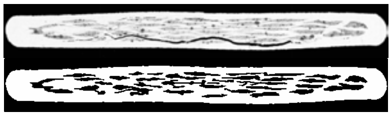
Fig.A4.60 BB5_Mg21_63xBSE and binary image

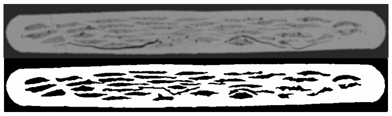
Fig.A4.61 BB5_Mg22_63xBSE and binary image

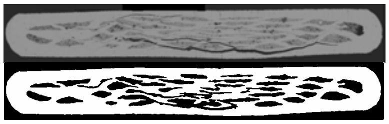
Fig.A4.62 BB5_Mg23_63xBSE and binary image

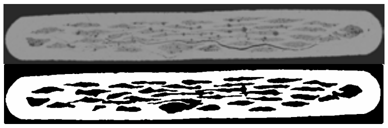
Fig.A4.63 BB5_Mg24_63xBSE and binary image

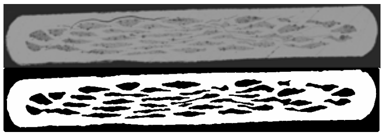
Fig.A4.64 BB5_Mg25_63xBSE and binary image

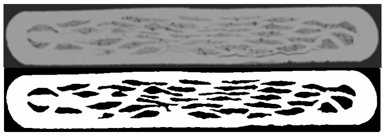
Fig.A4.65 BB5_Mg26_63xBSE and binary image

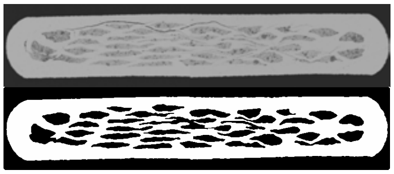
Fig.A4.66 BB5_Mg27_63xBSE and binary image

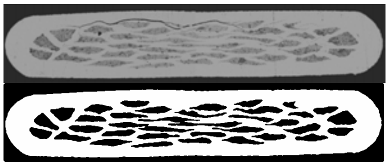

Fig.A4.67 BB5_Mg28_63xBSE and binary image

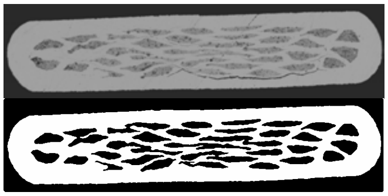

Fig.A4.68 BB5_Mg29_63xBSE and binary image

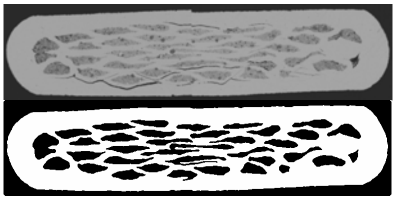

Fig.A4.69 BB5_Mg30_63xBSE and binary image

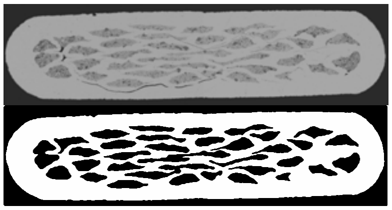

Fig.A4.70 BB5_Mg32_63xBSE and binary image

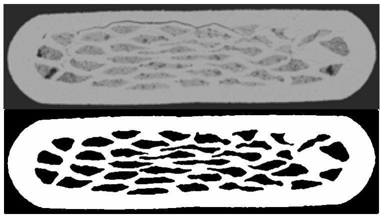

Fig.A4.71 BB5_Mg34_63xBSE and binary image

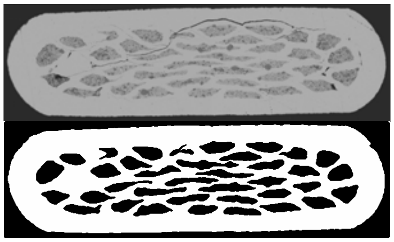

Fig.A4.72 BB5_Mg35_63xBSE and binary image

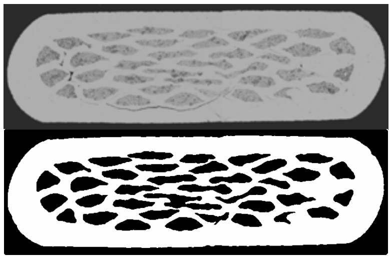

Fig.A4.73 BB5_Mg36_63xBSE and binary image

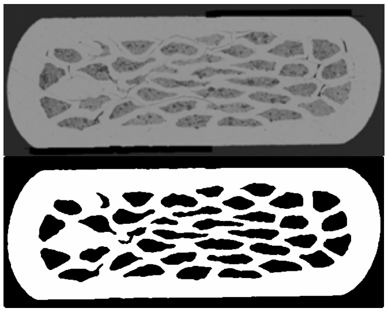

Fig.A4.74 BB5_Mg39_63xBSE and binary image

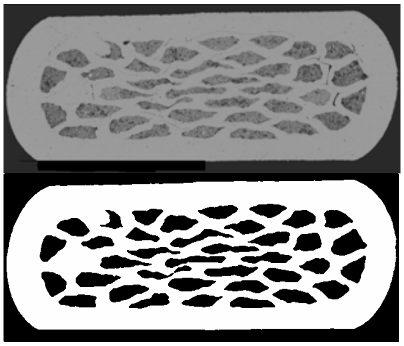

Fig.A4.75 BB5_Mg41_63xBSE and binary image

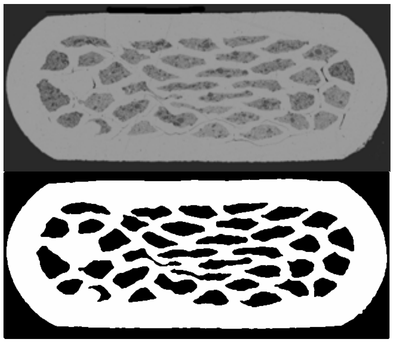

Fig.A4.76 BB5_Mg42_63xBSE and binary image

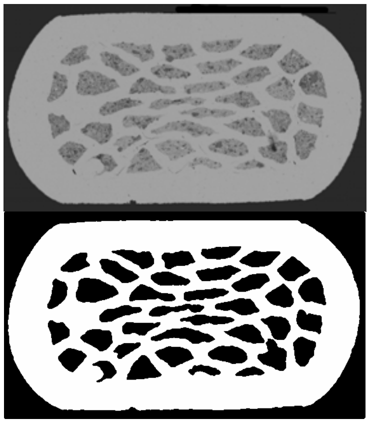

Fig.A4.79 BB5_Mg48_63xBSE and binary image

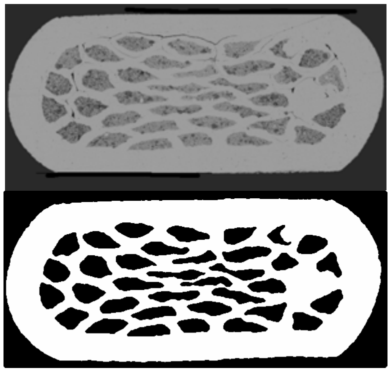

Fig.A4.77 BB5_Mg43_63xBSE and binary image

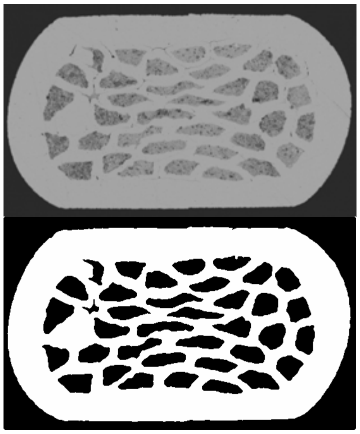

Fig.A4.80 BB5_Mg50_63xBSE and binary image

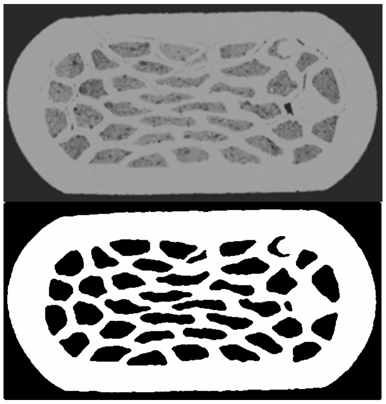

Fig.A4.78 BB5_Mg45_63xBSE and binary image

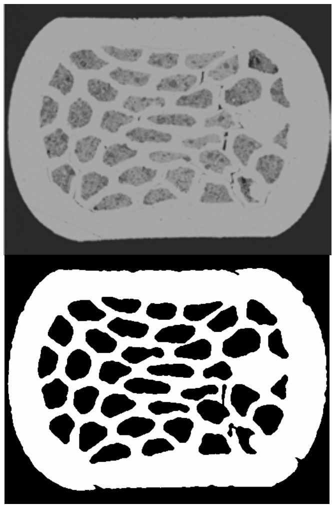

Fig.A4.81 BB5_Mg53_63xBSE and binary image

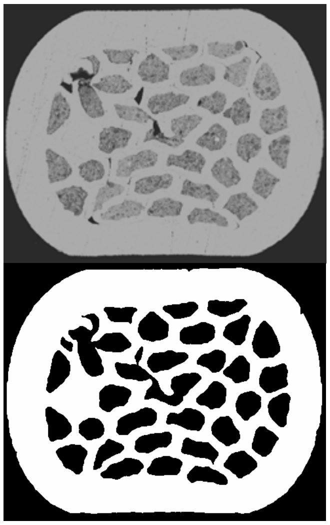

Fig.A4.82 BB5_Mg58_63xBSE and binary image

SEM (BSE) IMAGES OF 25% REDUCTION 0.0500" DIAMETER Ag FILAMENT-Mg TUBE MULTIFILAMENT TAPES

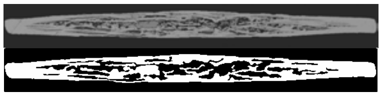

Fig.A4.121 BB6_Ag16T_63xBSE and binary image

Fig.A4.122 BB6_Ag16_63xBSE and binary image

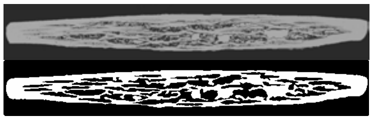

Fig.A4.123 BB6_Ag18_63xBSE and binary image.

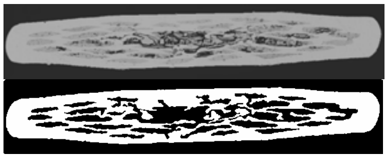

Fig.A4.124 BB6_Ag22_63xBSE and binary image

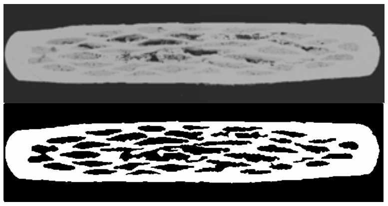

Fig.A4.125 BB6_Ag25_63xBSE and binary image

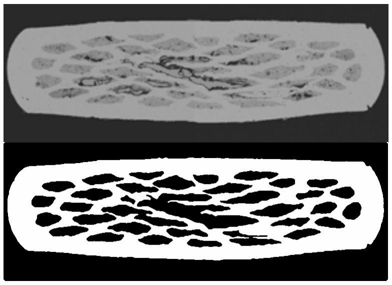

Fig.A4.126 BB6_Ag31_63xBSE and binary image

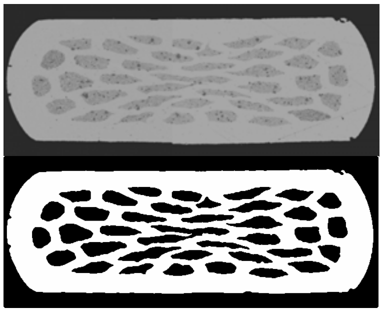

Fig.A4.127 BB6_Ag37_63xBSE and binary image

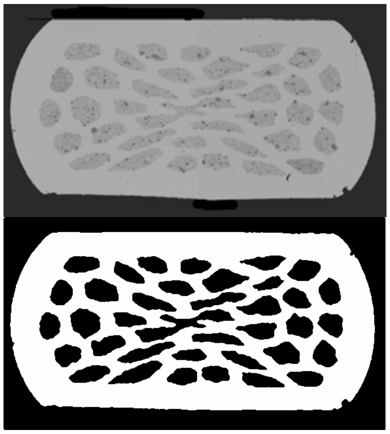

Fig.A4.128 BB6_Ag46_63xBSE and binary image

SEM (BSE) IMAGES OF 5% REDUCTION 0.0500” DIAMETER Ag FILAMENT-Mg TUBE MUTIFILAMENT TAPES

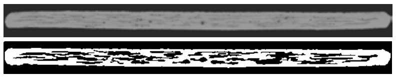

Fig.A4.100 BB7a_Ag16_63xBSE and binary image

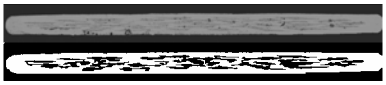

Fig.A4.101 BB7a_Ag17_63xBSE and binary image

Fig.A4.102 BB7a_Ag18_63xBSE and binary image

Fig.A4.103 BB7a_Ag19_63xBSE and binary image

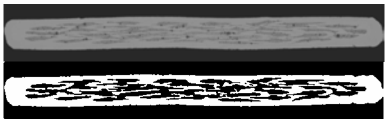

Fig.A4.104 BB7a_Ag20_63xBSE and binary image

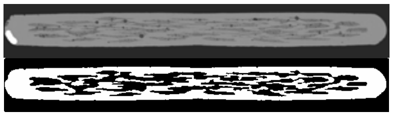

Fig.A4.105 BB7a_Ag21_63xBSE and binary image

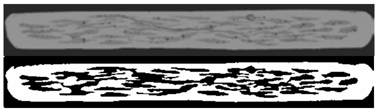

Fig.A4.106 BB7a_Ag22_63xBSE and binary image

Fig.A4.107 BB7a_Ag23_63xBSE and binary image

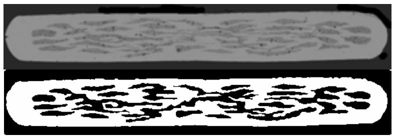

Fig.A4.108 BB7a_Ag24_63xBSE and binary image

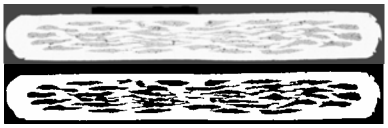

Fig.A4.109 BB7a_Ag25_63xBSE and binary image

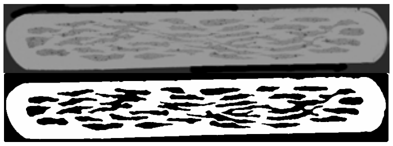

Fig.A4.110 BB7a_Ag26_63xBSE and binary image

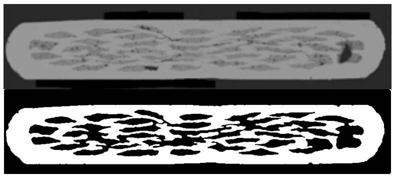
Fig.A4.111 BB7a_Ag27_63xBSE and binary image

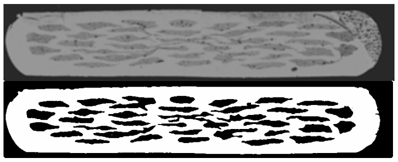
Fig.A4.112 BB7a_Ag28_63xBSE and binary image

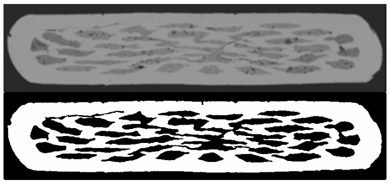
Fig.A4.113 BB7a_Ag29_63xBSE and binary image

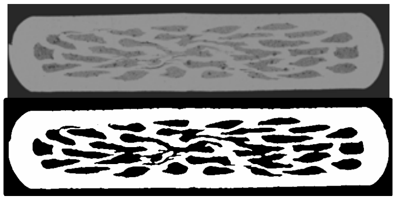
Fig.A4.114 BB7a_Ag30_63xBSE and binary image

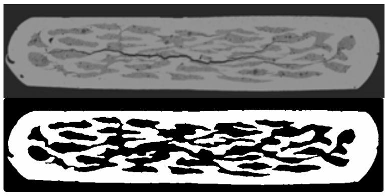
Fig.A4.115 BB7a_Ag32_63xBSE and binary image

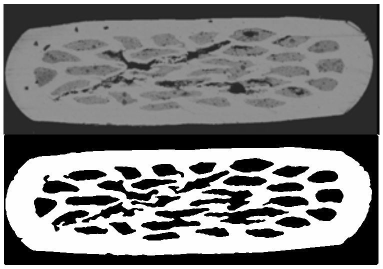
Fig.A4.116 BB7a_Ag34_63xBSE and binary image

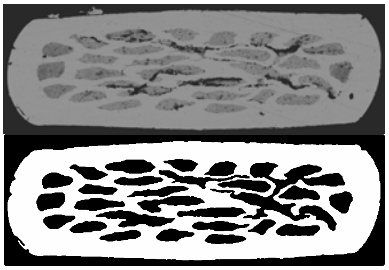
Fig.A4.117 BB7a_Ag35_63xBSE and binary image

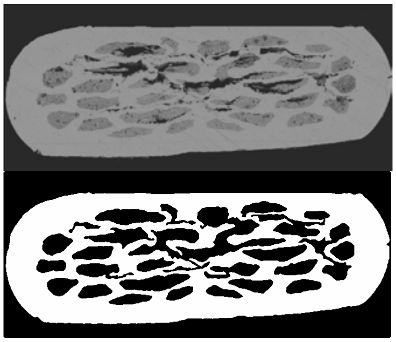
Fig.A4.118 BB7a_Ag36_63xBSE and binary image

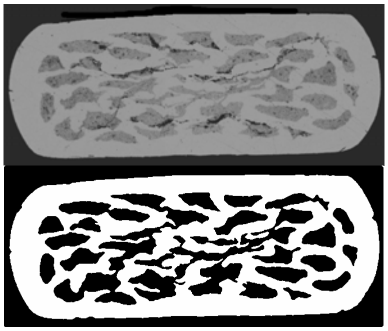
Fig.A4.119 BB7a_Ag39_63xBSE and binary image

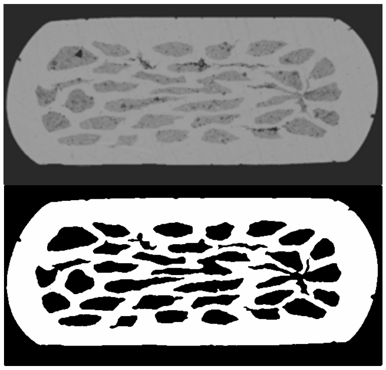
Fig.A4.120 BB7a_Ag41_63xBSE and binary image

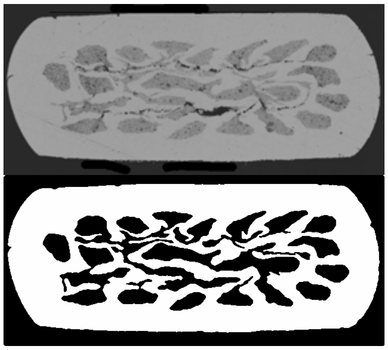
Fig.A4.121 BB7a_Ag42_63xBSE and binary image

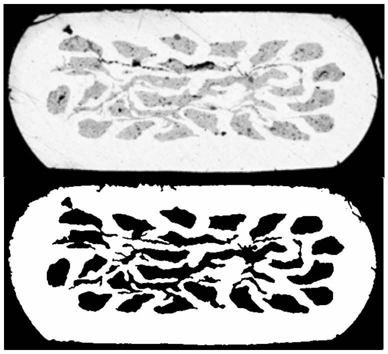
Fig.A4.122 BB7a_Ag43_63xBSE and binary image

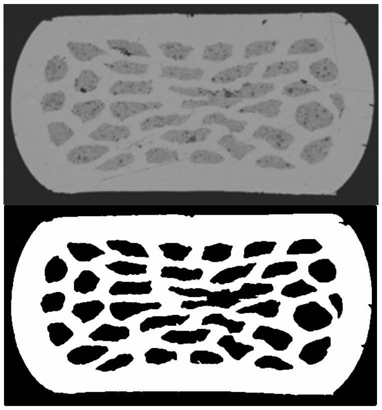
Fig.A4.123 BB7a_Ag45_63xBSE and binary image

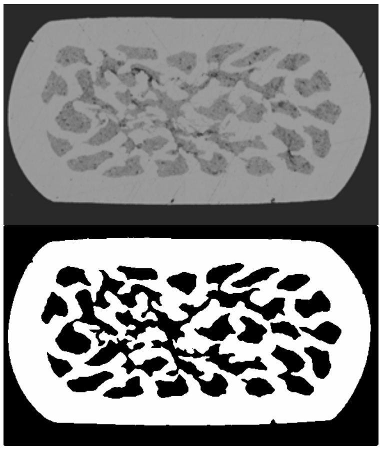
Fig.A4.124 BB7a_Ag48_63xBSE and binary image

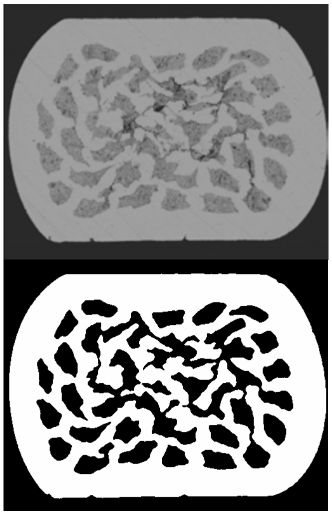

Fig.A4.125 BB7a_Ag50_63xBSE and binary image

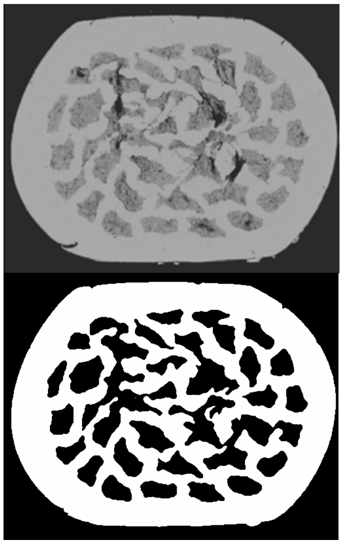

Fig.A4.127 BB7a_Ag58_63xBSE and binary image

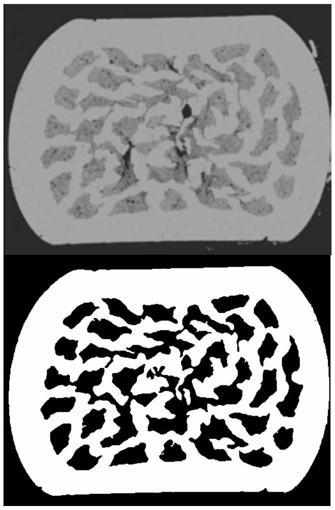

Fig.A4.126 BB7a_Ag53_63xBSE and binary image

SEM (BSE) IMAGES OF IR1 REDUCTION 0.0500” DIAMETER Ag FILAMENT-Mg TUBE MULTIFILAMENT TAPES


Fig.A4.128 BB8_Ag16T_63xBSE and binary image

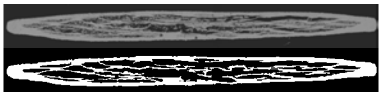
Fig.A4.129 BB8_Ag16_63xBSE and binary image

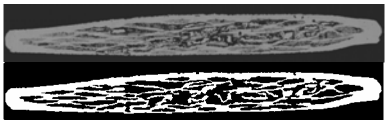
Fig.A4.130 BB8_Ag19_63xBSE and binary image

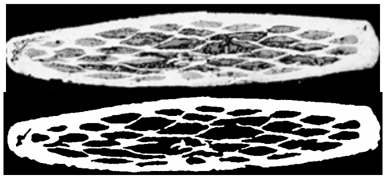
Fig.A4.131 BB8_Ag25_63xBSE and binary image

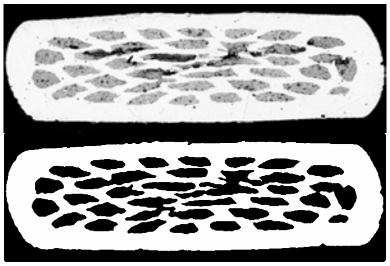
Fig.A4.132 BB8_Ag32_63xBSE and binary image

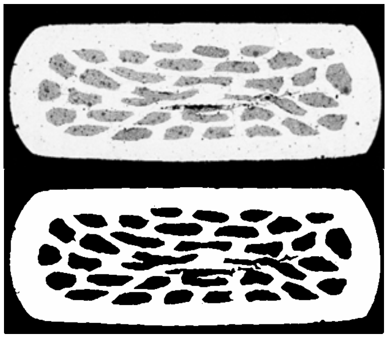
Fig.A4.133 BB8_Ag38_63xBSE and binary image

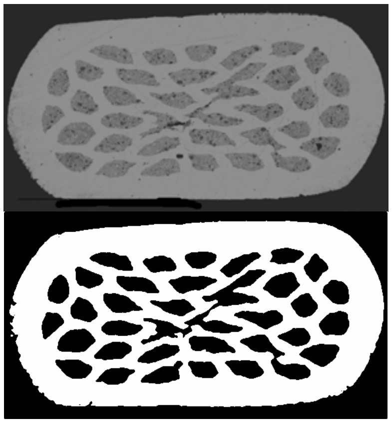
Fig.A4.134 BB8_Ag45_63xBSE and binary image

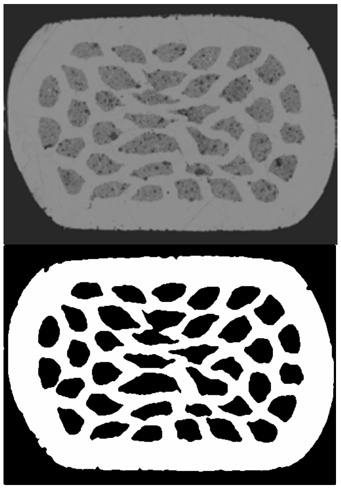

Fig.A4.135 BB8_Ag53_63xBSE and binary image

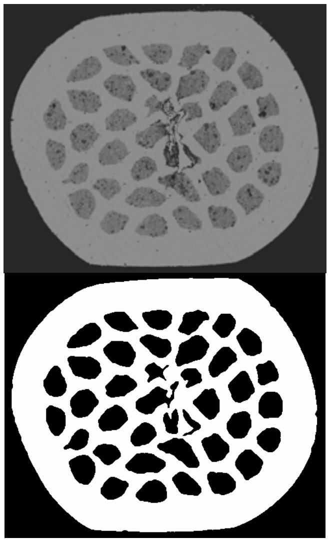

Fig.A4.137 BB8_Ag60_63xBSE and binary image

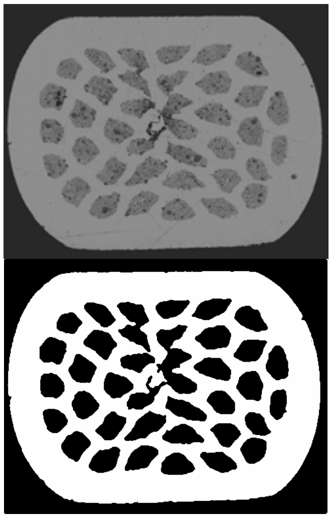

Fig.A4.136 BB8_Ag58_63xBSE and binary image

SEM (BSE) IMAGES OF IR1 REDUCTION 0.0500" DIAMETER Mg FILAMENT-Mg TUBE MULTIFILAMENT TAPES

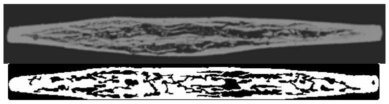
Fig.A4.138 BB8_Mg16_63xBSE and binary image

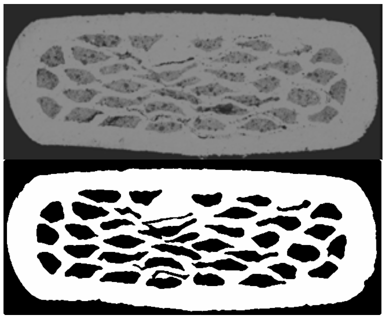
Fig.A4.142 BB8_Mg38_63xBSE and binary image

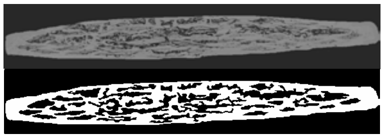
Fig.A4.139 BB8_Mg19_63xBSE and binary image

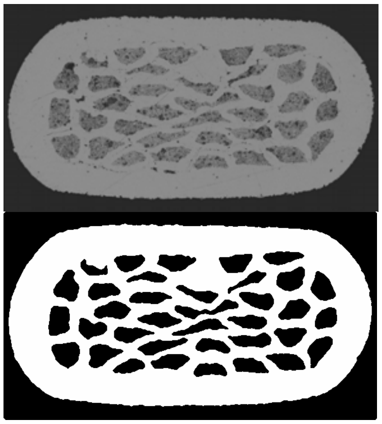
Fig.A4.143 BB8_Mg45_63xBSE and binary image

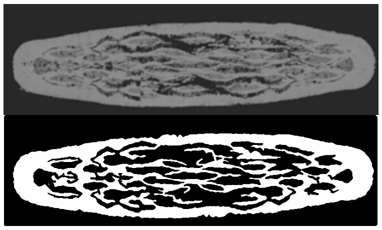
Fig.A4.140 BB8_Mg25_63xBSE and binary image

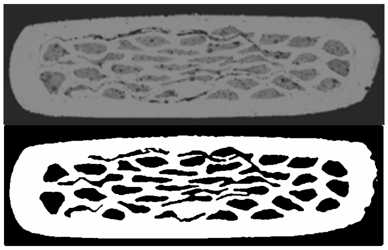
Fig.A4.141 BB8_Mg32_63xBSE and binary image

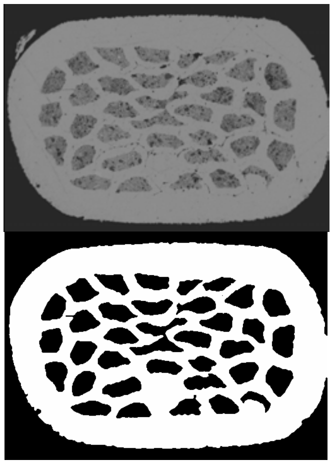
Fig.A4.144 BB8_Mg53_63xBSE and binary image

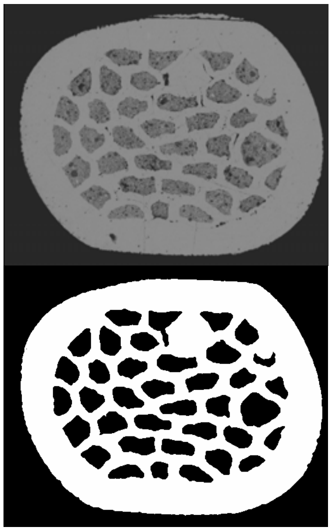

Fig.A4.145 BB8_Mg58_63xBSE and binary image

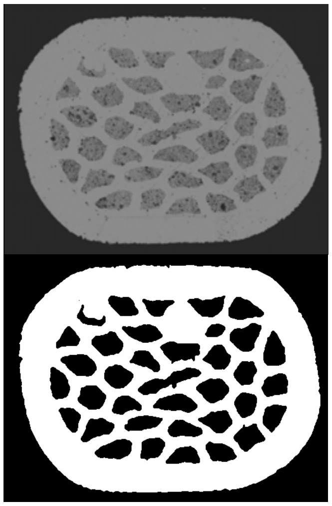

Fig.A4.146 BB8_Mg60_63xBSE and binary image

APPENDIX 5

SEM (BSE) IMAGES OF MONO AND MUTIFILAMENT WIRES LONGITUDINAL CROSS SECTIONS/CORE-SHEATH INTERFACE

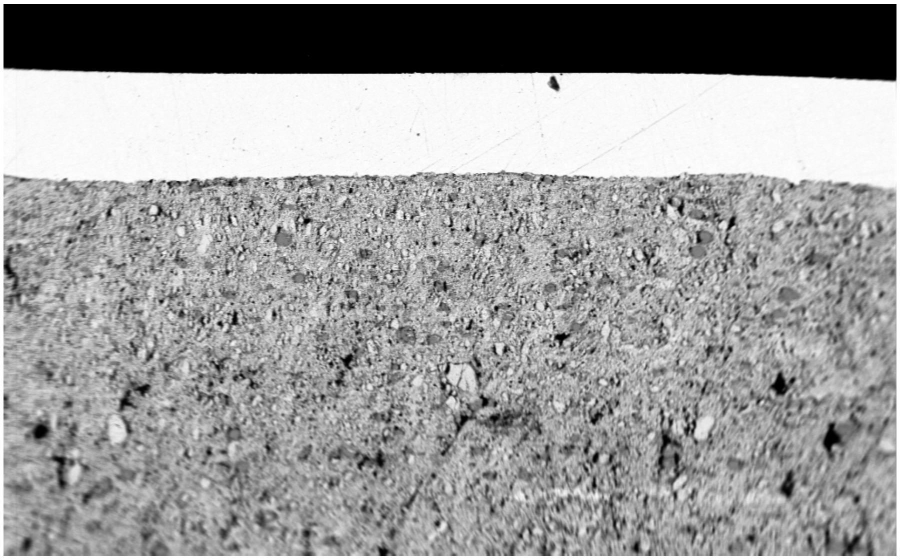

Fig.A5.1 BB9_mono45_63x_upper (Upper section of monofilament wire with 0.0450" diameter)

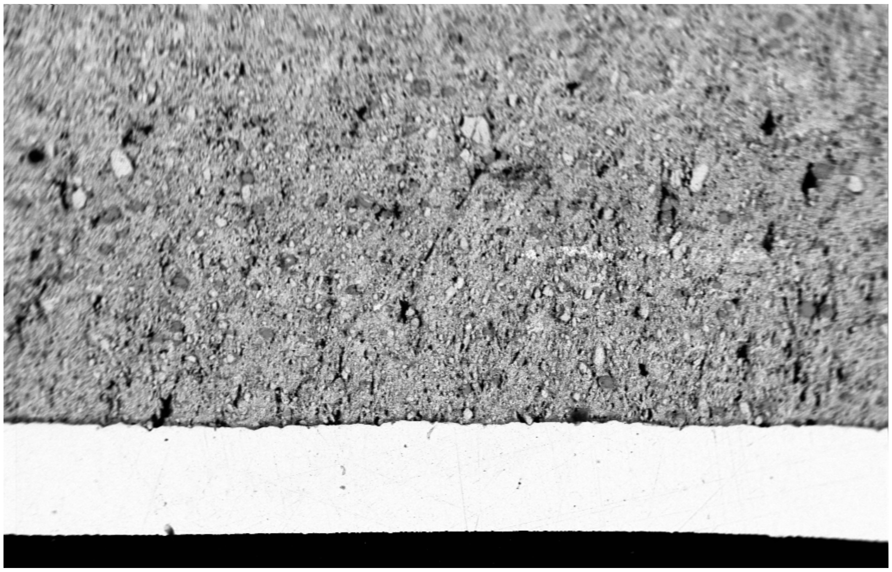

Fig.A5.2 BB9_mono45_63x_lower (Lower section of monofilament wire with 0.0450" diameter)

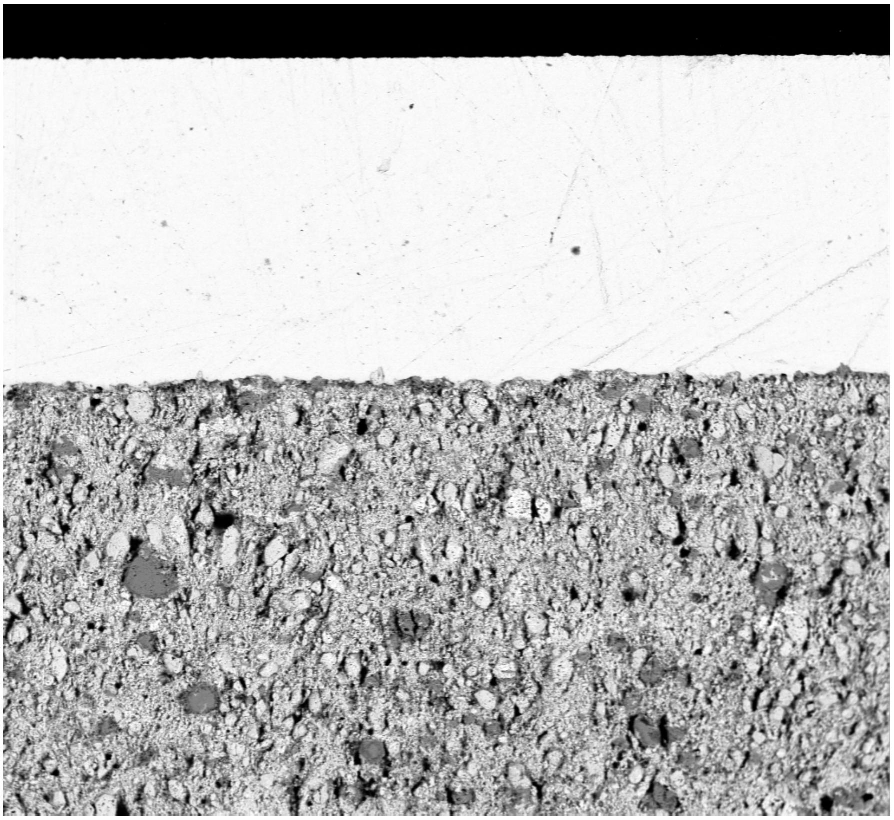

Fig.A5.3 BB9_mono45_200x_upper (Upper section of monofilament wire with 0.0450" diameter)

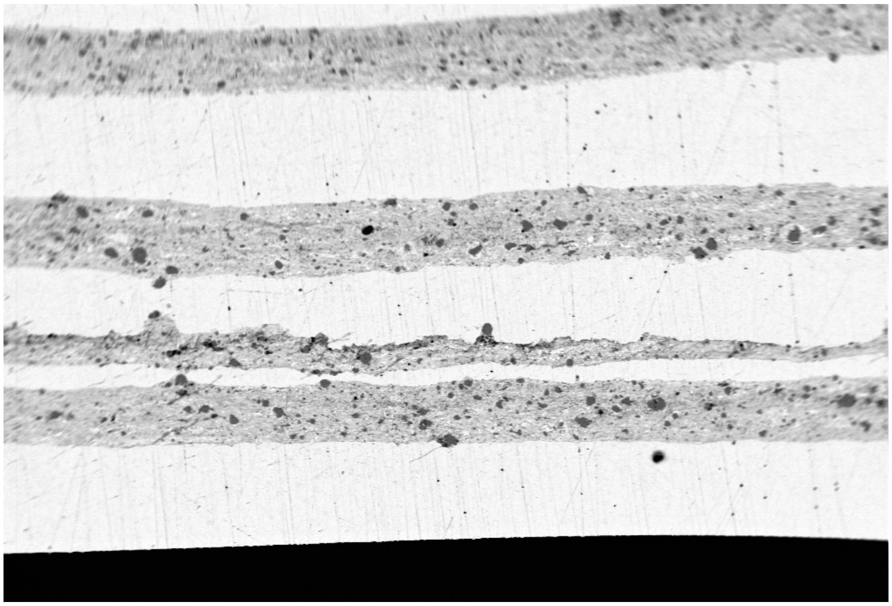

Fig.A5.4 BB9_multi50_63x_lower (Lower section of multifilament wire with 0.0500" diameter)

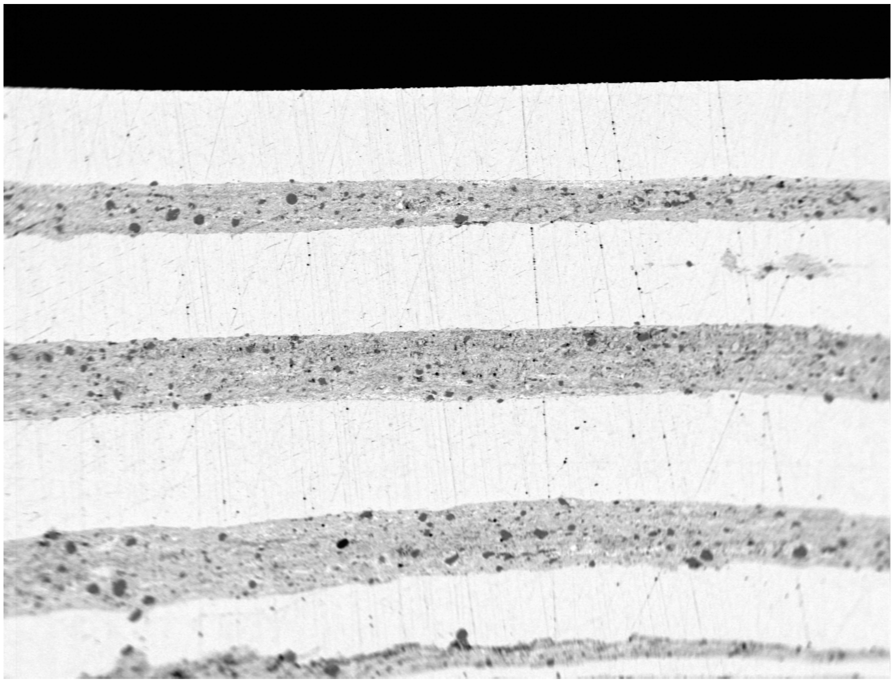

Fig.A5.5 BB9_multi50_63x_upper (Upper section of multifilament wire with 0.0500” diameter)

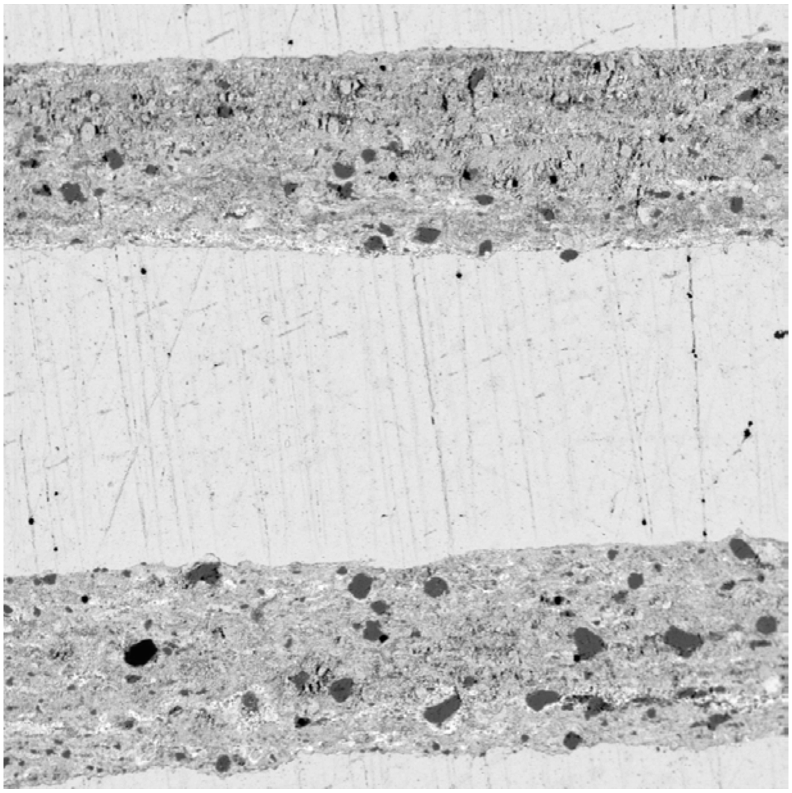

Fig.A5.6 BB9_multi50_200x_upper (Upper section of multifilament wire with 0.0500” diameter)

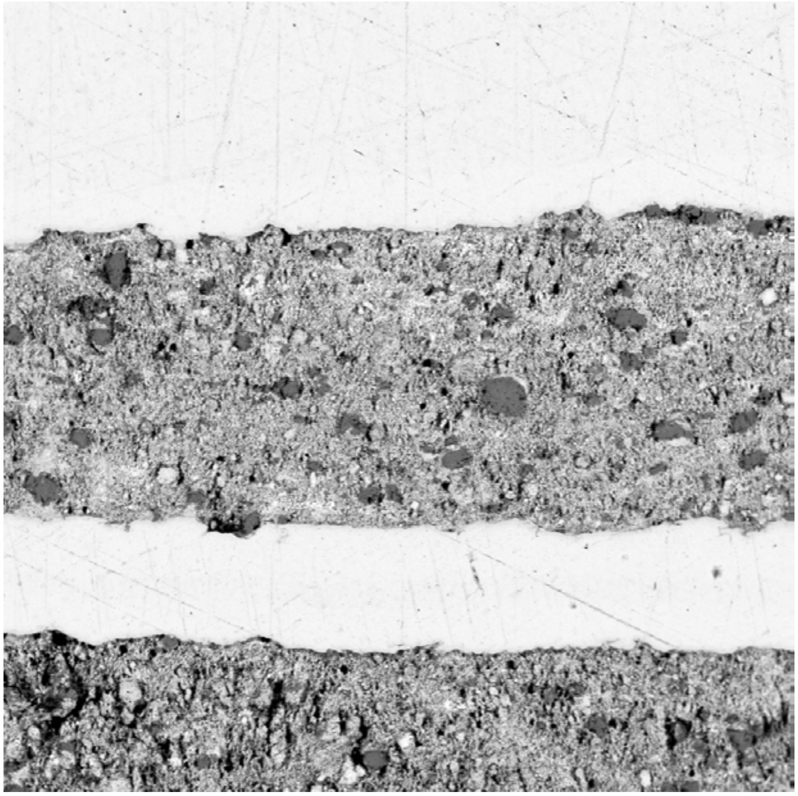

Fig.A5.7 BB9_multi96_200x_upper (Upper section of multifilament wire with 0.0960” diameter)

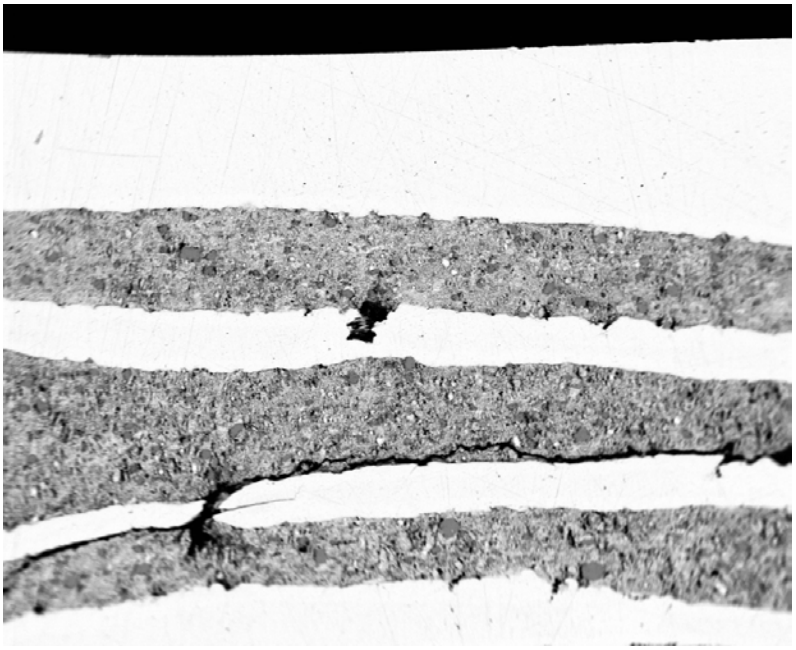

Fig.A5.8 BB9_multi96a_63x (Upper section-close look of filaments of multifilament wire with 0.0960” diameter)

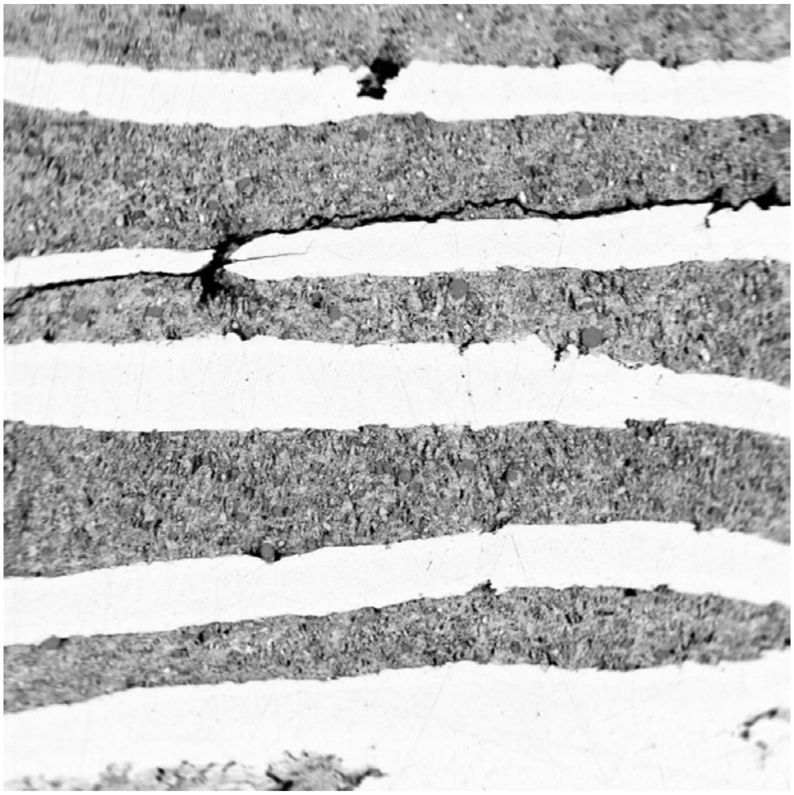

Fig.A5.9 BB9_multi96b_63x (Mid-section close look of filaments of multifilament wire with 0.0960” diameter)

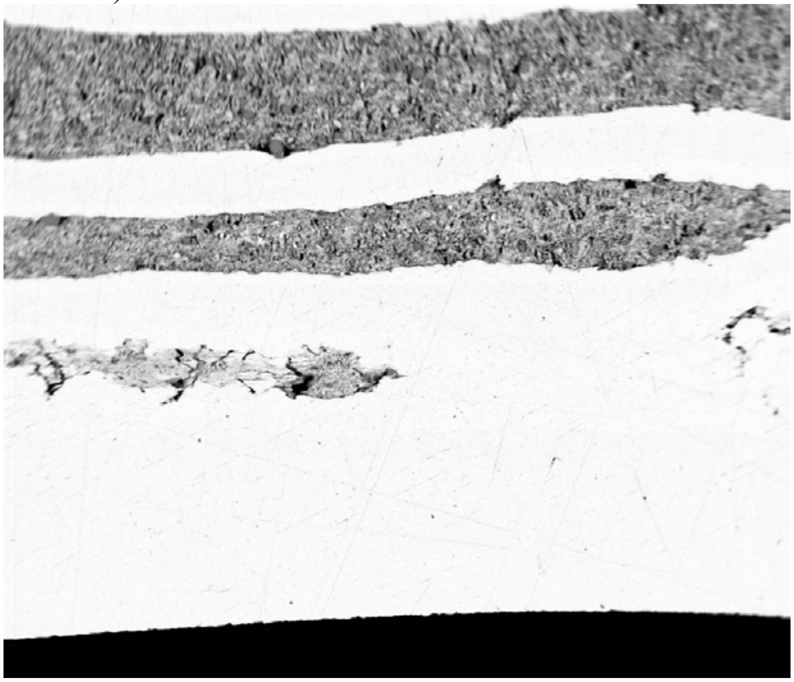

Fig.A5.10 BB9_multi96c_63x (Lower section-close look of filaments of multifilament wire with 0.0960” diameter)

Fig.A5.11 BB9_multi96d_63x (Lower section-close look of filaments of multifilament wire with 0.0960” diameter)

APPENDIX 6

SEM (BSE) IMAGES OF MONO AND MUTIFILAMENT TAPES LONGITUDINAL CROSS SECTIONS/CORE-SHEATH INTERFACE

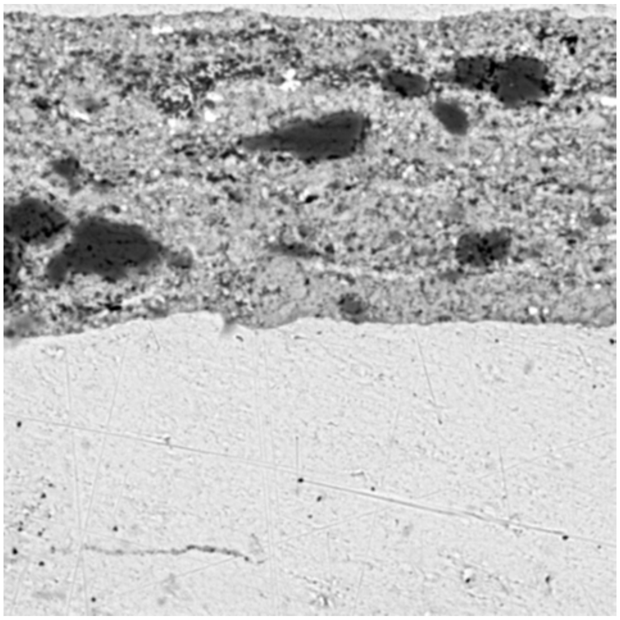

Fig.A6.1 BB9_AgT25_2000x (Section of Ag FILAMENT-Mg TUBE tape with thickness larger than final tape thickness, starting diameter 0.0500")

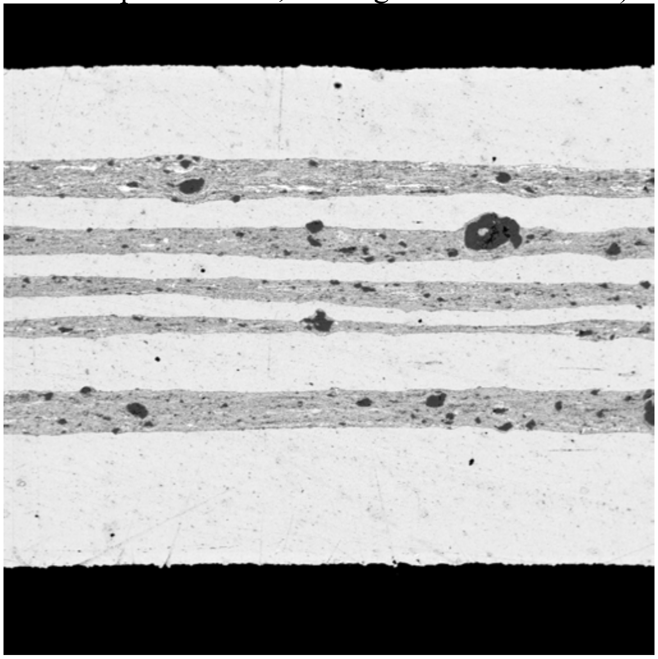

Fig.A6.2 BB9_AgT25_200x (Filaments of Ag FILAMENT-Mg TUBE tape with thickness larger than final tape thickness, starting diameter 0.0500")

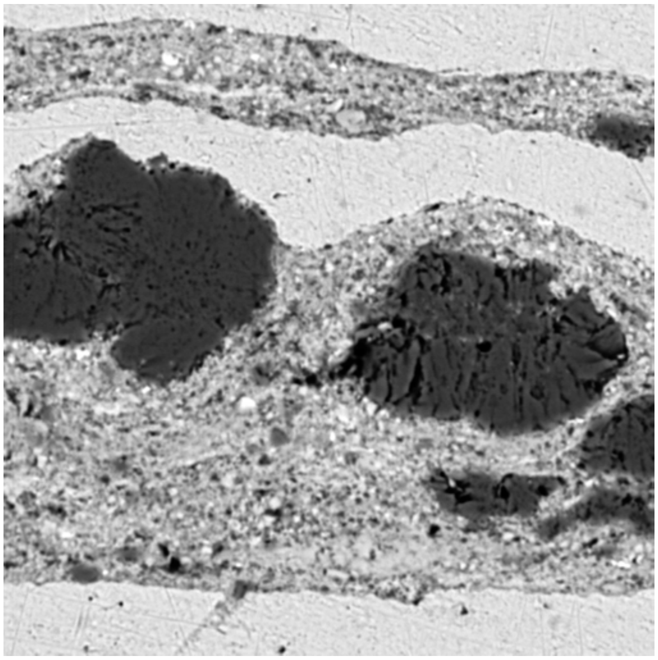

Fig.A6.3 BB9_AgT25_2000x (Large Cu grains interrupting the smoothness of interfaces, Ag FILAMENT-Mg TUBE tape with thickness larger than final tape thickness, starting diameter 0.0500")

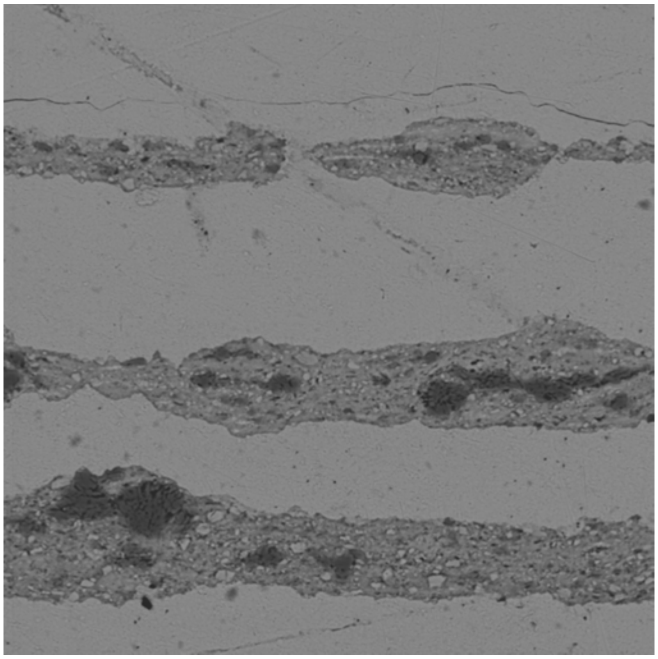

Fig.A6.4 BB9_AgT600_1000x (Discontinuity of filaments, Ag FILAMENT-Ag TUBE tape, starting diameter 0.0600")

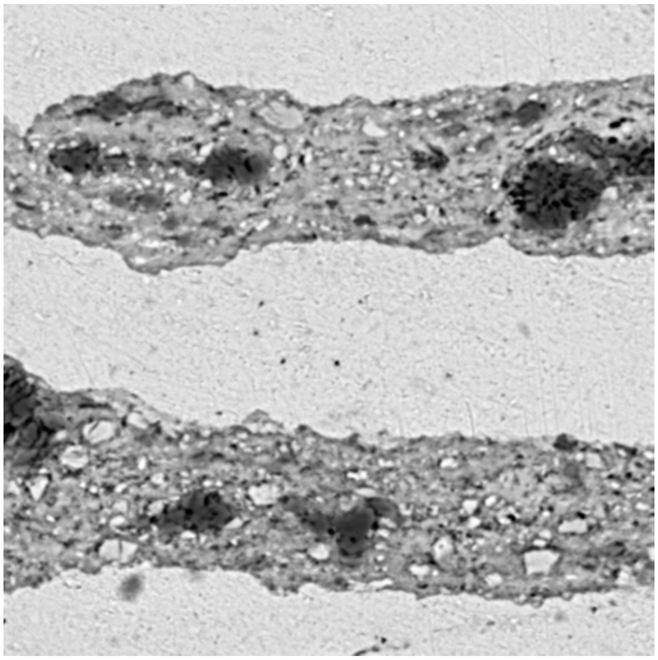

Fig.A6.5 BB9_AgT600_2000x (Closer look at filaments' interface, Ag FILAMENT-Ag TUBE tape, starting diameter 0.0600")

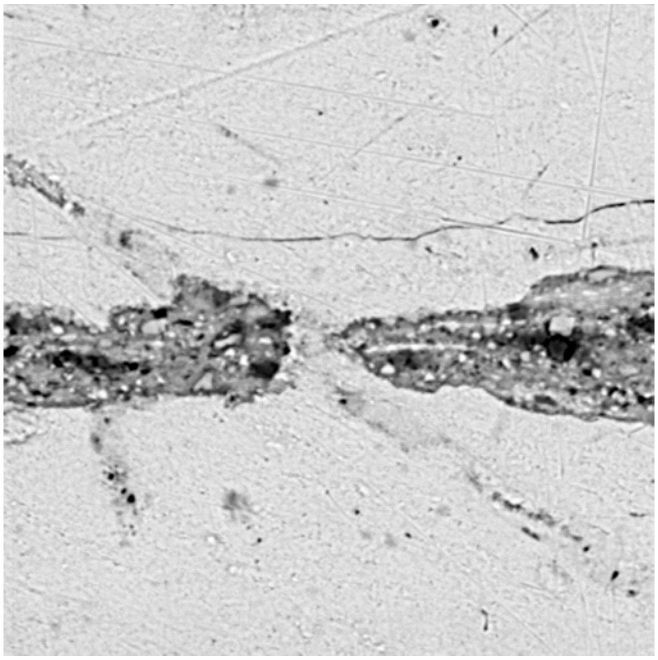

Fig.A6.6 BB9_AgT600a_2000x (Closer look at discontinuity of filaments, Ag FILAMENT-Ag TUBE tape, starting diameter 0.0600")

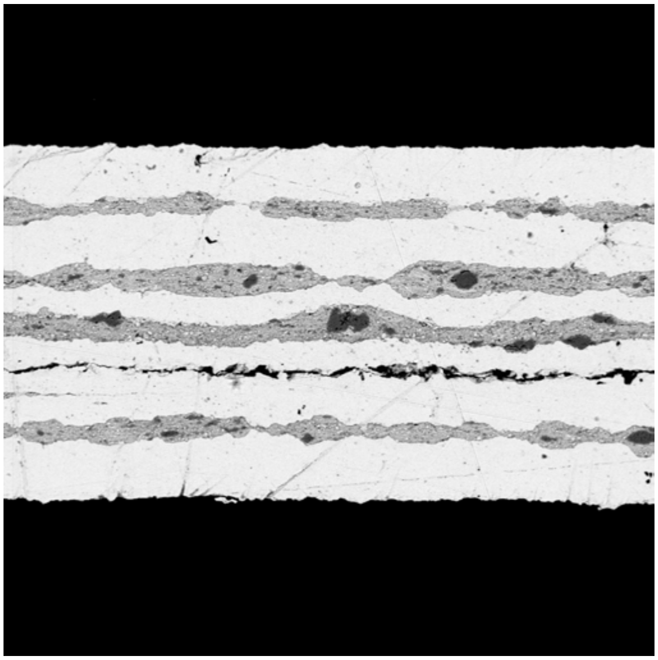

Fig.A6.7 BB9_AgT600a_300x (General view of filaments, Ag FILAMENT-Ag TUBE tape, starting diameter 0.0600”)

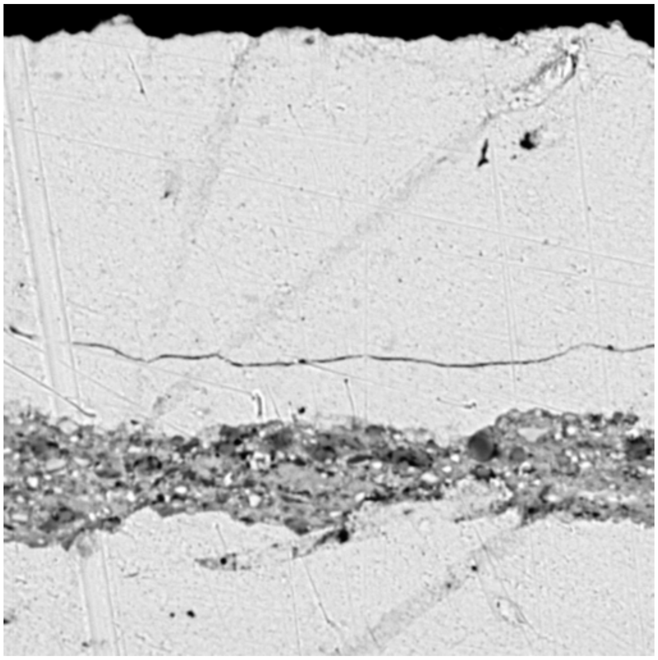

Fig.A6.8 BB9_AgT600b_2000x (Crack development in the outer TUBE and filament sheath interface, Ag FILAMENT-Ag TUBE tape, starting diameter 0.0600”)

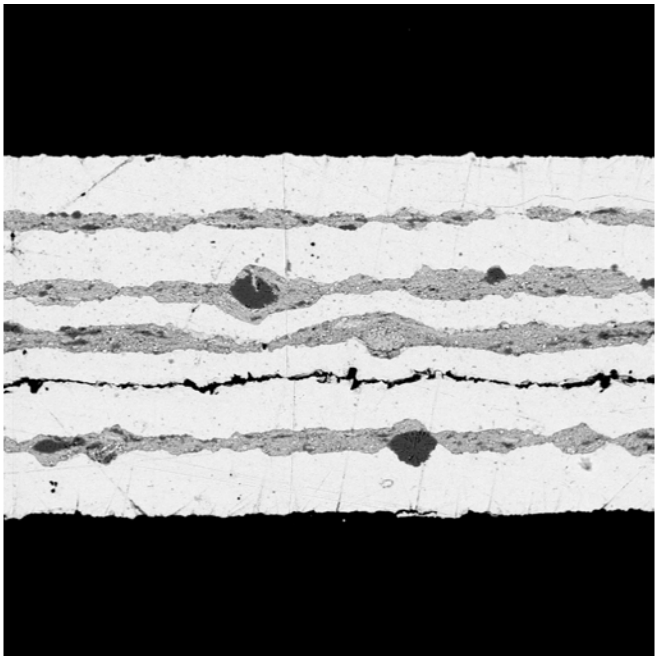

Fig.A6.9 BB9_AgT600b_300x (General view of filaments, sausaging and continuous crack, Ag FILAMENT-Ag TUBE tape, starting diameter 0.0600")

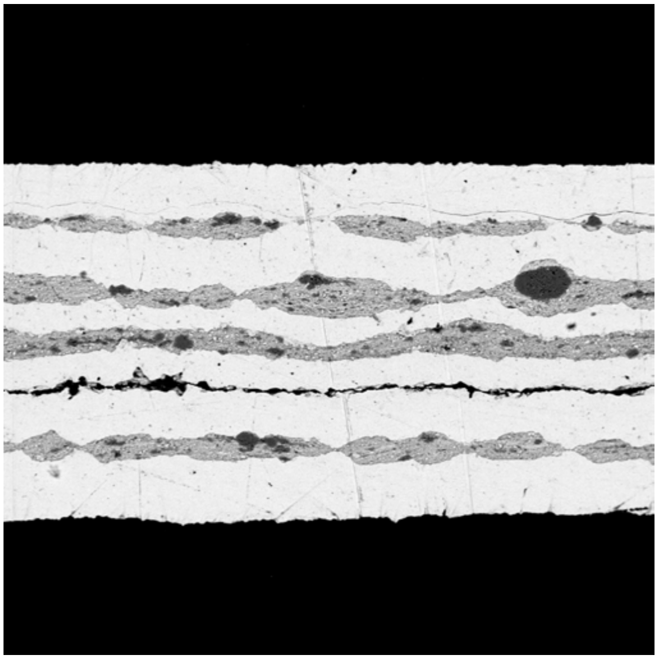

Fig.A6.10 BB9_AgT600c_300x (General view of filaments, sausaging and continuous crack, Ag FILAMENT-Ag TUBE tape, starting diameter 0.0600")

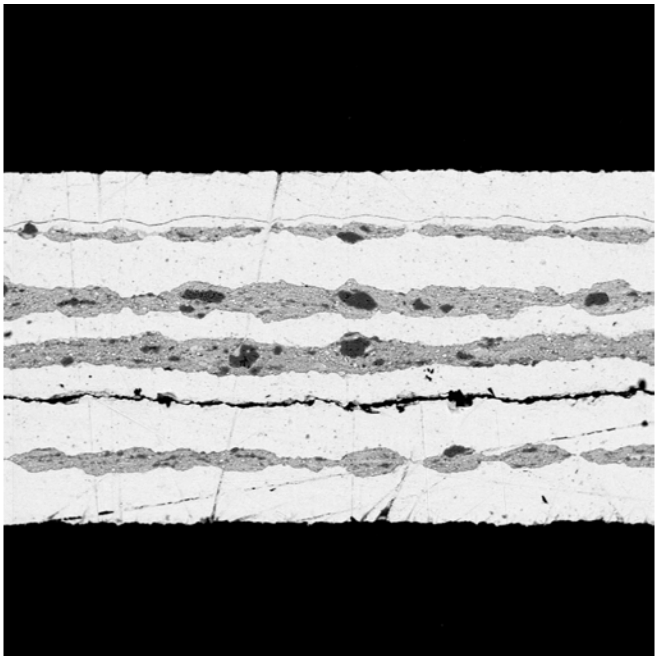

Fig.A6.11 BB9_AgT600d_300x (General view of filaments, sausaging and continuous crack, Ag FILAMENT-Ag TUBE tape, starting diameter 0.0600")

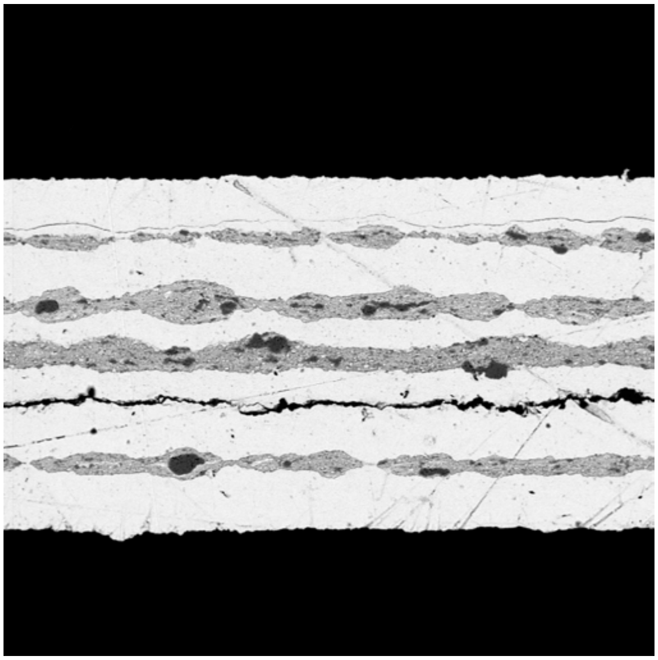

Fig.A6.12 BB9_AgT600e_300x (General view of filaments, sausaging and continuous crack, Ag FILAMENT-Ag TUBE tape, starting diameter 0.0600")

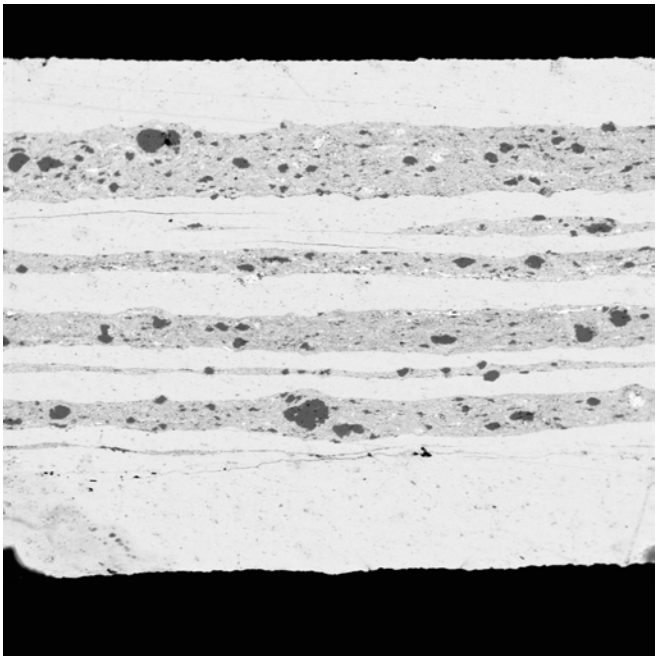

Fig.A6.13 BB9_MgT25_200x (General view of filaments, Mg FILAMENT-Mg TUBE tape with thickness larger than final tape thickness, starting diameter 0.0500”)

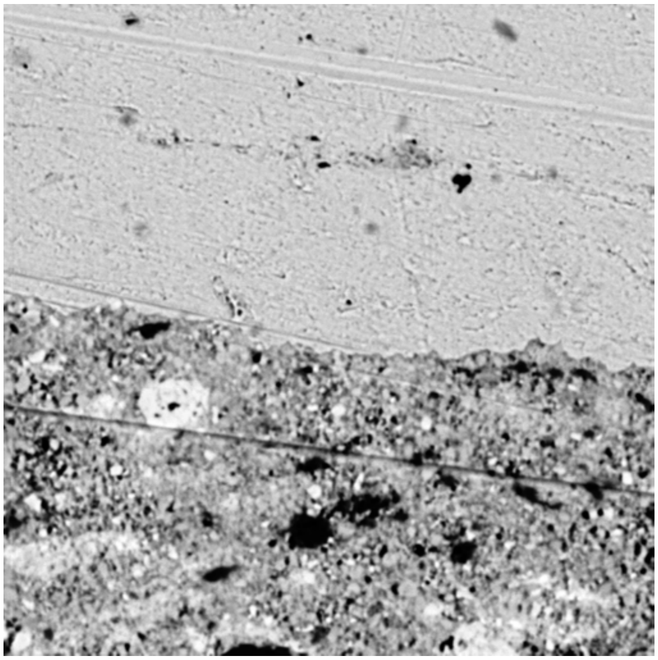

Fig.A6.14 BB9_MgT25_2000x (Close look at wavy sheath-core interface, Mg FILAMENT-Mg TUBE tape with thickness larger than final tape thickness, starting diameter 0.0500”)

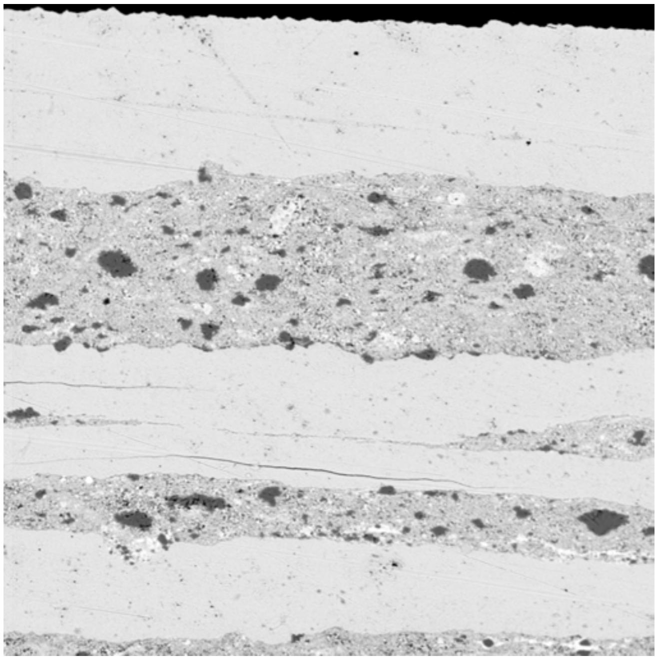

Fig.A6.15 BB9_MgT25a_500x (Sheath-core interface and discontinuing filament, Mg FILAMENT-Mg TUBE tape with thickness larger than final tape thickness, starting diameter 0.0500")

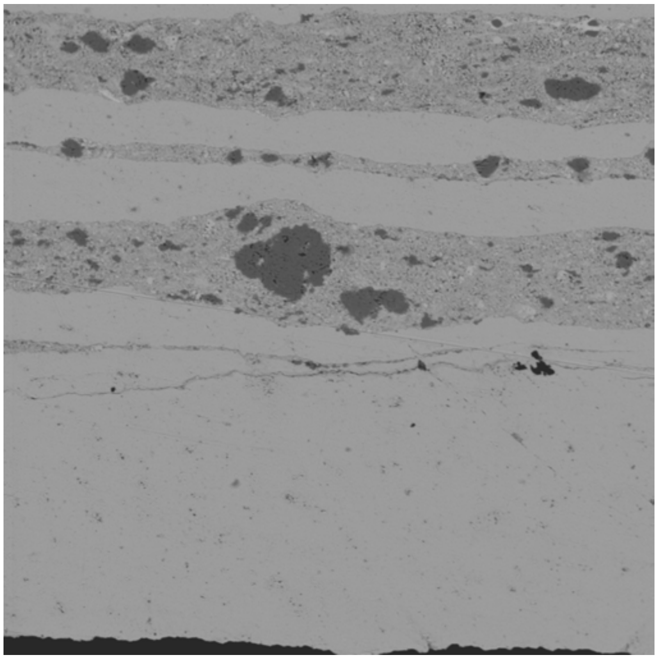

Fig.A6.16 BB9_MgT25B_500x (Sheath-core interface large Cu particle interrupting filament smoothness, Mg FILAMENT-Mg TUBE tape with thickness larger than final tape thickness, starting diameter 0.0500")

APPENDIX 7

CRITICAL CURRENT DETERMINATION OF WIRE SAMPLES BY GRAPHIC IMPLEMENTATION OF 1 μV CRITERION

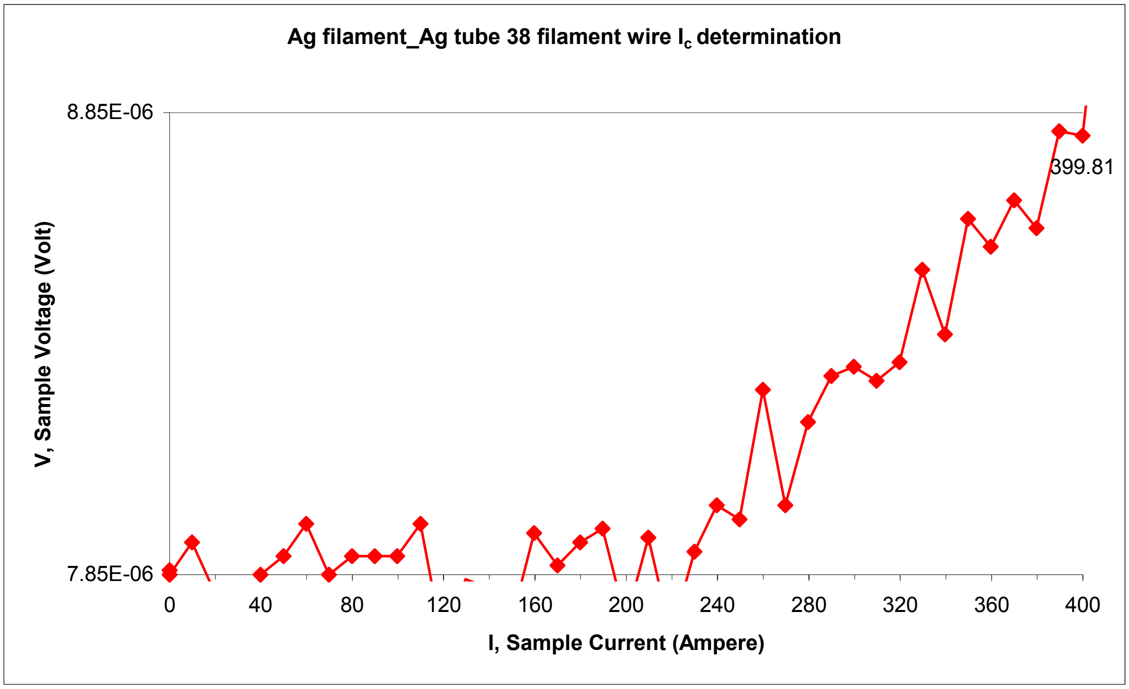

Fig.A7.1 Critical current determination of Ag filament-Ag tube multifilament wire

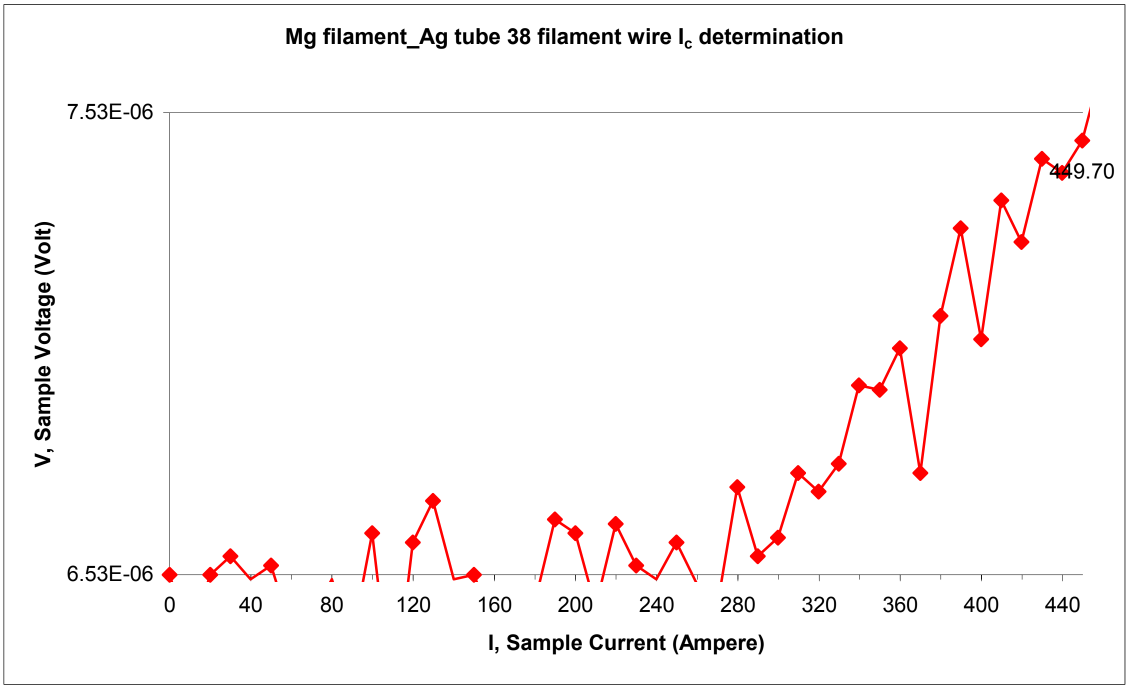

Fig.A7.2 Critical current determination of Mg filament-Ag tube multifilament wire

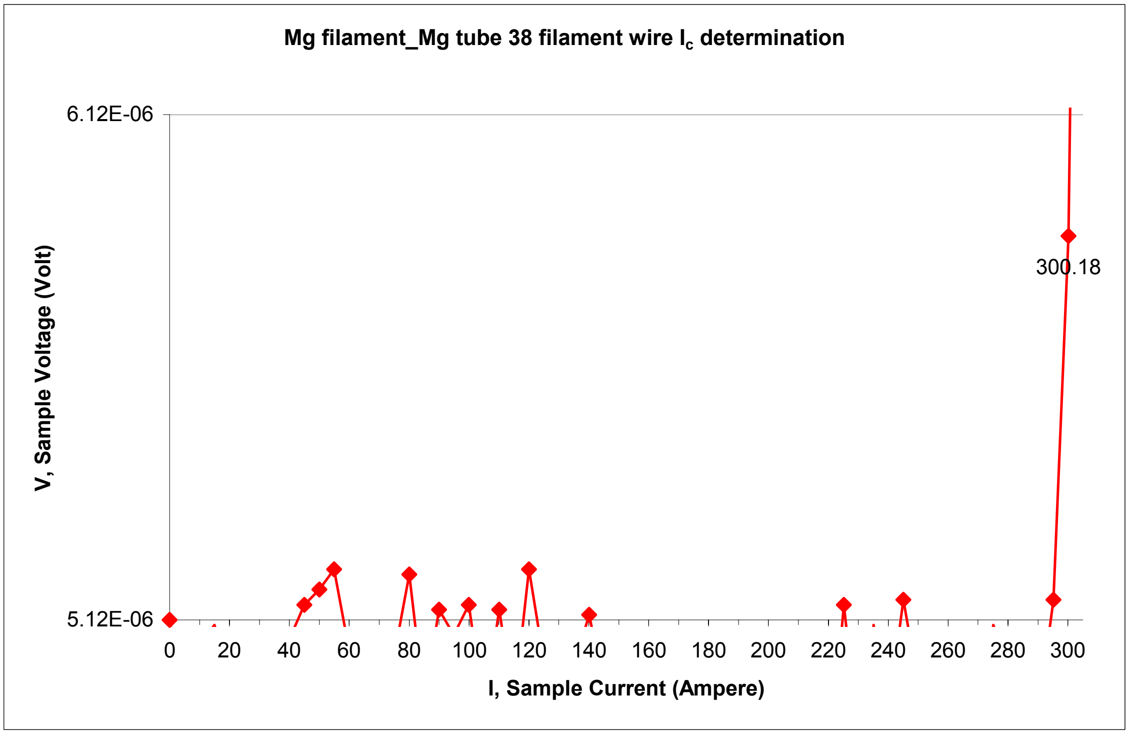

Fig.A7.3 Critical current determination of Mg filament-Mg tube multifilament wire

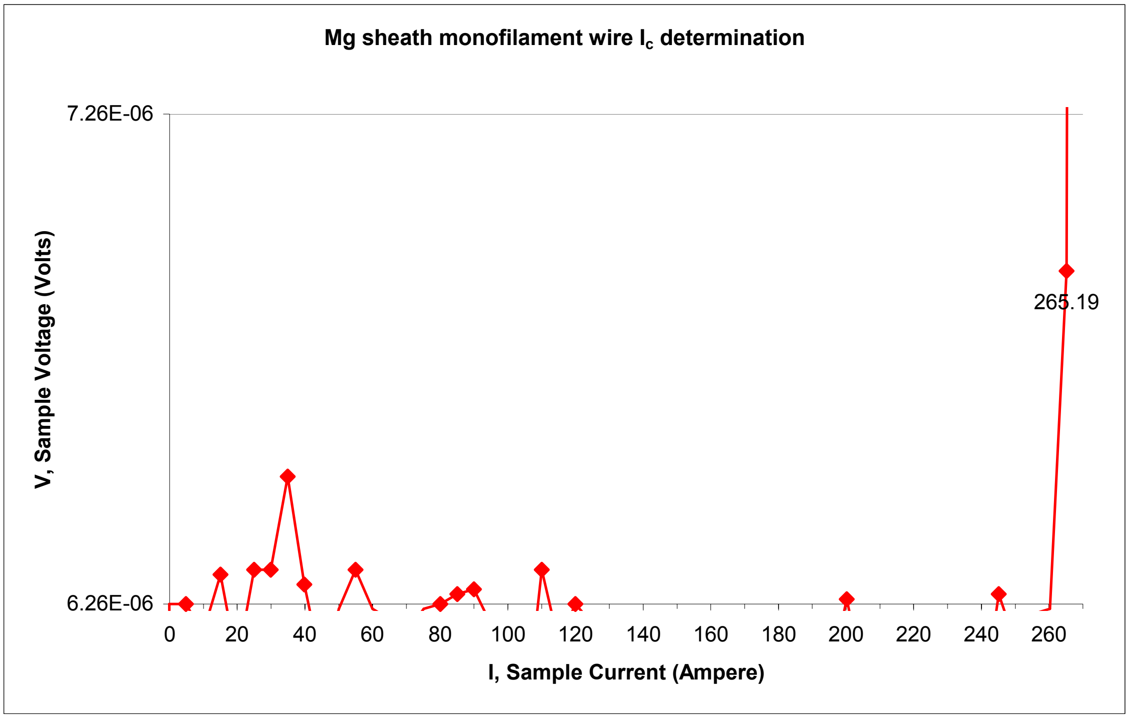

Fig.A7.4 Critical current determination of Mg sheath monofilament wire

APPENDIX 8

‘*AS DEFORMED*’ TAPE DEFORMATION SCHEDULE SAMPLES

Roller gauge read	Deformed sample by 5% reduction (MULTIFILAMENT, ∅ 0.0500)	Average thickness [x10^{-4} inch]
58		423
53		387
50		361
48		340
45		316
43		296
42		285
41		275
39		257
36		234
35		221
34		211
32		196
30		178
29		168
28		157
27		149
26		140
25		132
24		122

Fig.A8.1 5% reduction multifilament tape, Ag filament-Ag tube, 0.0500” starting diameter.

23		113
22		102
21		92
20		84
19		74
18		68
17		60

Fig.A8.1. continued.

Roller gauge read	**Deformed sample by 5% reduction (MULTIFILAMENT, ∅ 0.0600)**	**Average thickness [x10^{-4} inch]**
58		444
53		398
50		368
48		351
45		322
43		303
42	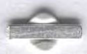	290
41		280
39		263
36		239
35		228
34		220
32		201
30		185
29		174
28		163
27		154
26		144
25		135
24		125

Fig.A8.2 5% reduction multifilament tape, Ag filament-Ag tube, 0.0600” starting diameter.

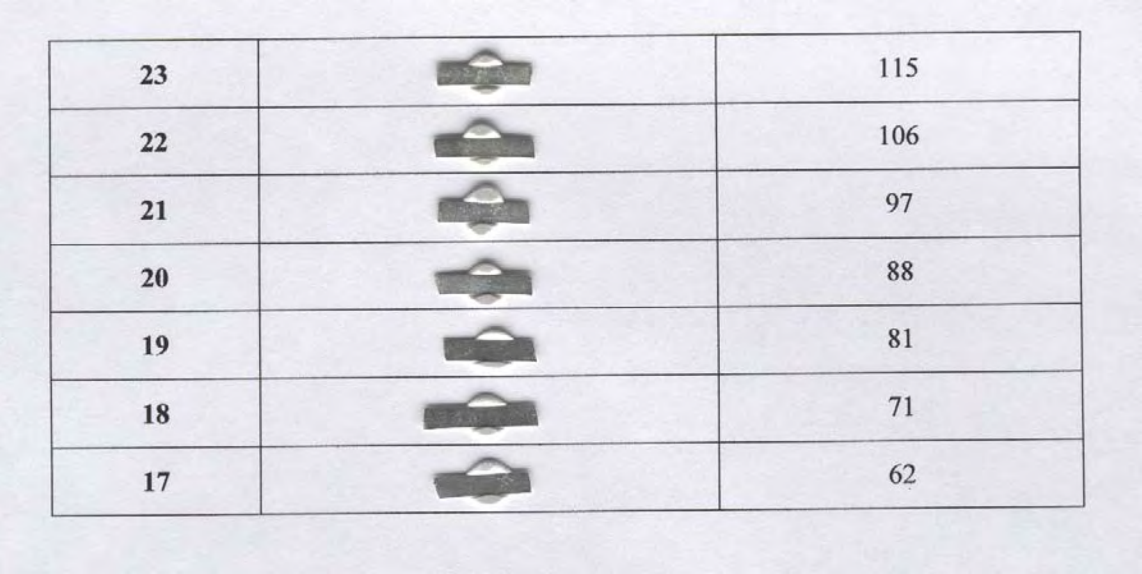

23		115
22		106
21		97
20		88
19		81
18		71
17		62

Fig.A8.2 continued.

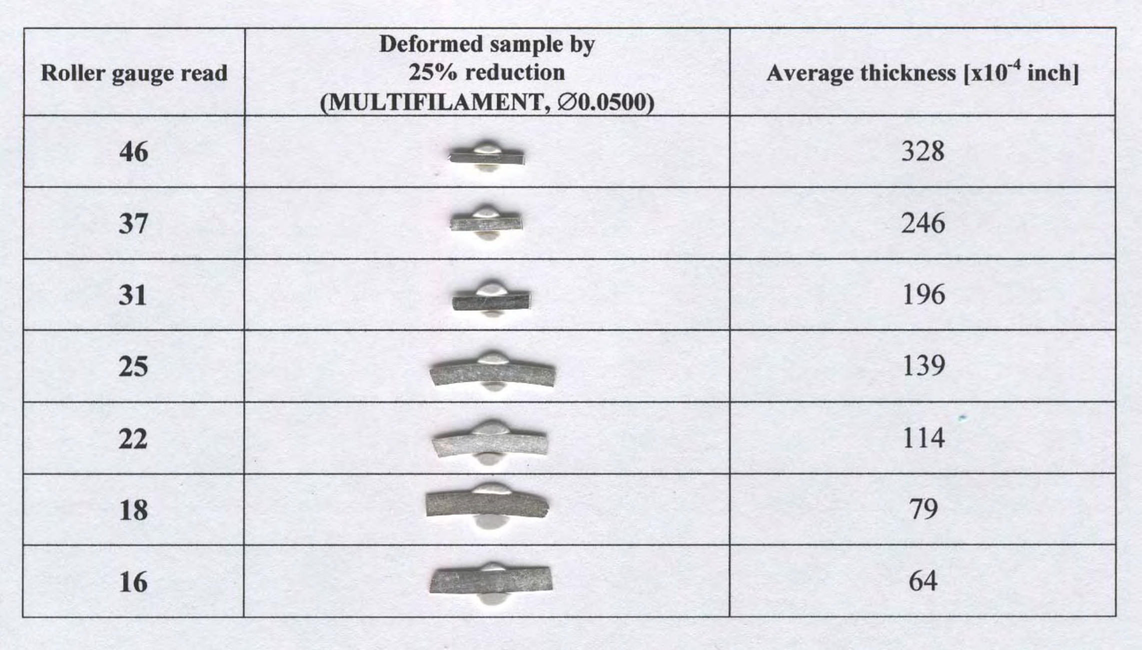

Roller gauge read	**Deformed sample by 25% reduction (MULTIFILAMENT, ∅0.0500)**	**Average thickness [x10^{-4} inch]**
46		328
37		246
31		196
25		139
22		114
18		79
16		64

Fig.A8.3 25% reduction multifilament tape, Ag filament-Ag tube, 0.0500” starting diameter.

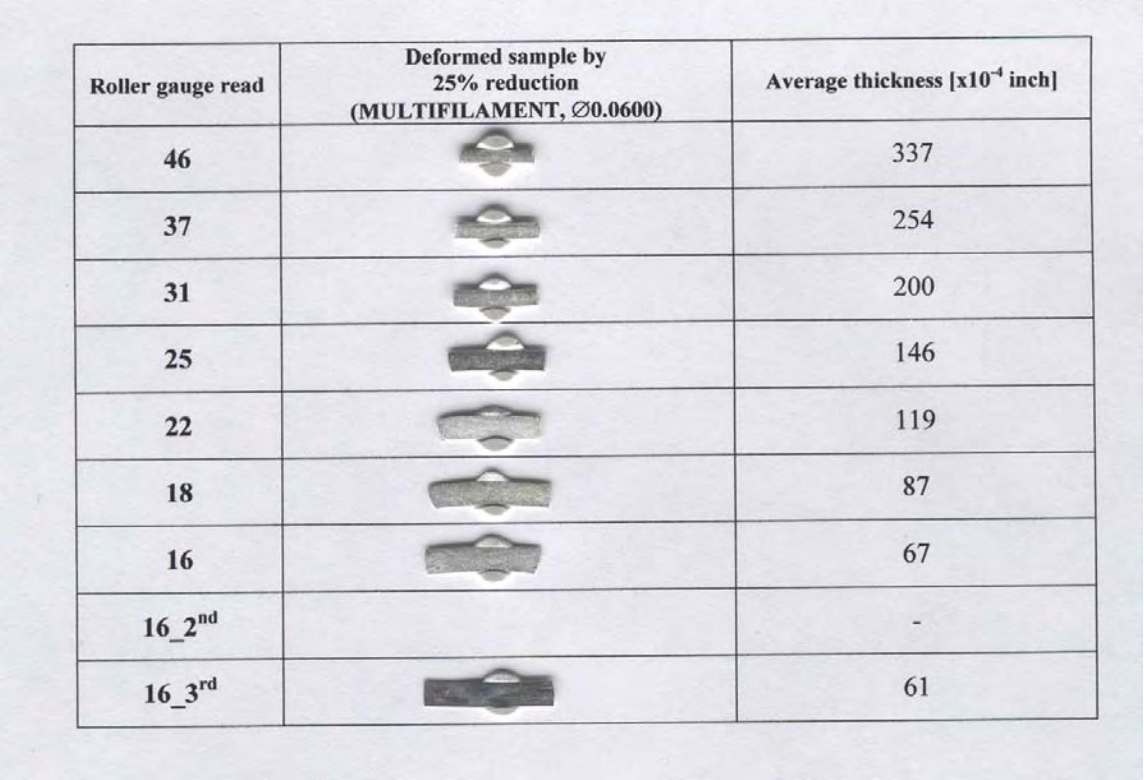

Roller gauge read	Deformed sample by 25% reduction (MULTIFILAMENT, ∅0.0600)	Average thickness [x10^{-4} inch]
46		337
37		254
31		200
25		146
22		119
18		87
16		67
16_2nd		-
16_3rd		61

Fig.A8.4 25% reduction multifilament tape, Ag filament-Ag tube, 0.0600" starting diameter.

Roller gauge read	Deformed sample by IR_1 reduction (MULTIFILAMENT, ∅ 0.0500)	Average thickness [x10^{-4} inch]
60		434
58 (5%)		414
53 (10%)		385
45 (15%)		316
38 (20%)		253
32 (25%)		202
25 (30%)		136
19 (35%)		89
16 (30%)		66

Fig.A8.5 IR1 reduction multifilament tape, Ag filament-Ag tube, 0.0500” starting diameter.

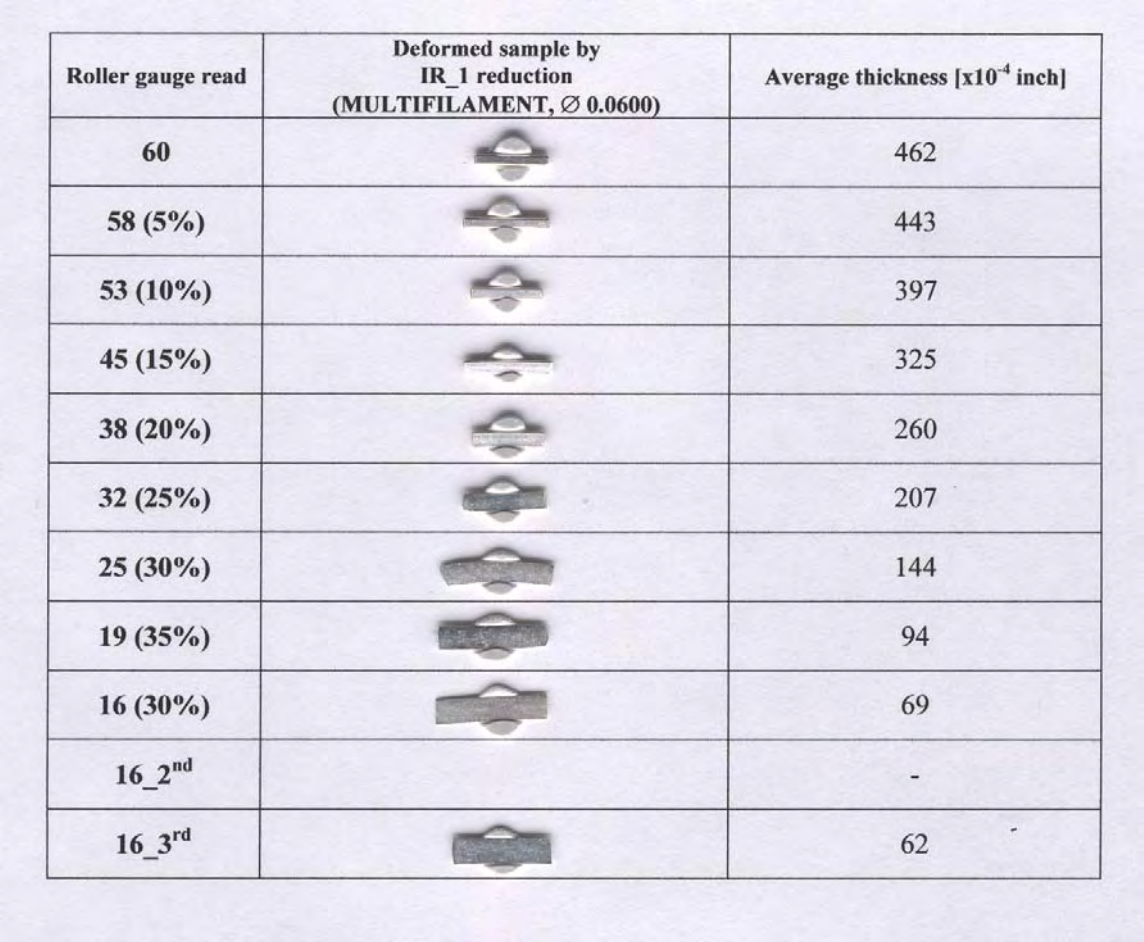

Roller gauge read	Deformed sample by IR_1 reduction (MULTIFILAMENT, ∅ 0.0600)	Average thickness [x10^{-4} inch]
60		462
58 (5%)		443
53 (10%)		397
45 (15%)		325
38 (20%)		260
32 (25%)		207
25 (30%)		144
19 (35%)		94
16 (30%)		69
16_2nd		-
16_3rd		62

Fig.A8.6 IR1 reduction multifilament tape, Ag filament-Ag tube, 0.0600" starting diameter.

Roller gauge read	Deformed sample by 5% reduction (MONOFILAMENT)	Average thickness [x10^{-4} inch]
58		413
53		379
50		360
48		342
45		327
43		297
42		287
41		277
39		258
36		232
35		221
34		212
32		197
30		179
29		170
28		161
27		155
26		144
25		135
24		127
23		117

Fig.A8.7 5% reduction monofilament tape, Ag tube, 0.0500” starting diameter.

22		107
21		98
20		92
19		84
18		78
17		72
16		64
15		56

Fig.A8.7 continued.

Roller gauge read	Deformed sample by 10% reduction (MONOFILAMENT)	Average thickness [x10^{-4} inch]
55		392
50	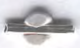	358
45		317
42		289
39		278
36		235
34		217
31		193
29		175
27		155
25		141
24		127
22		111
21		101
20		91
19		81
17		70
16		56

Fig.A8.8 10% reduction monofilament tape, Ag tube, 0.0500” starting diameter.

Roller gauge read	Deformed sample by 15% reduction (MONOFILAMENT)	Average thickness [x10^{-4} inch]
53		376
45		317
40		270
36		235
32		203
29		177
25		139
23		120
21		104
19		86
17		70
16		62

Fig.A8.9 15% reduction monofilament tape, Ag tube, 0.0500” starting diameter.

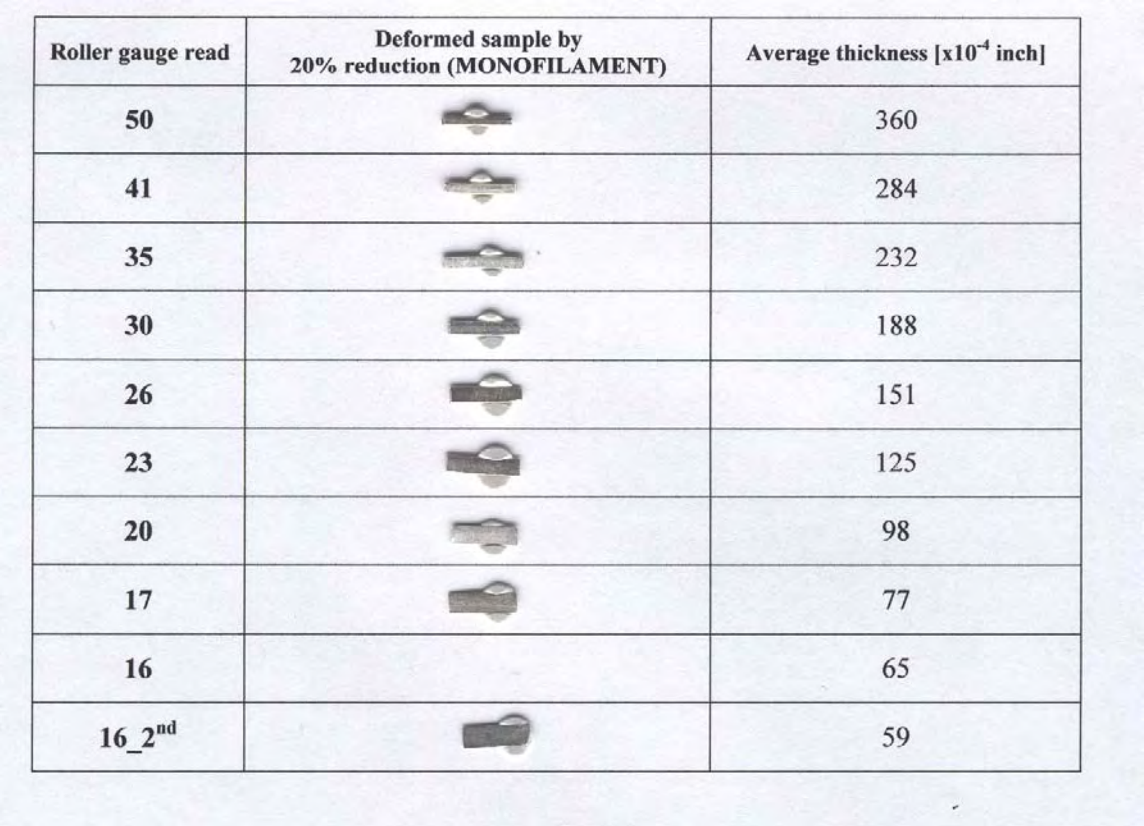

Roller gauge read	Deformed sample by 20% reduction (MONOFILAMENT)	Average thickness [x10^{-4} inch]
50		360
41		284
35		232
30		188
26		151
23		125
20		98
17		77
16		65
16_2nd		59

Fig.A8.10 20% reduction monofilament tape, Ag tube, 0.0500” starting diameter.

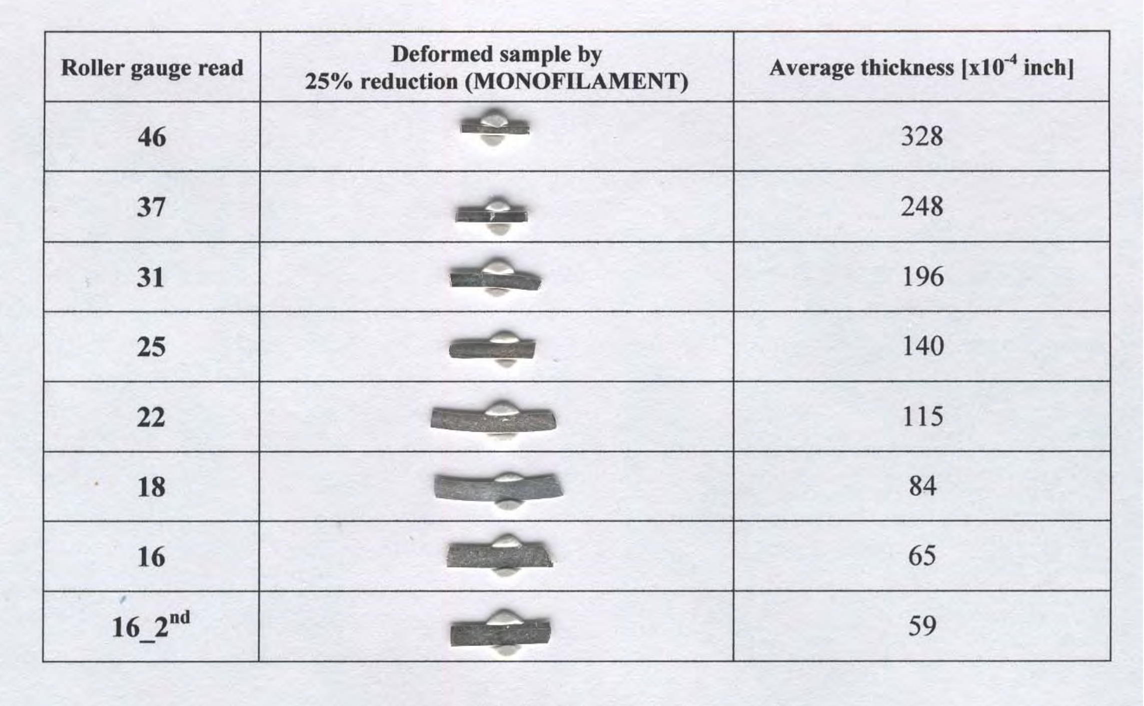

Roller gauge read	Deformed sample by 25% reduction (MONOFILAMENT)	Average thickness [x10^{-4} inch]
46		328
37		248
31		196
25		140
22		115
18		84
16		65
16_2nd		59

Fig.A8.11 25% reduction monofilament tape, Ag tube, 0.0500” starting diameter.

Roller gauge read	Deformed sample by 30% reduction (MONOFILAMENT)	Average thickness [x10^{-4} inch]
44		308
34		222
27		160
22		117
18		84
16		65
16_2nd		63
16_3rd		60

Fig.A8.12 30% reduction monofilament tape, Ag tube, 0.0500” starting diameter.

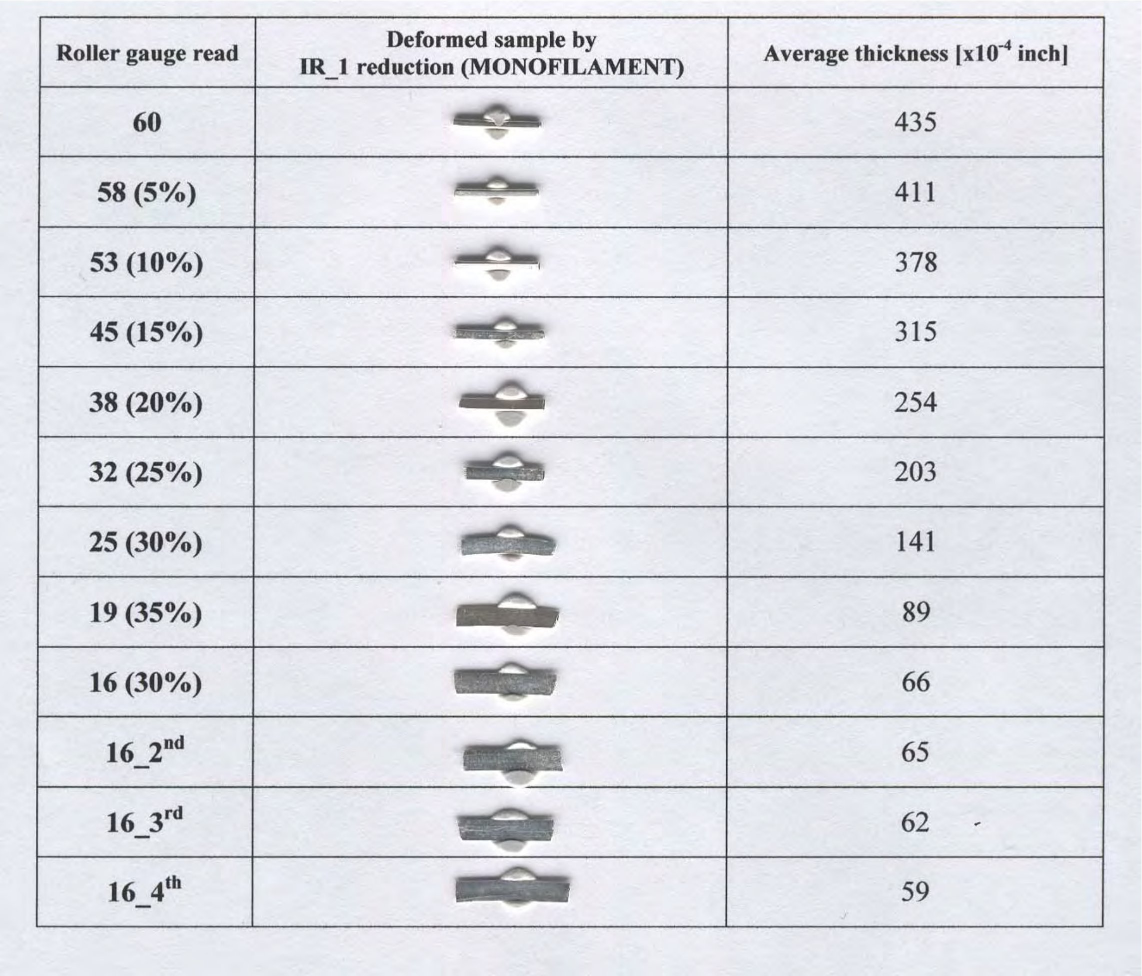

Roller gauge read	Deformed sample by IR_1 reduction (MONOFILAMENT)	Average thickness [x10^{-4} inch]
60		435
58 (5%)		411
53 (10%)		378
45 (15%)		315
38 (20%)		254
32 (25%)		203
25 (30%)		141
19 (35%)		89
16 (30%)		66
16_2nd		65
16_3rd		62
16_4th		59

Fig.A8.13 IR1 reduction monofilament tape, Ag tube, 0.0500” starting diameter.

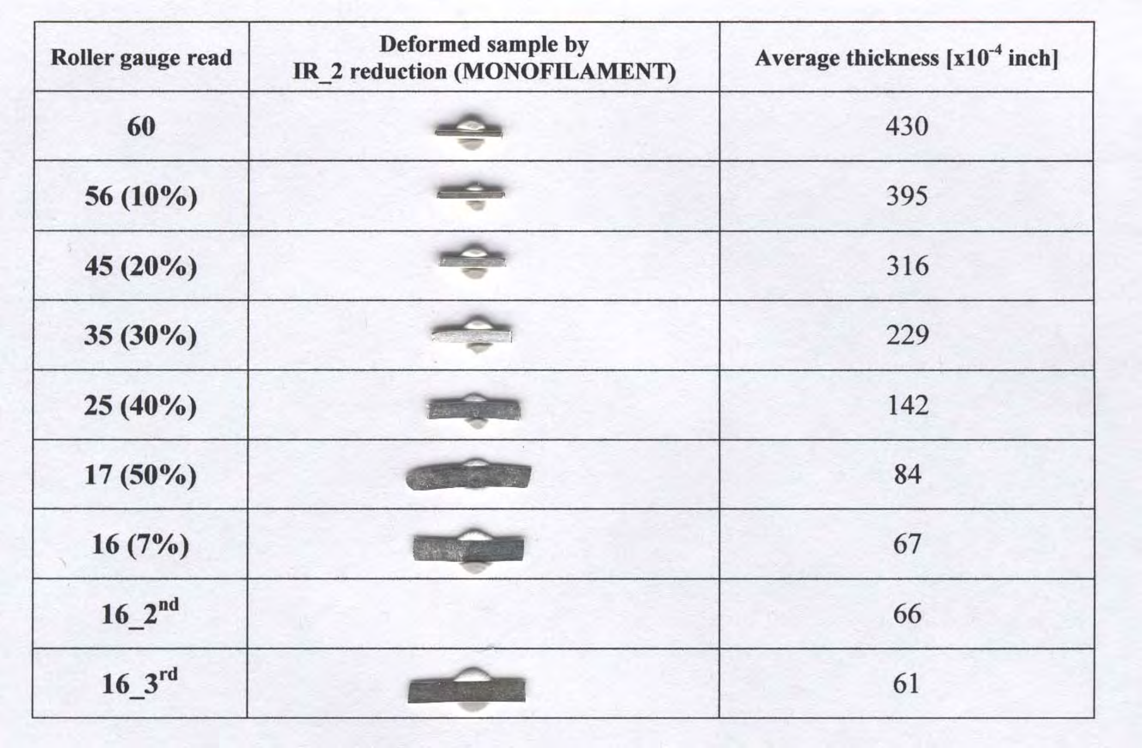

Roller gauge read	Deformed sample by IR_2 reduction (MONOFILAMENT)	Average thickness [x10^{-4} inch]
60		430
56 (10%)		395
45 (20%)		316
35 (30%)		229
25 (40%)		142
17 (50%)		84
16 (7%)		67
16_2nd		66
16_3rd		61

Fig.A8.14 IR2 reduction monofilament tape, Ag tube, 0.0500” starting diameter.

Roller gauge read	Deformed sample by 5% reduction (MONOFILAMENT_Mg)	Average thickness [x10^{-4} inch]
58		418
53		385
50		362
48		343
45		317
43		296
42		286
41		276
39		260
36		232
35		220
34		213
32		199
30		183
29		170
28		160
27		151
26		143
25		132
24		123
23		115

Fig.A8.15 5% reduction monofilament tape, Mg tube, 0.0500” starting diameter.

22		106
21		97
20		89
19	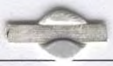	81
18		72
17		65
16		59

Fig.A8.15 continued.

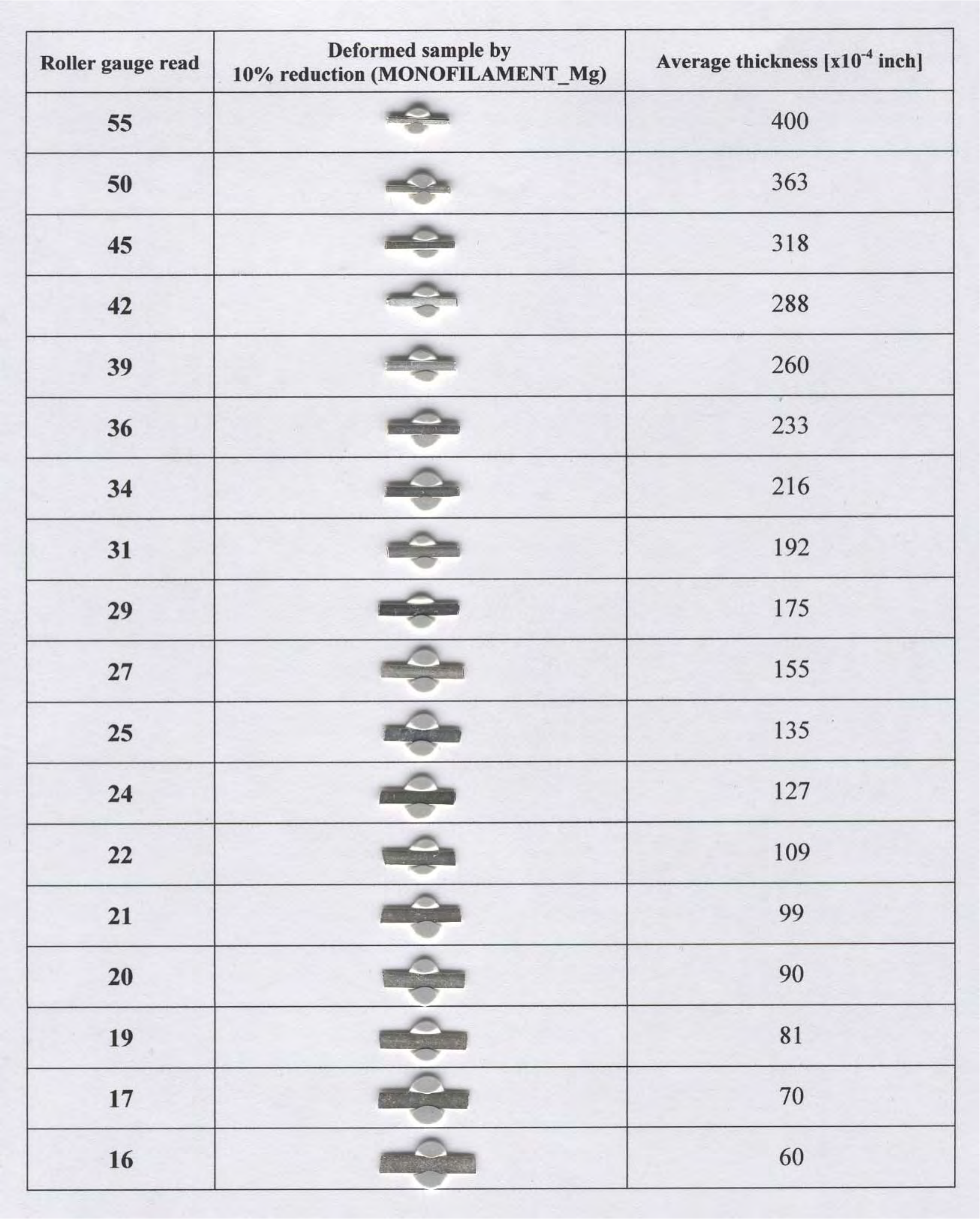

Roller gauge read	Deformed sample by 10% reduction (MONOFILAMENT_Mg)	Average thickness [x10^{-4} inch]
55		400
50		363
45		318
42		288
39		260
36		233
34		216
31		192
29		175
27		155
25		135
24		127
22		109
21		99
20		90
19		81
17		70
16		60

Fig.A8.16 10% reduction monofilament tape, Mg tube, 0.0500” starting diameter.

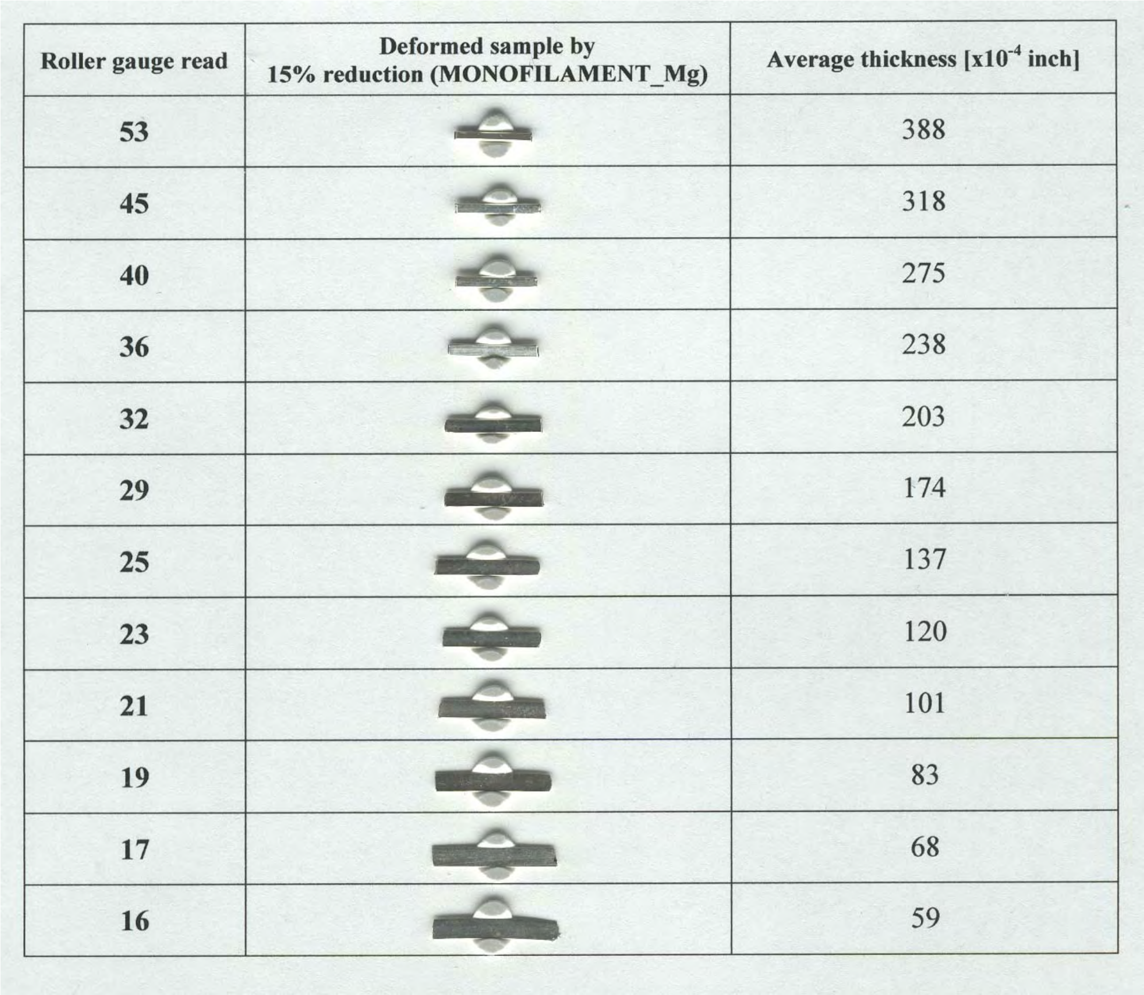

Roller gauge read	Deformed sample by 15% reduction (MONOFILAMENT_Mg)	Average thickness [x10^{-4} inch]
53		388
45		318
40		275
36		238
32		203
29		174
25		137
23		120
21		101
19		83
17		68
16		59

Fig.A8.17 15% reduction monofilament tape, Mg tube, 0.0500" starting diameter.

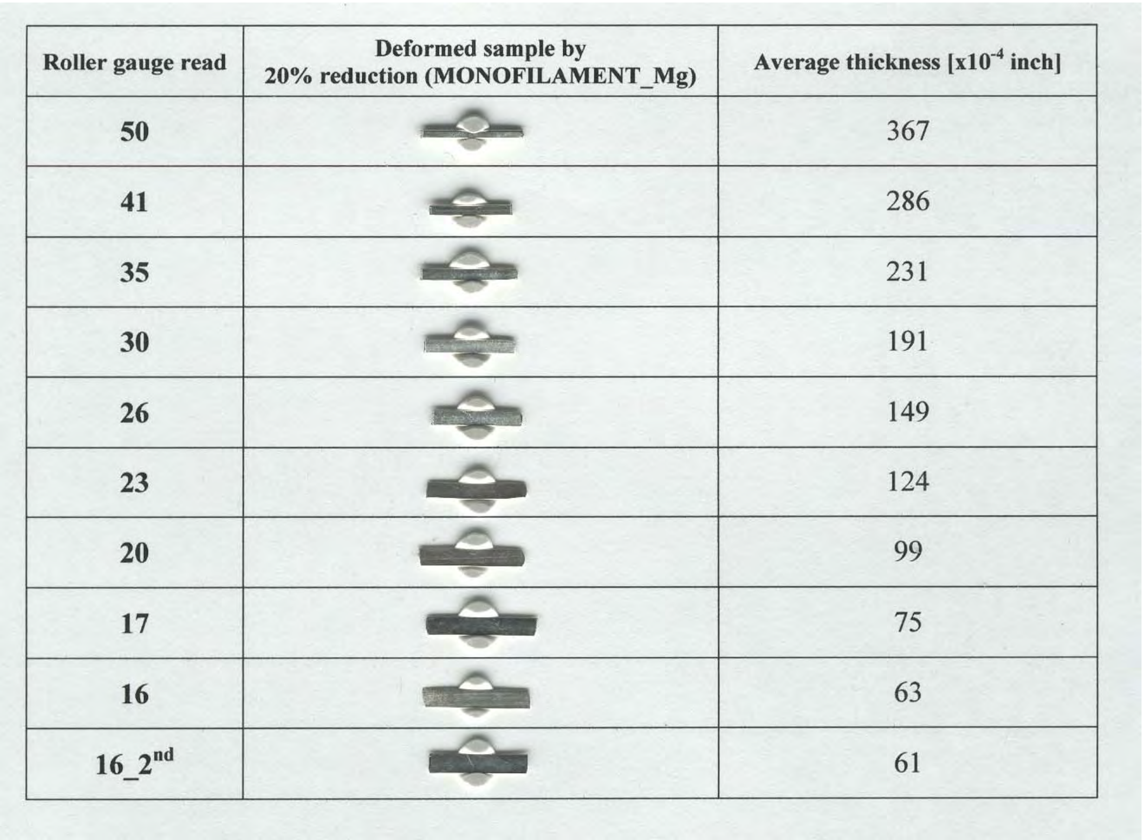

Roller gauge read	Deformed sample by 20% reduction (MONOFILAMENT_Mg)	Average thickness [x10^{-4} inch]
50		367
41		286
35		231
30		191
26		149
23		124
20		99
17		75
16		63
16_2nd		61

Fig.A8.18 20% reduction monofilament tape, Mg tube, 0.0500” starting diameter.

Roller gauge read	Deformed sample by 25% reduction (MONOFILAMENT_Mg)	Average thickness [x10^{-4} inch]
46		337
37		259
31		199
25		142
22		120
18		85
16		69
16_2nd		66
16_3rd		63

Fig.A8.19 25% reduction monofilament tape, Mg tube, 0.0500” starting diameter.

Roller gauge read	Deformed sample by 30% reduction (MONOFILAMENT_Mg)	Average thickness [x10^{-4} inch]
44		320
34		223
27		165
22		119
18		84
16		71
16_2nd		66
16_3rd		64

Fig.A8.20 30% reduction monofilament tape, Mg tube, 0.0500” starting diameter.

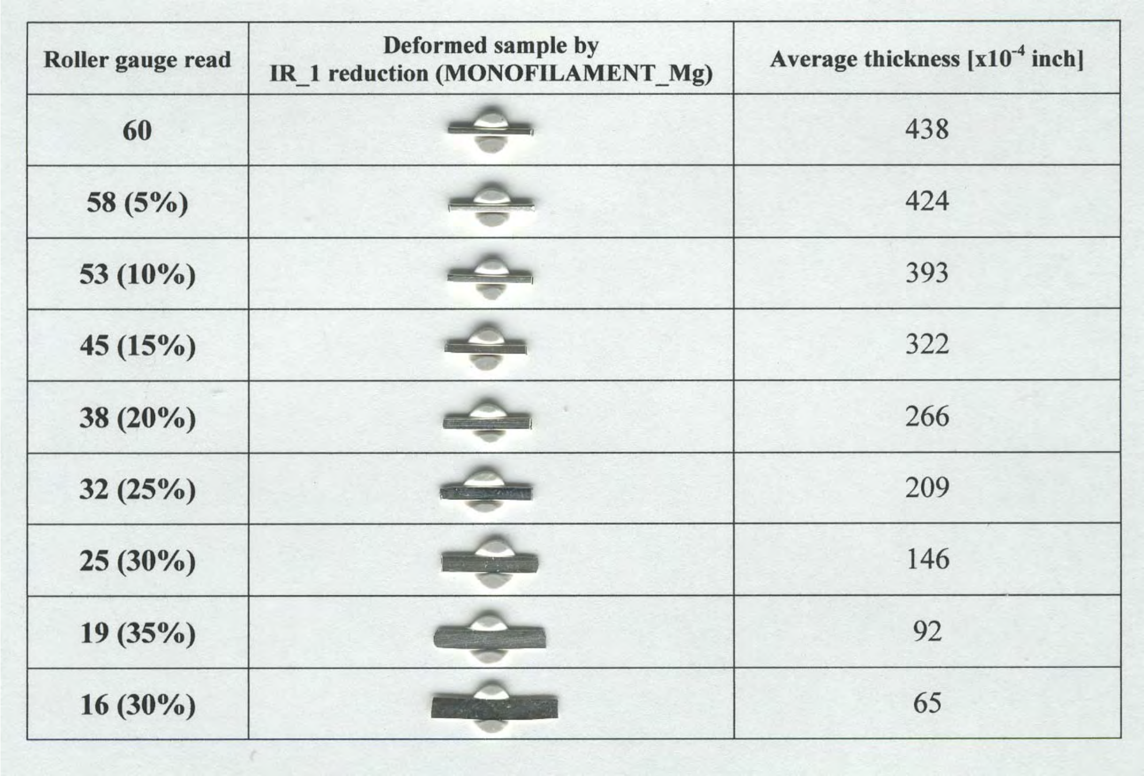

Roller gauge read	Deformed sample by IR_1 reduction (MONOFILAMENT_Mg)	Average thickness [x10^{-4} inch]
60		438
58 (5%)		424
53 (10%)		393
45 (15%)		322
38 (20%)		266
32 (25%)		209
25 (30%)		146
19 (35%)		92
16 (30%)		65

Fig.A8.21 IR1 reduction monofilament tape, Mg tube, 0.0500” starting diameter.

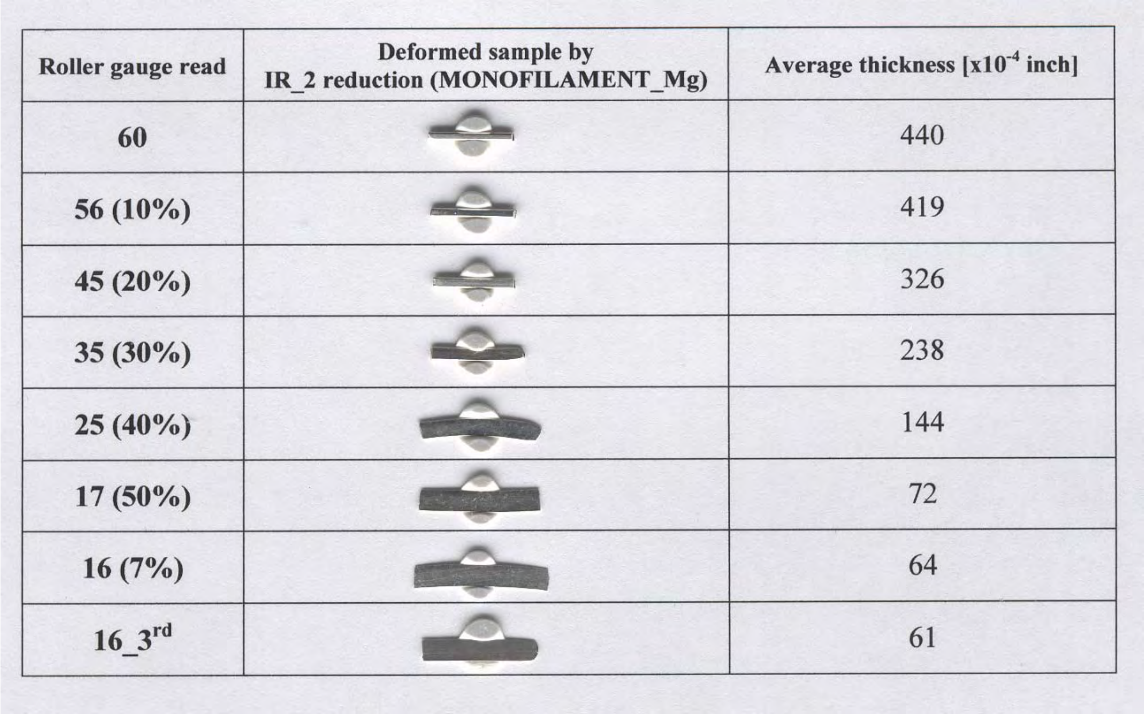

Roller gauge read	Deformed sample by IR_2 reduction (MONOFILAMENT_Mg)	Average thickness [x10^{-4} inch]
60		440
56 (10%)		419
45 (20%)		326
35 (30%)		238
25 (40%)		144
17 (50%)		72
16 (7%)		64
16_3rd		61

Fig.A8.22 IR2 reduction monofilament tape, Mg tube, 0.0500” starting diameter.

Roller gauge read	Deformed sample by 5% reduction (Mg FILAMENT-Mg TUBE, ∅ 0.0500)	Average thickness [x10^{-4} inch]
58		421
53		384
50		358
48		340
45		313
43		294
42		283
41		272
39		254
36		229
35		218
34		208
32		189
30		172
29		162
28		153
27		143
26		134
25		125
24		117

Fig.A8.23 5% reduction multifilament tape, Mg filament-Mg tube, 0.0500” starting diameter.

23		108
22		100
21		92
20		83
19		73
18		67
17		59

Fig.A8.23 continued.

Roller gauge read	**Deformed sample by 25% reduction (Mg FILAMENT-Mg TUBE, ∅0.0500)**	**Average thickness [x10^{-4} inch]**
46		324
37		247
31		191
25		136
22		109
18		76
16		60

Fig.A8.24 25% reduction multifilament tape, Mg filament-Mg tube, 0.0500” starting diameter.

Roller gauge read	Deformed sample by IR_1 reduction (Mg FILAMENT-Mg TUBE, ∅ 0.0500)	Average thickness [x10^{-4} inch]
60		432
58 (5%)		411
53 (10%)		380
45 (15%)		317
38 (20%)		248
32 (25%)		199
25 (30%)		137
19 (35%)		85
16 (30%)		63

Fig.A8.25 IR1 reduction multifilament tape, Mg filament-Mg tube, 0.0500” starting diameter.

Roller gauge read	Deformed sample by 5% reduction (Ag FILAMENT-Mg TUBE, ∅ 0.0500)	Average thickness [x10^{-4} inch]
58		419
53		393
50		383
48		342
45		315
43		295
42		285
41		276
39		258
36		232
35		220
34		211
32		195
30		177
29		166
28		156
27		146
26		137
25		133
24		122

Fig.A8.26 5% reduction multifilament tape, Ag filament-Mg tube, 0.0500" starting diameter.

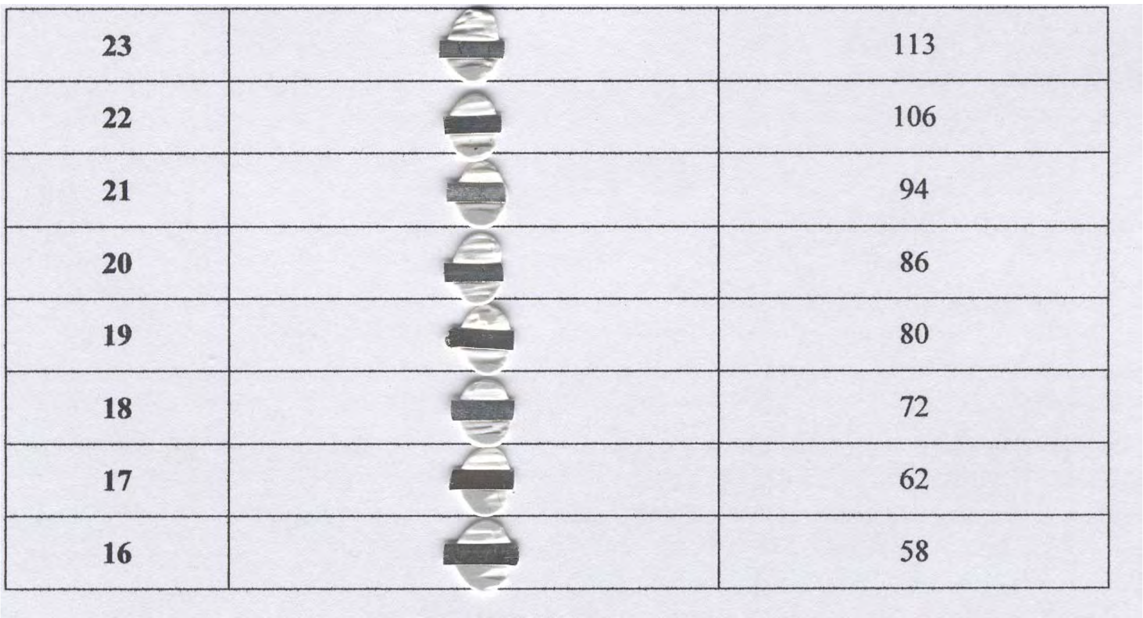

23		113
22		106
21		94
20		86
19		80
18		72
17		62
16		58

Fig.A8.26 continued.

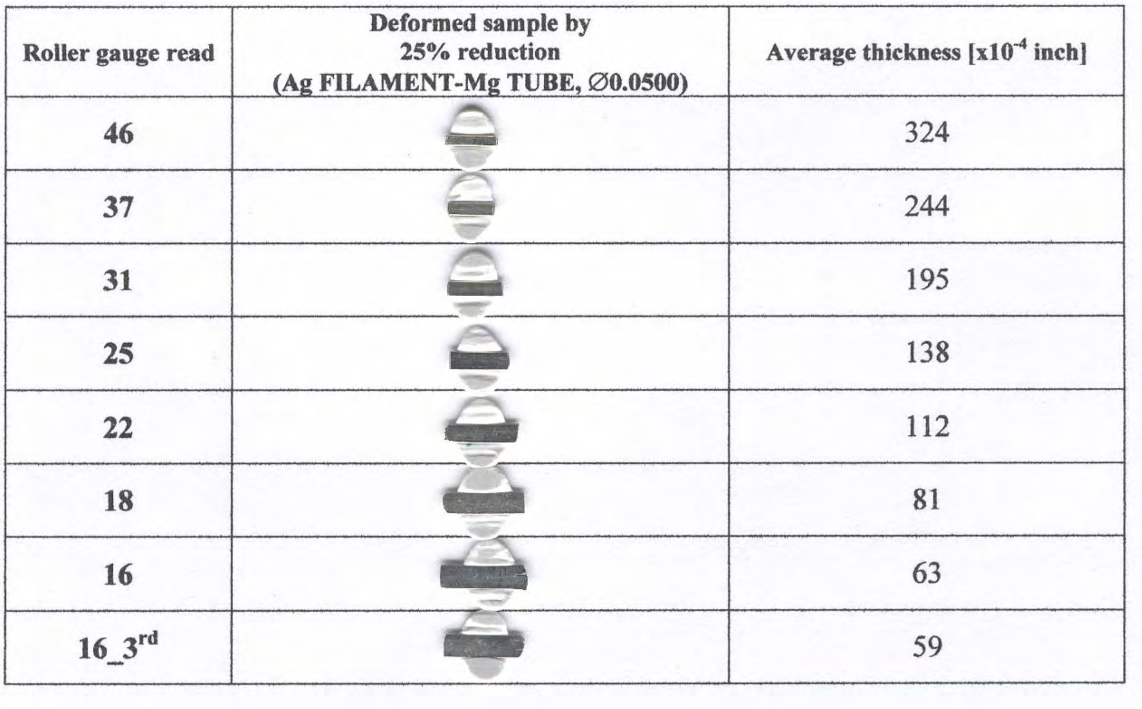

Roller gauge read	**Deformed sample by 25% reduction (Ag FILAMENT-Mg TUBE, ∅0.0500)**	**Average thickness [x10^{-4} inch]**
46		324
37		244
31		195
25		138
22		112
18		81
16		63
16_3rd		59

Fig.A8.27 25% reduction multifilament tape, Ag filament-Mg tube, 0.0500” starting diameter..

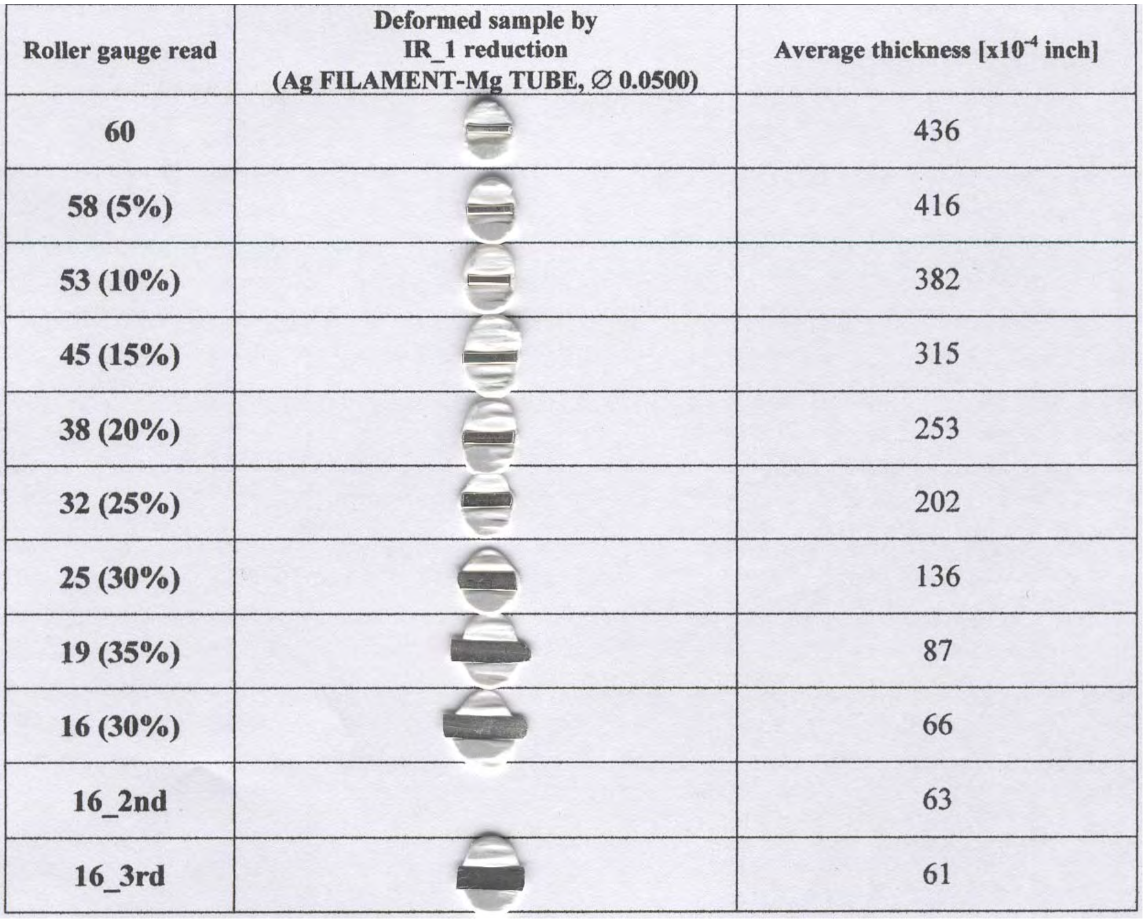

Roller gauge read	Deformed sample by IR_1 reduction (Ag FILAMENT-Mg TUBE, ∅ 0.0500)	Average thickness [x10^{-4} inch]
60		436
58 (5%)		416
53 (10%)		382
45 (15%)		315
38 (20%)		253
32 (25%)		202
25 (30%)		136
19 (35%)		87
16 (30%)		66
16_2nd		63
16_3rd		61

Fig.A8.28 IR1 reduction multifilament tape, Ag filament-Mg tube, 0.0500” starting diameter.

VITA

Mr. Burak Basaran was born in 1974, in Ankara, Turkey. He is a proud member of the class of ’96, Gazi Anatolian High, in Ankara. He acquired his Bachelor of Science (B.S.) degree in mechanical engineering from Osmangazi University (formerly known as Engineering and Architecture Faculty of Anadolu University), Eskisehir in 1996. One year later, he started his graduate studies as a Master of Science (M.S.) candidate in mechanical engineering department of Gazi University, Ankara. Meanwhile, he served there as a research/teaching assistant until June 2000.

When the Fulbright Program of International Educational and Cultural Exchange honored him with full scholarship, he attended Texas A&M University’s mechanical engineering graduate program in fall 2000. He holds another M.S. in mechanical engineering from Gazi University, conferred in June 2001.

His permanent address is: Gokdere Sokak, No: 12/17, 06550, Y. Ayranci, Ankara, Turkey. He can also be reached through his advisor, Dr. Mustafa Yavuz of Texas A&M University, Mechanical Engineering Department, College Station, TX, 77843.
E-mail: basaranb_tr@hotmail.com

Mr. Basaran strongly anticipates pursuing Ph.D. studies in solid mechanics and materials science, in the same department at Texas A&M University, starting in fall 2003.